Author:
Maraviglia, Nicola

Title:
Simulating open quantum systems in integrated photonics

Simulating open quantum systems in integrated photonics

By

NICOLA MARAVIGLIA

UNIVERSITY OF BRISTOL

A dissertation submitted to the University of Bristol
in accordance with the requirements of the degree of
DOCTOR OF PHILOSOPHY in the Faculty of Science.

SCHOOL OF PHYSICS

DECEMBER 2019

Word count: (approx) forty thousand

Abstract

Computational modelling of molecular dynamics and chemical reactions can lead to the discovery of new drugs and catalysts, with great social and economic repercussions. In general, the accurate quantum mechanical simulation of these systems is intractable to classical computers. Fortunately, a new computing paradigm that harnesses the properties of engineered quantum systems promises to close this computational gap.

With the aid of integrated photonics circuits, quantum optical systems are candidate platforms for near term quantum processors, with the required complexity to perform meaningful simulations. To achieve this goal, two conditions need to be met: certified reliable operation of the device and minimisation of the resource overhead for the simulation of accurate and realistic models. The results of this thesis support the development of integrated optics as a platform for quantum simulations by testing new protocols for device characterisation and demonstrating new mappings to simulate open quantum systems.

We started by testing a novel algorithm for the reconstruction of the transfer matrix of linear optical devices, and developed a characterisation procedure for the noise originated by the crosstalk between tunable components of the integrated circuit. We proceeded by using our quantum device to simulate molecular systems. We mapped the evolution of molecular vibrations on multi-photon states and modelled the thermalisation and the dephasing caused by an external environment. Additionally, we used the outcomes from our quantum simulator as a feedback for an optimisation routine aiming to improve the dissociation rate of ammonia. In a second set of simulations, we used our photonic device to reproduce the dynamics of non-Hermitian systems. We evolved a parity-time symmetric system with a time dependent Hamiltonian, testing its coherence in a noisy environment. Finally, we presented a new algorithm, tailored on quantum photonics applications, for more efficient simulations of system-environment interactions.

ACKNOWLEDGEMENTS

I'd like to thank my parents who supported my choice of moving abroad and are patiently waiting for me to come back. I am also happy to take the opportunity to thank the friends and colleagues that supported me during the PhD studies.

I start by thanking Anthony, my supervisor, for giving me these opportunities. I am also grateful to Dondü, Gary, Jorge, Nicky and Alberto who welcomed me here when I first started this new experience. In these years, I had the chance to learn from many great colleagues I worked with. Although he won't be able to read this, a special acknowledgement goes to Chris Harrold who guided my first steps in the lab. Then, I also had the good fortune to work with Chris Sparrow and Alex Neville to whom I owe a lot.

I enjoyed most of the time in Bristol together with the Italians of QETLabs. This experience would have been much less fun without Giacomo, Andreas, Caterina and Stefano. Thanks to you all for enriching these years. Special thanks to Stasja too: you are an amazing person and our chats have been some of the best moments for me in Bristol.

Further, I thank and wish the best of luck to Alex and Patrick for their generous help, the long scientific discussions, and the valuable time spent together. I am also thankful to Yogesh Joglekar, Ross and Levon who helped me navigating in the twisted field of non-conventional Hamiltonians.

Final acknowledgements to the friends and colleagues with whom I had inspiring and amusing conversations in the office and a variety of movie nights: many thanks to Rachel, Konstantina, Brian, Ross, Patrick, Alex and Jake.

AUTHOR'S DECLARATION

I declare that the work in this dissertation was carried out in accordance with the requirements of the University's Regulations and Code of Practice for Research Degree Programmes and that it has not been submitted for any other academic award. Except where indicated by specific reference in the text, the work is the candidate's own work. Work done in collaboration with, or with the assistance of, others, is indicated as such. Any views expressed in the dissertation are those of the author.

SIGNED: ..... DATE: .....

TABLE OF CONTENTS

Page

List of Figures **xi**

1 Introduction **1**
1.1 Thesis outline 2

2 Background **5**
2.1 Elements of quantum mechanics and quantum information 6
2.1.1 Representation of a quantum system 6
2.1.2 Composite systems and entanglement 8
2.1.3 Measurements and observables 9
2.1.4 Kraus operator formalism 10
2.1.5 Master equation and Lindblad formalism 11
2.1.6 Singular value decomposition and unitary dilation methods 13
2.1.7 Qubit and Pauli matrices 14
2.2 Elements of quantum optics 15
2.2.1 Algebra and quantum state representation 15
2.2.2 Some noticeable states of the electromagnetic field 16
2.2.3 Linear optical transformations 17
2.2.4 Hong Ou Mandel interference 19
2.2.5 Probabilities via permanent 21
2.2.6 Qubit encoding and quantum gates 22
2.3 Elements of integrated optics 23
2.3.1 Waveguide couplers 25
2.3.2 Thermal phase-shifters 26
2.3.3 Mach-Zehnder interferometers 27
2.3.4 Optical input-output 29
2.3.5 Photon sources 29
2.4 Considerations on experimental quantum photonics 30
2.4.1 Transfer matrix composition 30

2.4.2 Linear losses and post-selection . . . 32
2.5 Quantum simulation . . . 33
2.5.1 Quantum simulation with photonics . . . 35
2.5.2 Boson sampling . . . 35

3 Experimental setup 37
3.1 Uniaxial materials . . . 37
3.2 Photon pair sources . . . 39
3.3 Programmable integrated interferometer . . . 41
3.4 Photon detection . . . 42
3.5 Performance . . . 43
3.5.1 Photon interference . . . 43
3.5.2 Optical chip performance . . . 45

4 Characterisation of integrated optical circuits 47
4.1 Transfer matrix verification protocols . . . 48
4.1.1 Phaselift reconstruction algorithm . . . 49
4.1.2 Super-stable tomography . . . 54
4.2 Experimental reconstruction . . . 56
4.3 Extension of the phaselift algorithm . . . 62
4.4 Crosstalk study . . . 66
4.4.1 Experimental estimation of the crosstalk . . . 67
4.4.2 Results . . . 72
4.5 Discussion . . . 75

5 Quantum simulation of molecular vibrations 79
5.1 Atomic vibrations in molecules . . . 80
5.2 Simulations in the harmonic approximation . . . 82
5.2.1 Simulation mapping . . . 82
5.2.2 Experiment . . . 83
5.3 Simulating the effects of an environment . . . 88
5.3.1 Energy transfer in N-Methylacetamide . . . 88
5.3.2 Vibrational relaxation in liquid water . . . 89
5.4 Beyond harmonic dynamics . . . 92
5.4.1 Simulating anharmonic potentials . . . 92
5.4.2 Improving dissociation with a hybrid feedback algorithm. . . . 94
5.5 Discussion . . . 96

6 Quantum simulation of parity-time symmetric systems 99

6.1 Non-Hermitian Hamiltonians in quantum mechanics 100
6.2 Parity-time symmetric Hamiltonians 101
6.2.1 Pseudo-Hermiticity and state normalisation 103
6.2.2 Applications of PT-symmetric systems 104
6.3 Simulation of PT-symmetric systems 105
6.3.1 The simulation model we adopted 106
6.4 Simulation results 108
6.4.1 Unbroken and broken symmetry regimes 109
6.4.2 Time dependent Hamiltonian evolution 113
6.4.3 Evolution of coupled PT symmetric systems 116
6.5 Discussion 120

7 Perturbative open system quantum simulation with photonics 123
7.1 Collision model 124
7.2 Perturbative solutions of the open system dynamics 126
7.2.1 Numerical simulation 129
7.3 Photonic quantum simulations based on probabilistic heralded sources 131
7.3.1 Chip design 134
7.4 Discussion 135

8 Conclusion 139

A Simulation of molecular vibration: complementary information 141

B Quantum simulation of parity-time symmetric systems: complementary information 143

C Perturbative open system quantum simulation with photonics: complementary information 145

Bibliography 151

List of Figures

Figure **Page**

2.1 Integrated waveguide couplers 25
2.2 Schematics of MZI and asymmetric MZI 28
2.3 Universal interferometer circuits 31

3.1 Non-linear optical processes in χ^2 materials 38
3.2 Setup of the SPDC photon pair source 40
3.3 Schematic of the optical circuit of the integrated interferometer 42
3.4 Photon pair visibility 44
3.5 Chip characterisation 46

4.1 Experimental diagram for phaselift reconstructions 51
4.2 Simulated reconstruction performance of 5-dimensional unitaries 52
4.3 Resource scaling for the phaselift protocol 53
4.4 Scheme to implement the phaselift reconstruction in the integrated device 56
4.5 Examples of visibility curves for the super-stable reconstruction 59
4.6 Comparison between reconstructed transfer matrices 60
4.7 Unitary properties of the reconstructed transfer matrices 60
4.8 Experimental reconstruction distance for 3- and 5-dimensional transfer matrices 61
4.9 Extension of the phaselift application 63
4.10 Example of optical circuit controlled by external voltages 67
4.11 Map of the phase-shifters for the crosstalk measurement 69
4.12 Scaling factors distribution for several phase-shifters 73
4.13 Quadratic regression for different pairs of phase-shifter and control voltages . . 74

5.1 Mapping of the molecule evolution on the integrated chip 84
5.2 Quantum simulation of H_2CS with multiple vibrational excitations 86
5.3 Quantum simulation of a set of 4-atom molecules in harmonic approximation . . 87
5.4 Visual representation of localised backbone modes of N-Methylacetamide 88
5.5 Quantum simulation of NMA affected by a dephasing environment 90

5.6 Simulation of H_2O thermalisation 91
5.7 Simulation of anharmonic potential in H_2O 93
5.8 Optimisation of the dissociation rate of NH_3 96

6.1 Probability evolution of an excitation in the forward subsystem 109
6.2 Evolution of a $\mathcal{PT}$ system in multiple regions of the parameter space 110
6.3 Evolution of a 3-dimensional $\mathcal{PT}$ system initialised in three symmetric input states 112
6.4 Transition probability between two-photon states 113
6.5 Time dependent $\mathcal{PT}$ Hamiltonian evolution in a dephasing channel 115
6.6 Entropy evolution of an initially pure state 117
6.7 Entropy evolution of an initially completely mixed state 118
6.8 Expectation value of $\mathcal{P}$ as function of the coherence between forward and reverse subspaces. 119
6.9 Evolution of a pure global state 120

7.1 Relative error for different perturbation orders of the approximated solution . . 130
7.2 Event rate increase due to scattershot approach in the perturbative simulation . 134
7.3 Circuit layout and functional diagram for perturbative simulations 136

CHAPTER 1

INTRODUCTION

Quantum mechanics offered an extraordinary understanding of the microscopic structure of nature. In addition to all the benefits brought to chemistry [1–3], this knowledge made possible many of the revolutionary technologies of the last century: electronics [4], lasers [5, 6], nuclear energy [7], photovoltaics [8] and important imaging systems for medical diagnosis such as NMR and PET [9, 10], to mention but a few. Even counterintuitive predictions such as non-locality have been accurately verified [11, 12]. However, due to the level of complexity that the description of a quantum system can assume, the full predictive power of quantum mechanics is yet limited by the computational power available [13].

Over the last decades, the level of control of individual quantum systems has grown fast. We are now able to engineer, in controlled environments, coherent superpositions of macroscopic systems [14, 15], as well as generate and distribute entanglement between distant systems [16]. Alongside the experimental progress, a whole new research field has developed: quantum information and computation, based on the opportunity of storing informations in the states of quantum systems.

Among the future applications of the new quantum technologies, the most challenging objective is the realisation of a quantum computer [17, 18], a multipurpose device that can perform algorithms as a conventional computer but is able to outperform classical machines in important tasks [19]. As meeting this ambitious goal might yet require many decades, research centres are currently investigating the potentiality of alternative, more focused, quantum solutions to perform simulation of physical systems or optimisation algorithms [20–22]. Analogue simulators, dedicated to the exploration of physical properties of complex quantum systems, fall within this category [21, 23]. These simulators are based on the creation of an artificial replica of the complex system in which controllable or engineered

components replace the original constituents of the system. The numerical simulations are then replaced by a selection of measurements on the artificial system.

Based on this paradigm, the experimental and theoretical work presented in this thesis focuses on the use of discrete particles of light, photons, to perform simulations of other quantum systems. Cryogenic temperature and vacuum conditions are not fundamental requirements for the preservation of the quantum properties of the electromagnetic field. Compared with other potential platforms, this makes quantum optics a valid candidate for a more affordable realisation of quantum devices. Furthermore, the adoption of integrated optical circuit for the manipulation of the states of light provides a reliable solutions for the scaling up of the complexity of these experiments [24, 25].

Several technological challenges have to be faced in order to produce an optical quantum device able to replace a classical machine in practical applications. However, the experimental realisation of quantum protocols is the lifeblood for the development of quantum technologies, and benefits can arise from their implementation on any platform. The development of embryonic quantum technologies can stimulate models for error analysis and mitigation, new mapping solutions, schemes for resource optimisation, development of new computation paradigms, etc. In particular, optical systems can represent a test bed for protocols that can be replicated in other bosonic quantum systems such as microwaves, vibrations of trapped atoms, and superconducting resonators [26–31].

1.1 Thesis outline

The main body of this thesis is organised in 6 chapters supplemented by this introductory chapter, by a conclusion chapter and by a small appendix section. In Chapter 2, the background, I summarise the concepts required for a coherent understanding of the thesis. Although treated at a basic level, these cover the quantum description of a physical system, with particular attention to the electromagnetic field, and theoretical and experimental details of the manipulation of quantum states of light in integrated linear circuits. The chapter closes with few notions of quantum simulation. The preliminary part of this document continues in Chapter 3. This is dedicated to the description of the setup I used in the experiments presented in chapters 4-6. The original contributions of this thesis are distributed among the chapters 4-7.

In Chapter 4, I study the optical quantum device from the hardware prospective. Indeed, the precision of a large system simulation depends on the level of control we have on our device, that needs therefore to be assessed. The chapter is made of two blocks. The first consists in the implementation of a characterisation protocol for linear optical devices, named *phaselift*. The second concerns the investigation of thermal and electrical sources of crosstalk in integrated systems. In Chapter 5, I present a simulation protocol that

maps the evolution of atomic vibrations in molecules on optical quantum systems. The simulations include the effects of a surrounding environment by means of toy models of thermalisation and dephasing, as well as an example of quantum-classic hybrid algorithm that targets the dissociation rate of the molecule. Chapter 6 is dedicated to the simulation of systems governed by non-Hermitian Hamiltonians with particular attention to parity-time symmetric systems [32]. The mapping between our device and this family of systems is used to reproduce typical features of their evolution and observe their behaviour in a noisy environment. In particular, a series of time dependent Hamiltonian simulations is performed. In this chapter, I also simulate other forms of non-unitary evolution in an open quantum system model [33]. Finally, in Chapter 7, I present a design of a new protocol for the simulation of system-environment interaction that exploit the probabilistic nature of heralded processes in quantum optics.

At the beginning of every chapter, there is a prologue where I describe its contents and acknowledge the contributions that additional researchers made to that work. Then, a complementary explanation of the topics relevant for that particular chapter is given and the experimental and theoretical results are presented and discussed.

CHAPTER 2

BACKGROUND

Outline

In this chapter I will provide an introduction on recurrent topics of this thesis. The intent is to summarise the necessary definitions, equations and experimental considerations relevant to most of the chapters in this manuscript, covering aspects of quantum mechanics but also classical photonics. Additional information about characterisation of linear optical devices, molecular physics, non-Hermitian quantum systems and the collision model for the interaction of a system with the environment, will be provided in the related chapters 4, 5, 6, and 7, respectively.

In the first section I will recall few fundamentals of quantum mechanics and quantum information. The second section summarises quantum properties of the electromagnetic field, with greater attention to linear transformations. In this section I will also recall the connection between states of light and qubit gate operations typical of quantum information scenarios. The third section relates closely to the hardware realisation of an integrated device able to control the quantum state of light. I will list the functions of the building blocks appearing in the integrated optical circuits that are part of this work. In the fourth section, there is a description of few practical aspects of linear optical experiments. The conclusive section is reserved for a discussion about quantum simulation with special focus on the role played by linear optics and the description of boson sampling.

The topics and the level of details I chose for this chapter are strictly functional to offer an adequate understanding of what is presented in the subsequent chapters. The details of the derivation of the properties reported are generally omitted and can be found in the referred literature. Multiple textbooks offer a coverage of the subjects presented. Here are

the main ones I drew from to write down this chapter [34–37].

2.1 Elements of quantum mechanics and quantum information

2.1.1 Representation of a quantum system

Throughout the text we will make use of the Dirac notation to represent the vectors $|\psi\rangle$ of the Hilbert space $\mathcal{H}$. The inner product between $|\psi\rangle$ and an $|\phi\rangle$ is written as $\langle\phi|\psi\rangle$ where we assume the product to be antilinear in the first argument. To each quantum system is associated a Hilbert space $\mathcal{H}$. A *pure* state of this system is represented by a vector of $\mathcal{H}$ that, except when explicitly mentioned, we will assume to be normalised. A state vector multiplied by a phase factor $e^{i\phi}$ represents the same state of the system as the original vector.

In the Schrödinger representation, the time evolution of a pure state of an isolated system is described by the Schrödinger equation:

$$i\hbar\frac{\partial}{\partial t}|\psi\rangle = H|\psi\rangle. \tag{2.1}$$

In this equation, H is a self-adjoint operator: the *Hamiltonian* of the system. This is a system dependent operator whose spectrum of eigenvalues determines the possible outcomes of an energy measurement on the system. The adjoint $A^\dagger$ of an operator A is defined as the operator such that

$$|\phi\rangle = A^\dagger|\beta\rangle \implies \langle\phi|\psi\rangle = \langle\beta|\left(A|\psi\rangle\right)$$

for each $|\psi\rangle$ in the domain of A. A self adjoint operator is such that $A^\dagger = A$.

For a time independent H, the solution to the Schrödinger equation is obtained applying the unitary evolution operator $U(t,t_0) = \exp(-iH(t-t_0)/\hbar)$ to the initial state of the system.

$$|\psi(t)\rangle = U(t,t_0)|\psi(t_0)\rangle$$

In the text, we will often omit to specify t_0 when $t_0 = 0$. Similarly, in the following, $\hbar$ will be omitted assuming it as unit of action[1]. The selfadjointness of H, that for finite dimensional $\mathcal{H}$ corresponds to its Hermiticity[2], ensures that $U(t,t_0)$ is unitary. The "hat" symbol, used to mark endomorphism in $\mathcal{H}$ such as $\hat{H}$, will be used to prevent confusion, when necessary, and omitted, otherwise.

A mixed state of a system is represented by a linear operator $\rho : \mathcal{H} \to \mathcal{H}$, called *density matrix* or *density operator*. In order for ρ to represent a physical system, it needs to satisfy the following properties:

[1] We remind that, in the international system of units, $\hbar = 1.0546 \times 10^{-34} J \cdot s$.

[2] The Hermiticity condition states that for each choice of vectors in the domain of H, $\langle\phi|H|\psi\rangle = \langle\psi|H|\phi\rangle^*$

- ρ is an Hermitian semi-positive definite matrix: $\forall |v\rangle\,,\ \langle v|\,\rho\,|v\rangle \geq 0$;
- the trace of ρ is 1: $\mathrm{tr}[\rho] = 1$,

where we indicated with tr[·] the trace of an operator defined as

$$\mathrm{tr}[A] = \sum_n \langle n|\,A\,|n\rangle\,.$$

Here $|n\rangle$ represent the elements of an orthonormal basis of $\mathcal{H}$. We recall that the trace of an operator is independent of the particular choice of the basis and satisfies the cyclic property: $\mathrm{tr}[ABC] = \mathrm{tr}[CAB]$.

Operationally, the density operator can be considered as the effect of classical uncertainty on the state of the system. It can arise, for example, from a noisy, fluctuating, state preparation procedure in an experiment. Considering the eigenvalue decomposition of $\rho = \sum_i p_i \left|\psi_i\right\rangle\left\langle\psi_i\right|$ with normalised eigenvectors $\left|\psi_i\right\rangle$, each observation on the system can be treated as if the system was in any of the pure states $\left|\psi_i\right\rangle$ with probability p_i, respectively. The semi-positivity of ρ ensures that $p_i \geq 0$ and, since $\mathrm{tr}[\rho] = \sum_i p_i = 1$, p_i represents a well defined probability distribution. As we will discuss, the state of a system can be mixed also because of the effect of a measurement apparatus or due to entanglement with external degrees of freedom (see Sec. 2.1.2 and Sec. 2.1.3).

A density matrix can also be used to represent a pure state $\left|\psi\right\rangle$. In such a case $\rho = \left|\psi\right\rangle\left\langle\psi\right|$ is a projector in the Hilbert space, $\rho^2 = \rho$. The *purity* μ of a mixed state, defined as $\mu = \mathrm{tr}[\rho^2]$, is an indication of how much the state differs from a pure state. The generalisation of the Schrödinger equation to the density operator is the von Neumann equation, also referred to as Liouville-von Neumann equation:

$$i\hbar\frac{\partial}{\partial t}\rho = [H,\rho]\,, \tag{2.2}$$

where $[\cdot,\cdot]$ is the commutator symbol, $[A,B] = AB - BA$. The solution to the evolution of the system can be written using the same evolution operator previously introduced.

$$\rho(t) = U(t,t_0)\rho(t_0)U^\dagger(t,t_0) \tag{2.3}$$

In general, Eq. 2.3 can be used to recast any unitary transformation applied to the state vector into an equivalent transformation of the density matrix.

Using the eigenvalues p_i of ρ, it is possible to associate to a quantum state an entropy $\mathcal{S}$. We will use the definition by von Neumann:

$$\mathcal{S} = -\sum_i p_i \ln(p_i)$$

but we will adopt the convention of the log base two that results in a multiplicative factor $1/\ln(2) = 1.4427$ with respect to the standard value of $\mathcal{S}$. This definition of entropy is not

affected by unitary transformations applied to the density matrix, thus the evolution of an isolated system as a whole does not affect its entropy. In the next subsection we will reconsider this statement for the case of the entropy of a part of a composite system.

2.1.2 Composite systems and entanglement

Most of the physical systems are made of multiple constituents, often a myriad. Here we address the description of a system that can be described as made of two separate sets of components that constitute two subsystems we label as A and B. Generally, a pure state of a composite systems, composed by two individual entities associate to Hilbert spaces $\mathcal{H}_A$ and $\mathcal{H}_B$, can be written as a vector in a Hilbert space $\mathcal{H}$ that is a tensor product of the two spaces $\mathcal{H} = \mathcal{H}_A \otimes \mathcal{H}_B$. Indicating with $|w_n\rangle$ and $|v_m\rangle$ two orthonormal bases of $\mathcal{H}_A$ and $\mathcal{H}_B$, respectively, a pure state $\big|\psi\big\rangle$ of the composite system can be decomposed as:

$$\big|\psi\big\rangle = \sum_{n,m} c_{n,m} \, |w_n\rangle \, |v_m\rangle \tag{2.4}$$

where $c_{n,m}$ are the coefficients in the derived basis of $\mathcal{H}$. However, the Schmidt decomposition provides an alternative representation of the state as a combination of a particular state-dependent orthonormal bases $|\alpha_n\rangle$ and $\big|\beta_m\big\rangle$ of the two spaces $\mathcal{H}_A$ and $\mathcal{H}_B$, respectively,

$$\big|\psi\big\rangle = \sum_{n} d_n \, |\alpha_n\rangle \, \big|\beta_n\big\rangle \, . \tag{2.5}$$

This rule is generally not applicable for systems composed of more than two entities.

Pure states are defined as being *separable* if they can be written as

$$\big|\psi\big\rangle = |\alpha\rangle \, \big|\beta\big\rangle \, . \tag{2.6}$$

Their generalisation to mixed states is given by the relation

$$\rho = \sum_{i} c_i \rho_{A,i} \otimes \rho_{B,i} \tag{2.7}$$

where $\rho_{A,i}$ and $\rho_{B,i}$ are valid density operators of $\mathcal{H}_A$ and $\mathcal{H}_B$, respectively, and c_i are positive coefficients. A state that is not separable is called entangled. The generalisation of entanglement for multipartite systems with more than two parts is discussed in [38].

If a composite system is in an entangled state, an observer that only measures the state of one of the two parties of the system, will perceive the observed system as mixed. Its density matrix can be written by introducing the partial trace operation tr_B:

$$\begin{aligned} \rho_A = \mathrm{tr}_B \left[\rho\right] &= \sum_i (\mathbb{1}_{\mathbb{A}} \otimes \langle v_i|_B) \; \rho \; (\mathbb{1}_{\mathbb{A}} \otimes |v_i\rangle_B) \\ &= \sum_i \langle v_i|_B \left(\sum_{n,n',m,m'} \rho_{n,n',m,m} \, |w_n\rangle_A \, \langle w_{n'}|_A \otimes |v_m\rangle_B \, \langle v_{m'}|_B \right) |v_i\rangle_B \\ &= \sum_{n,n'} \left(\sum_i \rho_{n,n',i,i} \right) |w_n\rangle_A \, \langle w_{n'}|_A \, , \end{aligned} \tag{2.8}$$

where we added subscripts to indicate the Hilbert space where the operators act. As an example, let's consider an entangled pure state such as

$$\rho = 0.5\big(|w_1\rangle|v_1\rangle + |w_2\rangle|v_2\rangle\big)\big(\langle w_1|\langle v_1| + \langle w_2|\langle v_2|\big).$$

The reduced system of A is described by the mixed density matrix $\rho_A = 0.5\big(|w_1\rangle\langle w_1| + |w_2\rangle\langle w_2|\big)$. Contrarily, the reduced density matrix of a pure separable state is a projector that represents a pure state.

A unitary transformation on a composite system can change its entanglement property. However, when we consider simple *local* unitaries U that can be written as $U = U_A \otimes U_B$ where U_A and U_B, only act on $\mathcal{H}_A$ and $\mathcal{H}_B$, respectively, the entanglement of the system does not change. Furthermore, under the same local unitary transformation, the reduced state of the system evolves as $\rho_A \to U_A \rho_A U_A^\dagger$. In the general case, Hamiltonians of composite systems include interaction potentials that determine non local unitary evolution. This evolution, that is able to create entanglement between the parties of the system, is a source of *decoherence* for a system that interacts with a surrounding environment. Here, decoherence refers to a non unitary evolution that tends to reduce the purity of the state.

2.1.3 Measurements and observables

For the application of the *scientific method*, based on the empirical verification of proposed theoretical models, it is crucial to be able to perform quantitative measurements and predict their outcomes. In quantum mechanics, observable quantities are associated with Hermitian operators on $\mathcal{H}$. The real spectrum of the operator is made of the possible outcomes of the measurement of that observable. The eigenvectors $\{|\epsilon_i, \ell\rangle\}_\ell$ of an observable A, associated with the same eigenvalue ϵ_i, can be used to create a projector $\hat{P}_i = \sum_\ell |\epsilon_i, \ell\rangle\langle\epsilon_i, \ell|$ onto a subspace of $\mathcal{H}$. The probability p_i of an outcome ϵ_i, for a measurement performed on the state $|\psi\rangle$, is the squared norm of the projection of $|\psi\rangle$ over the subspace associated with ϵ_i.

$$p_i = \langle\psi|\hat{P}_i|\psi\rangle. \tag{2.9}$$

The expectation value of A is therefore $\langle A\rangle = \sum_i \epsilon_i \langle\psi|\hat{P}_i|\psi\rangle = \langle\psi|A|\psi\rangle$. The same relations for a mixed state ρ read:

$$p_i = \mathrm{tr}\big[\hat{P}_i\rho\big] \qquad \langle A\rangle = \mathrm{tr}\big[A\rho\big]. \tag{2.10}$$

Commonly, the measurement of a single photons coincides with its absorption. The energy of the photon is transferred to the measurement instrument and the detected particle ceases to exist. Few attempts to detect a photon without absorbing its energy are still at the research stage [39–42].

In different contexts, the measurement of a quantum system can be less invasive and be described by projective measurements. After a projective measurement the state "collapses", i.e. get projected, on the subspace associated to the measurement outcome. However, after the projection, the state vector is normalised once again. The probabilistic outcome and the irreversible transformation of the system upon measurement make it impossible to determine the state of a quantum system, as it was before a measurement, with only a copy of the state and no assumptions. Instead, when it is possible to recreate multiple times the same state, by building up a statistic distribution of the outcomes, it is possible to infer more information of the state of the system. As we will see for the single qubit case in Sec. 2.1.7, it is possible to choose a set of observables sufficient to fully determine the state of the system.

The effect of a projective measurement on a state, before knowing the outcome of the measurement, can be expressed as a mixed state

$$\rho = \sum_i \langle\psi|\hat{P}_i|\psi\rangle \frac{\hat{P}_i|\psi\rangle\langle\psi|\hat{P}_i}{\langle\psi|\hat{P}_i|\psi\rangle} = \sum_i \hat{P}_i|\psi\rangle\langle\psi|\hat{P}_i.$$

This representation of the state is also suitable to predict the outcome of a subsequent measurement on the state when the information of the first measurement is not accessible.

2.1.4 Kraus operator formalism

We have up to know stated that an isolated system, no matter if multipartite, evolves in time with a unitary evolution operator. We further affirmed that such transformations does not change the entropy of the system as a whole. Conversely, transforming a pure state from separable to entangled could change the entropy of a subsystem. We now explore a bit further this aspect.

If we assume that our system is not isolated, being part of an unknown multipartite system, the evolution of its density matrix ρ_A is not described anymore by a unitary transformation. However, it is possible to introduce an evolution map $\mathcal{E}(t,t_0)[\cdot]$ such that $\forall\rho_A(t_0),\quad \rho_A(t) = \mathcal{E}(t,t_0)\left[\rho_A(t_0)\right]$ where we imply that the transformation of the density matrix of the reduced system is linear. For example, the linearity can be assumed if the system A is not entangled with the rest of the multipartite system at $t = t_0$.

$$\mathcal{E}(t,t_0)\left[\rho_A(t_0)\right] = \mathrm{tr}_B\left[U(t,t_0)\rho_A\otimes\rho_B U^\dagger(t,t_0)\right] \tag{2.11}$$

In particular, for any *completely positive, trace-preserving, convex-linear map* $\mathcal{E}(t,t_0)$, it is possible to introduce a fictitious bipartite system $\mathcal{H}_A\otimes\mathcal{H}_B$, with $\dim(\mathcal{H}_B) = \dim(\mathcal{H}_A)^2$, such that the map can be expressed as in Eq. 2.11. Let's now clarify the three properties we assumed of $\mathcal{E}(t,t_0)$. A convex linear map is such that $\mathcal{E}(t,t_0)[\sum_i p_i\rho_i] = \sum_i p_i\mathcal{E}(t,t_0)[\rho_i]$ with positive coefficients p_i and any density matrices ρ_i. The trace preservation reads

$\mathrm{tr}\left[\mathcal{E}(t,t_0)[\rho]\right] = 1$. Finally, a completely positive transformation is such that for any dimension of $\mathcal{H}_C$, the composite map $\mathcal{E}(t,t_0)[\cdot]\otimes\mathbb{1}_C$ applied to a density operator of $\mathcal{H}_A\otimes\mathcal{H}_C$ returns a positive definite operator. The possibility of implementing a quantum map by unitarily transforming a larger composite system will be specifically invoked in Chapter 7.

When the three properties of $\mathcal{E}(t,t_0)$ are satisfied, the evolution of the system can equivalently be described by the so called operator sum representation. In this case, the evolution of the system can be written as

$$\rho(t) = \sum_n A_n(t,t_0)\ \rho(t_0)\ A_n^\dagger(t,t_0) \tag{2.12}$$

with the condition for the linear operators A_n that

$$\sum_n A_n^\dagger(t,t_0)A_n(t,t_0) = \mathbb{1}. \tag{2.13}$$

In these expressions, A_n are linear operators, named Kraus operators, depending on $\mathcal{E}(t,t_0)$. A representation where the operators used in the decomposition do not depend on $\mathcal{E}(t,t_0)$ is also possible,

$$\rho(t) = \sum_{n,m} \chi_{n,m}(t,t_0)\ E_n\ \rho(t_0)\ E_m^\dagger. \tag{2.14}$$

This expression is the basis of the process tomography that allows to experimentally determines the form of $\mathcal{E}(t,t_0)$. In this case, E_n form a basis of the space of linear operators on $\mathcal{H}$ and $\chi_{n,m}$ is an Hermitian complex matrix.

All the mentioned relations can be generalised to the case when $0 \le \mathrm{tr}\left[\mathcal{E}(t,t_0)\left[\rho_(t_0)\right]\right] < 1$ [34].

2.1.5 Master equation and Lindblad formalism

In the previous section we mentioned how the dynamics of a reduced system could be obtained solving the unitary evolution of the system+environment composite dynamics and applying the partial trace operation. However, we also mentioned that the evolution of the system can be described by a quantum map $\mathcal{E}(t,t_0)$, under the assumption that at time t_0 there are no system-environment correlations. However, we have not made any easy connection between the Hamiltonian of $\mathcal{H}_A\otimes\mathcal{H}_B$ and the resulting $\mathcal{E}(t,t_0)$ yet.

In this section we report about consolidate approaches to derive a differential equation for $\rho_A(t)$ from the Hamiltonian of the composite system. Its solution would give us $\mathcal{E}(t,t_0)[\rho_0]$, within some approximation. We will refer with the term *master equation* to a linear differential equation for the evolution of the density matrix:

$$\dot{\rho} = M\left[\rho, t\right]$$

where $M[f(t),t]$ is linear in its first argument.

From now on, we will adopt the subscript S and E for the system and the environment, respectively, in contrast to A and B previously used in the context of composite systems. In particular we will assume that $\mathcal{H}_E$ is much larger than $\mathcal{H}_S$. This will allow us to make two approximations named Born approximation and Markov approximation.

To begin with, S and E are initially assumed uncorrelated : $\rho_{S+E}(0) \approx \rho_S(0) \otimes \rho_E(0)$. Then, the Born approximation states that to predict the evolution of the $\rho_S(t)$, the composite system can be approximated by $\rho_{S+E}(t) \approx \rho_S(t) \otimes \rho_E(t)$ with the quantum correlations not affecting the dynamics significantly. Note that this does not neglect temporal correlations yet. Following, justified by the assumptions on the size of the environment and on a weak coupling between the two parts, the effects of the system on the environment are treated as a small perturbation so that $\rho_E(t)$ appears in the equation as a constant. With these assumptions, the evolution is described by an integro-differential equation. By writing the Hamiltonian of $S+E$ as

$$H = H_S + H_E + H_{\text{int}} = H_0 + H_{\text{int}},$$

with H_S and H_E acting locally on $\mathcal{H}_S$ and $\mathcal{H}_E$, respectively, the Born approximation reads

$$\frac{\mathrm{d}}{\mathrm{d}t}\rho_S(t) = -i\left[H_S, \rho_S(t)\right] - \mathrm{tr}_E\left[\left[H_{\text{int}}, \int_0^t e^{-iH_0(t-t')}\left[H_{\text{int}}, \rho_S(t') \otimes \rho_E\right] e^{iH_0(t-t')}\mathrm{d}t'\right]\right]. \tag{2.15}$$

where we assumed that $\forall \rho_S \quad \mathrm{tr}_E\left[\left[H_{\text{int}}, \rho_S \otimes \rho_E\right]\right] = 0$.

The Markov approximation further simplifies the equation transforming it in a time local differential equation assuming that the system evolves on time scales longer than the decay time of correlations with the environment (memory-less environment). The resulting master equation in the Born-Markov approximation reads:

$$\frac{\mathrm{d}}{\mathrm{d}t}\rho_S(t) = -i\left[H_S, \rho_S(t)\right] - \sum_\alpha \Big\{\left[A_\alpha, B_\alpha \rho_S(t)\right] + \left[\rho_S(t) C_\alpha, A_\alpha\right]\Big\}, \tag{2.16}$$

where A_α, B_α, C_α depend on the interaction between the system and the environment and on the properties of the environment.

Even though solving this equation is simpler than evolving the composite $S+E$ system, the approximation may result in undesired effects such as loss of positivity of $\rho_S(t)$ for some time intervals. Enforcing the positivity in Eq. 2.16 leads to the Lindblad equation:

$$\begin{aligned}\frac{\mathrm{d}}{\mathrm{d}t}\rho_S(t) &= -i\left[H_S, \rho_S(t)\right] + \frac{1}{2}\sum_{\alpha,\beta}\gamma_{\alpha,\beta}\Big\{\left[A_\alpha, \rho_S(t) A_\beta^\dagger\right] + \left[A_\alpha \rho_S(t), A_\beta^\dagger\right]\Big\} \\ &= -i\left[H_S, \rho_S(t)\right] - \frac{1}{2}\sum_\mu \Gamma_\mu\Big\{L_\mu^\dagger L_\mu \rho_S(t) + \rho_S(t) L_\mu^\dagger L_\mu - 2L_\mu^\dagger \rho_S(t) L_\mu\Big\},\end{aligned} \tag{2.17}$$

where Γ_μ is the list of non-negative eigenvalues obtained diagonalising $\gamma_{\alpha,\beta}$. The Lindblad equation[3] is the most general example of a time independent Markovian master equation [35, 43].

The Markovianity of the process is related to the possibility of predicting the state of the system at any time $t > t_0$ by knowing the current state of the system at t_0, and ignoring the evolution law of the system for time $t < t_0$, for any arbitrary t_0. If the dynamic of the system was not predictable by only knowing $\rho(t_0)$, some information that was stored in the system at $t < t_0$ conditions the evolution at time $t > t_0$ making its evolution dependent on information about its previous history. We note that, although less common, examples of local in time, time dependent, non-Markovian master equation that preserve the correct properties of the density operator are present in literature [44, 45].

2.1.6 Singular value decomposition and unitary dilation methods

During this thesis we will resort to the unitary dilation practice multiple times [46]. A unitary dilation of an operator M is a unitary transformation U, defined on a larger vector space than M, such that U acts as M when restricted to the original vector space. Calling $\hat{P}$ the projector onto the subspace where M is defined, we want $M = \hat{P}\ U\ \hat{P}$.

Before presenting an algorithmic construction of a unitary dilation, we will recall the property of singular value decomposition (SVD) in an n-dimensional vector space. For each endomorphism defined on this space, given its matrix representation M, we can find two unitary matrices V and W and a real and non-negative diagonal matrix D such that $M = V\ D\ W^{-1}$. The elements σ_i on the diagonal of D are named the singular values of M and characterise such matrix. The norm of an operator can be defined by means of such singular values. In the following we will adopt the convention $\|M\| = \max(\{\sigma_i\})$.

The form of unitary dilation that we will adopt requires M to be a contraction, i.e. $\|M\| \leq 1$. When this is not the case, we will be forced to rescale M accordingly. M's dilation is given by a $2n$-dimensional unitary of the form:

$$U = \begin{bmatrix} V & 0 \\ 0 & X \end{bmatrix} \begin{bmatrix} d & i\sqrt{\mathbb{1} - d^2} \\ i\sqrt{\mathbb{1} - d^2} & d \end{bmatrix} \begin{bmatrix} W^{-1} & 0 \\ 0 & Y \end{bmatrix} = \begin{bmatrix} \frac{M}{\|M\|} & iV\sqrt{\mathbb{1} - d^2}Y \\ iX\sqrt{\mathbb{1} - d^2}W^{-1} & XdY \end{bmatrix}, \tag{2.18}$$

where X and Y are arbitrary n-dimensional unitaries and $d = D/\|M\|$. Thanks to the normalisation, $\sqrt{\mathbb{1} - d^2}$ is a diagonal matrix with real positive values. The arbitrary choice of X and Y offers a large degree of flexibility. A choice that will be adopted throughout the Chapter 6 is $X = W$ and $Y = V^{-1}$. With this choice, the off-diagonal matrix blocks of U can

[3] Sometimes this equation is named Gorini–Kossakowski–Sudarshan–Lindblad, shortened as GKSL equation.

be rewritten as function of M as:

$$U = \begin{bmatrix} \frac{M}{\|M\|} & i\sqrt{\mathbb{1} - \frac{M\,M^\dagger}{\|M\|^2}} \\ i\sqrt{\mathbb{1} - \frac{M^\dagger M}{\|M\|^2}} & \frac{M^\dagger}{\|M\|} \end{bmatrix}.$$

Indeed, the bottom left block matrix satisfies:

$$\begin{aligned} \left(W\sqrt{\mathbb{1}-d^2}W^{-1}\right)^2 &= W\sqrt{\mathbb{1}-d^2}W^{-1}W\sqrt{\mathbb{1}-d^2}W^{-1} = W\left(\mathbb{1}-d^2\right)W^{-1} \\ &= W\left(\mathbb{1}-dV^{-1}Vd\right)W^{-1} = \mathbb{1}-WdV^{-1}VdW^{-1} \\ &= \mathbb{1}-\frac{M\,M^\dagger}{\|M\|^2}. \end{aligned}$$

A similar relation holds for the top right block matrix.

2.1.7 Qubit and Pauli matrices

A quantum system with a 2-dimensional Hilbert space is commonly referred to with the name *qubit*, since it generalises the classical concept of a bit. Quantum technology based on arrays of these two level systems can operate as digital devices concatenating a list of unitary operations on a single or multiple qubits. The two energy levels of the qubit are conventionally called $|0\rangle$ and $|1\rangle$. The choice of the particular basis to identify with the logical values of the system is, however, arbitrary and dictated by the practicality of measuring the system in that basis.

The operations on a single qubit are often written with the aid of a small set of 4 matrices, the identity matrix plus the Pauli matrices, whose explicit representation is

$$\sigma_0 = \begin{bmatrix} 1 & 0 \\ 0 & 1 \end{bmatrix} \qquad \sigma_1 = \sigma_x = \begin{bmatrix} 0 & 1 \\ 1 & 0 \end{bmatrix} \qquad \sigma_2 = \sigma_y = \begin{bmatrix} 0 & -i \\ i & 0 \end{bmatrix} \qquad \sigma_3 = \sigma_z = \begin{bmatrix} 1 & 0 \\ 0 & -1 \end{bmatrix} \tag{2.19}$$

Among the many properties of these matrices, we mention that these are all unitary and Hermitian matrices and form a basis, on the field of real numbers, for the 2-dimensional Hermitian complex matrices. This can indeed be used to characterise the density matrix of a qubit. In particular, the following identities hold

$$\begin{aligned} \rho &= \sum_{i=0}^{3} \mathrm{tr}\left[\sigma_i \rho\right] \frac{\sigma_i}{2} = \frac{\sigma_0}{2} + \sum_{i=1}^{3} \langle \sigma_i \rangle \frac{\sigma_i}{2}, \\ \mathrm{tr}\left[\rho^2\right] &= \sum_{i=0}^{3} \frac{\mathrm{tr}\left[\sigma_i \rho\right]^2}{2} = \frac{1}{2} + \sum_{i=1}^{3} \frac{\langle \sigma_i \rangle^2}{2}. \end{aligned} \tag{2.20}$$

Since a qubit state is completely described by the expectation values of the Pauli operators, these can be used to graphically represent it. Based on this, a qubit state can be represented on a 3-dimensional space as a point whose coordinates are $\langle \sigma_i \rangle$. Since for physical systems, the purity of the system cannot exceed 1, the point is constrained in the spherical region with $\sum_{i=3} \langle \sigma_i \rangle^2 \leq 1$. This qubit representation is named *Bloch sphere*.

2.2 Elements of quantum optics

2.2.1 Algebra and quantum state representation

Photons are the quantised excitations of the electromagnetic field. The evidence of their existence was at the heart of quantum mechanics revolution at the beginning of the 20th century [47–49] . Photons are treated in second quantisation [36, 50, 51]. In this formalism, the physical system to which we are associating an Hilbert space is the electromagnetic field itself, potentially restricted to a limited region of space. Let's consider the list of classical modes of the electromagnetic field in a free space, potentially supplied by desired boundary conditions, each of them defined by a given
correctedfrequency and a spatial distribution of the polarisation and of the electric field amplitude $\vec{E}_k(\vec{r})$. To each of them, we associate a Hilbert space, $\mathcal{H}_k$, with a Hamiltonian

$$H_k = \hbar\omega_k \left(a_k^\dagger a_k + \frac{1}{2}\right) = \hbar\omega_k \left(\hat{n}_k + \frac{1}{2}\right)$$

The creation and annihilation operators, $a_k^\dagger$ and a_k, respectively, satisfy the commutation relation typical of bosonic operators

$$\left[a_k, a_{k'}^\dagger\right] = \delta_{k,k'} \qquad \left[a_k^\dagger, a_{k'}^\dagger\right] = 0 \qquad [a_k, a_{k'}] = 0. \tag{2.21}$$

Each $\mathcal{H}_k$ has therefore the structure of a harmonic oscillator, all independent from each other. The "position" and "momentum" of this oscillator, in their dimensionless form, are the optical field quadratures

$$\hat{X}_k = \frac{1}{\sqrt{2}}\left(a_k^\dagger + a_k\right) \qquad \hat{P}_k = \frac{i}{\sqrt{2}}\left(a_k^\dagger - a_k\right).$$

Other than these, it is also possible to define a generalised quadrature

$$\hat{X}_k(\theta) = \frac{1}{\sqrt{2}}\left(e^{i\theta} a_k^\dagger + e^{-i\theta} a_k\right).$$

The eigenvectors of H_k are states $|n_k\rangle$ with a well defined number of photons. The action of the a_k and $a_k^\dagger$ on these states decreases or increases the number of photons, respectively. Furthermore, the norm of the state is not preserved, indeed a_k and $a_k^\dagger$ are not unitary operators,

$$a_k |n_k\rangle = \sqrt{n_k}\,|n_k - 1\rangle \qquad a_k^\dagger |n_k\rangle = \sqrt{n_k + 1}\,|n_k + 1\rangle \qquad a_k^\dagger a_k |n_k\rangle = \hat{n}_k |n_k\rangle = n_k |n_k\rangle. \tag{2.22}$$

The term vacuum state is used for the ground state of the system $|0\rangle$ in which no photons are present.

A state of the composite Hilbert space of m optical modes, $\mathcal{H} = \bigotimes_{k=1}^m \mathcal{H}_k$ is preferentially represented in the Fock basis made of the eigenvectors of the system $|n_1, n_2, \ldots, n_m\rangle = \bigotimes_{k=1}^m |n_k\rangle$.

In the Schrödinger representation, the time evolution of a Fock state reads

$$\exp\left(-i\sum_{k=1}^{m}\left(n_k+\frac{1}{2}\right)\omega_k t\right)|n_1,n_2,\ldots,n_m\rangle\,.$$

As alternative to the Schrödinger representation, quantum optics textbooks often adopt the Heisenberg picture. In this, the ket representing the state of the system is not a function of time. To determine the time evolution of the measurement outcomes of an observable represented by an operator $\hat{A}$, the operator itself is evolved in time based on the equation:

$$\frac{\mathrm{d}}{\mathrm{d}t}\hat{A} = +i\left[H,\hat{A}\right], \tag{2.23}$$

However, since the only observable we will measure is the photon number operator $\hat{n}_k$, that commutes with H, no time evolution is expected for this observable.

A more detailed description of the electromagnetic field in a relativistic field framework is available in [51].

2.2.2 Some noticeable states of the electromagnetic field

Besides the Fock states, we now mention few more states of the electromagnetic field that appear in this thesis. A single mode *coherent state* $|\alpha\rangle$, defined in $\mathcal{H}_k$ with $\alpha\in\mathbb{C}$, is the most common approximation for the state of light generated by a narrow bandwidth laser. The coherent state is also an eigenvector of the annihilation operator with eigenvalue α. Its representation in the Fock basis is

$$|\alpha\rangle = e^{-\frac{|\alpha|^2}{2}}\sum_{n=0}^{\infty}\frac{\alpha^n}{\sqrt{n!}}|n\rangle \qquad \hat{a}_k|\alpha\rangle = \alpha|\alpha\rangle\,. \tag{2.24}$$

$|\alpha\rangle$ can be obtained applying the unitary displacement operator $D(\alpha)$ to the vacuum state,

$$D(\alpha) = \exp\left(\alpha\hat{a}^\dagger - \alpha^*\hat{a}\right) \qquad |\alpha\rangle = D(\alpha)|0\rangle\,. \tag{2.25}$$

The photon statistics of the coherent state is Poissonian with mean value and variance $\bar{n} = \Delta^2 n = |\alpha|^2$

$$|\langle n|\alpha\rangle|^2 = e^{-|\alpha|^2}\frac{\left(|\alpha|^2\right)^n}{n!}$$

An example of an entangled state between two modes of light, k_1 and k_2, can be obtained applying the unitary two-mode squeezing operator $S_{k1,k2}(\xi)$ to the vacuum state,

$$S_{k1,k2}(\xi) = \exp\left(\xi^*\hat{a}_{k1}\hat{a}_{k2} - \xi\hat{a}^\dagger_{k1}\hat{a}^\dagger_{k2}\right). \tag{2.26}$$

The state $|\mathrm{TMS}(\xi)\rangle = S_{k1,k2}(\xi)|0_{k1}\rangle|0_{k2}\rangle$ is called two-mode squeezed vacuum state and its decomposition in the Fock basis is

$$|\mathrm{TMS}(\xi)\rangle = \frac{1}{\cosh(|\xi|)}\sum_{n=0}^{\infty}\left(e^{i\phi}\tanh(|\xi|)\right)^n|n\rangle_{k1}|n\rangle_{k2} = \sqrt{1-P}\sum_{n=0}^{\infty}e^{i\phi n}\sqrt{P^n}\,|n\rangle|n\rangle\,, \tag{2.27}$$

where $\phi = \arg(\xi)$, and $P = \tanh^2(|\xi|)$ is the probability of at least a pair of photons to be present. Indeed, by adding up the probabilities of projecting $|\mathrm{TMS}(\xi)\rangle$ onto a the Fock state with one or more photon pairs, we obtain:

$$(1-P)\sum_{n=1}^{n=\infty} P^n = P. \tag{2.28}$$

The state has a perfect correlation between the photons in the mode k_1 and those in k_2. Furthermore, the coherence between the different Fock terms determines correlations between quadrature measurements in the two modes. This form of entanglement closely resembles the property of the state described by Einstein, Podolsky and Rosen to question the completeness of the quantum mechanical theory [52, 53].

Two-mode squeezed states can be generated in the laboratory by means of non-linear processes such as spontaneous parametric down conversion (SPDC) and spontaneous four wave mixing (SFWM). The first one has been used as photon source for all the experiments reported in this thesis and the will be further discussed in Chapter 3. The second one is more common in integrated photonics and will be described in the source paragraph of Sec. 2.3. SFWM based photon pair sources will be part of the chip design in Chapter 7. An additional way to generate a two-mode squeezed state requires as resource two single mode squeezed states [54, 55].

A single mode squeezed vacuum state $|\xi\rangle$ is obtained by applying the unitary single mode squeezing operator $S(\xi)$ to the vacuum state,

$$S(\xi) = \exp\left(-\frac{1}{2}\left(\xi\left(a^\dagger\right)^2 - \xi^* a^2\right)\right). \tag{2.29}$$

Similarly to a two-mode squeezed vacuum state, $|\xi\rangle$ is a state with only even number of photons. Its decomposition in the Fock basis is

$$|\xi\rangle = \frac{1}{\sqrt{\cosh(|\xi|)}}\sum_{n=0}^{\infty}\frac{\sqrt{(2n!)}}{n!}\left(-\frac{1}{2}e^{i\phi}\tanh(|\xi|)\right)^n |2n\rangle\,. \tag{2.30}$$

2.2.3 Linear optical transformations

We are currently describing the quantum state of the optical field by associating a Hilbert space to each mode of the electromagnetic field. In the presence of optical elements intersecting the light, the mode of the electromagnetic field are not the same anymore. Instead of modifying the spatial modes to which each creation operator refers, it is possible to consider travelling wave packets [4] constructed from the modes of the "unperturbed" optical system before and after the optical element. The propagation of the wave packet across the

[4]Note that the definition of a wave packet requires to include a small interval of frequencies in the description of the electromagnetic field. In the limit of infinitesimal bandwidth of the wave packet, the properties of a monochromatic wave can be recovered.

optical elements can be described as a transformation between the modes defined in the incoming side of the optical element and the modes of the outgoing side of the same. This transformation can be formally derived by the Hamiltonian of the optical component using scattering theory.

Before proceeding, we will present a relation the allows us to transform Fock states, [56]. Given an invertible transformation G, its action on a state $|n_1,\dots,n_m\rangle = \otimes_{i=1}^{i=m}\left(a_i^\dagger\right)^{n_i}|0_1,\dots,0_m\rangle$ can be derived as

$$G|n_1,\dots,n_m\rangle = \left[\otimes_{i=1}^{i=m}\left(Ga_i^\dagger G^{-1}\right)^{n_i}\right]G|0_1,\dots,0_m\rangle = \left[\otimes_{i=1}^{i=m}\left(b_i^\dagger\right)^{n_i}\right]G|0_1,\dots,0_m\rangle\,, \tag{2.31}$$

where $b_i^\dagger = Ga_i^\dagger G^{-1}$. Moreover, if G is a unitary operator, $b_k^\dagger$ and $b_{k'}$ satisfy the same commutation relations as $a_k^\dagger$ and $a_{k'}$.

This thesis will mostly focus on linear optics. In the classical domain, this refers to the existence of a linear relation between the complex fields E_k^{in} in a region of space, or at an interface, and the resulting fields E_k^{out} emitted from that region. In absence of non-linear polarisation phenomena, time varying refractive index, and fluorescence phenomena, the emitted fields oscillate at the same frequency of the injected ones. In this regime, the relation between input and output fields of indexed modes k can be written as a matrix relation $E_k^{\text{out}} = \sum_{k'} T_{k,k'}E_{k'}^{\text{in}}$. Determining the fields, this matrix can also be used to calculate the re-emitted power in the different spatial modes. All the optical elements we will consider in our integrated circuits can be considered as linear optical elements with exception of the photon sources whose action is indeed non-linear.

In quantum optics, linear transformations can be defined as unitary operations $G = \mathcal{U}$ on $\mathcal{H}$ that linearly transform the creation operators of the different modes. We can therefore write:

$$b_k^\dagger = \mathcal{U}a_k^\dagger\mathcal{U}^{-1} = \sum_n c_{k,n}a_n^\dagger \qquad b_k = \mathcal{U}a_k\mathcal{U}^{-1} = \sum_n c_{k,n}^* a_n.$$

In particular, we will restrict ourselves to the case where no mixing between modes at different frequencies occurs. In such a case, to preserve the energy of the system, it is required that the matrix $c_{k,n}$ is unitary. We add that a unitary transformation in $\mathcal{H}$ with such properties does exist and can be written as a result of a bilinear Hamiltonian in $\{a_k^\dagger\}_k$ and $\{a_k\}_k$. The preservation of the energy also requires that $\mathcal{U}|0\rangle = |0\rangle$, up to an unimportant global phase.

A classical lossless linear transformation can be written with a unitary transfer matrix U that transforms the field of appropriately normalised optical modes. This unitary transfer matrix is in close relation to the matrix $c_{k,n}$. This relation can be summarised by the m relations [57]

$$\mathcal{U}a_k\mathcal{U}^{-1} = \sum_{i=1}^{i=m}\left[U^\dagger\right]_{k,i}a_i = \sum_{i=1}^{i=m}[U]_{i,k}^* a_i.$$

A single photon state,

$$|\psi\rangle = \sum_k c_k a_k^\dagger |0\rangle = \sum_k c_k \left(\bigotimes_{i=1}^{i=k-1} |0_k\rangle \, |1_k\rangle \bigotimes_{i=k+1}^{i=m} |0_k\rangle \right), \tag{2.32}$$

is a superposition of many single photon Fock states, each with a photon in a different mode. States with a well defined number of photons across a finite number of optical modes form a vector subspace. By choosing the single photon Fock states as basis, it is possible to define an isomorphism between the single photon states and $\mathbb{C}^m$:

$$|\psi\rangle \equiv \begin{pmatrix} c_1 \\ \vdots \\ c_m \end{pmatrix}$$

and, by applying a lossless transfer matrix U, such vector transforms as

$$\begin{pmatrix} c_1 \\ \vdots \\ c_m \end{pmatrix} \rightarrow \begin{pmatrix} c_1' \\ \vdots \\ c_m' \end{pmatrix} = U \begin{pmatrix} c_1 \\ \vdots \\ c_m \end{pmatrix}.$$

Therefore, one can easily evolve single photon quantum states once the linear transfer matrix of the system is known. Moreover, coherent states can be transformed as easily, although they do not form a subspace. Indeed, by applying a linear transformation to a multimode coherent state $|\alpha_1, \ldots, \alpha_m\rangle$, it transforms into $|\beta_1, \ldots, \beta_m\rangle$ where $\beta_k = \sum_\ell U_{k,\ell} \alpha_\ell$.

2.2.4 Hong Ou Mandel interference

The effect of a linear transformation applied to a coherent state or to a single photon can be reconstructed with a simple matrix-vector multiplication. Less intuitive consequences of the quantum nature of light are observed when linear transformations are applied to multi-photon Fock states. Arguably, the Hong Ou Mandel (HOM) interference is the most remarkable example of this property [58]. To describe this effect, we consider the transfer matrix $\mathrm{U_{BS}}$ of a balanced beam splitter (BS):

$$U_{\mathrm{BS}} = \begin{bmatrix} \frac{1}{\sqrt{2}} & \frac{1}{\sqrt{2}} \\ \frac{1}{\sqrt{2}} & -\frac{1}{\sqrt{2}} \end{bmatrix}.$$

We note that this represents a particular choice for the transfer matrix of a BS, a more general transfer matrix for this device will be discussed in Sec. 2.3, but the HOM effect is not dependent on the specific choice we made here. For a single photon injected into a single of the two ports of this device, the probability of observing it in the first or second output mode is 0.5 each. If we were to consider classical non interacting particles, by injecting a

photon in each of the two input ports of the BS, we would presume that the probability of the two particles to appear at the same output of the device would be 0.25 for each port. Instead the remaining 50% of the times they will appear split in the two ports. Moreover, in a classical wave interference problem, if any imbalance between the intensity at the two output ports was observed, this would also depend on the relative phase of the two beams interfering. In the quantum case, if two photons are entering the BS, each in a different input port, the photons would leave the system from the same port, 50% of the times from each, independently of additional phases acquired before impinging on the device.

$$\begin{aligned} \mathcal{U}_{BS}|1,1\rangle &= \mathcal{U}_{BS} a_1^\dagger a_2^\dagger |0\rangle = 0.5\left(a_1^\dagger + a_2^\dagger\right)\left(a_1^\dagger - a_2^\dagger\right)|0\rangle \\ &= \left(0.5\left(a_1^\dagger\right)^2 - 0.5\left(a_2^\dagger\right)^2\right)|0\rangle = \frac{1}{\sqrt{2}}|2,0\rangle - \frac{1}{\sqrt{2}}|0,2\rangle \end{aligned} \tag{2.33}$$

The expectation value of the number of photons in each output port is equivalent to the classical particle case but no $|1,1\rangle$ event is predicted.

These photon-photon interference effects are at the basis of the current methods to generate entanglement and perform computation with linear optical circuits. Originally, however, the HOM effect was introduced to test the spectral-temporal properties of single photons with an unprecedented resolution [58]. The introduction of temporal delays between two photons entering the BS reduces the interference effect and the probability of detecting a photon in each output mode does not vanish anymore. By scanning such delay while monitoring the coincidence rate of the two ports, a dip in the signal is visible when the photons perfectly overlap temporally. The width of such dip is related to the temporal properties of the two photons. The visibility of the dip is generally defined as

$$V = \frac{C - Q}{C}, \tag{2.34}$$

where C is the rate of coincidental detection at the two output ports of the beam splitter for completely distinguishable particles that act according to classical statistics, Q is the rate at the bottom of the interference fringe when the particles are as indistinguishable as possible.

The HOM dip appears whenever the distinguishability of the two photons can be controlled. Since the BS only manipulates some spatial properties of the photons, a pure separable state made of two partially distinguishable photons should be described as

$$|1,1\rangle = \left(\sum_k f_k a_{1,k}^\dagger\right)\left(\sum_\ell g_\ell a_{2,\ell}^\dagger\right)|0\rangle$$

where, for simplicity, we assumed that the auxiliary degree of freedom labelled with k or ℓ runs over a discrete set rather than being a continuous variable. We note that temporally localised photons must be composed of more than a single wavelength justifying the existence

of the additional degree of freedom. The normalisation condition on the single photon states reads:

$$\sum_k |f_k|^2 = \sum_k |g_k|^2 = 1$$

With this input state, the probability of the state $|1,1\rangle$ after the BS transformation is given by

$$P_Q = 0.5\left(1 - \left|\sum_k f_k^* g_k\right|^2\right).$$

A further reduction of the destructive interference may also appear because of statistical classical uncertainty about the state of the two photons. Assuming each input photon in the form

$$\rho_1 = \sum_k p_k a_k^\dagger |0\rangle\langle 0| a_k,$$

the probability of anti-bunched state is

$$P_Q = 0.5\left(1 - \sum_k p_k^2\right)$$

2.2.5 Probabilities via permanent

The calculation shown for the ideal case of the HOM interference is a particular case of a more general formula that can be applied to calculate the probability amplitude of transition between two Fock states with the same total number of photons N when a lossless linear optical device, with transfer matrix U, is used. For indistinguishable photons:

$$\langle n_1, n_2, \ldots, n_m | \mathcal{U}_U \left| n'_1, n'_2, \ldots, n'_m \right\rangle = \frac{\mathrm{Perm}\left(U_{\frac{n_1,n_2,\ldots,n_m}{n'_1,n'_2,\ldots,n'_m}}\right)}{\sqrt{\prod_{k=1}^m n_k!}\sqrt{\prod_{k=1}^m n'_k!}}, \tag{2.35}$$

where $U_{\frac{n_1,n_2,\ldots,n_m}{n'_1,n'_2,\ldots,n'_m}}$ represents an $N \times N$ matrix obtained by taking n'_k times the k^{th} column of U and by taking, from them, n_k times the k^{th} row. Perm() represents the permanent of the matrix defined as

$$\mathrm{Perm}(X) = \sum_{\sigma \in S} \prod_{i=1}^N X_{i,\sigma_i}$$

where S is the set of all the permutation of the integers between 1 and N.

This compact expression was originally suggested in the context of scattering between bosonic fields and later investigate in the context of linear optics to describe how a Fock state transforms [57, 59]. Even though very practical to determine the evolution of a few photons state, the complexity of the calculation of the above relation in a general case, with tens of photons, contributes to the complexity of the boson sampling problem [60].

2.2.6 Qubit encoding and quantum gates

For what described so far, optical systems do not appear as proper two level systems. Nonetheless, few possible mappings onto a qubit have been proposed. One of these, named single rail encoding, prescribes to consider the logical $|0\rangle$ as the vacuum state of an optical mode, and $|1\rangle$ as the state with a single photon in that mode. However, this solution tends to be unpractical and alternative schemes are generally used. Arguably, the most common solution is the so called dual rail encoding. Considering a single photon in any of two specific modes, the logical states correspond to the optical states $|1,0\rangle$ and $|0,1\rangle$. For example, a typical choice in free space optics, is to use collinear modes of light with orthogonal polarisation. In integrated photonics, the two modes are more often associate to fundamental modes of different waveguides [61].

In order to process the information stored in a qubit, the most traditional computation model is based on a sequence of gates, i.e. a set of single or multi qubit unitary transformations. However, any non local transformation between two photonic qubits contrast with the fact that photons do not interact with each other and the realisation of this transformation is a probabilistic process. The solution of this problem, with the aid of measurement induced non linearity [62], had given hope for the realisation of a quantum computer based on linear optics, electronics and quantum states of light [63]. Even though in this thesis we will not engage with gate based computation, the description of photonic two-qubit gates provides examples on how bosonic interference and measurements can be used to simulate interaction between photons.

The first example is the control phase operation (CZ) that in the logical qubit basis acts as follows:

$$\begin{aligned} CZ\,|0\rangle\,|0\rangle &= |0\rangle\,|0\rangle \qquad CZ\,|0\rangle\,|1\rangle = |0\rangle\,|1\rangle \\ CZ\,|1\rangle\,|0\rangle &= |1\rangle\,|0\rangle \qquad CZ\,|1\rangle\,|1\rangle = -|1\rangle\,|1\rangle \end{aligned} \tag{2.36}$$

In 2002, a postselected gate to perform this operation using a six modes interferometer was proposed [64, 65]. Two pairs of modes encode the input qubits in the dual rail formalism while the remaining two ancillary modes provide additional losses that allow to dilate the desired transfer matrix. The transformation succeeds when a single photon is detected in each of the pairs of modes on which the qubits are mapped onto, provided that input state was a superposition of possible logical two-qubit states. The success rate of this gate is 1/9. The specific projection required to establish the success of the gate limits its applicability. A fairly direct approach is to measure one of the two qubits and verify that only a single photon is present; if no photon was lost or detected in the ancillary modes, the remaining qubit can be used for further computation. Sadly, measuring a qubit projects the state and transforms it into a mixture affecting the quantum properties of the composite system. Furthermore, the common procedure to measure a photon is to absorb it, therefore the photon is not available

anymore for any encoding. However, any unitary that commutes with the projection onto the logic subspace of the dual rail qubit can be performed in-between the CZ gate and the projection. This includes local unitaries on a single qubit and, consequently, arbitrary single qubit measurements are feasible.

The addition of an Hadamard transformation[5] on each qubit before and after the CZ gate is sufficient to perform a C-Not transformation defined by the relations

$$\begin{aligned} &\text{C-Not}\,|0\rangle\,|0\rangle = |0\rangle\,|0\rangle \qquad \text{C-Not}\,|0\rangle\,|1\rangle = |0\rangle\,|1\rangle \\ &\text{C-Not}\,|1\rangle\,|0\rangle = |1\rangle\,|1\rangle \qquad \text{C-Not}\,|1\rangle\,|1\rangle = |1\rangle\,|0\rangle \end{aligned} \tag{2.37}$$

A more scalable scheme to perform the same operation without precluding further state manipulation was proposed by Knill et al. [63]. It is based on the creation of a single mode non-linear sign gate (NLS) that can perform the following transformation in the Fock space,

$$NLS\,(c_0\,|0\rangle + c_1\,|1\rangle + c_2\,|2\rangle) = (c_0\,|0\rangle + c_1\,|1\rangle - c_2\,|2\rangle)\,. \tag{2.38}$$

In this case the gate requires that the input state of light has a number of photon between 0 and 2. An additional ancillary photon needs to be provided to the interferometer that is composed of the target mode on which the gate acts, the mode of the ancillary photon, and an additional mode to dilate the desired transfer matrix. The success of the gate is heralded by the detection of a single photon in the ancillary mode and no photon observed in the third mode of the interferometer. It is important to note that for lossless devices, the success probability of this gate is 0.25 regardless of the particular input state within the allowed subspace. In the proposed scheme, the positive heralding of two NLS gates deterministically herald the success of the C-Not gate. In this case, arbitrary transformations can be performed on the two output qubits including non-local unitaries. Without providing additional resources to this scheme, the C-Not operation is successfully heralded 1/16 of the times. However, with the aid of active transformations conditioned on the outcomes of previous measurements (feed-forward), and many ancillary photons, it is theoretically possible to increase the success rate arbitrarily close to 1.

2.3 Elements of integrated optics

The work presented in this thesis is based on integrated optical circuits. Contrarily to bulk optics, where light mostly travels in free space, the propagation in an optical chip is guided along structures, waveguides, that confine the light in the transverse direction. In free space optics the transverse profile of the optical modes is of the order of millimetres, much larger than that of integrated optical modes, generally of the order of microns. The confinement

[5] The Hadamard gate is a single qubit unitary represented by the matrix $\begin{bmatrix} 1/\sqrt{2} & 1/\sqrt{2} \\ 1/\sqrt{2} & -1/\sqrt{2} \end{bmatrix}$

principle is analogous to that of optic fibres largely used in telecommunication. A higher refractive index region, the core, is surrounded by a lower refractive index material (cladding). The larger the index mismatch, the easier it is to confine the mode in the core region. While in ray optics this index contrast determines the limit angle for total internal diffraction, the reduced dimension of integrated waveguides forces one to resort to more accurate solutions of the Maxwell's equations to determine the guided optical modes. Generally, these are numerically solved by dedicated software. Few important considerations motivate the choice of integrated optical circuits over their counterpart. The small dimension of the optical modes permits to have many more controllable modes and cascade tens of optical elements in a space of few millimetres. Due to the solid nature of the chip that contains the optical elements, relative vibrations and slow drift of the optical components are drastically reduced, offering an improved phase stability to the experiments. Furthermore, the alignment of all the optical components necessary in standard optics, is replaced by the much simpler requirement of uninterrupted waveguides connecting each element. These advantages are already exploited for classical data routing and might become crucial to scale up the size of quantum optics experiments [24, 66].

When possible, it is common practice to operate with single mode waveguides. For a specific polarisation, let's say transverse electric field (no electric field along the propagation direction), these structures carry only a single mode of light. This choice is meant to ease the control over the linear optics operations between modes (see Sec. 2.3.1), and to mitigate the effect of fabrication imperfection. In absence of this precaution, roughness of the interfaces can generate unwanted mixing between modes carried by the same waveguide (intermodal optical crosstalk). In a single mode structure, instead, the same imperfections induce photon loss into radiating (not guided) modes and back scattering.

Besides the simple waveguides that replace the propagation in free space, an additional list of components are also available to replace most of the bulk optics components: beam splitters, phase-shifters, filters, non-linear crystals, etc. In particular, it is generally required to inject and extract light from chip, therefore, in addition to the normal functions, elements for optical input/output coupling must be considered. However, technology is progressing to incorporate light sources and detectors on chip, both in the classical domain where technology is more mature [67, 68], and in the quantum domain, where components have to meet high standards in terms of noise and efficiency [69–71]. In the following, we will briefly describe those optical elements that are part of the optical circuits discussed in this thesis.

Before proceeding, it is worth to mention that the light confinement on a chip has been achieved also by means of photonic crystal structures [72]. However, these are not part of the contents of this thesis.

2.3.1 Waveguide couplers

Multimode interferometers (MMIs) and *directional couplers* (DCs) are the main components used to replace beam splitters in integrated devices.

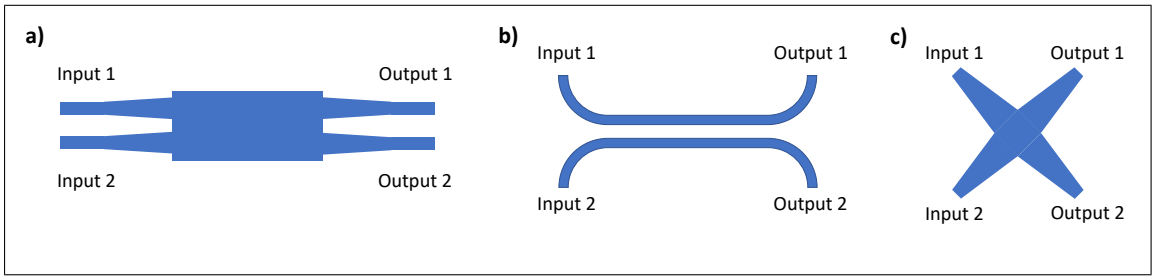

Figure 2.1: Integrated waveguide couplers Top view of schematics of integrated couplers. Blue region are filled with waveguide core material. Cladding material surrounds the structures. a) Multimode interferometer; b) directional coupler; c) waveguide crosser.

A MMI consists of an expanded waveguide section that can support multiple modes (see Fig. 2.1). Two single mode waveguides enter in this larger section so that the light transmitted excites a superposition of the many modes supported by the multi mode section. Because of their different phase velocity, the excited modes of light determine an interference pattern in the transverse section of the waveguide that changes along the propagation direction. After a propagation $2L$, the mirrored transverse mode profile at the input section of the MMI is, in good approximation, recreated. The length of the MMI section is then set to be L so that two spots appear in the transverse plane and light can be reinjected into two different waveguides [73]. In the final design of a 2×2 MMI, the two input waveguides and the two output ones are placed symmetrically with respect to the propagation axis.

A DC, also known as evanescent coupler, is made of two single mode waveguides brought close to each other in such a way that part of the optical modes, not contained in the waveguide cores, overlaps. This alters the optical modes supported by the system of the two waveguides. As result, part of the light from one waveguide gets coupled into the other and the intensity of the light entering in a single waveguide oscillates between the two along its propagation. By separating the two waveguides after the right propagation distance, the light injected in a single waveguide gets equally distributed in the two output modes. Alternative splitting ratios can be achieved by modifying the length of the device.

A DC induces a more adiabatic transformation of the optical modes without the sudden discontinuity at the multimode section interface. This permits, in principle, to have a device with less losses. However, the operation of the device critically depends on the correct combination of waveguide separation and length of the components resulting in a power splitting ratio that can fluctuate largely. On the other hand, MMIs are more resilient to fabrication imperfection and compensate the higher loss with a more reliable operation. For

what concerns the spectral response, MMI are less wavelength dependent allowing to use the same design for a large frequency window. The splitting ratio of DC is sensitive to the wavelength although more advanced designs to mitigate this problem have been proposed [74].

The most generic transfer matrix for a 2×2 lossless device is

$$\begin{aligned} U &= \begin{bmatrix} e^{i\phi_1}\cos\theta & -e^{i\phi_3}\sin\theta \\ e^{i\phi_2}\sin\theta & e^{i(\phi_3+\phi_2-\phi_1)}\cos\theta \end{bmatrix} \\ &= e^{i\phi_1}\begin{bmatrix} 1 & 0 \\ 0 & e^{i(\phi_2-\phi_1)} \end{bmatrix}\begin{bmatrix} \cos\theta & -\sin\theta \\ \sin\theta & \cos\theta \end{bmatrix}\begin{bmatrix} 1 & 0 \\ 0 & e^{i(\phi_3-\phi_1)} \end{bmatrix} \end{aligned} \tag{2.39}$$

with $0 \leq \theta \leq \frac{\pi}{2}$. Devices that separate the input power equally into the two output ports are characterised by $\theta = \pi/4$. We will ignore the global phase $e^{i\phi_1}$ assuming that each photon goes through the same number of components. In this work, the two diagonal matrices appearing on the RHS of Eq. 2.39 are accounted for in the phase-shifters characterisation. However, our final choice to represent integrated components the perform balanced beamsplitting operation is to formally set $\phi_1 = 0, \phi_2 = \pi/4,\ \phi_3 = -\pi/4$ so that

$$U_{\mathrm{DC}} = \begin{bmatrix} \frac{1}{\sqrt{2}} & \frac{i}{\sqrt{2}} \\ \frac{i}{\sqrt{2}} & \frac{1}{\sqrt{2}} \end{bmatrix}$$

This choice is motivated by the assumption that the physical device is symmetric with respect to a swap of the two waveguides.

A further "coupling" element that needs to be mentioned is the waveguide crosser. Since many integrated optical devices are planar light-wave circuits, i.e. all the optical elements are arranged on the same plane, waveguide paths often cross each other even when no coupling among their mode is intended. In this case, components named waveguide crossers are used (see Fig. 2.1). These generally broad band components are designed to introduce as low loss, inter-modal coupling, and inter-waveguide coupling as possible.

2.3.2 Thermal phase-shifters

Arguably, the second most used component in integrated photonics is the phase-shifter. This element introduces an extra phase along the propagation of the light that can be tuned by the user. It is important to have tunable systems not only to have a device that can perform more tasks, but also to compensate for additional phases in the fabricated device that can impede the desired linear transformation. Among the different technologies to achieve a phase-shift, we will focus on thermo-optic phase-shifters, since they are the only ones used in this work. We refer to the literature for alternative devices such as carrier injection modulators, electro optical modulators, micro-electro-mechanical systems (MEMS) [75–77].

A thermo-optic phase-shifter induces a local change of refractive index δn of the material by locally increasing the temperature of the waveguide by δT. In first approximation, the material response is linear with respect to the temperature variation, $\delta n = \alpha \delta T$, but strongly dependent on the material through the thermo-optic coefficient α. For example, the thermo-optic coefficient of silicon is about an order of magnitude higher than that of silica, facilitating the creation of tunable device in the first material [78, 79]. The change in temperature is usually achieved by heat dissipation from a resistor injected with current. This current can flow directly into the waveguide if based on conductive material, or can be applied to a secondary metallic resistor in close proximity of the waveguide. The geometry of the device is important to maximise the temperature change of the desired waveguide and limit the effects on other elements of the optical circuit. Additionally, the minimisation of the power dissipation is required to scale up the number of phase-shifters of the device.

Typically, the response time of a thermal device is slower than optical, electric or acoustic alternatives. In particular, two different characteristic times have to be considered: the time required to increase the temperature of the waveguide by ΔT, and the time for the system to relax to its previous temperature when required. A good thermal isolation of the heater+waveguide system, facilitated by the introduction of suspended structure or trenches, reduces the power consumption and the temperature rising time at the expense of a long cooling time. A better thermal conduction between the waveguide and an heat sink ensures a faster relaxation of the system but are less power efficient. In practice, an active heat extraction, in addition to surface radiation, is always needed to prevent an increase of temperature everywhere in the chip when a single heater is turned on [80, 81].

2.3.3 Mach-Zehnder interferometers

MMIs and DCs are static devices that cannot be reconfigured once fabricated. To provide access to tunable beam splitters, it is needed to combine tunable elements with intensity splitting components.

The simplest example is a two port interferometer that can implement a range of transfer matrices depending of the particular optical depth of its arms. The optical circuits included in this thesis are all based on Mach-Zehnder interferometers (MZIs) as depicted in Fig. 2.2. This composite structure consists of two 2×2 mode couplers (either two balanced DCs or two MMIs); the output modes of the first connected to the input ports of the second. A phase-shifter is included in either one or both arms that connect the two couplers. Assuming an ideal transfer matrix of the thermal phase-shifter[6], the transfer matrix of the whole

[6] Depending of the physical design of the chip, it is likely that a thermal phase-shifter can affect both the arms of a MZI with different intensity.

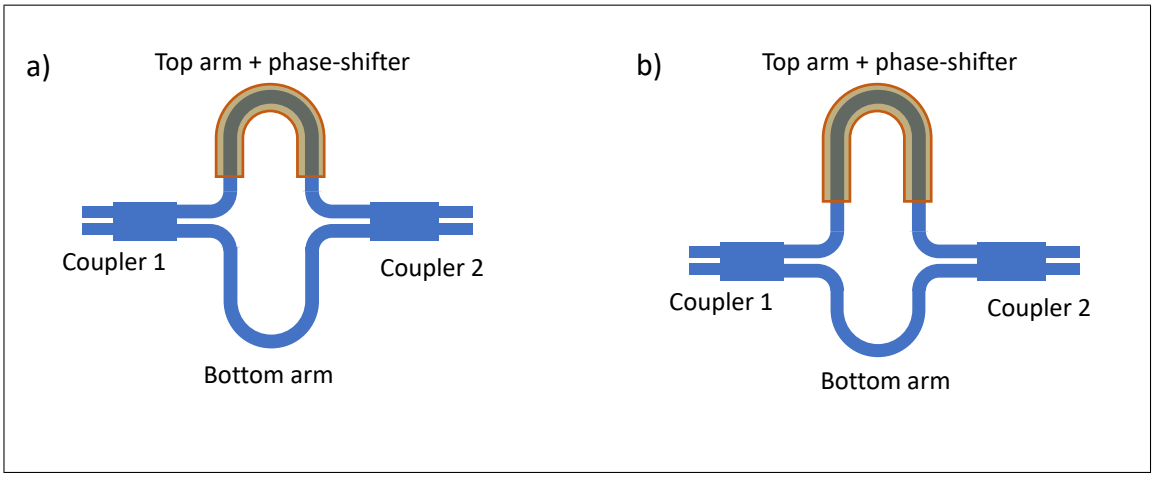

Figure 2.2: Schematics of MZI and asymmetric MZI Top view of schematics of integrated MZIs. Blue region are filled with waveguide core material. Bronze shaded area is covered with metal heater. Cladding material surrounds the structures. a) MZI structure to achieve tunable beam splitting operations; b) asymmetric MZI for wavelength dependent operations.

device can be modelled as:

$$U_{\mathrm{MZI}} = \begin{bmatrix} \frac{1}{\sqrt{2}} & \frac{i}{\sqrt{2}} \\ \frac{i}{\sqrt{2}} & \frac{1}{\sqrt{2}} \end{bmatrix} \begin{bmatrix} e^{i\phi} & 0 \\ 0 & 1 \end{bmatrix} \begin{bmatrix} \frac{1}{\sqrt{2}} & \frac{i}{\sqrt{2}} \\ \frac{i}{\sqrt{2}} & \frac{1}{\sqrt{2}} \end{bmatrix} = ie^{i\phi/2} \begin{bmatrix} \sin\frac{\phi}{2} & \cos\frac{\phi}{2} \\ \cos\frac{\phi}{2} & -\sin\frac{\phi}{2} \end{bmatrix} \tag{2.40}$$

A similar device, by tuning ϕ from 0 to π can recreate all the splitting ratios between the two modes. Note that there is also an additional phase acquired by both the output modes dependent of ϕ. When $\phi = 0$, $U_{\mathrm{MZI}} = i\sigma_x$; when $\phi = \pi$, $U_{\mathrm{MZI}} = -\sigma_z$.

For a beam injected into a single port of the MZI, to achieve perfect power extinction in the swap configuration, $\phi = 0$, i. e. to suppress the power transmitted in the same mode at the output, the two couplers of the MZI must be ideal, that is with a perfectly balanced splitting ratio. Instead, when $\phi = \pi$, achieving the perfect power extinction in the other output mode is easier and can be achieve even with imperfect components. Both these configurations are on the extremum of the $\sin\phi/2$ and $\cos\phi/2$ curves so we expect them to be more tolerant to phase noise in the phase-shifter. The extinction achieved in the swap configuration can be used as a metric of the quality of the integrated couplers. Extinction as high as 66 dB has been shown, [25].

2.3.3.1 Asymmetric MZI

An MZI structure can also be used to efficiently separate light at different wavelengths. To create a strong wavelength dependent behaviour of the device, one of the arms of the structure is made longer than the other giving the name asymmetric MZI (aMZI) to this structure. Because of this difference ΔL, the diagonal matrix describing the MZI arms

becomes wavelength dependent.

$$U_{\text{aMZI}} = \begin{bmatrix} \frac{1}{\sqrt{2}} & \frac{i}{\sqrt{2}} \\ \frac{i}{\sqrt{2}} & \frac{1}{\sqrt{2}} \end{bmatrix} \begin{bmatrix} e^{i\phi_0} e^{i\Delta L\beta(\lambda)} & 0 \\ 0 & 1 \end{bmatrix} \begin{bmatrix} \frac{1}{\sqrt{2}} & \frac{i}{\sqrt{2}} \\ \frac{i}{\sqrt{2}} & \frac{1}{\sqrt{2}} \end{bmatrix} = ie^{i\phi'(\lambda)/2} \begin{bmatrix} \sin\frac{\phi'(\lambda)}{2} & \cos\frac{\phi'(\lambda)}{2} \\ \cos\frac{\phi'(\lambda)}{2} & -\sin\frac{\phi'(\lambda)}{2} \end{bmatrix} \tag{2.41}$$

where $\beta(\lambda)$ is the propagation constant of the fundamental mode of the waveguide, as a function of the wavelength λ, and $\phi'(\lambda) = \phi_0 + \Delta L\beta(\lambda)$. Different wavelengths will experience different splitting ratios up to the extreme case where one wavelength is transmitted into the same mode and another one is swapped.

2.3.4 Optical input-output

To interface photonic chips with optical fibre networks or free space optical systems, it is necessary to supply the integrated device with suitable structures. The optical input and output from planar light-wave circuits is generally achieved with two techniques: edge coupling or grating coupling [82]. The former consists in terminating a waveguide at the edge of the chip and aligning the external mode of the light to the direction of the waveguide. When light coming from the chip arrives at the end of the device, this will propagate forward out of the chip provided that the internal back-reflection is prevented. To increase the coupling efficiency between the waveguide mode and the external optical mode it is necessary to act on the refractive index and mode profile mismatches.

Sometimes, in-plane optical couplers, that allow to extract light from every position on the chip, are more convenient and permit higher density of optical connections per unit area. The dominant design in this case is the grating coupler. This structure acts as a diffraction grating placed at the end of a waveguide and diffracts light at a suitable angle to be collected by an optical fibre nearly perpendicular to the chip.

Both coupling methods have been strongly engineered in the last decades achieving high efficiency coupling. Nonetheless, grating couplers are still strongly wavelength dependent because of their diffracting principle while edge couplers are mostly broad-band. Edge coupling is naturally suitable for platforms with low index contrast because the optical modes of their waveguides overlap better with the free-space field.

2.3.5 Photon sources

The experiment reported in this thesis are based on a bulk optics photon pair source. However, the integrated circuit in Chapter 7 includes several copies of an integrated squeezed state source designed to act either as a single photon heralded source or as a source of path entangled photon pairs. Although we will only describe this particular integrated source of non-classical light, alternative solutions are available on different materials used for optical chips including nano-diamond colour centre and SPDC [83, 84].

By exploiting the non-linear properties of silicon, with a χ^3 coefficient of about $6 \times 10^{-18} m^2/W$, it is possible to induce non-linear phenomena by simply applying a strong field in a long waveguide. In particular, pumping strongly the material, it is possible to induce spontaneous wavelength conversion in a sFWM process. The energy conservation imposes that the sum of the frequency ν_1 and ν_2 of the generated photons balances those of the two photons annihilated from the pump beam, $2\nu_0$. The Hamiltonian is of the form

$$H_{\mathrm{NL}} = K(\ell) a^\dagger_{\nu 1} a^\dagger_{\nu 2} a^2_{\nu 0} + K^*(\ell) a_{\nu 1} a_{\nu 2} (a^\dagger_{\nu 0})^2, \tag{2.42}$$

where ℓ is the length of the waveguide used as source. Due to the brightness and the classical nature of the pump beam, $a^\dagger_{\nu 0}$ and $a_{\nu 0}$ can be replaced by a scalar number proportional to the amplitude of the pump light. It results in a Hamiltonian that generates squeezing on the fields at ν_1 and ν_2. Phase matching determines $K(\ell)$ introducing a cosinusoidal behaviour on ℓ. However,a silicon waveguide in silica cladding is a particularly convenient platform for the generation of photons via sFWM. These waveguides, transparent around 1550 nm, in the range of wavelengths used for communication applications, can be modelled in such a way to have a period of the phase matching function longer than 10 cm [85].

Upon preventing light at wavelengths ν_1 and ν_2 from coupling into the waveguides, the generated state is a squeezed vacuum state whose squeezing parameter ξ depends linearly on the pump power. For low squeezing parameter, the probability of generating a photon pair is proportional to $|\xi|^2$, hence to the square of the pump power. Common practice is to add an on-chip filter to prevent the pump to couple into the remaining linear component of an optical circuit to prevent further undesired photon generation.

These non-linear processes can also be enhanced by enclosing the pump light in a resonant structure. Further details of the non-linear equations of an optical field in integrated devices, and more particularly in integrated photonics, can be found in [86, 87].

We add that it has been experimentally demonstrated that, by pumping multiple sources with a coherent light beam, the generated squeezed state of light retain the relative coherence and can be successfully interfered [88]. In particular, the state generated with this method can present an entanglement shared across many optical modes [89].

2.4 Considerations on experimental quantum photonics

2.4.1 Transfer matrix composition

In Sec. 2.3.3 we have tacitly adopted the composition rule that returns the transfer matrix T of a linear device by composing the matrix of each element with a standard matrix multiplication rule in the reverse order,

$$T = \ldots T_4 . T_3 . T_2 . T_1 .$$

When many optical modes are considered, for all the modes k and k' not affected by a particular optical element, the transfer matrix T will have $T_{k,k'} = \delta_{k,k'}$. The transfer matrix of a waveguide connecting two elements is represented by a diagonal matrix with a wavelength dependent phase factor at the mode of the waveguide. A path matching procedure on each mode is usually performed to reduce the wavelength dependence of T to a global factor [90]. We note that a similar wavelength dependent phase factor is part of many components including couplers that should therefore be taken into account in the matching procedure.

Knowing the transfer matrix of the individual elements is sufficient to predict the global transfer matrix. Importantly, the reverse process is also possible. Given a desired unitary transformation U of m optical modes, it is possible to efficiently organise a set of phase-shifters, couplers and MZIs to implement the desired transformation [91–93]. The algorithm described in [91] prescribes to find a sequence of two-mode transformations T_i such that $T_N \dots T_2 . T_1 U = \mathbb{1}$. This identifies a sequence of two-mode transformations $T_i^\dagger$ sufficient to implement U. In particular, this can be achieved with a sequence of nearest neighbour mode transformation implemented by $m(m-1)/2$ phase-shifters and as many variable beam splitters that can be realised with MZIs. These elements are concatenated in a triangular mesh, see Fig. 2.3. A more symmetric rearrangement of the same components, although with different parameter settings, is presented in [92]. In this case the authors demonstrated the feasibility of a squared mesh where each mode passes across n couplers at most. Such a geometry simplifies balancing losses and optical path-length of the multiple modes. Both these designs are universal in the sense that, by having access to all the possible splitting ratios of the MZIs and of phase shifts in the range $(0, 2\pi)$, all the possible unitary transformations of m modes can be achieved up to few multiplicative phase factors of the matrix rows.

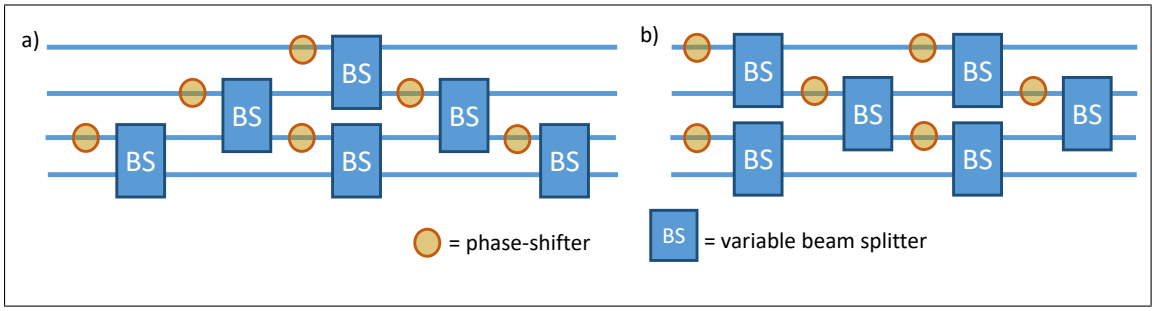

Figure 2.3: Universal interferometer circuits Circuital diagrams for 4-modes universal unitary interferometer decomposition based on variable beam splitters and additional phase-shifters. a) Decomposition proposed by Reck et al. ; b) Decomposition proposed by Clemens et al.

It is useful to note that in most cases[7] the transfer matrix of a linear device used in

[7]Here few exception can be related to the presence of the Faraday effect, a phenomenon that can be induced by magnetic fields but is unusual in integrated photonics [94].

the opposite direction (injecting light from the output port and collecting it into the input ports) is given by its transposed transfer matrix. In multiple occasions we aim to project a single photon state $|\psi\rangle$ on a target vector $|\phi\rangle$. This can be achieved by implementing a transformation U that has the conjugate transpose of the target state, $\langle\phi|$, as its transfer matrix first row. Making use of the transposition relation mentioned before, it is enough to design a circuit that transforms a state injected in the first output port into the state $(|\phi\rangle)^*$. A universal scheme to accomplish such task can be realised with $m-1$ MZIs and as many phase-shifters.

2.4.2 Linear losses and post-selection

A key obstacle to the realisation of a large scale optical quantum device is photon loss. Even though we have up to now considered lossless devices, the propagation of light in most materials has non-negligible loss. Propagating in a homogeneous material, the transmitted power follows the Beer-Lambert law

$$P_{\text{transmitted}} = e^{-\alpha z} P_{\text{injected}}$$

where z is the propagation distance. The same law can be applied to integrated waveguides whose loss coefficient α, however, is greater than the intrinsic one of the material constituting the core or the cladding. Indeed, the fabrication procedure may result in surface roughness, structural defects, chemical defects (dangling bonds, impurities, vacancy and substitution ...), and density fluctuations that act as additional scattering elements.

On top of this scattering, optical components include interfaces between regions described by different sets of optical modes resulting in back-reflection and losses into radiative (not guided) modes. Moreover, a large toll is paid at the input and output of the device, especially when access to state of the art solution is not available. Finally, the detection of photons itself cannot be considered as a unit efficiency process.

In classical photonics it is easy to include the effect of losses. The transfer matrix of a lossy element has an operator norm less than 1. Similarly, the propagation loss in a waveguide are taken into account with the Beer-Lambert-like law by introducing a specific transmissivity factor α characterising the waveguide. The quantum description of these processes it is commonly modelled with the presence of virtual beam splitters distributed along the system. A mode from the system enters one of the ports of the beam splitter while the vacuum state is considered in the other input port, one output mode of the splitter continues in the system while the second output port goes into a dumping mode. Using this formal description it is possible to imagine a myriad of beam splitters each of them with nearly unit transmission. The dumping modes include radiative losses and scattering but also back reflections and material absorption.

Adopting the many-beamsplitter method, the overall linear quantum transformation of the system is described in a very large Hilbert space. The details of the unitary transformation are not accessible but the sub-matrix that describes the relation between the guided mode of light are described by the classical lossy transfer matrix. The transmission of a multi-photon state results in a state with fewer photons in the guided modes. A widespread approach is to consider only those probabilistic events when the same number of injected photons is detected at the output (post-selection). For input Fock states, the probability of these events can be calculated using the permanent rule Eq. 2.35. If all the possible outputs with different number of photons were considered, the resulting state projected onto the system modes is mixed. A continuous evolution of the system density matrix can be performed using the Lindblad form of the master equation assigning $L_\mu^\dagger = a_k$. However, if the losses are not uniform, the knowledge of the Hamiltonian H_S that contributes to the unitary part of the evolution is required.

Clearly, the post-selection comes at a great cost. Assuming uniform losses, i.e. each column of the transfer matrix has the same norm $\eta_T < 1$, the probability of detecting a pattern scales exponentially with the number of photons N. By factoring η_T with the efficiency of output coupling and detection $\eta_D < 1$, the probability of successfully detecting an output pattern is proportional to $\left(\eta_T \eta_D\right)^N$. Additionally, in many applications, the size of the system grows together with the number of photons decreasing η_T. This results in a super-exponential dependence of the detection rate with the number of photons.

It is important to note that post-selection on fewer photons than the initial state generates errors. A typical example is the approximation of a squeezed state as a source of photon pairs. Although occurring with increasingly lower probability, any number of photon pairs could be generated.

2.5 Quantum simulation

The foreseen applications of quantum technologies span from secure communication [95], improved sensitivity [96], to more efficient solutions to computationally intensive calculations [19, 97, 98], including machine learning and neural networks approaches [99, 100].

The computational advantage of quantum devices is evident when dealing with the simulation of quantum systems [23]. Even for small scale systems composed by few particles each with an handful of degrees of freedom, the size of the Hilbert space that describes the composite system is exponentially large. To make two small examples: the possible configuration of a 8×8 square lattice populated with a single spin-half particle on each of the vertices are $2^{64} \approx 2 \cdot 10^{18}$, the possible patterns that can be generated distributing 14 identical particles among 196 sites are $\binom{209}{14} \approx 2 \cdot 10^{21}$. A quantum state of these systems can generally be a superposition of all those configurations therefore many complex floating

numbers should be saved on a classical device if one wanted to describe a generic state. This representation problem affects the possibility of computing expectation values on these systems without adopting approximations that might compromise the accuracy of the simulation. Contrarily, a quantum device composed of a number of particles comparable with the physical system we want to model can be prepared in the superposition of many states and the multitude of configurations achievable becomes a strength rather than a burden, at least in principle.

For a digital quantum device, that encodes the information in the state of a multi-qubit system, the physical properties of the model to simulate are encoded in a sequence of gate operations between the qubits [98]. The application of a sequence of non commuting transformations can be used to approximate the evolution of more complex but local Hamiltonians using the Trotter relations [34] :

$$
\begin{aligned}
e^{i(A+B)\Delta t} &= e^{i(A)\Delta t} e^{i(B)\Delta t} + O(\Delta t^2), \\
e^{i(A+B)\Delta t} &= e^{i(A)\frac{\Delta t}{2}} e^{i(B)\Delta t} e^{i(A)\frac{\Delta t}{2}} + O(\Delta t^3).
\end{aligned}
\tag{2.43}
$$

Additional simulation strategies are in place for non digital quantum architectures. These are based on the realisation of an artificial quantum system that can be accurately controlled in the lab. In particular, the interaction among its components can be tuned to reproduce the dynamics of desired Hamiltonian models. These devices can be used as analogue simulators: the evolution of the system due to an Hamiltonian is not decomposed in a myriad of alternative sequential transformations but is continuously generated by the Hamiltonian engineered on the device. This approach has also been reinterpreted to look for solutions to problems different from a physical system simulation by encoding the problem in the Hamiltonian of a system and measuring its physical properties [20].

We note that the final measurements performed at the end of a quantum simulator should not aim to entirely reconstruct the quantum state of the system. As mentioned before, this would require to extract an exponential amount of storage memory as well as an exponential number of different measurement settings. However, the initial state of a simulation can be parametrised with a limited number of degrees of freedom and these optimised based on outcomes of a simulation that would be intractable for a classical device [101].

One of the advantages of analogue simulators is that they appear less demanding of a universal quantum computer. Unfortunately, it is not clear how error correction schemes could be applied to these systems. The validity of the results from these simulators directly depends on the fidelity of their operation and the ultimate complexity achievable with an analogue simulator is limited by its noise level [22].

2.5.1 Quantum simulation with photonics

Several examples of quantum evolution in linear optics and photonic platforms have already been demonstrated implementing quantum walks and mappings on different physical systems [102–106]. However, increasing the number of indistinguishable photons interfering is very challenging, due to losses and probabilistic generation of the single photon sources [107, 108]. Even more complicated is the simulation of interaction between photons that are by their nature non-interacting Bosons.

2.5.2 Boson sampling

Arguably the more favourable task for a multiphoton linear optical experiment is *boson sampling*. The aim is to produce samples from a distribution hard to compute, proportional to the permanents of sub matrices of a given complex transfer matrix U. By injecting N photons in the first N inputs of a linear interferometer implementing U, the generation of random samples is achieved by simply looking at the output detector patterns in the Fock basis. For a random choice of U, the problem is supposed to be intractable for a classical PC when the number of photons N increases [60]. The effective number of photons necessary to claim advantage over classical computers depends on the optimisation of the classical algorithm but optical experiments have not reached such a level [109]. The classical complexity partially arises from the size of unstructured distribution from which the samples can be drawn from, but mainly from the hardness of computing permanents, whose exact calculation requires 2^N multiplications [110].

To lift some of the extra limitations faced by optical experiments, several variants of boson sampling have been proposed that increase the sampling rate of the outputs. Examples such as scattershot boson and driven boson sampling increase the probability of generating an N-photon input state [111–113]. In these examples more than N probabilistic photon pair sources are used and successful events are associated to the generation of N pairs from distinct sources with a combinatorial increase in generation rate.

It is interesting to note how, without feedforward and photo-photon interactions, linear optical experiments with single photon detection are equivalent to a boson sampling experiment, although with a particular choice for the transfer matrix U.

CHAPTER 3

EXPERIMENTAL SETUP

Outline

The experiments presented in this thesis are all realised with the photon source and the programmable integrated optical circuit that I will describe in this chapter. The current state of the photon source, originally set up by Anthony Laing, was last configured by Jacques Carolan. The latter also performed the first calibration of the integrated photonics device. Consequently, the system I am going to describe is also reported in several dissertations and publications [93, 114–116]. In the first section of this chapter, I will recall a few properties of birefringent and second order non-linear materials. An in-depth description of the optical properties of these materials can be found in [37]. The second section contains the explanation of the photon source setup. The third and fourth sections cover the description of the photonic chip and the photon detection, respectively. In the last section I will present few data describing the performance of the overall setup.

3.1 Uniaxial materials

An external electric field applied to a material generates a polarisation of the material itself. Such polarisation acts as a source of an additional electric field. In the linear regime, when periodic fields are applied at optically relevant frequency, the effect of this polarisation can be summarised in a frequency dependent refractive index $n(\nu)$ that determines the dispersion relations of the light propagating in this material

$$k = \frac{2\pi\nu n(\nu)}{c} \qquad E_x(x,y,z,t) = E_{0x}e^{i(kz-2\pi\nu t)},$$

where $E(x,y,z,t)$ represents the x-component of the electric field of a plane-wave propagating along z. The wavenumber k determines the distance between the wave-fronts of the plane wave. However, the microscopic structure of some materials is strongly anisotropic and the polarisation induced depends on the direction of the electric field.

We will now focus on uniaxial materials. The optical properties of these materials do not change if they are rotated around a specific axis of their structure while different polarisation response is observed when the material is rotated around a different axis. For a uniaxial material, only two out of the three eigenvalues of the permittivity matrix that relates the electric field vector to the induced linear polarisation are identical. For each propagation direction identified by $\vec{k}$, it is possible to define a polarisation direction of the electric field orthogonal to the material axis. The refractive index experienced by this wave is named ordinary refractive index $n_o(\nu)$. The alternative polarisation is subject to the extraordinary refractive index $n_e(\nu,\theta)$, where θ is the angle between the symmetry axis and the wave-vector.

The lack of crystallographic centro-symmetry, compatible with birefringent materials but absent in materials such as silicon or glass, is necessary for the existence of second order non-linear phenomena. In these materials, when strong electric fields are applied, the polarisation has an additional contribution P^{NL} proportional to the square of the electric field E.

$$P_i^{\mathrm{NL}} = \chi^2_{i,j,k} E_j E_k$$

In addition to the symmetry requirement, the presence of an extraordinary refractive index permits to find frequencies that satisfies the phase-matching condition inside the material,

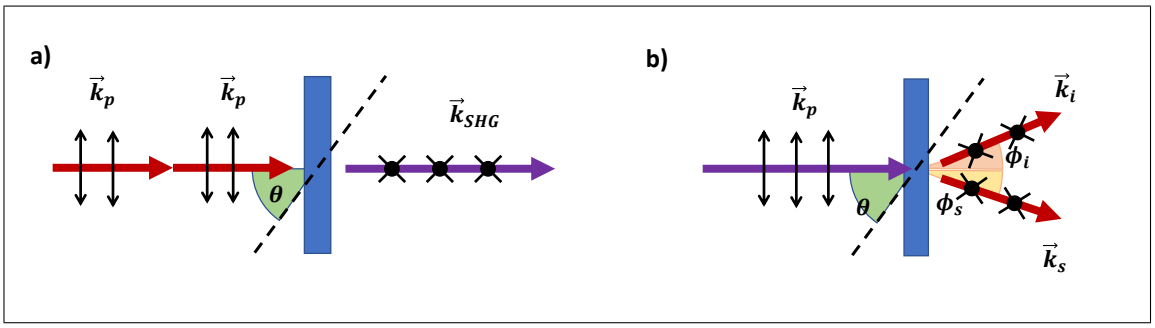

Figure 3.1: Non-linear optical processes in χ^2 materials. The pictures represent the frequency conversion passing through a non-linear crystal. The optical axis of the material is indicated by the dashed line and lies on the figure plane. Double headed arrows on the figure plane and crosses represent polarisation of the electric field subject to extraordinary and ordinary refractive index, respectively. a): co-linear second harmonic generation. The phase matching condition can be tuned adjusting the angle θ. b): spontaneous parametric down conversion. Tuning θ affects the angle of the photon emission ϕ_s and ϕ_i.

$$2\nu_p n_e(\nu_p,\theta_p) = \nu_{\mathrm{SHG}} n_o(\nu_{\mathrm{SHG}}), \qquad 2\nu_p = \nu_{\mathrm{SHG}}. \tag{3.1}$$

$$\begin{aligned} \nu_p n_e(\nu_p,\theta_p) &= (\cos\phi_s)\nu_s n_o(\nu_s) + (\cos\phi_i)\nu_i n_o(\nu_i), \\ (\sin\phi_s)\nu_s n_o(\nu_s) &= (\sin\phi_i)\nu_i n_o(\nu_i) \qquad \nu_p = \nu_s + \nu_i. \end{aligned} \tag{3.2}$$

Eq. 3.1 refers to co-linear second harmonic generation (SHG), a process that generates a field at double the frequency of the injected light. Eq. 3.2 refers to the spontaneous parametric down conversion (SPDC) process where light at signal and idler frequencies, ν_s and ν_i, respectively, are generated. ϕ_1 and ϕ_2 are the emission angles of the generated photons. In Fig. 3.1 we show a geometrical representation of the two processes. It is worthy to mention that the dispersion relation of isotropic materials generally prevents the opportunity of achieving phase-matching condition.

We note that the spontaneous generation of photons is not predicted in classical wave optics when the complete absence of electromagnetic fields at frequencies ν_i and ν_s is assumed. The closest classical phenomena is the optical parametric amplification, also equivalent to the difference frequency generation. In this process, the non linear interaction between pump and signal field generate a third wave at frequency $\nu_i = \nu_p - \nu_s$ that triggers the conversion of more optical power from the pump to the signal wave.

From a quantum mechanical point of view, the three mentioned non-linear processes are equivalent and are described by the following Hamiltonian

$$H_{\chi 2} = K\, a^{\dagger}_{\nu 1} a^{\dagger}_{\nu 2} a_{\nu 0} + K^* a_{\nu 1} a_{\nu 2} a^{\dagger}_{\nu 0}. \tag{3.3}$$

Given this interaction, the three optical phenomena are characterised by significantly different initial states of the system.

3.2 Photon pair sources

The Fock states we used in the experiments are low power approximation of squeezed states generated outside the chip and than injected into it. In Fig. 3.2 we present a block diagram representation of the photon generation stage. A mode-locked Ti:Sapphire laser is tuned to emit light at around 808 nm. The nominal pulse duration, as provided by the Coherent laser company that produced the laser, is 140 fs. The repetition rate is approximately 80 MHz. The power emitted by the laser needs to be externally adjusted to control the level of squeezing produced by the source. For this purpose, a half-wave plate rotates the polarisation

direction of the linearly polarised light from the laser. Then a polarisation cube attenuates the intensity of the beam deflecting the vertically polarised component. Depending on the orientation of the half-wave plate, a fraction of the laser power is damped in a beam block. The remaining intensity of the light pulses is used to generate light pulses at 404 nm in a barium borate (BBO) non-linear crystal by means of SHG. The up-converted pulses are collinear with the direction of the pumping light. Then, a sequence of four dichroic mirrors route the light at 404 nm removing the light at 808 nm from the beam.

The remaining pulses at 404 nm are focused on a second non-linear crystal made of bismuth borate (BiBO). In this, a type I SPDC occurs generating pair of photon with the same polarisation. The energy of the impinging photons is converted in pairs of photons at around 808 nm. The phase matching condition of the crystal imposes that the generation is not collinear with the pumping beam. In fact, frequency degenerate photons appear on a cone of emission symmetric with respect to the pumping direction. After the generation, a notch filter with 3 nm bandwidth centred at 808 nm discards the 404 light and increases the spectral indistinguishability of the photons.

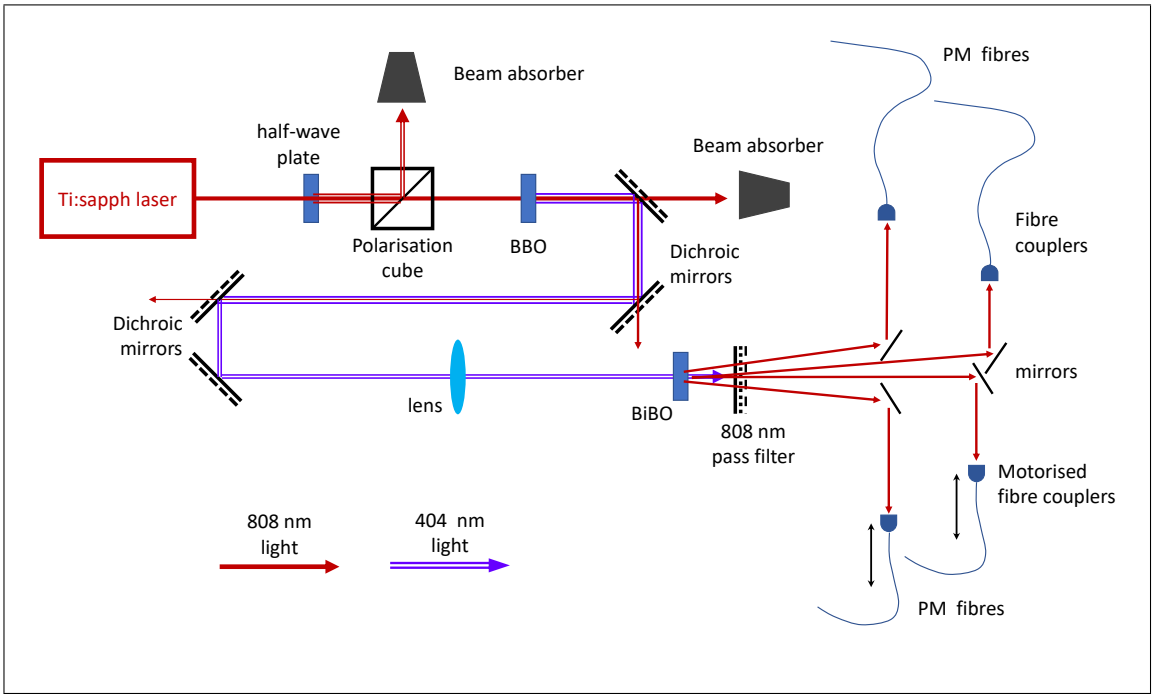

Figure 3.2: Setup of the SPDC photon pair source. A Ti:Sapphire laser induces a second harmonic generation process in a barium borate (BBO) non-linear crystal. The 404 nm light is reflected by dichroic mirrors to remove the light at 808 nm. The 404 nm pulses are focused on a bismuth borate non-linear crystal generating squeezed vacuum state of light at 808 nm. Light is filtered and collected in 4 PM fibres.

We use the emission cone as a double photon pair source. 4 mirrors, placed at the edge of two orthogonal diameters of the emission cone, divert the photons to 4 collection stages that

couple the light into polarisation maintaining (PM) fibres. The two modes of light collected at the extremes of the same diameter are in a two mode squeezed state. We will refer to each of this squeezed state as a photon pair source. The statistic of the two photon pair source are independent. On top of the degrees of freedom needed to couple the light in the PM fibres, the four collection stages can be translated along the propagation line of the photons. This allows us to control the arrival time of the photons to the chip, by modifying the free space path-length of the photons, and therefore their distinguishability. In each photon pair source, one of the translational stage is motorised and can be controlled via software offering a practical solution for recording HOM dips.

3.3 Programmable integrated interferometer

The programmable integrated interferometer we used was produced by the Japanese communication company Nippon Telegraph and Telephone [93]. The system was delivered optically and electrically packaged with an access to a Peltier cooling unit for temperature stabilisation [117]. The optical input-output interface is based on two v-grooved fibre arrays[1] edge coupled to the chip and glued in place. The system is a planar lightwave circuit with silica cladding and waveguide cores made of germanium doped silica. The cross-section of the doped region is $3.5\mu m \times 3.5\mu m$. The tunability of the system is based on thermal phase-shifters consisting in $1\mu m$ thick strips of Ta_2N deposited on top of the cladding layer. Trenches are used to thermally isolate the waveguide from each other and increase the efficiency of the heaters.

The circuit is designed to perform arbitrary unitary transformations across 6 fundamental TE waveguide modes implementing the scheme described in [91], with integrated components. For this scope, 15 pairs of DCs and as many thermal phase-shifters are used to implement 15 variable beam splitters in a MZI configuration. 15 additional phase-shifters are interposed between the MZI in the triangular arrangement. In Fig. 3.3, the conceptual circuit of the chip is shown.

The resistance of the individual heaters is about 100 Ω while the electrical wiring account for extra 10 Ω. During chip calibration and operation, voltages ranging from 1.8 V to 9.6 V are applied with an average dissipated power of the order of 10 W. Through the Peltier cooling system, the heat-load of the chip is mainly transferred to the optical table and then dissipated into the air conditioned environment. A proportional-integrated-derivative (PID) control unit reacts to the change of dissipated power between different chip settings. The unit stabilises the substrate temperature of the chip by adapting the cooling power of the Peltier element. In the experiments, the temperature was stabilised up to few hundredths of

[1]Although we are not informed of the actual brand of fibre array used, a description of the v-grooved technology is present in the OZ optics catalogue [118].

a degree. Depending on the difference in the heat load applied, a latency of more than 10 s between different chip configuration was required.

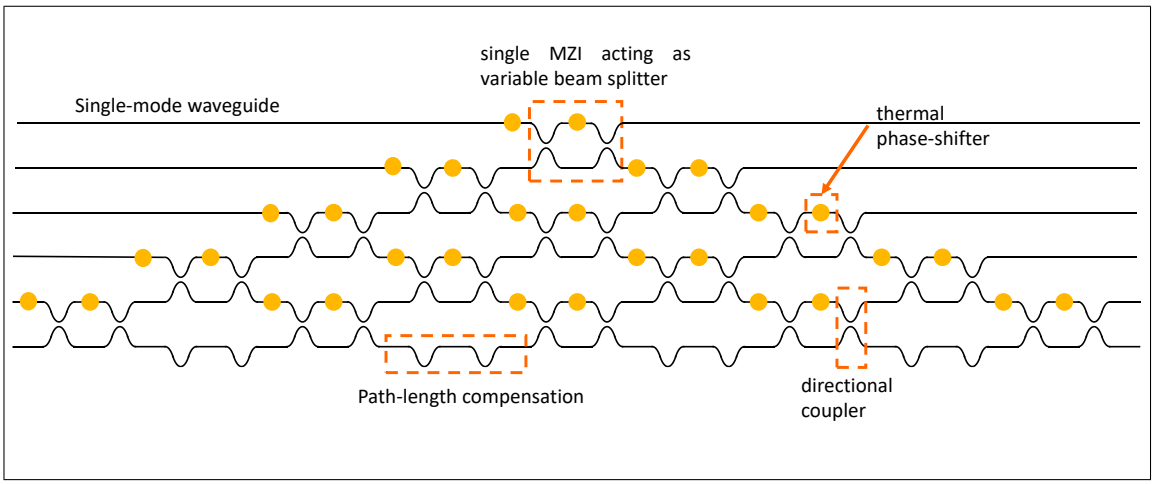

Figure 3.3: Schematic of the optical circuit of the integrated interferometer. Six single mode waveguides interfere with each other through multiple MZI acting as variable beam splitters. Each MZi is composed of two directional couplers and a thermal phase-shifter.

We inform that, along the period spanned by this thesis, the input port directly connected to the bottom mode became inaccessible. The optical mode was then only addressable through the 5th input fibre and the adjacent MZI.

3.4 Photon detection

The detection of the single photon is entrusted to an array of 12 silicon based single photon avalanche detectors. Each of them, with an efficiency between 50% and 60%, can distinguish between the vacuum state and a populated state of the Hilbert space. We note that the detector efficiency refers to a single photon Fock state. The probability of a detector click for a for a state with an higher number of photons is expected to be higher. In the experiments, photons from the source were either routed directly to the detector array or injected into the interferometer and detected afterwards. While all the connections are based on PM fibres, the chip itself induces polarisation rotation, especially due to the degeneracy between the fundamental TE and TM modes[2]. To remove this effect, each optical fibre coming from the chip is connected to fibre optic polarisation beam splitters that removes the TM component.

The signal coming from the detectors are converted in a list of time tagged coordinates by a commercial counting logic card. The system can accept up to 16 input channels. The

[2]In a symmetric waveguide geometry, the optical mode chatacterised by no electric field in the propagation direction (TE) and no magnetic field along the propagation direction (TM) modes, are related by a $\pi/2$ rotation and propagated with the same phase velocity. This exacerbates the probability for a photon to be scattered in the orthogonal guided mode.

correlation between the arrival times of the photon is analysed by a software designed by Pete Shadbolt [116]. A digital delay can be associate to each input channel to account for temporal delays in the signal processing by the counting card that do not reflect the actual time passage through the chip. These delays compensate for mismatch in the fibre length, electronic signal processing and signal propagation. In particular, a large time delay occurs between photon directly measured from the source and photons processed by the integrated circuit because of the additional fibre connections. The digitally corrected arrival times are considered coincidental if occurring within a coincidence window. Due to electronic jitter, that introduces independent fluctuations in the arrival time of the signal at each channel, the coincidence time window must be at least 0.4 ns. During the experiments this was usually set to be 2 ns.

3.5 Performance

3.5.1 Photon interference

The rate of coincidences detected from a single photon pair source can be adjusted modifying the power of the pulses used in the non-linear photon conversions. In experimental conditions, if a single source was plugged straight into the detectors, we could detect a two photon coincidences at up to 18 kHz[3], depending of the level of squeezing. The ratio between single photon events from at a single detector and coincidental detection was $\sim 10-12\%$. By taking into account the detector efficiency, we can estimate that each generated photon had a $20-25\%$ probability of being collected into the PM fibre. In Fig. 3.4 we report examples of HOM interference fringe for the photons generated by our sources. The HOM interference between photons generated from the same source, as measured at a fibre optic beam splitter, gave a visibility of 98% with a feeble wiggling due to residual entanglement between the two photons [119–121]. The interference between two single photons heralded from the two pair sources, gave a HOM dip visibility of 92%. The fringe was taken with a low enough squeezing such that the multiphoton generation was not the dominant source of error. However, a significant squeezing was necessary to have enough four-fold coincidence events before drifting of the source properties occurred. In the low power approximation, the state generated can be described expanding a couple of two-mode squeezed states up to the four

[3]Taking into account photon losses and detector efficiency, this corresponded to $\tanh(|\xi|) \sim 0.15$

photon terms,

(3.4)

$$
\begin{aligned}
|\mathrm{TMS}(\xi)\rangle_{1,2} \otimes |\mathrm{TMS}(\xi)\rangle_{3,4} \approx (1-P)\left(|0,0\rangle + \sqrt{P}\,|1,1\rangle + P\,|2,2\rangle\right)_{1,2} \otimes \left(|0,0\rangle + \sqrt{P}\,|1,1\rangle + P\,|2,2\rangle\right)_{3,4} \\
= (1-P)\left[|0,0,0,0\rangle + \sqrt{P}\left(|1,1,0,0\rangle + |0,0,1,1\rangle\right)\right]_{1,2,3,4} \\
+ (1-P)P\left[|1,1,1,1\rangle + |2,2,0,0\rangle + |0,0,2,2\rangle\right]_{1,2,3,4} \\
+ (1-P)\sqrt{P}^{3}\left[|2,2,1,1\rangle + |1,1,2,2\rangle\right]_{1,2,3,4} + O\left(P^{\frac{3}{2}}\right).
\end{aligned}
$$

The second line in Eq. 3.4 represents states with less than 4 photons. The third line includes the possible four photon states. Upon an heralding signal on mode 1 and 4, we rule out the states $|2,2,0,0\rangle$ and $|0,0,2,2\rangle$. The two remaining modes are then made to interfere at a beam splitter for the heralded HOM dip measurements. The terms in the third line are potential source of noise.

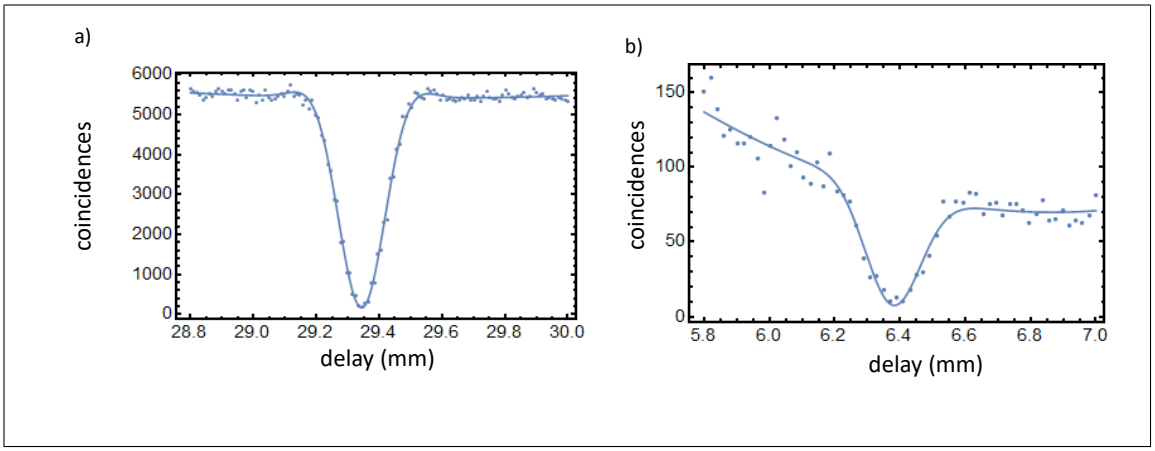

Figure 3.4: HOM fringes between the generated photon pairs a) example of HOM dip recorded using two photons belonging to the same photon pair source. b) example of heralded HOM dip probing the interference visibility between photons from different sources.

The reduction of the visibility observed in the measurements is ascribed to the spectral-temporal entanglement shared by the photons from the same source. The heralding process, that traces out the degrees of freedom of heralding photon, explain the mixed nature of the heralded photon interfering at the beam splitter.

The length of the photon wave-packet measured scanning the spatial delay of one of the photons in the HOM interference was about 0.25 mm. The coincidental detection of a photon at each output mode of the beam splitter, as function of the position x of the translational stage, was analysed with the fitting function:

(3.5)
$$
f(x) = \left(a + bx + cx^2\right) \times \left(1 - V\exp\left(-a_2(x-x_0)^2\right)\sinh\left(\frac{x-x_0}{a_3}\right)\right).
$$

The coefficients a, b, c describe the evolution of the rate of two-photon states that enter into the beam splitter. While collecting the interference fringe, this can vary because of slow drift of the source generation rate, or because of the reduction of the fibre coupling efficiency occurring along the translation. x_0 is the centre of the dip, corresponding to the minimal temporal distinguishability of the photons, a_2 and a_3 are fitting parameter to adjust to the width of the wave packet, and V is the fringe visibility.

3.5.2 Optical chip performance

Based on silica doped technology, the footprint of the integrated circuit is $10cm \times 4cm$. This is much larger than what can be achieved with alternative semiconductor materials such as silicon or gallium arsenide with higher refractive index. However, the resulting device benefit from low insertion losses, thanks to the large mode overlap with optical fibres and to low loss MZI. The overall end-to-end transmission from the input to the output fibre is, on average, 58%.

The calibration of the voltage-phase relation of the phase-shifters is based on a cubic relation $\phi(V) = \phi_0 + c_1 V^2 + c_2 V^3$. Jacques Carolan performed the first calibration of the chip that included a linear transformation between external voltages and voltage drop resulting at the phase-shifter, based on an estimation of the resistivity of the different components of the wiring circuit. We further investigate the effect of electrical and thermal crosstalk in the device in Chapter 4.

The high extinction ratio observed in the MZIs is indicative of the good performance of the DCs. In fig Fig. 3.5 we report a fringe obtained scanning the voltage controlling the phase-shifter included in the MZI at the top of the chip. By dialling a large set of random unitaries on the chip, and injecting single photons in the bottom mode of the chip, it was possible to perform a benchmark on the chip as well as estimate the relative output losses and detector efficiency of the different modes. In Fig. 3.5 we report the distribution of statistical fidelities defined as

$$\mathcal{F} = \frac{\sum_{i=1}^{i=6} \sqrt{p_i \cdot f_i \cdot d_i}}{\sqrt{\sum_j f_j d_j}}, \tag{3.6}$$

between the observed frequency of single photon detection f_i, and the corresponding probability p_i predicted from the dialled matrix. Correction for the detector efficiency d_i are obtained, independently from the dialled unitary, optimising the average fidelity across all the measurements.

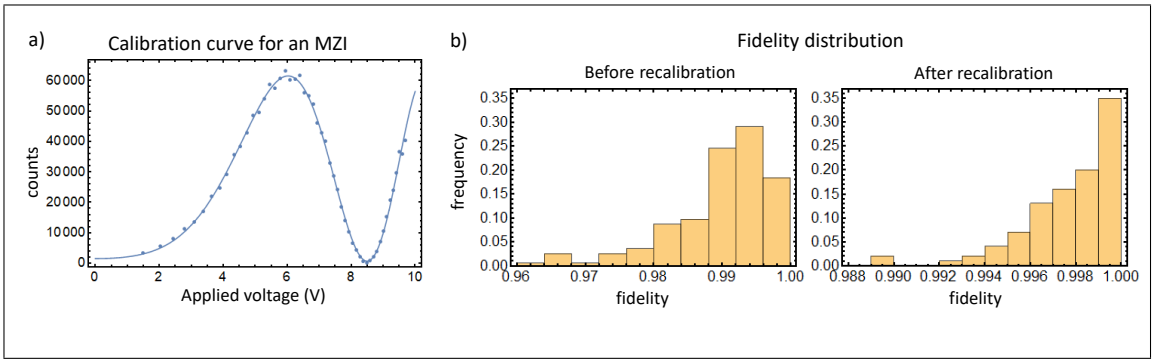

Figure 3.5: Chip characterisation a) Example of a calibration curve for an heater controlling a variable beam splitter. The plot shows the number of single photons transmitted in the same mode as function of the external applied voltage keeping the generation rate constant. To avoid hysteresis effects and compensate for fluctuation in the photon generation rate, the voltage is increase from 1.5 V to 9.6 V, then lowered and increased again while recording the data. The data refer to a uniform spacing of the voltage square. b) Distribution of statistical fidelities several months after the last calibration and after redoing the calibration procedure.

CHAPTER 4

CHARACTERISATION OF INTEGRATED OPTICAL CIRCUITS

Outline

In this chapter I present few results concerning the characterisation of programmable interferometers, particularly relevant for integrated circuits. The contents are organised in three sections dedicated to transfer matrix verification, calibration of crosstalk in phase-shifters, and finally a discussion concerning device characterisation. The experiments were all performed on the optical chip described in Chapter 3.

I will begin the first section by introducing the main characterisation method: the phaselift algorithm, recently proposed for the transfer matrix reconstruction of large linear optical circuits [122, 123], and then present some numerical simulations of the performance of this algorithm. Before showing the experimental demonstration of the algorithm, I will introduce an alternative reconstruction method, the super-stable tomography (SST) [124], I used to compare the phaselift algorithm against. Both mentioned algorithms have been tested on the photonic chip configured to implement a set of 3- and 5-dimensional unitaries. I will conclude the section proposing an extension of the phaselift algorithm.

In the second section, I will discuss the problem of the crosstalk between tunable components such as phase-shifters that are supposed to be independently controlled. Such a problem is emphasised in integrated circuits, where a multitude of different components is localised in a restricted volume [80]. I will present a set of measurements that I used to give a first order approximation of the phenomenon that does not require the knowledge of the physical properties of the device, such as heater resistivities, distance between the components on the chip etc, so that it could be applied to a black box for which only the circuit diagram is known.

In the conclusive section, I will comment on the observed results and discuss the potential applications of the methodology presented in this chapter.

Contributions

The phaselift project is a collaboration with the group of David Gross at the university of Cologne that adapted the algorithm to the context of linear optics. The design of the reconstruction experiment is due to Daniel Suess, Chris Sparrow and myself. The data acquisition was primarily performed by me. In the data collection and analysis I also benefit from the collaboration of Alexandre Mainös and Patrick Yard and from code scripted by Daniel Suess. I and Chris Sparrow investigated the extension of the phaselift algorithm and I elaborated the proof presented in this chapter. I individually conceived, performed and analysed the crosstalk measurements.

4.1 Transfer matrix verification protocols

In current and future applications, integrated optical devices aim to gather thousands of elementary components, such as directional couplers and phase-shifters, on a single chip. Each component is susceptible to fabrication imperfections due to manufacturing tolerance and often tuning of components after fabrication is required. Once all the active and passive precautions are in place (tunability and resilient design), we are left to assess the quality of the resulting device. For complex systems, individual component errors and inaccuracy of the calibration of tunable elements build up and can generate significant deviation from the ideal performance in the final operation of the whole device. Arguably, once the tunable parameters of an optical circuit are set, the most complete characterisation of a linear interferometer is by determining its transfer matrix. Similarly, for programmable devices whose tunable elements can be set to achieve a multitude of target configurations, the verification of the device can be approached by testing the transfer matrix of the system for a set of different configurations.

Multiple possible solutions are present in literature to experimentally determine the transfer matrix of a linear optical device [125–128]. When choosing the best strategy, the most common compromise to be considered are the accuracy of the reconstruction, how the reconstruction time scales with the size of the system, the necessity of a second trusted device etc. Here we experimentally explore a characterisation method named *phaselift* [122], and compare it to results derived from an alternative reconstruction protocol based on the SST[124].

4.1.1 Phaselift reconstruction algorithm

The phaselift algorithm answers the following mathematical problem:

- Assuming the following relations among an unknown complex matrix M, any complex vector α, and the real valued vectors I,

$$\beta_j = \sum_i M_{j,i}\ \alpha_i, \tag{4.1}$$

$$I_j(\alpha) = |\beta_j|^2, \tag{4.2}$$

  determine, up to multiplicative phase factors for each row, the complex matrix M by having only access to the quantities $I_j(\alpha)$ for a chosen finite set of α.

We note that any multiplication of the rows of M by phase factors does not affect I hence, with the given data, M can only be reconstructed up to these unknown phases. Additionally, the task would be trivial if all the entries of M were positive since, choosing α such that $\alpha_k = 0 \ \ \forall k \neq j$, $M_{\ell,j} = \sqrt{I_\ell(\alpha)/|\alpha_j|^2}$.

In linear optics, we can map M to the transfer matrix T of a system and α and β to the amplitudes of the light in the input and output modes, respectively. In doing so, the vector I can be treated as the intensity or the power measured at the output modes (see Fig. 4.1). Therefore, the phaselift algorithm can be used to reconstruct the transfer matrix of linear optical circuits having access to classical input-output relations from the device. For simplicity of notation, in the following we will refer to the j-th row of the matrix M as $\langle M_j|$. The phaselift procedure will reconstruct each $\langle M_j|$ and doing so it retrieves the full M.

In an experimental scenario, the data acquired, I^k, will suffer noise and can be modelled as

$$I_j^k = \left|\left\langle M_j \middle| \alpha^k \right\rangle\right|^2 + \epsilon_k = \mathrm{tr}\left[\left|\alpha^k\right\rangle\left\langle\alpha^k\middle|M_j\right\rangle\langle M_j|\right] + \epsilon_k, \tag{4.3}$$

where the index k distinguishes between different choices of α and ϵ_k represents a random error on that particular measurement. In this representation, the problem becomes to retrieve the vector $\langle M_j|$ given the results of a set of projections $|\alpha^k\rangle\langle\alpha^k|$. The idea is then to *lift* the problem moving it to a higher dimension where efficient optimisation methods can be applied. The problem translates into finding the best Hermitian semi-positive defined matrix $Z_j \geq 0$ that approximates the m observed data $\left\{I_j^k\right\}_{k=1}^{k=m}$.

$$Z_j = \underset{Z\geq 0}{\arg\min} \sum_{k=1}^{m} \left|\mathrm{tr}\left[\left|\alpha^k\right\rangle\left\langle\alpha^k\middle|Z\right]\right| - I_j^k\Big|. \tag{4.4}$$

While in the ideal case, with vanishing ϵ_k, $Z_j = |M_j\rangle\langle M_j|$ and rank(Z_j)=1; in the real world scenario,we expect that the minimisation will result in a matrix with an eigenvalue

significantly greater than zero and all the others close to zero. The row $\langle M_j|$ is then obtained conjugating the main eigenstate of Z_j scaling it so that its norm becomes the square root of the corresponding eigenvalue. By means of this scaling procedure, the reconstruction method encodes information about the losses in the reconstructed M. Although this isn't a true estimation of the device losses, as it can be affected by external factors such as coupling and detector efficiency, the phaselift reconstruction remains a valid instrument to detect the effects of path dependent losses that would result in a non orthogonal reconstructed matrix. Among the features of the phaselift algorithm, it is important to mention the existence of a performance guarantee that relates the scaling of the number m of probing vectors α to the probability of getting a final matrix within a bounded error from the true transfer matrix [123]. Such bound is constrained to the optimisation of the undetected phases of each row.

Mathematically, this is described as : $\exists\ \delta,\ \eta,\ \gamma > 0$ such that $\forall\ M_j$, the probability P of

$$\min_{\phi} \left\| e^{i\phi} |\tilde{M}_j\rangle - |M_j\rangle \right\|_2 > \delta \frac{\epsilon_0}{\| |M_j\rangle \|_2} \tag{4.5}$$

is $P < \gamma e^{-\eta m}$. Here $|\tilde{M}_j\rangle$ represents the best estimation from the phaselift algorithm of the true vector $|M_j\rangle$, $\epsilon_0 = \sum_{k=1}^{m} |\epsilon_k|/m$ is the averaged absolute error of the different measures and we represented with $\|\cdot\|_2$ the Frobenius norm.

Once applied to each row of M, the above relation ensures a performance guarantee for the reconstruction of the full matrix with an error bound that scales linearly with the dimension of M. While this mathematical bound holds for generic form of noise ϵ_0, we will see that less generic noise allow reconstruction errors below the above threshold.

The above statements is proved to be valid for α^k drawn from suitable distributions. A typical choice for these vectors is to draw them uniformly form the complex unit sphere ($\|\alpha^k\|_2^2 = 1$). An alternative distribution has instead been suggested by the collaborators in Cologne [129]. They proved that choosing α^k with components

$$\alpha_i^k = \begin{cases} = \pm 1, \pm i & \text{with probability p/4} \\ = 0 & \text{with probability 1-p} \end{cases}, \tag{4.6}$$

satisfies the requirements whenever $p \neq 0, 1$. This random distribution was given the name *randomly erased complex Rademacher* (RECR). If the vector from the RECR distribution are normalised before their usage they are still valid for the application of the phaselift protocol. Note that in the simulations and in the experiments we will refer to the RECR distribution meaning its normalised version and to the uniform distribution meaning the uniform distribution on a complex unit sphere.

Daniel Suess provided an open source tool[1] to numerically test the performance of the phaselift reconstruction.

[1] https://github.com/dseuss/pypllon

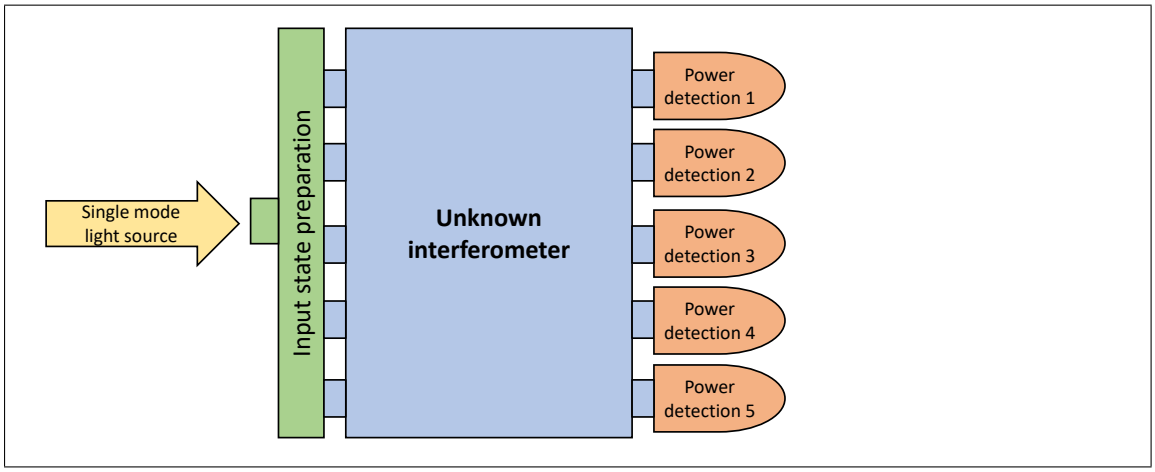

Figure 4.1: General experimental scheme for the phaselift reconstruction. A trusted state preparation circuit transform the light coming from a single mode source into a desired superposition across the N input modes (input state preparation) of the unkown interferometer we are testing. Recording the power exiting the circuit at each output modes for a set of different input states suffices to retrieve the transfer matrix of the circuit if the input states are randomly generated from a suitable distribution.

Here is the overall procedure to perform the transfer matrix reconstruction according to the phaselift protocol.

- Draw a sufficient number (see numerical simulations) of random vectors α^k from a valid distribution such as the uniform or the RECR distribution.

- For each chosen vector, prepare a state of light superposed across the N modes of your system according to α^k. This can be done with classical (coherent) light or with single photons using the following relations

$$\begin{aligned} &\text{single photon state } \left|\psi^k\right\rangle: \qquad \left|\psi^k\right\rangle = \sum_j \alpha_j^k a_j^\dagger |0\rangle^{\otimes N} \\ &\text{multimode coherent state } \left|\alpha^k\right\rangle: \qquad \left|\alpha^k\right\rangle = \otimes_{j=1}^N \left|\alpha_j^k\right\rangle \end{aligned} \tag{4.7}$$

  Experimentally, drawing from a distribution of vectors with the same norm would mean to adopt the same input power during the whole set of measurements or normalise the output power based on the measure of the input power for each data acquisition.

- Inject the states of light described above into your device and record the intensity at each output detector. The reconstruction of all the rows of the matrix can be done injecting only once each input vector if enough detectors at the output are available.

- Analyse the set of data associated to each detector by means of the phaselift algorithm (Eq. 4.4) and retrieve each of the rows of the matrix from the main eigenvector of the matrices Z_j.
- To compare the reconstructed transfer matrix $\tilde{M}$ to the ideal matrix M, optimise a unitary diagonal matrix D of dimensions N such that $\|D.\tilde{M} - M\|_2$ is minimal.

In this protocol, the most stringent requirement is the access to a trusted, phase-stable and flexible state preparation. For these reasons, a mechanism that only requires a fixed number of possible phases to be set on each component of the state preparation stage (as for the RECR example) might be preferred. Also, for a single photon source, the estimation of the input power injected into the device can be challenging.

4.1.1.1 Numerical simulation of Phaselift reconstruction

In the following we present some numerical simulation of the performance of the phaselift reconstruction. In Fig. 4.2 we report the reconstruction error, $\|M_{\text{phaselift}} - M_{\text{ideal}}\|_2$, for an

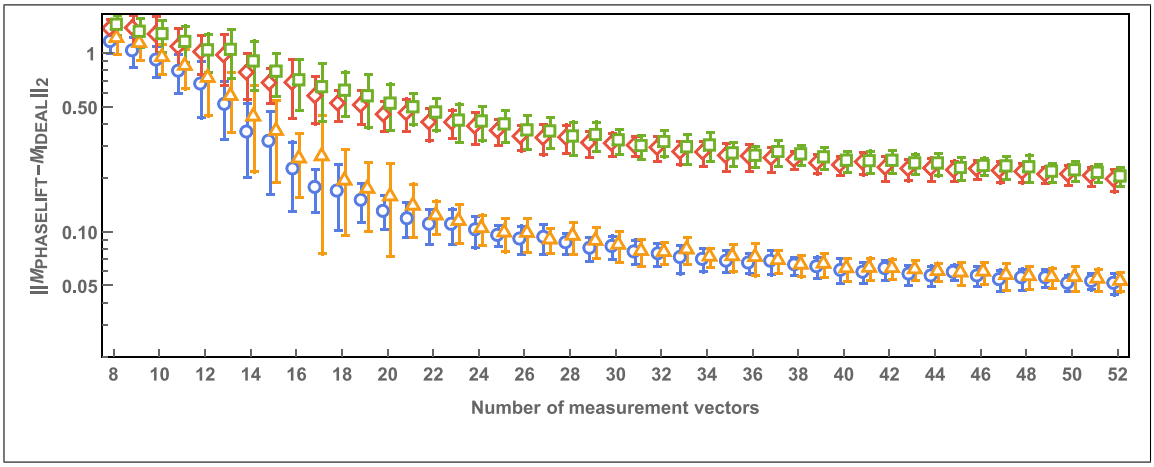

Figure 4.2: Simulated reconstruction performance of a 5-dimensional unitary. Frobenius distance between the ideal unitaries and the matrices reconstructed using the phaselift protocol with an increasing number of measurement vectors drawn from the uniform (blue/red) or RECR (orange/green) distributions. The error bars displayed are the estimate of the standard deviation of the distribution of the L-2 distances obtained from a set of 50 reconstruction of random matrices. The noise applied to each simulated measurement is drawn from a normal distribution with $\sigma = 0.01(0.04)$ for the lower (upper) curve.

increasing number of measurement vectors, for 5-dimensional Haar random unitaries. The error bars represent an estimation of the standard deviation of the reconstruction error distribution while the markers show the mean values. Each point is obtained by averaging over a set of 50 Haar random unitaries with input vectors drawn randomly from a preselected set of 150 input vectors. An independent random error, drawn from a Gaussian distribution

with mean 0, is associated to each triple choice of measurement vector, output detector and random matrix.

Both uniform distribution (in blue/red) and RECR distribution (in orange/green) show similar behaviours with a rapid decreasing of the error from the minimum required number of measurement to about 20-25 input vectors. After this threshold, a change in trend shows a slower performance improvement that is not granted by the analytic proof but probably arises from the Gaussian nature of the simulated noise. Furthermore, the standard deviation of the reconstruction decreases at this turning point. The performance of the two alternative measurement vector distributions is nearly identical but a large difference is visible for the two simulated noise levels $\sigma \in \{0.01, 0.04\}$ represented by the blue/orange , red/green data. The noise level affects the mean error after the threshold number of measurements is reached.

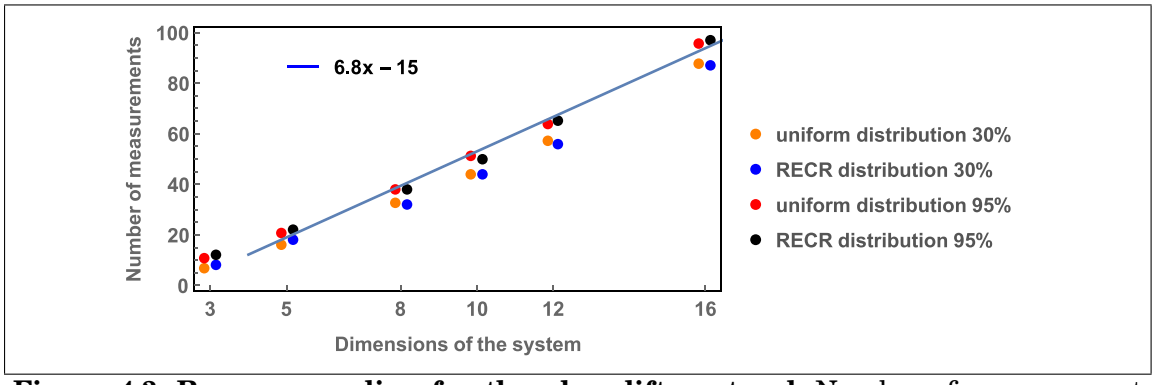

Figure 4.3: Resource scaling for the phaselift protocol. Number of measurement necessary for different size of the system to cross the reconstruction error threshold $\|M_{\text{phaselift}} - M_{\text{ideal}}\| < 4\sigma N$ where N is the number of modes of the system and σ characterises the Gaussian noise on each measurement of the output powers. The reconstruction is performed on a set of 50 unitaries for each system dimension with an increasing number of measurement vectors and then the percentage of reconstruction with error below threshold is found. Dots show the number of measurement necessary for two success probabilities of 30% and 95%, for uniform distributed input vectors and for the RECR distribution slightly displaced at the sides for better reading. The blue line represents the linear trend for $5 < N < 16$ for a success probability of 95%

Fig. 4.3 shows the scaling of the number of measurement vectors required to obtain a reconstruction error below a given threshold, for an increasing size of the system. Taking from [123], the threshold is set to be $4\sigma N$ where N is the number of modes and σ is the standard deviation of the noise for a single detector. For each N, 50 different transfer matrices were sampled and then the phaselift reconstruction simulated with an increasing number of random measurement vectors. Each measurement was subject to additive Gaussian noise with a standard deviation of 0.01 for each detector. The orange and blue dots indicate the necessary number of measurements for obtaining 30% of the reconstructed matrices with

reconstruction error below threshold when sampling from the uniform and RECR distribution, respectively. Red and black dots indicate the necessary number of measurements to reconstruct 95% of the tested unitaries with error below threshold. The simulation shows how the reconstruction error sharply decreases below the threshold for a number of measurement vectors that scales approximately linearly with the size of the system. The number of measurements necessary for a highly successful reconstruction can be approximated with $\tilde{m} = 6.8N - 15$ for low values of N.

4.1.2 Super-stable tomography

The SST is a characterisation process devised for unitary linear optical transfer matrices featuring input and output coupling losses [124]. The general form of the transfer matrix T for these systems is of the form:

$$T = \begin{pmatrix} l_1 & 0 & \dots \\ 0 & l_2 & \dots \\ \vdots & \vdots & \ddots \end{pmatrix} . U . \begin{pmatrix} g_1 & 0 & \dots \\ 0 & g_2 & \dots \\ \vdots & \vdots & \ddots \end{pmatrix}, \tag{4.8}$$

where U is a generic unitary matrix that we want to reconstruct up to phases on both the rows and columns. The two diagonal matrices of positive real numbers account for the input, g_i, and output, l_i, coupling losses. The main strength of this algorithm is that the two diagonal matrices could also be made of complex numbers with randomly fluctuating phases and the protocol could still be successfully performed. Indeed, the name of this protocol refers to the complete stability against phase fluctuations at the input and output ports of the interferometer. The modulus of g_i and l_i can also include the efficiency of the injected light and the detection efficiency of the detectors, respectively.

Using data obtained from single photon experiments it is possible to obtain direct information about $|T_{a,b}|^2$ by injecting light into the mode b and detecting light at the output port a. Combining multiple input and output observations it is possible to reconstruct:

$$\frac{|T_{i,i'}|^2 |T_{j,j'}|^2}{|T_{i,j'}|^2 |T_{j,i'}|^2} = \frac{g_{i'}^2 l_i^2 |U_{i,i'}|^2 g_{j'}^2 l_j^2 |U_{j,j'}|^2}{g_{j'}^2 l_i^2 |U_{i,j'}|^2 g_{i'}^2 l_j^2 |U_{j,i'}|^2} = \frac{|U_{i,i'}|^2 |U_{j,j'}|^2}{|U_{i,j'}|^2 |U_{j,i'}|^2}. \tag{4.9}$$

Note that we implicitly assumed that the injected power is kept constant but this last statement is also practically valid if only terms $T_{a,b}$ with the same b are measured with the same input power.

Instead, injecting two single photons in the device and observing the HOM interference they generate, it is possible to measure the HOM visibility V given by

$$V_{i,j,k,h} = \frac{C_{i,j,k,h} - Q_{i,j,k,h}}{C_{i,j,k,h}}, \tag{4.10}$$

where the term $C_{i,j,k,h}$ is proportional to the rate of twofold coincidences for classical distinguishable particles and $Q_{i,j,k,h}$ is the analogue quantities for indistinguishable bosons. Here, k,h indicate the input modes for two single photons and i,j are the output ports at which coincidental detections are recorded. In terms of the transfer matrix, the two quantities are given by

$$\begin{aligned} C_{i,j,k,h} &= |T_{i,k}|^2|T_{j,h}|^2 + |T_{i,h}|^2|T_{j,k}|^2, \\ Q_{i,j,k,h} &= |T_{i,h}T_{j,k} + T_{i,k}T_{j,h}|^2. \end{aligned} \tag{4.11}$$

From these definitions, it is possible to write V as function of the relative phases of the elements of U

$$\begin{aligned} V_{i,j,k,h} &= -\frac{|T_{i,k}||T_{j,h}||T_{i,h}||T_{j,k}|}{|T_{i,k}|^2|T_{j,h}|^2 + |T_{i,h}|^2|T_{j,k}|^2} 2\cos\left(\arg\left(U_{i,k}U_{j,h}U_{i,h}^*U_{j,k}^*\right)\right) \\ &= -\left(\frac{|T_{i,k}||T_{j,h}|}{|T_{i,h}||T_{j,k}|} + \frac{|T_{i,h}||T_{j,k}|}{|T_{i,k}||T_{j,h}|}\right)^{-1} 2\cos\left(\alpha_{i,k} + \alpha_{j,h} - \alpha_{i,h} - \alpha_{j,k}\right), \end{aligned} \tag{4.12}$$

where $\alpha_{i,j} = \arg\left(U_{i,j}\right)$. Therefore, we see that, by measuring the set of HOM visibilities $V_{i,j,k,h}$, we can extract the phases of the transfer matrix elements. In particular, since the reconstruction obtained with this technique is not sensitive to the input and output phases, to determine a final transfer matrix an assumption has to be made on the particular phases of at least $2N-1$ elements $U_{i,j}$. A common choice is to assume both first row and first column of the matrix to be real and non-negative. These "known" phases are used as starting point to trigger an iterative process that unveils the phases of the other matrix elements using the visibility data. Additionally, because of the parity of the cosine function, the visibility only returns information about the absolute difference of phases of the elements, $|\alpha_{i,k} + \alpha_{j,h} - \alpha_{i,h} - \alpha_{j,k}|$. This means that our knowledge of $\alpha_{j,k}$ from a single visibility is conditional on knowing $\alpha_{i,k}, \alpha_{j,h}, \alpha_{i,h}$ and is limited to

$$\alpha_{j,k} = \alpha_{i,k} + \alpha_{j,h} - \alpha_{i,h} \pm |\alpha_{i,k} + \alpha_{j,h} - \alpha_{i,h} - \alpha_{j,k}|. \tag{4.13}$$

A way to circumvent such obstacle is to collect multiple visibilities and choose $\alpha_{i,j}$ to be consistent with all observations. Finally, an arbitrary sign for a further matrix element phase needs to be chosen. This last degree of freedom can be understood by considering that every measurement used in the super-stable reconstruction is invariant under a complex conjugation of the whole matrix. This symmetry is broken in the phaselift reconstruction by the presence of the trusted state preparation stage.

Indicating with N the dimension of the linear optical system, the accessible visibility measurements are approximately $N^4/4$ while the algorithm requires about $2N^2$ two-photon interference visibilities. Once all the phases of the matrix elements are determined, the algorithm can run by constructing a matrix whose elements are $|T_{i,j}|e^{i\alpha_{i,j}}$ and then the

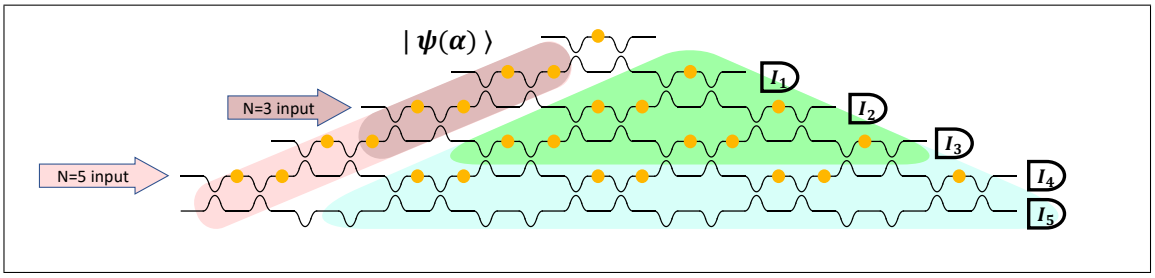

Figure 4.4: Scheme to implement the phaselift reconstruction in an integrated device. Target unitaries are implemented by a triangular subset of the integrated components on the right hand side of the chip. A linear cascade of interferometer on the left prepare the desired input states $|\psi(\alpha)\rangle$. The darker regions are used for 3-dimensional matrices. Detectors are connected to the 5 different outputs.

unitary of interest can be obtained by optimising two real diagonal matrices G and L such that $G.T.L$ is unitary. Alternatively, using the relation in Eq. 4.9, the elements of the unitary, $U_{i,j}$, could be parametrized as function of other $2N-1$ real values, such as $|T_{i,j}|$ of the top-left matrix border elements. Those real values have then to be optimised in order to enforce unitarity condition.

As described above, this reconstruction requires access to a source of distinguishable photon pairs and single photon detectors, equipment that is generally not available in classical optics labs. Alternatively, two photons statistics could be simulated by phase randomised coherent states [130].

4.2 Experimental reconstruction

We tested the two reconstruction algorithms with the integrated chip for 3- and 5-dimensional unitaries. The transfer matrices under examination are programmed on a smaller interferometer composed of a fraction of the components of the whole chip as shown in Fig. 4.4. For the phaselift algorithm, a cascade of MZIs is used to prepare the single photon input states $\psi(\alpha)$; for the SST, this cascade is set to implement an identity transformation. For both dimensions, we set the tested interferometer, composed of a triangular arrangement of MZIs (green and light blue in Fig. 4.4), to implement an identity transformation, a Fourier transform, and three randomly chosen unitaries.

Phselift measurements

We tested both the uniform and RECR distributions of the phaselift protocol using heralded single photons injected into the second from bottom mode of the tested circuits. A set of 30 random input vectors from the uniform distribution and other 31 input vectors from the RECR distribution are used for the phaselift reconstruction of the 3-dimensional matrices.

For the 5 dimensional matrices, a set of 40 and 39 random input vectors from the uniform and RECR distribution are used. The detected counts are rescaled based on the relative detector efficiency and then are normalised, for each combination of input vector and unitary, imposing the total detected power to be 1.

Two-photon interference data.

The two-photon interference visibilities required for the SST were obtained by injecting pairs of indistinguishable photons, generated by a single photon pair source (see Chapter 3). Sequentially, all the possible pairwise combinations of the input modes of the interferometer under examination have been probed, with the exception of the (4,5) input. To correct for residual distinguashibility between the two photons, we measured HOM interferences on an MZI close to the input of the chip and tuned as a 50:50 beam splitter, for each combination of input modes. The visibility of the interference curves collected in this configuration, usually about 97.5%, were used to rescale all the visibilities recorded with the same combination of input modes. These reference curves also provide the dip position and scanning interval required for the actual measurement. For each combination of input photons, after finding the position of the relative delay required to make the photons from the source indistinguishable in time, we performed a fine-grained scan of the optical delay between the two photons to record the HOM dip profile of the reference. We used 91 consecutive positions of the translation stage that linearly span 1.2 mm centred around a first preliminary estimation of the dip position. Subsequently, we used the same parameters to measure the visibility after programming the chip to perform the desired unitary. The integration time for each data point of a visibility curve is taken to be 7s or higher. These values were chosen as trade-off between statistical noise level, stability of the rate of photon pairs and density of sampling of the curve.

The fitting function used was

$$f(x) = \left(a_4 + a_5 x + a_6 x^2\right) \times \left(1 - a_1 \exp\left(-\frac{(x-a_2)^2}{a_3^2}\right) \sinh\left(\frac{x-a_2}{a_7}\right)\right). \tag{4.14}$$

However, in some cases, when there was no convergence, the degrees of freedom of the parameters a_2, a_3, and a_7 were removed and those coefficients set to be the same as those of the reference curve.

We used the two photon interference measurements to obtain a reconstruction of the effective transfer matrix implemented on the chip that was independent of the phaselift procedure and that could potentially constitute a reference more accurate than the ideal unitary. Assuming that the effective transfer matrix does not differ substantially from the ideal matrix, we solved the problem of sign ambiguity of the cos function explained in

Sec. 4.1.2 by simply taking the correct sign from the ideal matrix. This permitted us to select only the visibility estimations with a better signal to noise ratio (see for example Fig. 4.5).

Unitarity measurement

To give a numerical value to the unitarity of a matrix M, we chose the following function:

$$f[M] = \sqrt{0.5\|M.M^\dagger - \mathbb{1}\|_2^2 + 0.5\|M^\dagger.M - \mathbb{1}\|_2^2} \tag{4.15}$$

where $\|A\|_2 = \sqrt{\sum_{i,j}|A_{i,j}|^2}$ is the Frobenius norm of a matrix. In particular, for a unitary U, $f[U] = 0$. The free parameter optimisation of the SST was performed minimising $f[M] = f[G.T.L]$.

Results

In Fig. 4.6 we show the difference, expressed through the Frobenius norm, between the phaselift reconstructions obtained using the uniform and the RECR distribution as well as between these reconstructions and the ideal unitary. Additionally, we also report the distance between the transfer matrix reconstructed with the uniform distribution and the alternative reconstruction obtained with the SST. In this last case, the distance is given after optimising the SST reconstruction over the $2n-1$ degrees of freedom associated with the multiplicative phases of columns and rows. Two reference lines for 3- and 5- dimensional matrices correspond to the numerically averaged distance between two random unitary matrices with optimised row phases.

We note that the discrepancy between the ideal target unitary and the two phaselift reconstructions is larger than the distance between the two phaselift reconstruction themselves. This suggests that the deviation observed originates from actual imperfections in the implemented transfer matrix. The absolute value of this separation is indeed accentuated for the 5-dimensional matrices. While the reconstruction error is expected to increase with the number of rows in the reconstructed matrix, the magnitude of this discrepancy cannot be justified entirely by the scaling of the reconstruction. Furthermore, comparing the transfer matrices obtained with the super-stable tomography reconstruction with the results of the phaselift algorithm with uniform input vectors, the distance observed is similar to what is observed between the two alternative phaselift reconstructions.

In Fig. 4.7 we also plot the unitarity estimator $f[M]$ for the different reconstructions. Similarly, the two reference lines are the numerical average for random matrices with normalised rows. Surprisingly, the phaselift reconstruction returns a transfer matrix with higher unitarity than the SST, despite the step in the algorithm that specifically optimises for unitarity. This could be due to some violation of the assumption of this method such as path dependent loss or fluctuation of the input losses described by the matrices L and

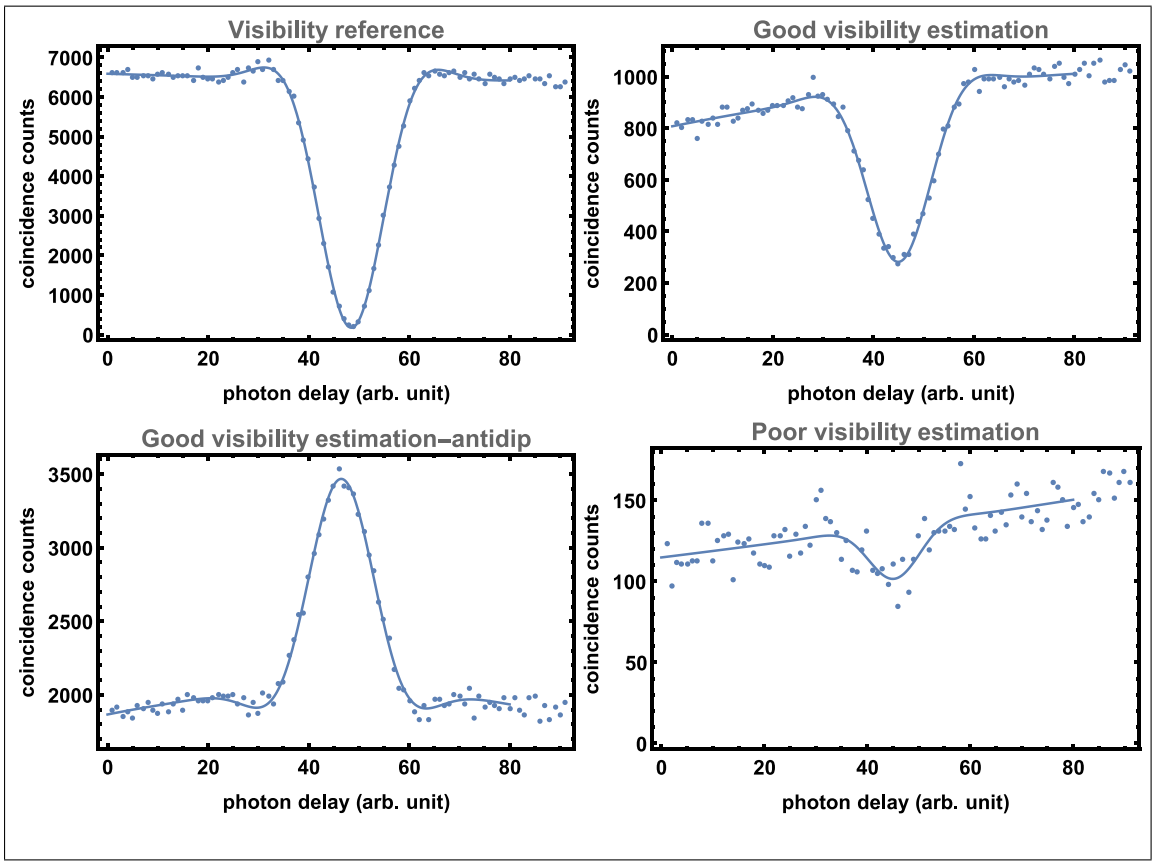

Figure 4.5: Examples of visibility curve for the super-stable reconstruction. The four examples show the effect of constructive or destructive two-photon interference depending on the phases of the matrix elements probed with the photon pair. Top-left: reference HOM dip interference measured on an MZI set to implement a 50:50 beam splitter. Residual distinguishability determines visility less tham 100%. Top-right: example of good quality destructive interference signal. Bottom-left: example of good quality constructive interference signal. Bottom-right: example of noisy visibility estimation due to lower count rates associated to a specific input-output modes combination.

G in Eq. 4.8. We regularly have to connect and disconnect the PM fibres from the source connection to the input modes; this process of changing optical fibres could lead to the input losses changing from run to run.

Finally, in Fig. 4.8 we compare the reconstructed transfer matrices with the unitaries ideally dialled on the chip as function of the number of input vectors used in the reconstruction. Error bars are generated resampling from the set of measured input vectors 36 and 50 times. Dashed reference lines correspond to the estimation obtained using the full set of available data. The reconstructions show a similar threshold behaviour as in the simulations (see Fig. 4.2) but the 5-dimensional phaselift reconstructions show an asymptotic distance from the ideal transfer matrix that largely fluctuates depending on the tested matrix. A

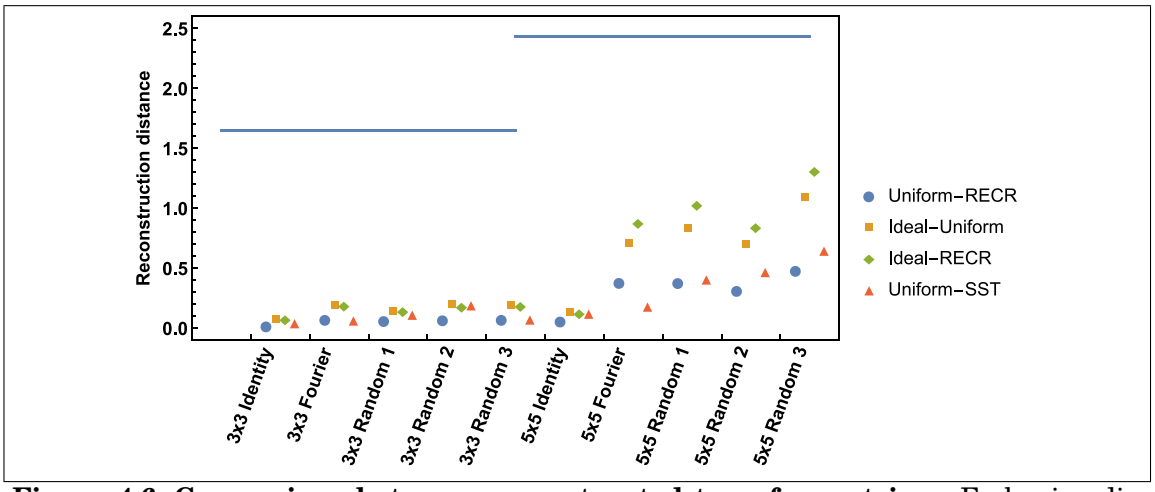

Figure 4.6: Comparison between reconstructed transfer matrices. Frobenius distance between pairs of experimentally reconstructed transfer matrices obtained with alternative input vector distribution of the phaselift algorithm: uniform distribution and RECR or with SST. The phaselift reconstruction is also compared to the ideal transfer matrix dialled on the chip. The reference lines indicate the average distance between random unitary after optimising over the row phases.

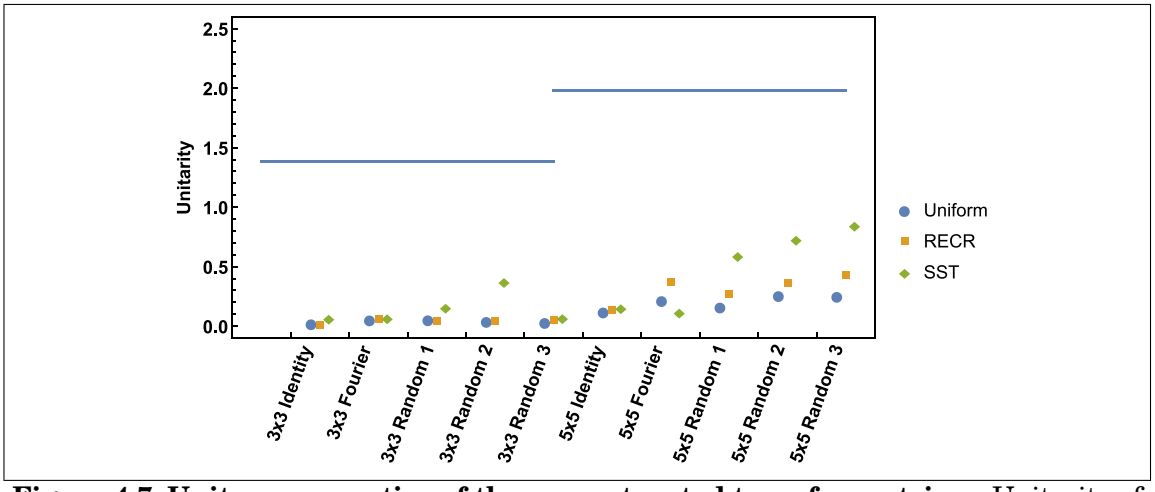

Figure 4.7: Unitary properties of the reconstructed transfer matrices. Unitarity of the reconstructed matrices based on the expression Eq. 4.15. The reference line refer to the average value for random transfer matrices with normalised rows.

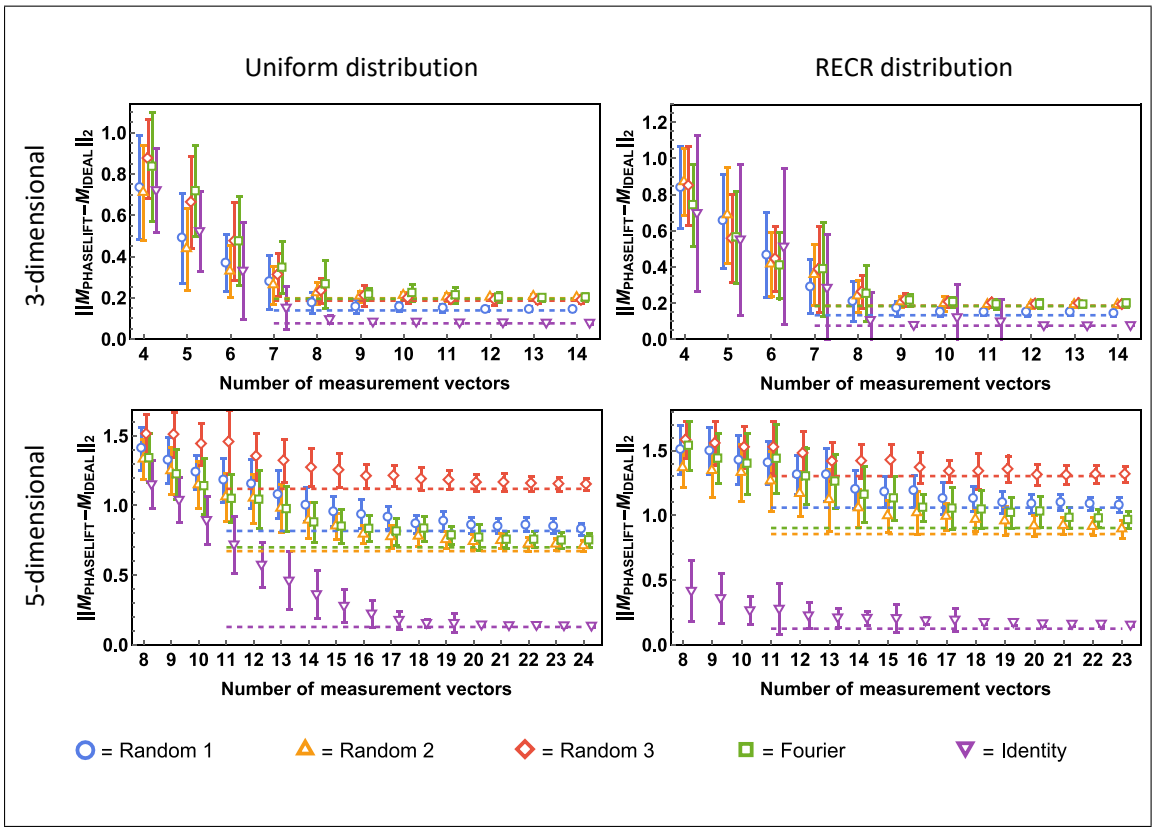

Figure 4.8: Experimental reconstruction distance for 3- and 5-dimensional transfer matrices. Distance between the reconstructed transfer matrices and the ones ideally dialled in the photonic chip. The dotted lines shows the distance obtained using all the measurement collected for that input vector distribution. The error bars are obtained choosing 36 and 50 random subsets of the full set of measurements for performing the phaselift algorithm.

reduction of the reconstruction uncertainty is also observed when the number of input vector approaches the threshold value, although the estimation of the standard deviation of the reconstruction distribution experiences an artificial reduction because of the finite size of the accessible set of input vector to be used for resampling.

Finally, it is worth to note that the uncertainty of the identity matrix reconstruction with the RECR set of input vectors shows some spikes because it is a sparse matrix. The absence of at least an input vector with zero intensity for each of the input modes can cause a large distance between the reconstructed matrix and the true transfer matrix that disappears otherwise; if this happens for one or few re-sampled sets, the estimated variance of the distribution increases drastically.

4.3 Extension of the phaselift algorithm

The phaselift algorithm can use classical interference to determine the transfer matrix of a linear optical device but requires that our detectors can resolve all degrees of freedom of the optical modes. What would happen, for example, if we characterise the interferometer by using horizontally polarised light and the interferometer itself introduces some (path dependent) polarisation rotation that is not detected by our power meter? The detected intensities will be the sum of both polarisation intensities. In this case, the transfer matrix of the device is actually an $2N \times 2N$ unitary but we only use as input the first N optical modes corresponding to horizontally polarised light. With the aid of polarisation resolving detectors, we could reconstruct the $2N \times N$ transfer matrix of the horizontal input light. In their absence, we are tricked into reconstruct an $N \times N$ transfer matrix that does not correspond to the real physical transfer matrix.

In a more general case, for an interferometer with N spatial modes, the transfer matrix of the system could be considered as having $l \times N$ rows, where l is the dimension of the extra degrees of freedom, and only N columns that are experimentally accessible. If we assume only N detectors, each of them measuring the power associated with l different rows of the transfer matrix, the usual relation of the phselift algorithm (Eq. 4.3) becomes:

$$I_j^k = \sum_{h=1}^{h=l} \left| \left\langle M_{j,h} \middle| \alpha^k \right\rangle \right|^2 + \epsilon_k = \sum_{h=1}^{h=l} \mathrm{tr}\left[\left| \alpha^k \right\rangle \left\langle \alpha^k \middle| M_{j,h} \right\rangle \langle M_{j,h} | \right] + \epsilon_k . \tag{4.16}$$

When the convex optimisation of the phaselift is applied (Eq. 4.4), the retrieved matrix will approximate

$$Z_j = \sum_{h=1}^{h=l} |M_{j,h}\rangle \langle M_{j,h}| . \tag{4.17}$$

And, by making the element of Z_j explicit, we obtain:

$$[Z_j]_{s,p} = \sum_{h=1}^{h=l} [M_{j,h}]_s [M_{j,h}]_p^* . \tag{4.18}$$

For each detector, even if we knew l and we looked for a matrix with rank less or equal to l, the main l eigenvectors of Z_j (i.e. the eigenvectors with the largest eigenvalues) do not generally correspond to the original rows of the matrix that describes the modes connected to the detector j. Nonetheless, the eigenvectors we retrieve represent an orthogonal choice of vectors that determines the same expectation values at the detectors for classical light and single photon experiments.

In the following, we are going to show that if two linear systems are characterised by the same matrices Z_j associated with their cumulative detectors, they determine the same multiphoton statistics in a number resolving boson sampling problem regardless of the

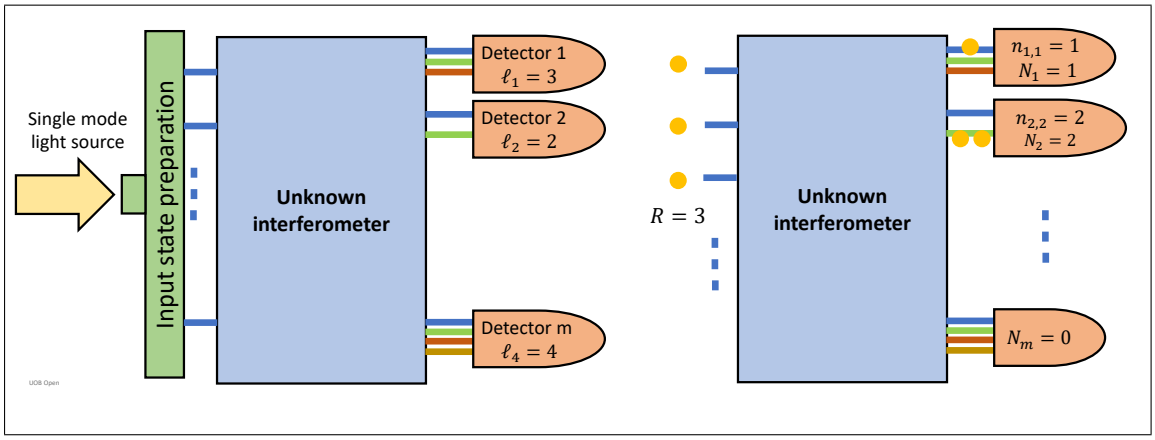

Figure 4.9: Extension of the phaselift application. A trusted state preparation circuit transform the light coming from a single mode source into a desired superposition across the m input modes. Detectors measure the power exiting the circuit adding contributions from multiple output modes. After the phaselift reconstruction, it will be possible to predict multiphoton output patterns $(N_1, N_2, \ldots, N_m)$ produced in those detectors.

specific details of their transfer matrix. This means that, when using cumulative detectors in multi photon quantum experiments, the exact knowledge of the rows of the transfer matrix of the interferometer would not be necessary to predict experimental outcomes if the quantity Z_j are known.

Proof

Let's consider a linear transfer matrix of a system whose ℓ_1 first output optical modes are connected to a single photon-number resolving detector that is not able to distinguish between the ℓ_1 optical modes; the next ℓ_2 output modes from ℓ_1+1 to $\ell_1+\ell_2$ are all interfaced with the second number resolving detector unable to distinguish between the l_2 optical modes and similarly the output modes from $(\sum_{x<k-1} \ell_x + 1)$ to $(\sum_{x\leq k} \ell_x)$ are connected to the k-th detector, and ℓ_x represents the degeneracy of the x detector (see Fig. 4.9 for a graphic illustration). Furthermore, we will assume R photons each injected in a separate input mode of an interferometer and with $M_{a,b}$ we will represent the elements of the transfer matrix M of dimension $L_{\text{tot}} \times R$ where $L_{\text{tot}} = \sum_{x\leq m} \ell_x$ assuming a total of m detectors.

We are going to give an expression of the probability of a macroscopic detection pattern $(N_1, N_2, \ldots, N_m)$ where N_k are the photon observed in the k-th cumulative detector. Such expression will be a function only of the pattern and of the Z_k matrices, therefore not depending of the particular matrix rows that determine Z_k.

The probability $P_{(N_1,N_2,\ldots,N_m)}$ of detecting a macroscopic pattern is given by the sum of the probabilities of all possible microscopic patterns $\left(n_{1,1}, \ldots, n_{1,\ell_1}, n_{2,1}, \ldots, n_{m,\ell_m}\right)$ with the constrain $\sum_{i=1}^{l_k} n_{k,i} = N_k$ associated with Fock states of the unknown hidden modes of the

device. The first subscript of $n_{k,i}$ indicates the cumulative detector that detects the photon and the second index distinguishes between the hidden modes that are routed to that same detector.

$$P_{(N_1,N_2,\ldots,N_m)} = \sum_{\substack{(n_{1,1},\ldots,n_{1,\ell_1},n_{2,1},\ldots,n_{m,\ell_m}) \\ \text{such that} \\ \forall_{k\leq m}\ \sum_{i=1}^{i\leq \ell_k} n_{k,i}=N_k}} P_{(n_{1,1},\ldots,n_{1,\ell_1},n_{2,1},\ldots,n_{m,\ell_m})} \tag{4.19}$$

These probabilities can be calculated using the relation

$$P_{(n_{1,1},\ldots,n_{1,\ell_1},n_{2,1},\ldots,n_{m,\ell_m})} = \frac{\left|\sum_{\sigma\in S}\prod_{i=1}^{R} M_{j_i,\sigma_i}\right|^2}{\prod_k\prod_{i=1}^{l_k} n_{k,i}!}, \tag{4.20}$$

where S is the set of all possible permutations of the integer numbers from 1 to R, σ is a possible permutation and σ_i is its i-th element. The index j_i that defines the output mode of the transfer matrix is defined by the following relations

$$j_i = \begin{cases} 1 \quad \text{if} \ \ 1 \leq i \leq n_{1,1} \\ 2 \quad \text{if} \quad 0 < i - n_{1,1} \leq n_{1,2} \\ \vdots \\ \sum_{k=1}^{k=x-1}\ell_k + y \quad \text{if } \sum_{t=1}^{t=y-1} n_{x,t} < \left(i - \sum_{k=1}^{k=x-1} N_k\right) \leq \sum_{t=1}^{t=y} n_{x,t} \end{cases} . \tag{4.21}$$

By expanding the module square of the sum we can write

$$\frac{\left|\sum_{\sigma\in S}\prod_{i=1}^{R} M_{j_i,\sigma_i}\right|^2}{\prod_k\prod_{i=1}^{i=l_k} n_{k,i}!} = \sum_{(\sigma,\rho)\in S^2} \frac{\prod_{i=1}^{R} M_{j_i,\sigma_i} M^*_{j_i,\rho_i}}{\prod_k\prod_{i=1}^{i=l_k} n_{k,i}!}. \tag{4.22}$$

In the last expression we used S^2 to represent the Cartesian product $S \times S$.

We note that the left-hand-side term of Eq. 4.22 does not change if we transform $j_i \to j_{\tau_i}$ for any $\tau \in S$. Then, we choose to apply all the permutations $\tau = \alpha$ that satisfies the following relation: for all k, the N_k-tupla $\left(j_{\alpha_y} | 0 < \left(y - \sum_{i=1}^{i=k-1} N_i\right) \leq N_k\right)$ is a *multiset permutations*[2] of the N_k-tupla $\left(j_y | 0 < \left(y - \sum_{i=1}^{i=k-1} N_i\right) \leq N_k\right)$. Such permutations correspond, fixed the set of input photons that are associated with the k-th detector, to reassign in a different way those photons into the same pattern $(n_{k,1},\ldots,n_{k,\ell_k})$. For convenience of notation, we further define

$$\alpha_{[k]} = \left\{ \alpha_y \,\middle|\, 0 < \left(y - \sum_{i=1}^{i=k-1} N_i\right) \leq N_k \right\} \tag{4.23}$$

[2] Multiset permutations are anagrams with repetitions. For example the multiset (A,A,B) has 3 valid permutations (A,A,B), (A,B,A) , (B,A,A).

so that the sum over all α can be expressed as a sum over all possible sequences $\left(\alpha_{[1]},\ldots,\alpha_{[m]}\right)$.

Given a multiset with ℓ different symbols with multiplicity $n_1, n_2, \ldots, n_\ell$, the number of multiset permutations is $(\sum_i n_i)! \,/ \prod_{i=1}^{i=l}(n_i!)$. Because of this, the probability of a microscopic configuration can be written as:

$$P_{(n_{1,1},\ldots,n_{1,\ell_1},n_{2,1},\ldots,n_{m,\ell_m})} = \frac{\sum\limits_{(\alpha_{[1]},\ldots,\alpha_{[m]})} \left| \sum\limits_{\sigma\in S} \prod_{i=1}^{R} M_{j_{\alpha_i},\sigma_i} \right|^2}{\prod\limits_{k=1}^{k=m}\prod\limits_{i=1}^{i=l_k} n_{k,i}!} \frac{\prod\limits_{k=1}^{k=m}\prod\limits_{i=1}^{i=l_k} n_{k,i}!}{\prod\limits_{k=1}^{k=m} N_k!}. \tag{4.24}$$

Substituting the relation in Eq. 4.22, we obtain:

$$P_{(n_{1,1},\ldots,n_{1,\ell_1},n_{2,1},\ldots,n_{m,\ell_m})} = \sum_{(\alpha_{[1]},\ldots,\alpha_{[m]})} \sum_{(\sigma,\rho)\in S^2} \frac{\prod_{i=1}^{R} M_{j_{\alpha_i},\sigma_i} M^*_{j_{\alpha_i},\rho_i}}{\prod\limits_{k=1}^{k=m} N_k!}. \tag{4.25}$$

The expression for the macroscopic detection pattern becomes:

$$P_{(N_1,N_2,\ldots,N_m)} = \sum_{(\sigma,\rho)\in S^2} \left[\sum_{\substack{(n_{1,1},\ldots,n_{1,\ell_1},n_{2,1},\ldots,n_{m,\ell_m}) \\ \text{such that} \\ \forall_{k\leq m}\ \sum_{i=1}^{i\leq \ell_k} n_{k,i}=N_k}} \sum_{(\alpha_{[1]},\ldots,\alpha_{[m]})} \frac{\prod_{i=1}^{R} M_{j_{\alpha_i},\sigma_i} M^*_{j_{\alpha_i},\rho_i}}{\prod\limits_{k=1}^{k=m} N_k!} \right]. \tag{4.26}$$

We note that the two summations inside the squared brackets correspond to sum over all the possible sequence $B = \left(\beta_{[1]}\ldots,\beta_{[m]}\right)$ such that

$$\beta_{[k]} \in \left\{ y\in\mathbb{Z} \,\middle|\, 0 < \left(y - \sum_{i=1}^{i=k-1} \ell_i \right) \leq \ell_k \right\}^{\times N_k}, \tag{4.27}$$

where $\{\cdot\}^{\times n}$ is used to represent the n-ary Cartesian product. With this notation, the expression for the probability of macroscopic patterns reads:

$$P_{(N_1,N_2,\ldots,N_m)} = \sum_{(\sigma,\rho)\in S^2} \left[\sum_{B=(\beta_{[1]},\ldots,\beta_{[m]})} \frac{\prod_{i=1}^{R} M_{B_i,\sigma_i} M^*_{B_i,\rho_i}}{\prod\limits_{k=1}^{k=m} N_k!} \right]. \tag{4.28}$$

Since the choice of $\beta_{[k]}$ and $\beta_{[k']}$ with $k \neq k'$ are independent, the above relation can be rewritten as

$$P_{(N_1,N_2,\ldots,N_m)} = \sum_{(\sigma,\rho)\in S^2} \left[\prod_{k=1}^{k=m} \left(\sum_{\beta_{[k]}} \frac{\prod_{g=1}^{N_k} M_{\beta_{[k]},g,\sigma_{i(k,g)}} M^*_{\beta_{[k]},g,\rho_{i(k,g)}}}{N_k!} \right) \right], \tag{4.29}$$

where $i(k,g) = \sum_{0<x<k} N_x + g$.

Furthermore, each component of $\beta_{[k]}$ assumes each value of the set $L_k = \left\{ y \in \mathbb{Z} \middle| 0 < \left(y - \sum_{i=1}^{i=k-1} \ell_i \right) \leq \ell_k \right\}$ independently from the other components so that the above expression simplifies into:

$$P_{(N_1,N_2,\ldots,N_m)} = \sum_{(\sigma,\rho)\in S^2} \left[\prod_{k=1}^{k=m} \left(\frac{\prod_{g=1}^{g=N_k} \sum_{h\in L_k} M_{h,\sigma_{i(k,g)}} M^*_{h,\rho_{i(k,g)}}}{N_k!} \right) \right]; \tag{4.30}$$

that written with the notation introduced in Eq. 4.18 reads:

$$P_{(N_1,N_2,\ldots,N_m)} = \sum_{(\sigma,\rho)\in S^2} \left[\prod_{k=1}^{k=m} \left(\frac{\prod_{g=1}^{g=N_k} [Z_k]_{\sigma_{i(k,g)},\rho_{i(k,g)}}}{N_k!} \right) \right]. \tag{4.31}$$

4.4 Crosstalk study

In Sec. 2.4.1 we mentioned that particular linear optical circuits, such as those described by Clements and Reck [91, 92], allow to implement any desired unitary transfer matrix of the right size by accurately tuning a set of phase-shifters. Similarly, the transfer matrix of a generic linear optical circuit can be constructed so long as the complex transfer matrices of the individual elements, the connections between the elements and the optical phases accumulated between them are known. Therefore, a proper control over the phases accumulated along their propagation by the different modes of an optical circuit is necessary for a successful usage of the device. A reasonable design of a reprogrammable interferometer attempts to associate a single external control parameter for each phase that needs to be set. Ideally, this would results in a device where it is easy to calibrate each phase independently and achieve a high fidelity control of the device. However, its practical realisation, due to the presence of many components condensed in a small space, deviates from this ideal description. Often, for example, tuning a single external voltage significantly changes a specific phase in the circuit but it marginally affects other phases too.

Let's consider the circuit in Fig. 4.10 where black lines represent optical paths and the other lines represent metallic tracks. We aim to address the phase ϕ_1 by tuning the input voltage V_1, and similarly for the phases ϕ_2 and ϕ_3 by tuning V_2 and V_3, respectively. Such a schematic is an example of an integrated interferometer based on thermal phase-shifters as the ones used in our experiments. The currents flowing through the metallic resistors R1, R2, R3 locally heat the waveguides causing a change of the refractive index. However, current flowing into parasitic resistors r1 and r2 also dissipates heat, resulting in undesired phase shifts. Not only that, but in this scheme with common connections to the ground (GND), the voltage V3 also alters the current flowing in the resistor R1 and R2 since it determines an additional potential at the left end of the shared parasitic resistor r2. Finally,

the heat generated at each of the phase-shifters propagates in all directions, by an amount depending on the local conductivity and on the boundary conditions of the device. As result of all the crosstalk contributions, each phase is generically described as follows

$$\begin{aligned} \phi_1 &= \phi_1(V_1, V_2, V_3), \\ \phi_2 &= \phi_2(V_1, V_2, V_3), \\ \phi_3 &= \phi_3(V_1, V_2, V_3). \end{aligned} \tag{4.32}$$

For practical use, each function ϕ_k should be approximated as a polynomial of the voltages or be tabulated and interpolated for every use. Without any approximation, in order to characterise N phase-shifters, we would need to explore the N-dimensional space of parameters that map on all possible transfer matrices that could be implemented on the chip. In such case, the number of possible configuration to test would increase exponentially with N. Conversely, if the device was ideal, we would have

$$\begin{aligned} \phi_1 &= \phi_1(V_1), \\ \phi_2 &= \phi_2(V_2), \\ \phi_3 &= \phi_3(V_3), \end{aligned} \tag{4.33}$$

and the number of measurements needed to characterise the device would be linear with N.

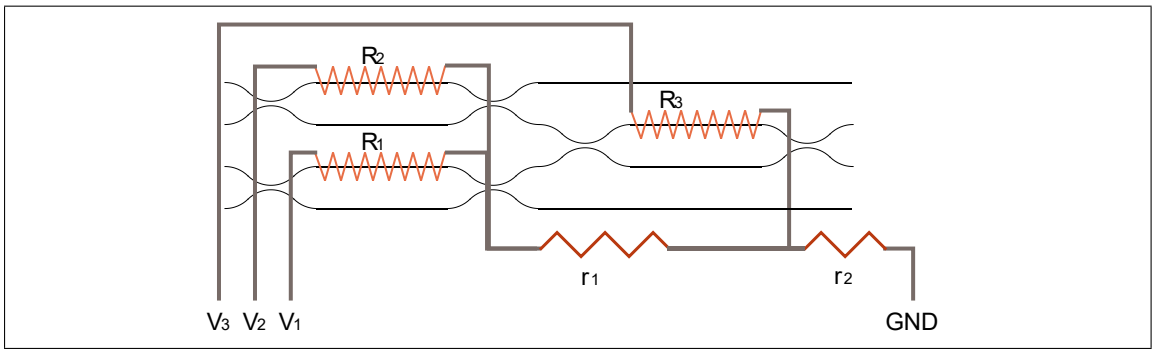

Figure 4.10: Example of optical circuit controlled by external voltages. V_1, V_2 and V_3 are external voltages applied to the circuit to control the heat dissipated in the resistors R_1, R_2 and R_3, respectively. r_1 and r_2 symbolise parasitic resistances arising from shared electrical connection towards the common ground GND. Black lines indicates optical waveguides while thick grey lines are used for low resistance electrical wiring.

4.4.1 Experimental estimation of the crosstalk

The chip we used for our experiments is based on metallic thermo-optic phase-shifters. In this technology, we can find the sources of crosstalk discussed in the previous examples: electrical crosstalk arising from shared ground connection (r1 and r2 in Fig. 4.10), and thermal crosstalk due to diffusion of the heat in the chip and to heat generation by parasitic

resistors. Assuming that these are the only dominant sources of crosstalk, we can simplify the expression of the crosstalk relation in Eq. 4.32. To a first approximation, the electrical crosstalk manifests itself as a linear transformation between the list of input voltages and the voltages effectively applied at the resistors of the phase-shifters. Contrarily, the thermal crosstalk could be approximated as an additive effect proportional to the heat dissipated by the other heaters, hence approximated as an additive term proportional to the squares of the voltages applied on the other heaters. Within these approximations, we can write the phase ϕ_i of each phase-shifter as

$$\phi_i = \phi_i(V_1, \ldots, V_i, \ldots, V_N) \approx \phi_i\left(\left|V_i + \sum_{k\neq i} c_{i,k} V_k\right|\right) + \sum_{k\neq i} d_{i,k} V_k^2, \tag{4.34}$$

where we have enforced that the sign of the applied voltage to a resistor is not relevant.

To perform measurements sensitive to the change of phase ϕ_i in one location of the interferometer, it is necessary to translate this information into an intensity variation that can be observed at the detectors. This is routinely done by including the phase to monitor in an MZI. In Fig. 4.11 we represent the optical schematic of the tested chip where numbers are associated with phase-shifters for which the effect of the crosstalk was estimated. Additionally, letters label other heaters which are investigated as sources of the crosstalk.

Some of the phase-shifters in our chip (see for example elements 1 and 5 in Fig. 4.11) are already enclosed by two directional couplers that create a small MZI acting as tunable beam splitters. Other heaters, for example element 10 in Fig. 4.11, can be considered as a part of a larger MZI including nearby tunable beam splitters that needs to be set to suitable configurations. Heater 10, for example, is better characterised if the phases in 1, 7, 2 and 6 are set to be π, π, $\pi/2$ and $\pi/2$, respectively. With these settings, the corresponding small MZIs are set to perform two identities and two balanced beam splitters, respectively. The crosstalk analysis between a voltage V_j and the phase ϕ_i is further complicated by the fact that the signal we recover from the chip can be altered by the effect of V_j on ϕ_j or generally on phases other than ϕ_i. For these reasons, it is convenient that the remaining degrees of freedom of the interferometer are set in such a way that the light monitored at each detectors only comes from a single output port of the MZI without further interference between the light exiting the two ports of the MZI.

Since all the measurements we performed for the crosstalk characterisation are made with a setup configured to be used with single photons, the power measurements are actually coincidence measurements between each output detector and a fixed heralding single photon detector integrated over many seconds. With reference to the circuit map in Fig. 4.11, the experimental determination of the crosstalk coefficients proceeded as follows.

1) Determination of the voltage configuration for heaters in MZIs 1, 2, 3, 4, 5 for implementing identity and swap operations.

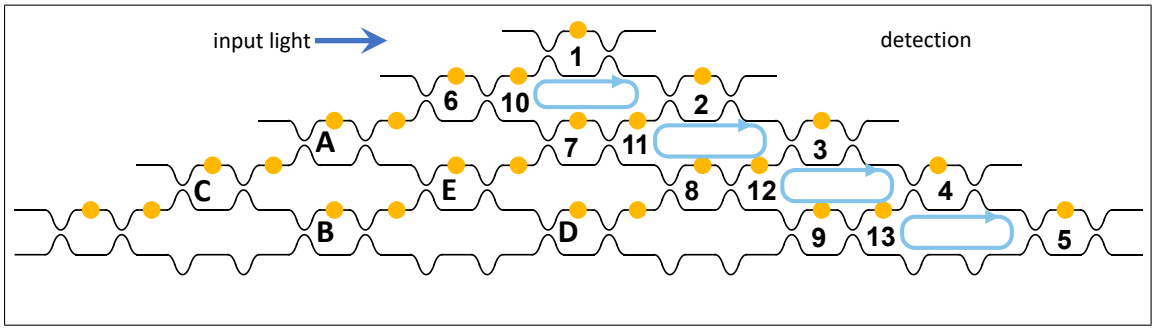

Figure 4.11: Map of the phase-shifters for the crosstalk measurement. The black lines represents optical waveguides. 30 evanescent couplers, designed to implement a balanced beam splitter, are present wherever two black lines are brought close together. Yellow dots indicate the position of metallic phase-shifters. The numbers and letters next to the phase-shifters are used in the main text and in the plots to explain the sequence of measurements performed. Few light blue oval lines help identify the presence of a possible MZI for phase-shifter characterisation.

2) Measurement of the relative detector efficiency at the 6 outputs of the chip.

3) Rough evaluation of the voltage V_i for achieving a 50:50 beam splitting operation in MZIs 1, 2, 3, 4, 5.

4) Actual crosstalk measurement for heaters 1, 2, 3, 4, 5 consisting in output measurements from the target MZIs while feeding current to other heaters on the circuit. However, coefficients $c_{i,k}$ and $d_{i,k}$ for the pairs
$(i,k) \in \{(2,1), (3,2), (3,1), (4,3), (4,2), (4,1), (5,4), (5,3), (5,2), (5,1)\}$
are excluded from this scheme.

5) Rough evaluation of the voltage V_i for achieving a 50:50 beam splitting operation in MZIs 6, 7, 8, 9.

6) Actual crosstalk measurements for heaters 6, 7, 8, 9. However, coefficients $c_{i,k}$ and $d_{i,k}$ for the pairs $(i,k) \in \{(7,6), (8,7), (8,6), (9,8), (9,7), (9,6)\}$ are not recorded.

7) Rough evaluation of the voltage V_i for achieving a 50:50 beam splitting operation in MZIs 10, 11, 12, 13.

8) Measurement of the crosstalk for heaters in MZIs 10, 11, 12, 13 due to other heaters on the circuit.

The overall procedure was facilitated by a previous calibration of the device operated by Jacques Carolan that eased the search for the voltage configuration in steps 1), 3), 5) etc. Further calibration of the other components can be performed finding the identity configuration for the heaters 6, 7, 8, 9 but the level of noise in the measurement would grow.

Few considerations help to justify the previous routine.

- We took advantage of the fact that the swap and identity configurations of an MZI are those where an error in the phase causes the least absolute change of the output signal of the MZI thus granting more phase tolerance in the step 1).

- Operating near the balanced beam splitting condition in steps 3) and 5) offers more sensitivity to small phase changes thus allowing characterisation of smaller crosstalk contributions. At the same time, when approximations are in place, the parameters obtained from a calibration of a tunable elements are more accurate around the real configuration adopted during the calibration procedure. Since, for the MZIs that feature a single phase-shifter, a 50:50 splitting condition also corresponds to the configuration of the MZI that requires the most accurate phase setting for a correct operation, it is a further advantage to measure the crosstalk with the chip in this configuration.

- While steps 3) and 5) are helpful for increasing the sensitivity, it is not neccesarily required that we operate exactly at this point. For each tested phase-shifter, we measured the response of the heater around the operation point and used this information to calibrate the crosstalk measurements. In particular this removes biases due to incorrect splitting ratio of beam splitters composing the MZI and also to the inaccuracy of the phase setting.

- Splitting the light coming from the MZI under scrutiny into multiple detectors would introduce false signals depending on how much light is deflected to the detector with highest efficiency if the relative detection efficiency was not measured. The calibration of the detectors, instead, permits to test voltages controlling phases closer to the detectors than the probed MZI thus allowing to probe extra pairwise terms such as (2,3), (2,4) ,(2,5) ....

- The measurements in steps 6) and 8) are performed using the information retrieved in the previous steps about the crosstalk contribution affecting the other tested heaters in order not to account multiple times for the same source of crosstalk.

The relative detector efficiency characterisation in the step 2) was obtained using 6 voltage settings found in the step 1) for which the light, injected in the top port of the chip, is routed into each of the 6 output ports separately. Thanks to the good quality of the chip, each of these settings was able to achieve at least 20 dB extinction between the power measured by the target detector and the power registered by the other 5 detectors. We iterated multiple times between the 6 voltage settings to moderate the effect of fluctuations in the power

injected into the photonic circuit. In particular, the sequence of detector illumination (0, 2, 4, 1, 3, 5, 4, 0, 3, 5, 2, 1) was repeated 4 times giving a total integration time for each detector of 200 s. The power measured by each detector when the light was directed to it gave the relative system detection efficiency. Normalised over the best performing detector, the measured efficiency were (0.83, 0.89, 0.86, 0.67, 0.89, 1).

Calling I_1 and I_2 the power exiting the top and bottom ports of the MZI used for measuring the crosstalk contribution, we chose to use the quantity

$$S_i = \frac{I_1}{I_1 + I_2}(V_i) \tag{4.35}$$

to characterise the crosstalk effect. Experimentally, I_1 and I_2 are obtained adding up power observed at multiple detectors while rescaling the powers by the measured relative detector efficiencies. We proceeded in the crosstalk measurement for each phase-shifter by setting the associated voltage V_i close to the balanced beam splitting condition as in step 3). Then, we found δV such that the variation ΔS of the signal S

$$\Delta S_i = \frac{I_1}{I_1 + I_2}(V_i + \delta V) - \frac{I_1}{I_1 + I_2}(V_i - \delta V) \approx \pm 0.1 \approx \frac{\partial S_i}{\partial \phi_i}\left(2\delta\phi_i\right) \approx -\delta\phi_i, \tag{4.36}$$

where we used that $S \approx \cos^2\left(\phi/2\right)$. This ensures that the following approximation can be considered valid:

$$\frac{\Delta S_i}{2\delta V} \approx \frac{\partial S_i}{\partial \phi_i}\frac{\delta\phi_i}{\delta V_i} + \frac{1}{3}\frac{\partial^3 S_i}{\partial^3 \phi_i}\frac{\left(\delta\phi_i\right)^3}{2\delta V} \approx \frac{\partial S_i}{\partial \phi_i}\frac{\delta\phi_i}{\delta V_i} + \frac{1}{6}\frac{o\left(0.1^3\right)}{\delta V}. \tag{4.37}$$

Note that for variation δV too small, although the approximation would be more effective, it would be more affected by background noise in the experiments. This framework is then ready to estimate the crosstalk terms $c_{i,k}$ and $d_{i,k}$ related to a second heater controlled by V_k using the estimation of $\frac{\Delta S}{2\delta V}$ as scaling factor between signal oscillations and equivalent voltage correction.

For each setting of V_k, we must recover the power I_1 and I_2 as determined by the MZI with ϕ_i. In the experiment, the light emerging from the top port of the MZI was kept in the same spatial mode while the light coming from the second port of the MZI was freely distributed to multiple modes closer to the bottom of the chip. We then recorded

$$\begin{aligned} S_{i+}(V_{k,n}) &= \frac{I_1}{I_1 + I_2}\left(V_i + \delta V, V_{k,n}\right), \\ S_{i-}(V_{k,n}) &= \frac{I_1}{I_1 + I_2}\left(V_i - \delta V, V_{k,n}\right), \end{aligned} \tag{4.38}$$

for $V_{k,n}$ between 1 V and 8.5 V. To avoid memory effects of the system potentially arising from thermal effects, the actual sequence of applied voltage was

$$(2.0,\ 7.0,\ 1.0,\ 8.0,\ 4.0,\ 6.0,\ 3.0,\ 5.0,\ 7.5,\ 1.5,\ 4.5,\ 8.5,\ 6.5,\ 3.5,\ 2.5,\ 5.5)V.$$

4.4.2 Results

The data from each accessible heater k were analysed obtaining an averaged scaling factor α_i for the phase-shifter ϕ_i given by the average of the following pairwise scaling factors $\alpha_{i,k}$:

$$\alpha_{i,k} = \frac{1}{16}\sum_n \frac{\left(S_{i+}(V_{k,n}) - S_{i-}(V_{k,n})\right)}{2\delta V}. \tag{4.39}$$

Using the relation in Eq. 4.37, the scaling factor $\alpha_i = \sum_k \frac{\alpha_{i,k}}{\#\{k\}} \approx \frac{\partial S_i}{\partial V_i} = \frac{\partial S_i}{\partial \phi_i}\frac{\partial \phi_i}{\partial V_i}$ is used to relate changes in the signal S_i with changes in the voltage V_i that would generate an equivalent effect. We referred with $\#\{k\}$ to the number of heaters that have been tested in conjunction with i to determine its response. The estimation of α_i, valid when the heater-voltage is set at V_i, is independent of a pre-calibration of the device and is valid in good approximation regardless of the details about losses and splitting ratio of the components involved.

In Fig. 4.12 it is possible to observe the distribution of the pairwise scaling factors associated with some of the phase-shifters ϕ_i expressed in units V^{-1}. These histograms show the appropriateness of the approximation Eq. 4.39 (note that δV is about 0.1 V) and confirms that the coefficients $\alpha_{i,k}$ are reasonably independent from k.

The aim is to perform a quadratic regression based on the formula

$$S_i\left(\phi(V_i, V_k)\right) \approx S_i\left(\phi_i(V_i, 0)\right) + \frac{\partial S_i}{\partial V_i} c_{i,k} V_k + \frac{\partial S_i}{\partial \phi_i} d_{i,k} V_k^2, \tag{4.40}$$

and gain information about the linear and quadratic crosstalk terms $c_{i,k}$, $d_{i,k}$. For each pair of crosstalk elements studied, we performed a quadratic fit of the set of 16 data points

$$\left\{\left(V_{k,n},\ \frac{S_{+,i}(V_{k,n}) + S_{-,i}(V_{k,n})}{2\alpha_i}\right)\right\}_{n=1}^{n=16}, \tag{4.41}$$

considering the statistical uncertainty for each data point due to the Poissonian statistics.

Note that with this approach we will retrieve $c_{i,k}$ and $\left(\frac{\partial \phi_i}{\partial V_i}\right)^{-1} d_{i,k}$. $\frac{\partial \phi_i}{\partial V_i}$ could be retrieved by the heater calibration curve.

Many of the estimated coefficients are negligible, however, some terms significantly differ from zero. In Fig. 4.13 we show some of the analysed data organised in 5 sets, each with different features:

1. For some heater/voltage pairs, the measured signal is dominated by noise. As result, the estimated coefficients resulted compatible with zero, within statistical errors.

2. Some combinations of heaters and voltages are dominated by linear crosstalk probably due to the shared connection to the ground. In these cases the expected sign of the crosstalk is negative because we expect lower voltage drop across heaters affected by this form of crosstalk (note that we only apply positive voltages).

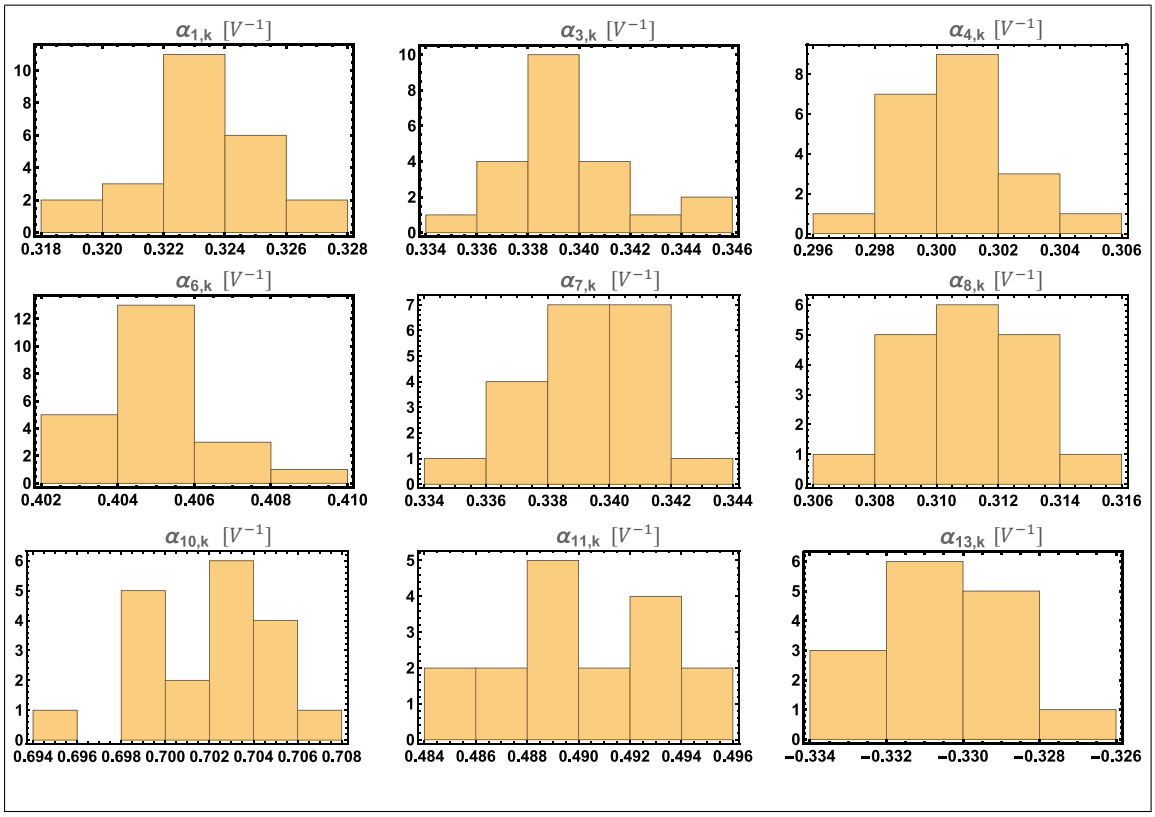

Figure 4.12: Scaling factors distribution for several phase-shifters. Histograms of the scaling factors associated with different phase-shifters ϕ_i due to competitive voltages applied V_k

3. A few combinations of phases (in large MZI) and voltages are dominated by quadratic crosstalk. Larger MZI are more sensitive to difference of temperature in the two arms because the phase difference accumulates along the propagation in the arms. The sign of the crosstalk term indicates if the temperature change in the arm with the phase-shifter is higher (positive) or lower (negative) than the one in the second arm of the MZI.

4. A non-monotonic dynamics can be observed when there is competition between linear and quadratic terms. Strangely, sometimes the linear term appears to be positive.

5. There are cases when the observed data could be justified by imperfection in the detector efficiency calibration but this consideration can only be applied to voltages that control phase-shifters closer to the detector than the target MZI.

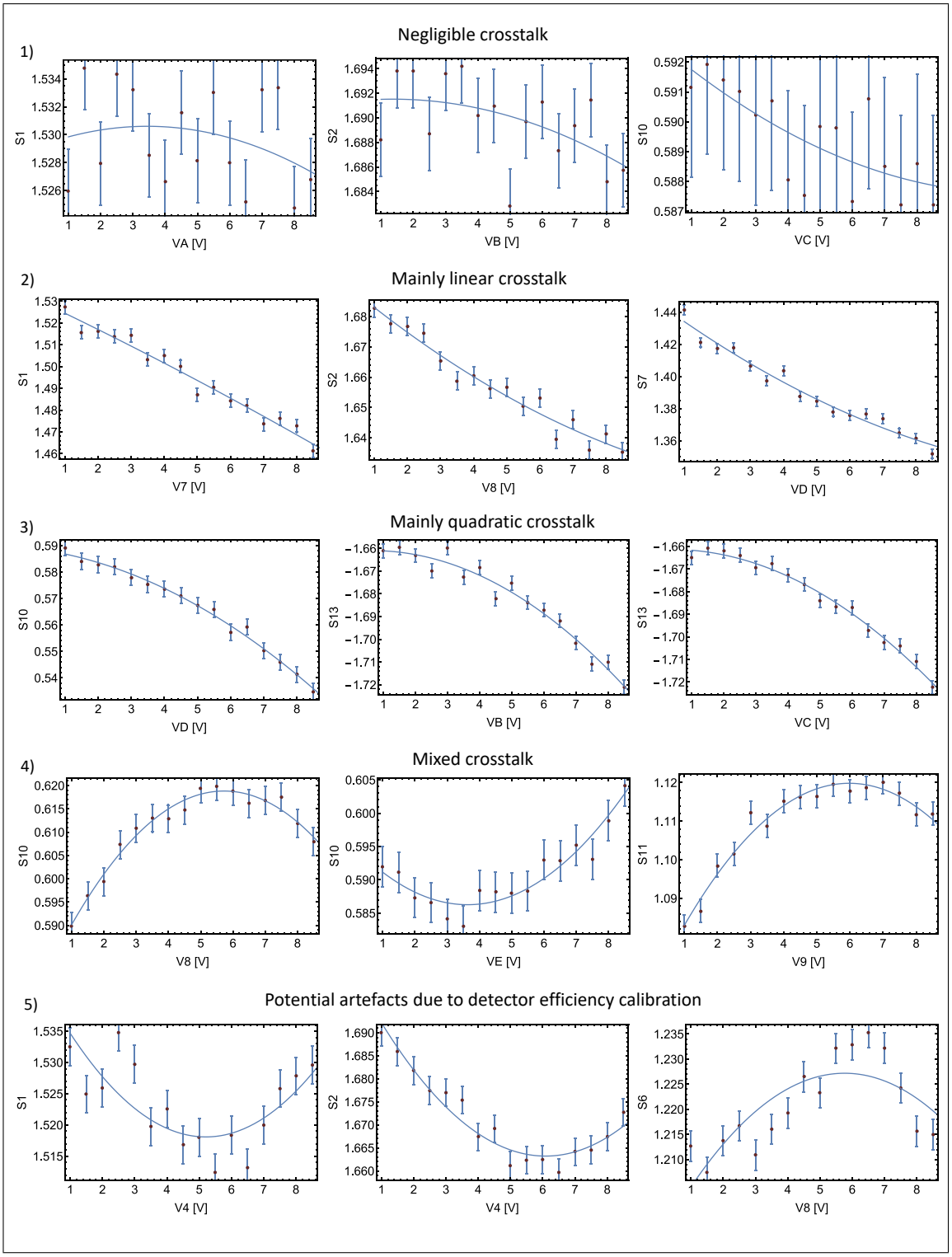

Figure 4.13: Quadratic regression for different pairs of phase-shifter and control voltages. Examples of 5 different behaviours observed analysing the crosstalk signals S at different heater due to voltages V applied to other heater described in Eq. 4.11.

4.5 Discussion

Prospectives on phaselift algorithm

Estimating the transfer matrix of an arbitrary system constituted by N input modes and M output modes requires the determination of $2N \times M$ real numbers. Even if certifying the transfer matrix of a $10^4 \times 10^4$ system that could be used for quantum simulation applications might be unfeasible, using characterisation methods on intermediate devices is a validation task necessary for quantifying the development of the technology.

The phaselift protocol we have tested is a very fast method to retrieve the transfer matrix of a linear system. For an N dimensional system, we recommend to use $\approx 7 \times N$ input vectors that for our setup translates into an order of magnitude faster acquisition compared to the super-stable tomography, without including the time overhead for rearranging the input fibres and finding the approximate dip position. A faster performance might be possible for the SST if the visibility measurements were performed with single shot measurements, for example by changing the photons from distinguishable to fully indistinguishable with a single unitary transformation of the polarisation. Furthermore, since the transfer matrix of the device is generally wavelength dependent, it is important to use a characterisation light source with the same spectrum as the light used in the following application of the device. We decided to perform our reconstruction with the same photon pair source we use to perform quantum experiment but, for classical application, the same procedure can be followed with the laser used for the designed application further speeding up the procedure. Additionally, the algorithm does not need to propagate information from one reconstructed element of the matrix to the others, therefore, if no biases are present in the state preparation stage, the reconstruction errors are evenly distributed.

Unfortunately, the need for a calibrated and phase-stable state preparation stage, required for the phaselift, partially limits the applicability of this technique. If the calibration of the state preparation is taken into account, the resource counting of the phaselift procedure exceeds what is necessary for the routine described in [125]. The advantage is re-obtained when the same preparation stage can be reused to characterise multiple devices or it is plugged in front to a programmable device as in our case. Nonetheless, if the device needs to be randomly tested against a large set of configurations, the operator can find it sufficient not to reconstruct the full transfer matrix but only to evaluate a less expensive performance witness, as for the statistical fidelity in Fig. 3.5. To summarise, due to the requirements of the phaselift reconstruction, this technique is mostly advantageous in integrated experiments for high dimensional systems were few particular configurations of the circuit are of interest.

The reconstruction distance from the target unitary observed in our measurement is

higher than desired. This is more likely to derive from imperfect calibration of the circuit and additional crosstalk than to the reconstruction itself, since the alternative reconstruction provides similar results. We also point out that this type of experiment represents the greatest challenge for our interferometer since the photon is forced to pass, in superposition, through all the passive components and phase-shifters. Furthermore, both input vector distributions tested showed comparable performance, when enough input vectors were used, and in future application it might be possible to take advantage of the more structured RECR input vector distribution. We also observed that the calibration of the detection efficiency, given a well balance loss distribution in the circuit, was sufficient to obtain reconstructed matrix close to unitary.

Applications of the system equivalence proof

The result derived in section 4.3 opens new possibilities for the phaselift protocol, offering an additional diagnosis tool for optical systems. However, we note that the presence of extra degrees of freedom, that can manifest as multiple eigenvalues of the Z_j matrix significantly above zero, needs to be compared to the effect of detector noise in the characterisation procedure. We also point out that the mathematical equivalence shown can be used for alternative applications. For example, in experiments performed with broad spectrum photons, the small wavelength dependence of each component can accumulate and jeopardise the final performance of the device. In these applications, modelling the circuit during its calibration as an hidden mode device, regardless of the actual characterisation protocol, can provide a better description of the system.

From the computational perspective, we showed that in boson-sampling experiments performed with number resolving detectors, if the output patterns are binned by adding up the photon number measured by a subset of ℓ detectors, as we assumed in our demonstration, the theoretical distribution could be calculated from an equivalent matrix. We note, though, that every time that ℓ is larger than the number of photons of the experiment, the equivalent matrix has fewer rows than the original matrix, making the theoretical calculation of the overall distribution simpler. For example, given N photons in N^2 modes, we can choose subsets of $d = 2N$ detectors and sum up their results. Without simplifications, calculating the probability of a pattern $\left(N_1,\ldots,N_{\frac{N}{2}}\right)$ would require the calculation of

$$\prod_i^{\frac{N}{2}} \binom{d+N_i}{N_i} \approx \binom{2N+2}{2}^{\frac{N}{2}} \approx 2^{\frac{N}{2}} N^N$$

non independent permanents while simplifying the transfer matrix this reduces to

$$\prod_i^{\frac{N}{2}} \binom{N+N_i}{N_i} \approx \binom{N+2}{2}^{\frac{N}{2}} \approx 2^{-\frac{N}{2}} N^N.$$

However, we note that in the limit of too many detectors binned together, the associated matrix Z_j might approximate a scalar matrix and the problem would loose its complexity.

Comments on the crosstalk characterisation

The crosstalk issue is a very intricate problem that affects the calibration of a device and therefore becomes more relevant as the size of the system increases. The first effort has to be performed on a design level: preferring current control of the heater over voltage control, avoiding asymmetries of the circuit, provide adequate thermal dissipation, careful positioning of metal tracks that can distribute heat in unwanted regions. Attempts have also been made for introducing thermal barriers between waveguides [80, 81].

Here we developed a set of measurements to estimate the level of crosstalk between selected component pairs. On the one hand, an estimation of the level of error due to crosstalk effects could be performed modelling it with average fluctuations of the phases set and comparing the prediction of the model against the system average performance. On the other hand, knowledge of the crosstalk relation is necessary if calibration correction is to be used. Doing so, the main challenge consisted in reducing the noise level enough to directly probe such effects.

An alternative solution could be to perform an optimisation protocol to program the chip to implement a desired transformation and then locally optimise the control parameters to move the effective transfer matrix as close as possible to the target values.

To calibrate the crosstalk, also alternative estimation protocols could be adopted but we advocate the importance of the adoption of a simplified relation between the control parameter and the phase-shifters and a pragmatic approach that rule out effects due to imprecise calibration or unbalanced splitting ratio or losses.

Finally, we want to remark that we only concentrated on memoryless crosstalk problems. Potentially, the history of the chip configurations could also affect the operation of the device.

CHAPTER 5

QUANTUM SIMULATION OF MOLECULAR VIBRATIONS

Outline

In this chapter I present a quantum simulation project that addressed the evolution of vibrational excitations in molecules. Using the linear optical system described in Chapter 3, we were able to simulate prototypical quantum systems of potential interest for science and industry applications, with a promising scaling of the resources required. Contents of this chapter are also part of a published peer reviewed article [131].

The first section of the chapter will contain a brief reminder of the quantum description of the atomic motion in a molecular system. In the subsequent section, I will explain the simulation model used to map the vibrational dynamics onto our experimental setup. Using this framework, it was possible to simulate the vibrations of arbitrary 4-atom molecules once provided with information about their *energy landscape*. In the same section, I will also show the experimental results for single and multiple excitations in a selection of 4-atom molecules. The third section will be dedicated to the simulation of molecular behaviours originated from the interactions with an external environment. In it, I will describe the experiments performed to simulate decoherence and thermalisation effects. In the fourth section, I will discuss the possibility of simulating physics beyond the *harmonic approximation* showing results based on a measurement induced non-linear gate and on a hybrid feedback algorithm that exploits our linear optics quantum simulator and a classical computer to investigate molecule dissociation. I will conclude the chapter with a discussion section about the potentiality and the criticality of our simulation method.

Contributions

Many researchers contributed to the scientific contents presented in this chapter and are co-authors of the related publication [131]. Anthony Laing and Enrique Martín Lòpez conceived the mapping between linear optics and the dynamic of vibrations in molecules. David Tew provided us with the information regarding the energy landscape of the simulated molecules, including unitary transformations between alternative basis and the corrections for non-harmonic potentials. Chris Sparrow solved the model for the simulation of open system dynamics with inputs from Yogesh N. Joglekar and Anthony Laing. The extensions beyond the harmonic approximation, including the dissociation experiment with the hybrid algorithm, were largely due to Alex Neville and Chris Sparrow with minor contribution from myself and directions from Anthony Laing. The data collection was performed by myself, Alex Neville and Chris Sparrow who also performed most of the data analysis. The results presented in this chapter are also discussed in [115].

5.1 Atomic vibrations in molecules

The interaction between the nuclei and the electrons in a molecule is described by an Hamiltonian H that includes the kinetic energy of the two sets, T_n and T_e respectively, and also the electromagnetic interactions within the electronic system, among the nuclei, and between electrons and nuclei that are described by the potential energy terms V_{e-e}, V_{n-n} and V_{n-e}, respectively[1].

$$H = T_e + T_n + V_{e-e} + V_{n-n} + V_{n-e} \tag{5.1}$$

However, because of the big mass difference between the nuclei and the electrons, the energy spectrum of a molecule shows high energy transitions primarily associated with electronic orbitals, and finely separated resonances due to degrees of freedom of the nuclei. Commonly, core electrons near a nucleus require x-rays or UV light in order to get promoted to external orbitals. Instead, transitions between electronic orbitals that take part in the covalent bonds are described by energies in the visible or in the UV regime. Infrared transitions are usually associated with the vibrational motion of atoms and rotational degrees of freedom are expected to be observed at microwave regimes.

This structure of the energy spectrum reflects the so called Born–Oppenheimer approximation that prescribes to write the overall wave-function of a molecule as a product:

[1]The description of the dynamics of atoms in the harmonic approximation is an essential topic in matter physics and spectroscopy textbooks. An introduction to the quantum mechanical treatment of this subject can be found in [132].

$\Psi_k(\mathbf{x}_e,\mathbf{X}_n)\Gamma_{k,r}(\mathbf{X}_n)$ where $\Psi_k(\mathbf{x}_e,\mathbf{X}_n)$ is a function of the electronic degrees of freedom[2] $\mathbf{x}_e$ and is parametrised by the nuclear spatial coordinates[3] $\mathbf{X}_n$; $\Gamma_{k,r}(\mathbf{X}_n)$ is instead a function of $\mathbf{X}_n$. The index k and the list of indices r represent the quantum numbers indexing the energy eigenstates. Note that in many applications, it is sufficient to consider the most internal atomic electrons as unaffected by the presence of the other atoms. In this case the $\mathbf{x}_e$ coordinate would only refer to more external electrons and the nuclei would be treated as finite dimensional, positively charged ions [132]. The heart of the Born–Oppenheimer approximation is that the electronic and nuclear degrees of freedom can be treated separately. Leaving out the kinetic contribution of the nuclei, the Hamiltonian problem can be solved for the electronic component of the wave function,

$$(T_e + V_{e-e} + V_{n-e} + V_{n-n})\Psi_k(\mathbf{x}_e,\mathbf{X}_n) = E_k(\mathbf{X}_n)\Psi_k(\mathbf{x}_e,\mathbf{X}_n). \tag{5.2}$$

Note that this partial Hamiltonian problem is diagonal in the basis of the coordinate of the nuclei so that the nuclei are essentially treated as classical objects and the retrieved energy can be interpreted as the electronic energy of the system given a well defined position of the atoms in the space. $E_k(\mathbf{X}_n)$ is usually referred to as the *energy landscape* of the molecule. A different electronic excitation of the molecule determines a different energy landscape. Once that $E_k(\mathbf{X}_n)$, the electronic contribution to the energy, is calculated, it is possible to evaluate the remaining terms of the energy that relates to the motion of the atoms in the molecule,

$$(T_n + E_k(\mathbf{X}_n))\Gamma_{k,r}(\mathbf{X}_n) = E_{k,r}\Gamma_{k,r}(\mathbf{X}_n). \tag{5.3}$$

The position $\overline{\mathbf{X}}_n$ around which the atoms arrange in the molecule are obtained finding the nuclear coordinates that correspond to the minimum of $E_k(\mathbf{X}_n)$. However, in the absence of external fields, $E_k(\mathbf{X}_n)$ is invariant for rigid translation and rotation of the molecule. Therefore, it is necessary to fix these degrees of freedom in order to unambiguously assign the atomic positions. Generally, such degrees of freedom are 6 but they become 5 for a linear molecule such as C_2H_2. Once $\overline{\mathbf{X}}_n$ are known, the problem in Eq. 5.3 can be approximated, near the equilibrium configurations, as a quadratic expression that, as it will be clear soon, is also known as harmonic approximation,

$$\left(\sum_i \frac{\partial^2}{2m_i\partial^2\mathbf{X}_{n,i}} + E_k\left(\overline{\mathbf{X}}_n\right) + \left(\overline{\mathbf{X}}_n - \mathbf{X}_n\right)\cdot\frac{\partial^2 E_k}{\partial\mathbf{X}_{n,i}\partial\mathbf{X}_{n,j}}\left(\overline{\mathbf{X}}_n\right)\cdot\left(\overline{\mathbf{X}}_n - \mathbf{X}_n\right)^{\mathrm{T}}\right)\Gamma_{k,r}(\mathbf{X}_n) = E_{k,r}\Gamma_{k,r}(\mathbf{X}_n). \tag{5.4}$$

The second index i in $\mathbf{X}_{n,i}$ is used to enumerate the elements of the list $\mathbf{X}_n$ making the kinetic energy term explicit. We represented the Hessian matrix of the energy landscape with $\frac{\partial^2 E_k}{\partial\mathbf{X}_{n,i}\partial\mathbf{X}_{n,j}}$ and we further assumed $\hbar = 1$.

[2] We will symbolically represent the three spatial coordinate as well as the spin degree of freedom of all the electrons as a list of parameters $\mathbf{x}_e$.

[3] This statement assumes for example that the norm of Ψ_k is constant with respect to the nuclear coordinates.

The equation appears as an ensemble of coupled harmonic oscillators but the eigenvalue problem can be rewritten as a sum of *independent* harmonic oscillators in a new set of coordinates $\mathbf{Q}_n$, plus an additional kinetic term associated with the rigid rotation and translation of the whole system. An orthogonal transformation relates $\mathbf{Q}_n$ to the mass weighted coordinates $\left\{\frac{\mathbf{X}_{n,i}}{\sqrt{m_i}}\right\}_i$. With this change of coordinates, neglecting the kinetic energy associated with rigid movements of the molecule, the Hamiltonian problem can be written in terms of bosonic creation operators $a_i^\dagger$ as:

$$\left[\sum_i \omega_i \left(a_i^\dagger a_i + \frac{1}{2}\right)\right] \overline{\Gamma}_{k,r}\left(\mathbf{Q}_n\right) = \left(E_{k,r} - E_{k,0}\right) \overline{\Gamma}_{k,r}\left(\mathbf{Q}_n\right) \tag{5.5}$$

where $\overline{\Gamma}_{k,r}\left(\mathbf{Q}_n\right)$ is the solution of the multidimensional harmonic oscillator. In particular, the relation between $\mathbf{Q}_n$ and $\mathbf{X}_{n,i}$ tells the relation between the relative displacement vector of the atoms, from their equilibrium position, in the different independent harmonic oscillator indexed by r. $E_{k,0}$ is the energy of the system when all the quantum numbers of the harmonic oscillators are null. The oscillators found in the harmonic approximation are known as vibrational modes or normal modes of the molecule.

5.2 Simulations in the harmonic approximation

5.2.1 Simulation mapping

To simulate the evolution of vibrational excitations in molecules, the mapping that we propose requires to know in advance the properties of the normal modes of the molecular systems. In our experiments, we were provided with the coordinates transformation and eigen-energies by Dr. David Tew who numerically solved the electronic problem of the Born–Oppenheimer approximation with coupled cluster methods [133]. The simulation model then proceeds by mapping each vibrational mode of the molecule to a specific single mode of the linear optical circuit. Multiple vibrational excitations of the molecule are mapped to indistinguishable single photons in the optical modes associated with the vibrational modes. The free evolution of this system, in the basis of the energy eigenstates, consists in the accumulation of phases that can be implemented applying a phase shift in each optical modes as function of the time parameter of the simulation. A complex dynamics manifests in those observables whose eigenvectors are superpositions of multiple eigenstate of H.

Localised modes

In our simulations, we mainly investigated the evolution, i. e. the propagation, of spatially localised excitations. Such perturbations of the state of the molecule can be conceived as

obtained through a transformation of the normal vibrational modes that concentrates the kinetic energy in single atoms [134–136].

The orthogonal transformation that defines $\mathbf{Q}_n$ can be used to write the momentum of single atoms, and their kinetic energy K_i, as a weighted sum of the energy associated with the vibrational modes of the molecule and additional terms associated with rotations and translations of the whole molecule. Conversely, for each unitary transformation of the vibrational modes of the molecule, excluding rotations and translations, it is possible to evaluate K_i of each atom and estimate the level of energy concentration.

Note that due to the absence of the translational and rotational modes in the accepted superpositions the retrieved transformation differs from the one diagonalising the hessian matrix. In the following, we will indicate with U_L the unitary transformation that converts the localised modes $a^\dagger_{\mathrm{L},i}$ to the normal modes $a^\dagger_j$:

$$a^\dagger_j = \sum_i [U_L]_{i,j}\, a^\dagger_{\mathrm{L},i}. \tag{5.6}$$

Time evolution

Assuming initialisation and detection in the localised modes, the dynamics of the system is then reproduced setting the interferometer to implement:

$$U_{\mathrm{chip}}(t) = U_L . D(\omega, t) . U_L^{-1} \tag{5.7}$$

for a sequence of time steps $t \in \{t_k\}$. The diagonal matrix $D(\omega, t)$ introduces additional phases in each optical mode. The diagonal elements of $D(\omega, t)$ are $\omega_i t$ where the angular frequency are those in Eq. 5.5. With this mapping, single photons injected in the different input modes correspond to localised excitation of the system and evolve accordingly. The output photons are finally measured in the localised basis providing information about the propagation of the energy in the molecule. It is important to note that the probability of detecting a specific output pattern is governed by the permanent of a submatrix of $U_{\mathrm{chip}}(t)$ as for the boson sampling problem Sec. 2.5.2.

The overall scheme to map the evolution of the molecule on our chip is summarised in Fig. 5.1

5.2.2 Experiment

Using the setup described in Chapter 3, we simulated the evolution of multiple 4-atom molecules with up to four excitations. Single photon simulations were performed using a single photon pair source looking at coincidental detection between the heralding photon and the photon injected into the system. Two-photon simulations with input state $|1,1,0,0,0\rangle$ were obtained injecting both photons from a single down conversion source into the top

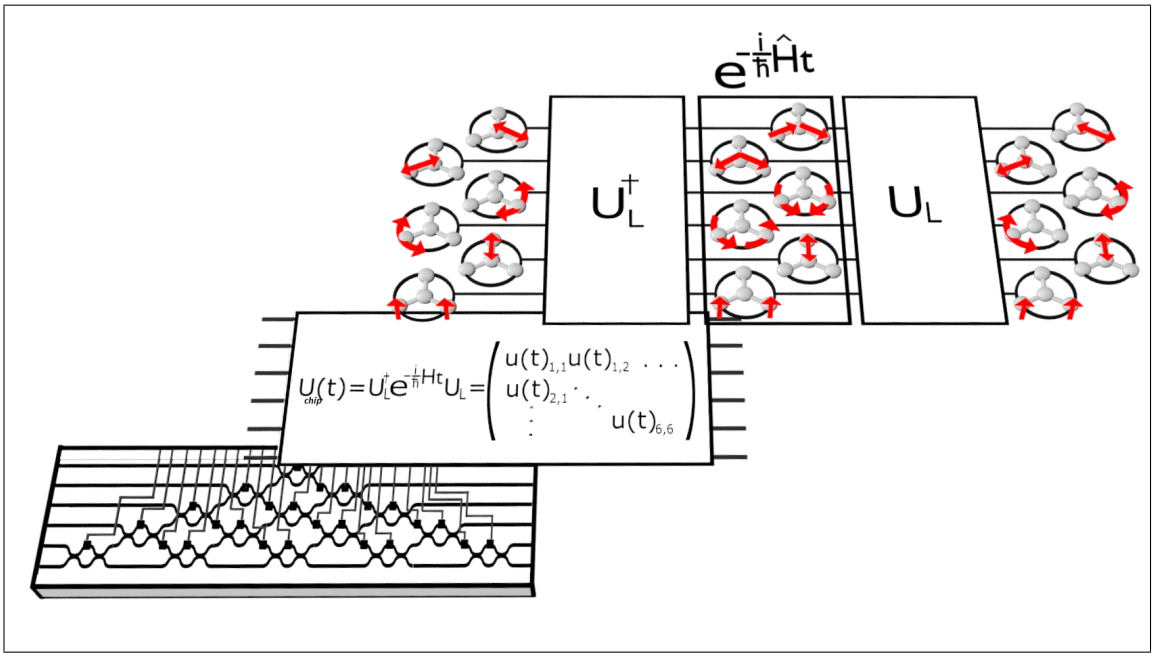

Figure 5.1: Mapping of the molecule evolution on the integrated chip The input modes of the device are associated to localised excitation of the molecule. These are transformed by $U_L^\dagger$ into excitation superposed across different single modes waveguides that map onto normal modes of the chip. These are then evolved according e^{-iHt}; in the harmonic approximation, such transformation is diagonal in the normal modes basis. Photons travelling into the chip are then projected back onto the local excitations of the molecule by U_L. In our experiments the overall transformation is condensed in a single unitary $U_{\text{chip}}(t)$ that is dialled on the chip tuning the thermal phase-shifters of the device.

two input ports of the device; the same configuration was also used for the input state $|2,2,0,0,0\rangle$. The input state $|1,1,1,0,0\rangle$ was obtained connecting a photon pair source to the first two modes of the chip and separating the photons from the second photon pair source. One of them was injected into the third mode and the other used as heralding channel. The detection of the heralding photon, coincidental to a threefold coincidence signal from the detectors connected to the chip is registered as successful input state preparation.

Indistinguishability of the photons was assessed with Hong Ou Mandel interference performed right before the simulation measurements. The level of squeezing of the sources was increased in the three and four photons experiments to increase the rate of multi pair generation. Similarly, longer acquisition time was used for these measurements. For a fixed input state configuration, the chip was reprogrammed to implement the $U_{\text{chip}}(t)$ for a sequence of linearly separated time steps for each simulated molecule. Additionally, a permutation matrix was included in $U_{\text{chip}}(t)$, when needed, to make it possible to constantly used the same input modes of the chip to represent different localised input excitations.

Detector efficiency corrections

To account for the relative efficiency of the output modes that would otherwise alter the frequentist estimated probabilities of the different patters, we corrected the photon statistics collected from the array of detectors. Detector efficiency was obtained by alternatively routing the input power injected in the top mode of the circuit into the each output mode individually. Assuming constant generation rate, the ratio between the counts measured in each output mode returns the relative detector efficiency, also assuming perfect routing. Indicating with μ_i the detector efficiency normalised dividing by the highest detector efficiency, we corrected the count rate for an output pattern $(n_1, n_2, n_3, n_4, n_5, n_6)$ with occupancy numbers $n_i \in \{0, 1\}$ by multiplying the experimental rate by a factor $\prod_i \mu_i^{-n_i}$

Pseudo number resolving detection

To distinguish between output patterns with multiple photons in the same modes, some experiments were performed with additional fibre beam splitters (FBS) connected at each output mode of the device. In this way, there was a finite probability of separating a pair of photons exiting from the same output port resulting in the detection of a (1,1) pattern from the two detectors connected to that port. The measurement of the relative detector efficiency was performed with a procedure similar to what has been described above but the measured efficiency $\nu_i = \tau_i \mu_i$ included the transmissivity τ_i at the output ports of the FBSs. To take into account the probabilistic nature of the pseudo-number resolving scheme, the experimental count rate of a pattern

$$((n_{1,1}, n_{1,2}), (n_{2,1}, n_{2,2}), (n_{3,1}, n_{3,2}), (n_{4,1}, n_{4,2}), (n_{5,1}, n_{5,2}), (n_{6,1}, n_{6,2}))$$

was divided by

$$\prod_{i=1}^{i=6} \nu_{i,1}^{n_{i,1}} \nu_{i,2}^{n_{i,2}} (n_{i,1} + n_{i,2})! \tag{5.8}$$

Finally, the rate of the output pattern $(N_1, N_2, N_3, N_4, N_5, N_6)$ with $N_k = n_{k,1} + n_{k,2}$ was determined by averaging rates of equivalent detection patterns[4].

Results

In Fig. 5.2 we present the results of the simulation of 1, 2, 3 and 4 excitations in H_2CS (thioformaldehyde). The pseudo-number resolving scheme was adopted for the 2 and 4 photons cases. All the experimental probabilities are estimated with a frequentist approach normalising them to the subset of experimentally available patterns. The theoretical lines

[4]For example, ((1,0),(1,0),(0,0),(0,0),(0,0),(0,0)) is equivalent to ((1,0),(0,1),(0,0),(0,0),(0,0),(0,0)) since both correspond to the output pattern $(1,1,0,0,0,0)$

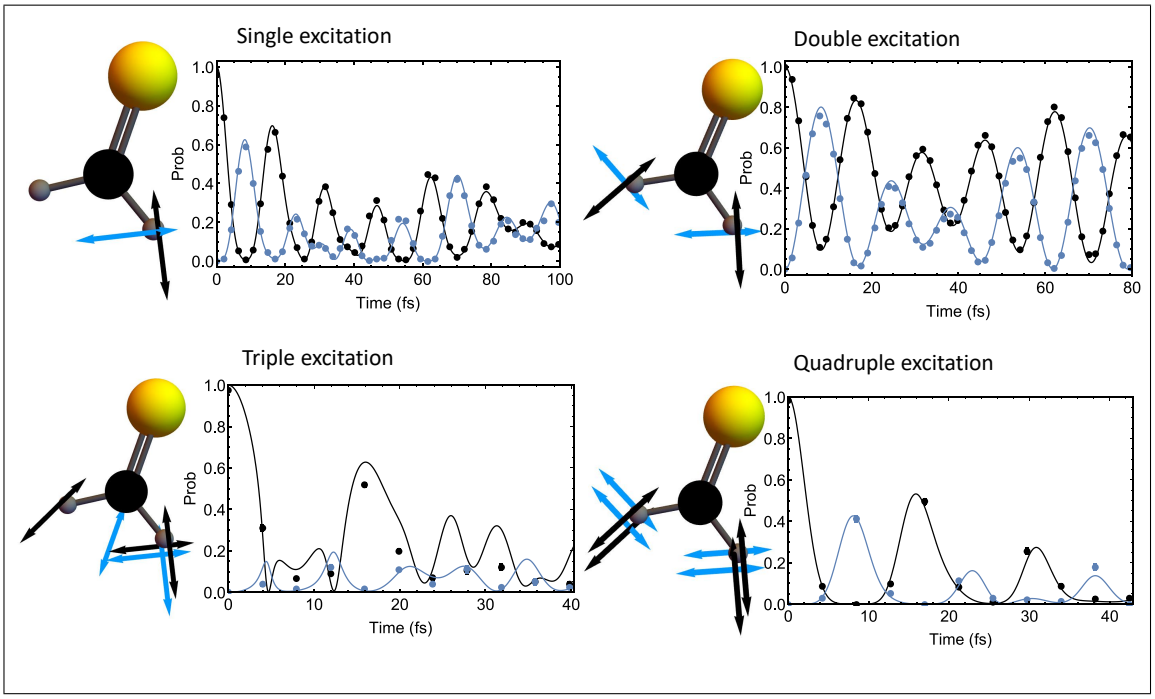

Figure 5.2: Quantum simulation of H_2CS with multiple vibrational excitations. Evolution of localised excitations schematically described by arrows in the molecule diagrams. Lines represent theory curves and points correspond to experimental data. Black elements indicate the initial molecule configuration; blue ones refer to an alternative observed excitation configuration. Probability for single and triple excitations are normalised over the set of possible unbunched output configurations of the local excitation Fock space. Probability for double and quadruple excitations are normalised over the set of possible output configurations of the local excitation Fock space with up to two bunched photons events.

showed as comparison are based on the same assumption. The data represent the probability of observing two of the possible output patterns of the molecule. The localised excitation involved in this pattern are schematically represented by blue arrows in the molecule diagram. Black arrows (and black data points) refer to the initial configuration of the molecule.

In Fig. 5.3 we show simulation results for many other 4-atom molecules. A collection of single and double excitation experiments are shown; molecules examined are P_4, N_4, SO_3, HNCO, HF-HF. We report the probability of observing two alternative combinations of local excitations in the molecules adapting the evolution time window for a clearer visual representation. Arrows in the molecule diagrams represent either the displacement of the atom with the largest kinetic energy of the tracked local excitations, or the molecular bond mostly perturbed by the excitation if the kinetic contribution of the two bonded atoms is balanced. Error bars, estimated with bootstrap method [137], are smaller than point size.

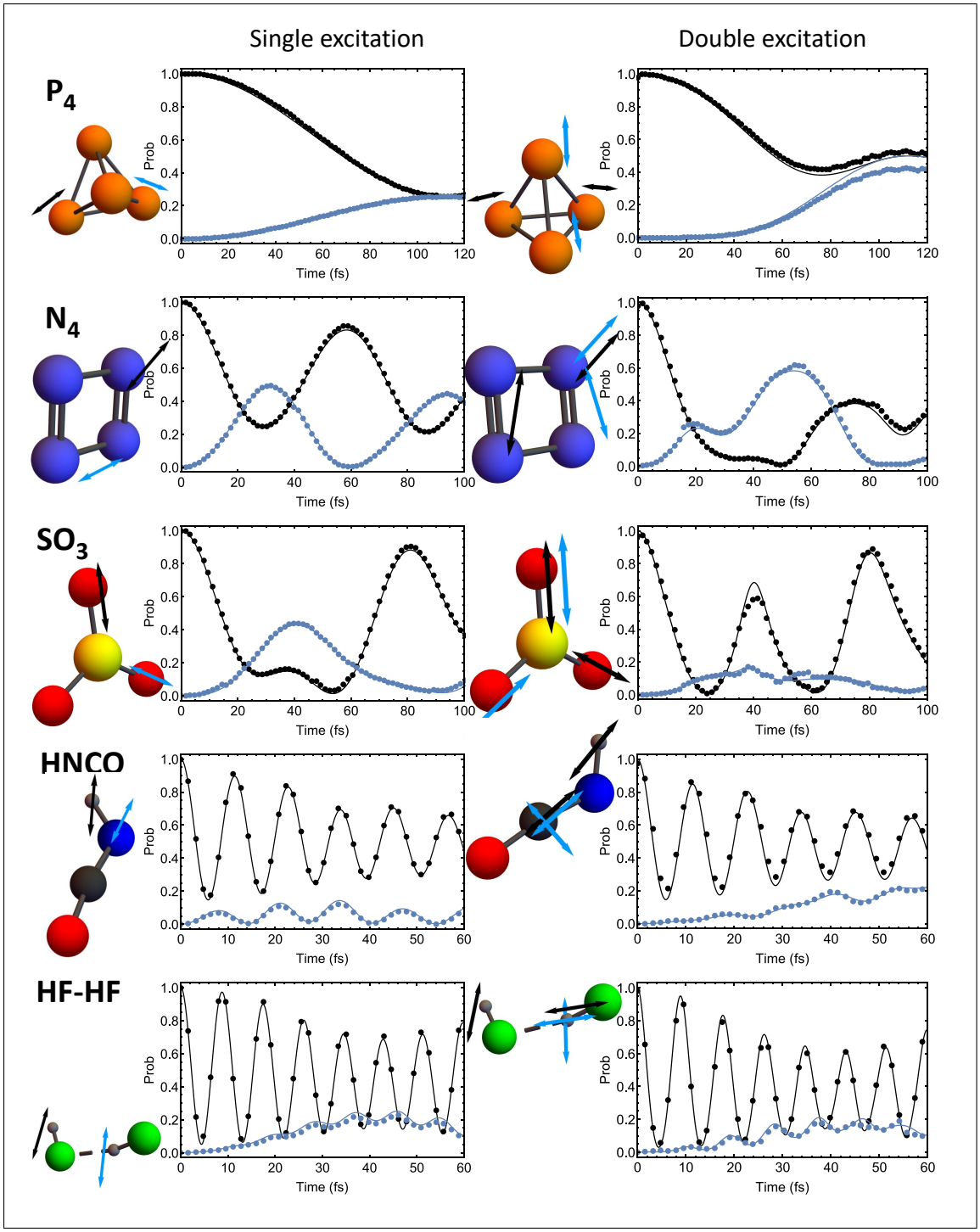

Figure 5.3: Quantum simulation of a set of 4-atom molecules in harmonic approximation. Evolution of single and double localised excitation. Arrows in the picture indicate the main atoms or molecular bonds involved in the motion. Lines represent theory curves and points correspond to experimental data. Black features indicate the initial excitations while blue represent an alternative observed excitation pattern.

5.3 Simulating the effects of an environment

The dynamics of large, complex molecules is of interest for biological research. In this context, a molecule is surrounded by an environment whose interaction may alter significantly the evolution of the system. A similar problem is also present in molecular experiments when it is not possible to sufficiently isolate individual molecules. Because of this, to make our simulator more suitable for practical applications, we also addressed models of open system dynamics. The two particular cases described in this section concern the intramolecular transport of energy in a dephasing environment and thermalisation processes.

5.3.1 Energy transfer in N-Methylacetamide

Here we bring our attention to a larger molecule: N-Methylacetamide (NMA). Even if our setup does not have enough degrees of freedom to describe the whole molecule, we simulate the subspace of six vibrational modes localised along the "backbone" of the molecule that are more coupled to each other (see Fig. 5.4). The six modes are the two rocking oscillation

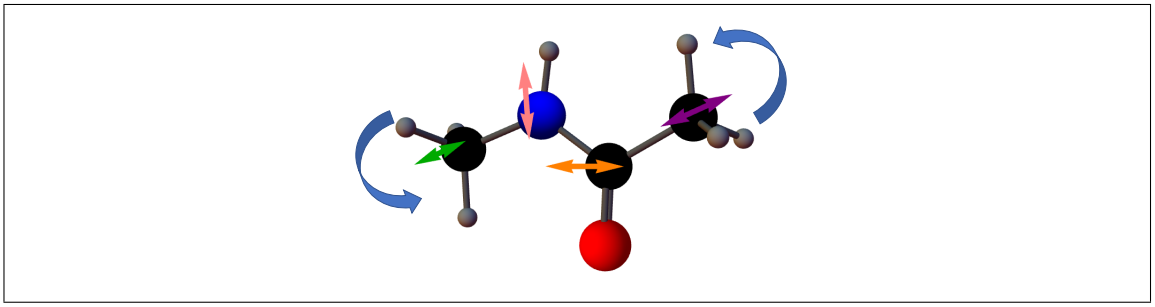

Figure 5.4: Visual representation of localised backbone modes of N-Methylacetamide (NMA). In blue, two rocking modes of the methyl groups at the end of the chain. Purple and green, stretching modes of the external carbon atoms. Orange and pink, movement along the backbone chain of the internal carbon and nitrogen atoms.

around the carbons at the two ends of the molecule, the displacement of the 3 carbons along the molecule chain and the transverse excitation of the nitrogen.

For this system, we considered a master equation of the form:

$$\dot{\rho} = -i\left[\hat{H},\rho\right] + \frac{\Gamma}{6}\sum_{k=0}^{5}\left(\hat{Z}_k\rho\hat{Z}_k^\dagger - \frac{1}{2}\left\{\hat{Z}_k^\dagger\hat{Z}_k,\rho\right\}\right) = -i\left[\hat{H},\rho\right] + \frac{\Gamma}{6}\sum_{k=0}^{5}\left(\hat{Z}_k\rho\hat{Z}_k^\dagger - \rho\right) \tag{5.9}$$

where $\hat{Z}_k = \exp\left(\sum_{j=0}^{5} i2\pi jka_j^\dagger a_j/6\right)$ are unitary matrices and Γ is the dephasing rate. The evolution of the system can be described by introducing 6 time-dependent Kraus operators

that are proportional to $\hat{Z}_k$ (see App. A).

$$M_0(t) = \sqrt{\frac{1+5e^{-\Gamma t}}{6}}\ \mathbb{1} = \sqrt{\frac{1+5e^{-\Gamma t}}{6}}\,\hat{Z}_0, \qquad M_{k>0}(t) = \sqrt{\frac{1-e^{-\Gamma t}}{6}}\,\hat{Z}_k. \tag{5.10}$$

With the aid of these, the evolution map of the system can be written as:

$$\rho(t) = \sum_k M_k(t)\, e^{-i\hat{H}t}\, \rho(0)\, e^{i\hat{H}t} M_k^\dagger(t) \tag{5.11}$$

The simulation of the system consisted in a set of 6 experiments for each time t corresponding to the 6 unitaries $U_{\text{chip}}(t,k) = U_L Z_k e^{-i\hat{H}t} U_L^{-1}$ where $[Z_k]_{i,j} = \langle \text{vac}|\, a_i \hat{Z}_k a_j^\dagger \,|\text{vac}\rangle$. The statistics collected from each of the 6 experiments were then weighted by the square of the time dependent factors in Eq. 5.10 so to reproduce the properties of the system we want to simulate.

Results

In Fig. 5.5 we present the evolution of a single and double excitation propagating along the backbone chain of the NMA. Dots represent the results of the simulation of dephasing through the evolution and are plotted against their theoretical curve showed with solid lines; dashed lines, instead, represent the expected evolution in the absence of dephasing. It is visible how the system tends toward a steady state with constant probability of detecting the different patterns. In particular, the two photon experiment compares the possibility of two excitation at different ends of the molecule to bunch together around the nitrogen atom, a phenomenon that is initially enhanced after the first 50fs and then occurs with a constant and lower probability later in the evolution as a result of the dephasing.

5.3.2 Vibrational relaxation in liquid water

In classic thermodynamics, an isolated system composed of two bodies that can exchange heat will incur a thermalisation process where all the parts of the systems reach the same temperature. If we consider a single molecule immersed in a surrounding environment, we expect the molecule to be found, after sufficient time, in a state that is representative of the temperature of the environment. In quantum mechanics, this process is commonly described by a Lindblad equation that includes stochastic energy exchange with the environment and probabilistic hopping between the different energy levels of the system. Assuming relaxation rates as reported in [138], we simulated the evolution of a single excitation in a water

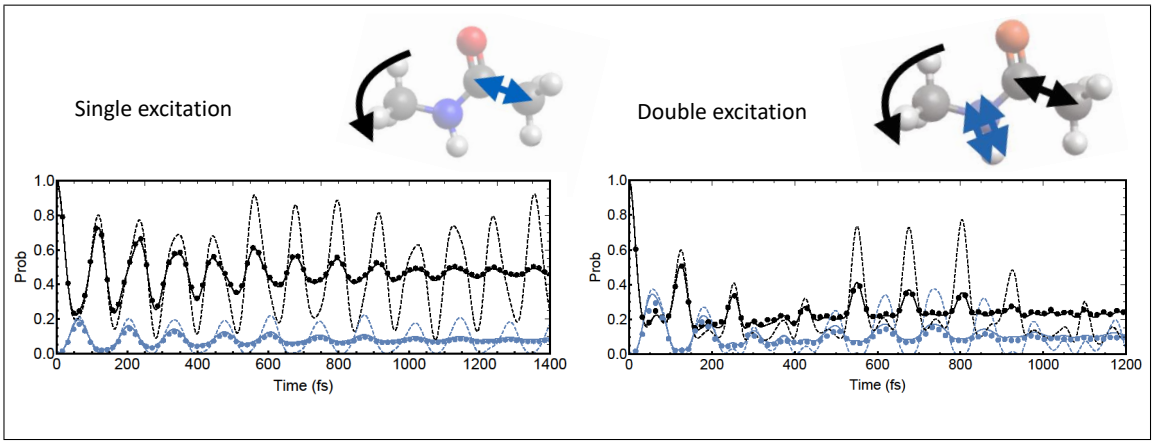

Figure 5.5: Quantum simulation of NMA affected by a dephasing environment Single and double excitations evolution in a N-Methylacetamide. Experimental points and theory solid line refer to the evolution affected by a dephase rate $\Gamma = 1/530\text{fs}^{-1}$. The evolution in absence of any dephase is reported with dashed lines. Color coded arrows in the molecule diagram indicate the localised excitations tracked in the plots. The periodic features in both examples are smeared out by the dephasing.

molecule described by the following master equation:

$$\begin{aligned}\dot{\rho} = -i\left[\hat{H},\rho\right] + \Gamma_1 \sum_{j=1,2}\left(|3\rangle\langle j|\,\rho\,|j\rangle\langle 3| - \frac{1}{2}\left\{|j\rangle\langle j|,\rho\right\}\right) + \Gamma_2\left(|0\rangle\langle 3|\,\rho\,|3\rangle\langle 0| - \frac{1}{2}\left\{|3\rangle\langle 3|,\rho\right\}\right) \\ + \Gamma_3 \sum_{j=1,2}\left(|0\rangle\langle j|\,\rho\,|j\rangle\langle 0| - \frac{1}{2}\left\{|j\rangle\langle j|,\rho\right\}\right)\end{aligned} \tag{5.12}$$

where $|0\rangle$ indicates the vacuum state $|\text{vac}\rangle$ and $|j\rangle = a_j^\dagger|\text{vac}\rangle$ are the states with a single vibrational excitation of the normal modes with decreasing energy. The transition rates between the energy levels are represented also in Fig. 5.6. The particular form of the Lindblad equation is obtained assuming an environment at room temperature and noting that in comparison to the vibrational energy of the molecule, $k_B T$ is negligible. The evolution of the system can be solved with a set of six Kraus operators:

$$\begin{aligned} M_1(t) &= \sqrt{1-e^{\Gamma_1 t}}\,|3\rangle\langle 1|, & M_2(t) &= \sqrt{1-e^{\Gamma_1 t}}\,|3\rangle\langle 2| \\ M_3(t) &= \sqrt{1-e^{\Gamma_2 t}}\,|0\rangle\langle 3|, & M_4(t) &= \sqrt{1-e^{\Gamma_3 t}}\,|0\rangle\langle 1| \\ M_5(t) &= \sqrt{1-e^{\Gamma_3 t}}\,|0\rangle\langle 2|, & M_0(t) &= \sqrt{\mathbb{1} - \sum_{i=1}^{5} M_i^\dagger(t) M_i(t)}\,. \end{aligned} \tag{5.13}$$

With these, the solution of the differential equation can be written as

$$\rho(t) = \sum_{k<3} M_k(t) e^{-i\hat{H}t}\rho(0)e^{i\hat{H}t}M_k^\dagger(t) + \sum_{k>2} M_k(t) e^{-i\hat{H}t}\rho(0)e^{i\hat{H}t}M_k^\dagger(t). \tag{5.14}$$

We note that the second summation on the left hand side determines the probability of finding the molecule in the vibrational ground state. The desired statistics for the simulated

system can be obtained by averaging the results of the experiments with transfer matrices $T_{0<i<3}(t) = U_L |3\rangle \langle i| e^{-iHt} U_L^\dagger$ and $T_0(t) = U_L M_0(t) e^{-iHt} U_L^\dagger$ that describe the evolution for the populated levels of the molecule, and applying an effective $\Gamma_i t$ dependent detector efficiency. In contrast to the NMA example, two important differences are present. The transfer matrices we described are non unitary so a dilation procedure was required (see Sec. 2.1.6), and T_0 is a time dependent matrix that cannot be written as a product of a scaling factor times a time independent matrix. The ratio of the decay rates determines T_0. Thus, contrarily to the previous dephasing example, the settings of the simulator are fixed by the decay rates of the system. The probability of observing $|\text{vac}\rangle$ can be retrieved by the complement to 1 of the trace of the state obtained from $T_{i<3}$.

Results

The 6 modes of the chip are enough for implementing arbitrary linear non-unitary transformation over 3 modes and are therefore suitable for the simulation of a three-atomic system such as H_2O.

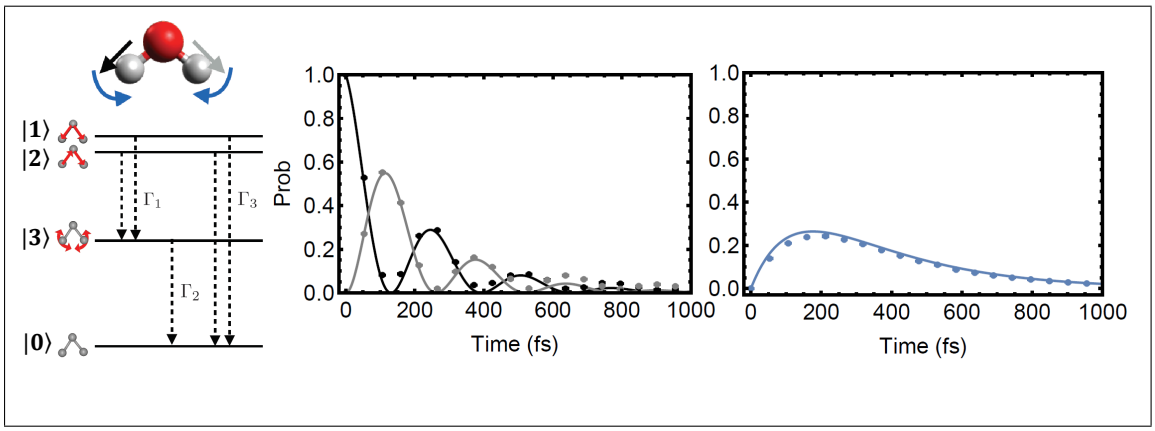

Figure 5.6: Simulation of H_2O thermalisation. A single excitation is initialised in a stretch mode of the water molecule. The system evolves exchanging energy with the environment. Transition rates between normal modes of the molecule are depicted in the energy diagram on the left. The colours of the arrows in the molecule diagram match the data point in the plots and the corresponding theory lines.

In Fig. 5.6, we report the evolution of a single stretch excitation localised in a O-H bond and oscillating in the stretching subspace while decaying into the scissoring mode and finally disappearing leaving the molecule in its vacuum state. The peak in the population of the lowest energy vibrational state corresponds to the balance between the probability of an excitation to decay from a higher energy configuration and the probability of the scissoring excitation to decay into vacuum. The decay rates used are $\Gamma_1 = 0.24$ ps, $\Gamma_1 = 0.26$ ps, $\Gamma_3 = 1.36$ ps, as measured in [138].

5.4 Beyond harmonic dynamics

The lack of significant photon-photon interaction makes naturally easy, with an optical system, to simulate independent harmonic oscillators, such as the vibrational modes of a molecule in the harmonic approximation. However, this approximation is often not suitable to describe real systems when more excitations localise around the same atom. The potential where the ions oscillate is often asymmetric and this results in the impossibility to decouple the different nuclear degrees of freedom of the molecule.

5.4.1 Simulating anharmonic potentials

A potential approach is to retain the basis described by the independent harmonic oscillators and to expand the Hamiltonian of the system with non linear terms [139]. The first correction to the Hamiltonian can be written as

$$\hat{H}_{an} = \hat{H} + \sum_{i \leq j} \frac{x_{ij}}{2} \sqrt{\omega_i \omega_j} \left(a_i^\dagger a_i + a_j^\dagger a_j + 2 a_i^\dagger a_j^\dagger a_i a_j \right)$$

The higher order term in this Hamiltonian represents what is usually known with the names cross-phase modulation, for $i \neq j$, and self-phase modulation, when $i = j$. In integrated optics, achieving a significant contribution from these non-linear terms, when only few photons are involved, is currently a major challenge. Here we opted for a probabilistic measurement induced non-linearity while examples of alternative avenues, based on quantum dots or graphene properties, are reported in [140, 141].

Focusing on a two photon subspace, we wanted to implement the following transformation:

$$a_0 |0\rangle + a_1 |1\rangle + a_2 |2\rangle \rightarrow a_0 |0\rangle + a_1 e^{i\phi_1} |1\rangle + a_2 e^{i2\phi_1 - i\delta\phi} |2\rangle$$

This was achieved by means of an ancillary photon and a heralded non-linear phase gate that generalises the famous non linear sign gate described in [63], and further investigated in [62]. By considering the target state encoded in the first mode of a small interferometer and an ancillary photon injected in the second mode, the desired transformation can be generated by the following transfer matrix:

$$M = \begin{pmatrix} 1 - \sqrt{1 - e^{-i\delta\phi}} & x \\ \frac{y}{x} \sqrt{1 - e^{i\delta\phi}} & y \end{pmatrix} \begin{pmatrix} e^{i\phi_1} & 0 \\ 0 & 1 \end{pmatrix}. \tag{5.15}$$

The transformation is probabilistic, the success of the operation can be heralded by the detection of a single photon in the ancillary channel after the application of the gate. The probability of success for such gate is y^2 if we assume that $\|M\|_2 = 1$. Indeed, to dial M as part of a unitary transformation, we needed to dilate it using the methods described in Sec. 2.1.6.

Experiment

Making use of the non-linear gate, we were able to simulate a water molecule including the anharmonic corrections. Note that the non-linear gate requires two additional modes to be implemented reducing the size of the molecule we can simulate on our device. Since in H_2O the two high frequency modes associated with the symmetric and antisymmetric stretch modes are almost decoupled from the motion of the oxygen atom, with an approximation of less than 1% in U_L, we treated the subspace of the stretch modes as independent from the third vibrational (scissoring) mode. In the two waveguides that represent the stretching modes of our system, the state can be represented in the $\{|2,0\rangle, |1,1\rangle, |0,2\rangle\}$ Fock basis. Within this framework, we report the evolution of a double localised stretch excitation of the $O-H$ bond in Fig. 5.7. In particular, we show the probability for the two excitations to separate into different localised modes or to be found in the bunched initial state. Data, along with the theoretical curves, are displayed for both anharmonic and harmonic approximations demonstrating remarkable differences in their behaviour.

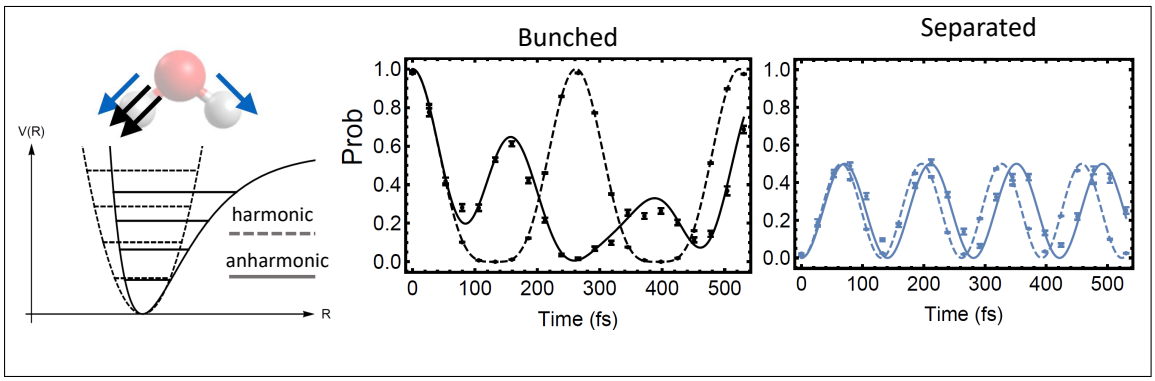

Figure 5.7: Simulation of anharmonic potential in H_2O The evolution of a double excitation of a localised stretch mode is simulated. On the left conceptual diagram of the non harmonic nature of the energy landscape of the O-H bond. The two plots show the evolution in the harmonic (dashed lines) and anharmonic (solid lines) treatment. Data and theory lines are coloured according to the localised excitations depicted by the arrows in the molecule diagram.

For each evolution time, we computed the necessary transfer matrix

$$U_{\text{chip}} = U_L . U_{\text{NLG}}(t) . U_L^{-1} . U_{\text{input}}$$

where U_{input} probabilistically transforms the injected state $|2,0,2,0,0,0\rangle$ into the state needed to perform the non linear gate: $|2,0,1,0,1,0\rangle$; U_L encodes the change of basis between the stretch subspace and the local $O-H$ modes and acts as identity on the additional modes; $U_{\text{NLG}}(t)$ is the dilated unitary corresponding to the non-linear gate at time t. FBSs were used at the first two outputs of the system to observe the photon bunching events. A single photon pair source was used for these experiment. Heralding the successful generation of

the input state required the detection of a photon in the 5th mode and three photons in the top 4 modes of the chip. The success of the non-linear gate was signalled by a photon detected in the 3rd mode and two photons exiting the the first two modes of the device.

5.4.2 Improving dissociation with a hybrid feedback algorithm.

We finally performed an experiment inspired by the adaptive feedback control (AFC) technique [142, 143], that consists in dynamically modifying the parameters controlling the experiment based on the evaluation of an objective function in an optimisation routine. This is currently considered an efficient laboratory practise to optimise the properties of a laser field (divergence, intensity spectrum, chirping etc.) in order to maximise a particular outcome from its interaction with a target molecular system. Indeed, due to the elevated complexity of modelling microscopic physical systems together with the details of the macroscopic experimental environment, an a-priori calculation would often result in mediocre results. Contrarily, using the feedback determined by the results of the actual experiment, it naturally accounts for the real experimental conditions and it is not computationally expensive.

We adopted the AFC approach in the problem of molecule dissociation. In particular, we considered ammonia molecules (NH_3), for which it has already been shown how the particular dissociation products, generated once the molecule is electronically excited, depend on the vibrational state of molecule before the excitation [144]. Coincidentally, ammonia also has a critical importance in chemistry industry being the precursor for the production of fertilisers, cleaning and pharmaceutical compounds. The dissociation of the molecule can be interpreted qualitatively as the result of a loosely confining energy landscape. In this case the anharmonic behaviour of the potential dominates and a hydrogen atom, if provided with sufficient kinetic energy, can escape the energy potential barrier.

In our toy model, we assumed that a prolonged double occupancy of a localised vibrational mode, in an electronically excited NH_3, leads to the separation from the molecule of the hydrogen involved in the vibration. Furthermore, depending in which mode the bunching occurs, we associated two alternative reaction products. Given these presuppositions, the goal of our algorithm was to search for the best initial vibrational state for NH_3 in its electronic ground level, such that, once electronically excited, the dissociation rate in one channel dominates over the other.

Experimentally, unitaries implemented on our chip were

$$U_{\text{chip}} = U_{LE}.e^{iH_E t}.U_{\text{GE}}.U_{\text{input}}(\vec{\theta}), \tag{5.16}$$

and we injected in the device two excitations split into two distinct vibrational modes of the electronic ground state; a pictorial representation of the experiment is shown in Fig. 5.8. The

parametrised transformation $U_{\text{input}}(\vec{\theta})$ encoded the set of initial states of the molecule that we were able to prepare. The 14 degrees of freedom listed in $\vec{\theta}$ permitted arbitrary linear transformation of the two excitations among the first 5 vibrational modes of the system. In U_{GE} we encoded the approximated transformation between the vibrational modes of the ground state and the equivalent modes of the electronically excited molecule. Generally, in the harmonic approximation, this transformation consists in a combination of mode-mixing, displacement and squeezing[5] acting on the initial vibrational state of the system [145]. However, having access to a linear optical circuit, we restricted the transformation to a single rotation among the vibrational modes. In Eq. 5.16, the Hamiltonian, as well as the normal modes to local excitation transformation U_{LE}^{-1}, refers to the electronic excited NH_3.

The output statistics produced by our device was fed to a classical algorithm that evaluated the objective function C and performed the optimisation algorithm for the free parameters $\vec{\theta}$ of our simulation. The cost function C, that we aimed to minimise, was calculated over a time interval that we divided in $N = 5$ intermediate evolution time steps t_i and reads

$$C = -\alpha \sum_i w_i \frac{\left(p_i^+ - p_i^-\right)}{N}. \tag{5.17}$$

In this equation, p_i^+ is the probability of favourable bunching events at time t_i as opposed to p_i^- that is the probability of bunching in unwanted localised vibrations. We considered as positive excitations those happening along the localised stretch modes of the hydrogen while negative contribution were due to excitation of the tangential or out-of-plane motion of the atoms. The weights w_i account for the probability of the molecule not being dissociated yet and are recursively defined as:

$$w_1 = 1, \qquad w_{i>1} = \prod_{k=1}^{i-1} \left(1 - \frac{\left(p_k^+ + p_k^-\right)}{N}\right)$$

and the normalisation factor α bounds the cost function in the interval $[-1, 1]$ and corresponds to

$$\alpha = \frac{1}{1 - \left(\frac{N-1}{N}\right)^N}$$

For the experiment we chose an overall evolution time window of 10 fs. The classical processor performed a Nelder-Mead minimisation algorithm until no further improvement of the cost function was observed [146]. The overall procedure was then replicated six times with random initial values of $\vec{\theta}$. The algorithm converged to alternative phase configurations but similar values of the cost function were obtained with an average final value of $\bar{C} = -0.845$.

[5] See Sec. 2.2.2 for a description of the unitary transformation in the Fock space corresponding to the displacement and squeezing operations.

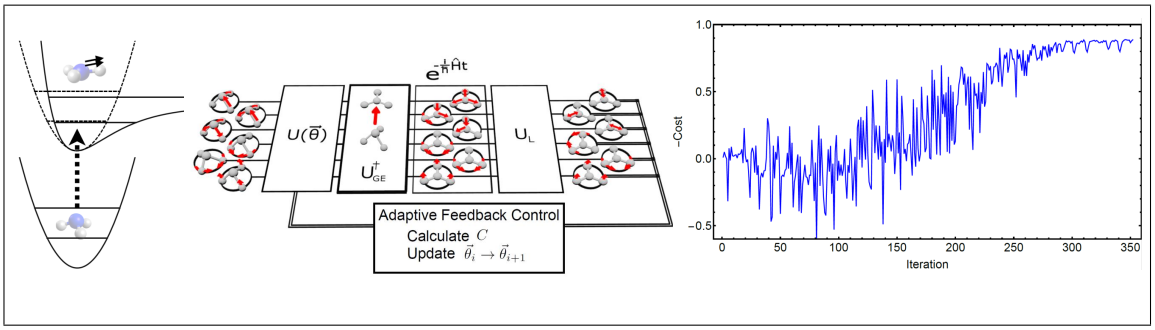

Figure 5.8: Optimisation of the dissociation rate of NH3 On the left, schematic diagram of the dissociation process induced by the double occupancy of a localised vibrational mode of the NH_3 in its electronically excited state. The chip is programmed to search in the space of possible vibrational states in the electronic ground state, to transform the vibrational state mimicking the electronic excitation of the molecule, to simulate the evolution of the molecule and project the system in a localised basis of the electronically excited state. From the output of the simulator, the cost-function C can be estimated and the initial state of the molecule optimised. The plot shows the improvement of the cost-function during subsequent iterations of the algorithm.

5.5 Discussion

Among the most promising applications for a quantum computer is the speed up of optimisation problems and the simulation of quantum systems that are inherently too resource demanding to be simulated on a classical computer. In the near term, it is likely that such tasks will not be accomplished by a universal computer but rather by specialised piece of quantum hardware in the so called NISQ[6] era. For the simulation of quantum systems, this could be an analogue device. Examples of quantum simulations performed with an optical system, including integrated devices, have already been shown for small dimensional Hilbert spaces [102, 105, 147, 148]. In particular, an interesting relation between the evolution of photons in a linear optical system and properties of the vibrational degrees of freedom of molecules was presented in [145], centred around the evaluation of the Franck-Condon absorption profile.

Here, we presented a quantum simulation protocol for molecular vibration that can be performed with conventional linear optics and takes advantage of the programmability of integrated optics to track physical properties of the system during its evolution. Even though for each time t we dialled a particular phase in each of the phase-shifters that permit the decomposition of the unitary, this simulation protocol is better described as an analogue computation. Indeed, if U_L and U_L^{-1} are implemented by two fixed individual interferometers, the time evolution would consist in the application of the particular Hamiltonian for a time t. In the harmonic approximation, the Hamiltonian is described by linear phases applied

[6]Noise Intermediate Scale Quantum (devices) [22]

to the photons according to the vibrational modes they are mapped onto. The simulator could further benefit from non-linearity as we showed in a particular case exploiting a new measurement induced non-linear gate that is, however, a poorly scalable solution for larger systems due to the increasing need of ancillary photons and its probabilistic behaviour. Looking at the interesting physics to be described, further non-linear behaviour that does not preserve the number of excitation are worth being addressed. This is especially true for large molecules with a higher density of accessible states that can lead to resonant behaviour between vibrational overtones [149].

The quantum advantage of our simulation is due to two properties that are in common with the boson sampling problem to which our procedure is closely related. Even though the number of modes of a molecule scales linearly with the number of atoms, the dimension of the Hilbert space described by N excitations in an M-atom system is $\binom{3M+N-7}{N}$ realising a large Hilbert space with few photons. Additionally, the transition probability at time t between two Fock states of this Hilbert space is given by the permanent of a complex matrix whose calculation requires a number of operation exponential in the number of excitations. For non structured transfer matrices, determining the output distribution probability of our experiments is computationally hard and also sampling from a similar distribution is supposed to be classically hard [60]. Conversely, our simulator naturally samples from such distribution. Within this topic, we showed a toy example that combines our quantum device with a classical processing of the data in a feedback loop algorithm. An interesting application can be deduced adapting the results in the paper [150] where the goal is to find the main peaks of the sampled distribution by testing fewer output patterns hence computing fewer permanents. Our simulator can therefore suggest the elements of the output distribution for which analytically evaluate the probability to find those with largest probability, as opposite to randomly searching them.

One criticism that could be given is that the standard complexity theory associated to the boson sampling problem assumes that the system is described by an Haar random unitary and that permanents of submatrices of this unitary have to be computed. In the harmonic approximation, the unitary depends on the fixed change of basis and on the time parameter by means of the different frequency factors. This results in a few considerations:

- The continuity of all the mathematical functions involved causes that for sufficiently close evolution time t and $t+\delta t$, the two unitaries describing the system can be made similar within an additive error. However, increasing the number of excitations makes the output distribution more sensitive to changes in the applied unitary. Therefore, smaller δt are required in order to generate non-distinguishable output distributions.

- The space of the parameters for a unitary transfer matrix, among a fixed number of modes, is finite. Therefore there will be a long time Δt for which the system returns,

within a bounded distance, to its previous state. Even if the evolution was not linear, the finite dimension of the Hilbert space, for a fixed number of excitation, is finite [151].

We argue that the ratio $\frac{\Delta t}{\delta t}$, estimating the number of distinct unitaries occurring during the evolution of a molecule, can be many orders of magnitude in physically relevant situations. The non-harmonic evolution is expected to further stress the above statement while the interaction with an environment generally introduces a further dominant time scale after which the state is in a trivially evolving mixture as showed in the dephasing and thermalisation examples. We further note that the number of excitations to be simulate in order to get significant advantage has to be many tens [109]. The number of modes, that scales linearly with the number of atoms, can easily be a few thousands for biologically relevant molecules, such as proteins of RNA filaments. However, for these systems, the determination of the energy landscape could result in an unfeasible task, too [152].

Being an analogue simulator, the results of the experiment are affected by noise in the quantum system and imperfection in the hardware without the opportunity of a general purpose error correction protocols. However, differently from other analogue simulators, for any evolution time, we can compute the value of the phase to be applied modulo 2π so that the noise of our results does not increase for long simulation time.

CHAPTER 6

QUANTUM SIMULATION OF PARITY-TIME SYMMETRIC SYSTEMS

Outline

Quantum mechanics and quantum field theory have up to now provided the best model for interpreting and predicting phenomena ranging from matter to particle physics and astronomic spectroscopic observations. Nonetheless, there are still "pieces of the puzzle" that elude a clear understanding within this theory: a description of general relativity, dark matter and the origin of particle-antiparticle asymmetry, to mention a few. Since we cannot yet believe that this is the ultimate theory, quantum theories, as we know them, might hold potential for improvement.

Numerical simulations have been part of scientific research for a long time now, providing theoretical predictions for highly complex physical models and helping their validation. However, the complexity of simulating quantum mechanical systems composed of hundreds of particles has already proved challenging to classical calculators and has spurred research into quantum devices capable of undertaking this task. For these reasons, it is legitimate to believe that, in future, quantum computers and simulators might be used to formulate numerical predictions for post standard quantum mechanics theories.

This chapter concerns the simulation of an unconventional extension of quantum mechanics based on the relaxation of the Hermiticity condition of the Hamiltonian operator. In this context, I performed a set of quantum simulations of a family of non-Hermitian systems that present a parity-time symmetric Hamiltonian ($\mathcal{PT}$ Hamiltonian in the following). Most of the content in this chapter is part of an article in preparation. In the first section, I will discuss the role played by non-Hermitian Hamiltonians in quantum mechanics. The description of $\mathcal{PT}$-symmetric systems and their properties will be the topic of the second

section. In this, I will also comment on the choice of the metric for the probabilistic interpretation of the theory; the section will conclude with an overview of the application of $\mathcal{PT}$ Hamiltonians in classical and quantum technology. In the third section, I will give a brief overview of the currently known methods for simulating $\mathcal{PT}$-symmetric quantum systems, most of which have been developed in the last few years. I will then introduce our simulation model based on the unitary dilation technique described in Sec. 2.1.6. The proposed model couples together two $\mathcal{PT}$ systems otherwise evolving in opposite directions in time and offers the possibility of interpreting the $\mathcal{PT}$ dynamics as a restriction on half of the Hilbert space of a highly symmetric larger system. In the last section, the results from our simulator are presented. These include the spontaneous symmetry breaking occurring in some regions of the parameter space of the Hamiltonian, the evolution of a qubit subject to a time dependent $\mathcal{PT}$ Hamiltonian and propagating through a dephasing channel, and the observation of dynamics beyond the $\mathcal{PT}$ Hamiltonian due to the open system character of our simulation model.

Contributions

The project and the methods used for simulating $\mathcal{PT}$ Hamiltonian were conceived by Anthony Laing and Yogesh N. Joglekar. Across the years, many colleagues contributed to this research including Jaques Carolan, Chris Harrolds, Andrew Harter and Chris Sparrow. The more recent experiments included in this chapter are a joint effort from me, Patrick Yard, Levon Chakhmakhchyan and Ross Wakefield. I set up the experiments, collected and analysed all the data presented with significant help from Patrick Yard for the time dependent Hamiltonian simulation.

6.1 Non-Hermitian Hamiltonians in quantum mechanics

The standard formalism of quantum mechanics postulates the Hermiticity[1] of the Hamiltonian of an isolated quantum system. When such a Hamiltonian is used in the Schrödinger equation, it ensures a unitary time evolution of the system preserving the norm of the states as well as the scalar product between them. Furthermore, the eigenvalues of an Hermitian operator are real and therefore well suited to represent possible outcomes of an energy measurement. It is also easy to see that in the Hermitian formulation, if the Hamiltonian is

[1]Given the scalar product $(\cdot,\cdot)$ of the Hilbert space, the Hermiticity condition can be stated as $(H\phi,\psi) = (\phi,H\psi)$. However, the exact postulate of quantum mechanics states that the Hamiltonian is a self-adjoint operator: $H^\dagger = H$ and includes that H and $H^\dagger$ have the same domain. The adjoint operator $A = H^\dagger$ is defined by the relation that $(H\phi,\psi) = (\phi,A\psi)$ for each vector ψ in the domain of A and each vector ϕ in the domain of H. However, in the chapter we are mainly focusing on finite dimensional Hilbert spaces for which being Hermitian is the same as being self-adjoint.

not explicitly time dependent, the energy of a system is constant. Yet, in some circumstances, this formulation of quantum mechanics is unsatisfactory.

If we try to model a system quantum mechanically, notwithstanding that it is actually embedded in a larger environment that we are ignoring or, rather, that it is impossible for us to exactly deal with, we realise that the unitarity condition of the evolution appears flawed. We have seen how, under some approximations, this could be taken into account by additional terms in the Von Neumann equation for the density matrix evolution (see Sec. 2.1.5). In particular, when our description ignores the full extent of the Hilbert space of the system by overlooking scattering channels, a non-Hermitian Hamiltonian would allow us to formulate an effective dynamics in the subspace to which we want to restrict our observation. A recent review of this topic centred about mesoscopic systems can be found in [33] but this class of problems is ubiquitous in quantum physical problems including nuclear reactions, molecule spectra, particle decays and electronic scattering [153–157].

While the previous examples mainly refer to open systems, renouncing the Hermiticity property of the Hamiltonian has been necessary in more theoretical topics such as the description of particles with special dispersion relations, for instance tachyons or neutrinos, and investigation of a wider class of potential quantum field models that includes for example higher order derivative terms [158–160].

As we will see, in the absence of Hermiticity, the eigenvalues of the Hamiltonian can present a positive (or negative) imaginary part that produces an exponential increase (or decrease) of the norm of the corresponding eigenvector. Furthermore, the eigenvectors do not necessarily form an orthogonal basis of the Hilbert space; not only because they can be not orthogonal, but also because in some cases the set of eigenvectors of the Hamiltonian operator does not span the full Hilbert space. Parametrised non-Hermitian Hamiltonians can therefore present a so called exceptional point at which multiple eigenvectors coalesce, that is, they merge into the same vector. It is important that, depending on the specific non-Hermitian Hamiltonian, not all these features manifest. As showed by C. Bender and S. Boettche in 1998 [32], a family of non-Hermitian Hamiltonians, that present an elevated degree of symmetry, is characterised by the complete realness of their spectrum of eigenvalues. The symmetry, that will be discussed in details in the following section, is the invariance under a joint parity reflection $\mathcal{P}$ and time reversal $\mathcal{T}$ transformation ($\mathcal{PT}$ symmetry).

6.2 Parity-time symmetric Hamiltonians

Even though the interest towards extensions of quantum mechanics featuring a complex potential originated in the context of continuous variables [32], their experimental investigation as well as potential applications are often discussed in the context of finite dimensional

systems. With the intent of keeping the description simple and relevant for our experiments, in the following we will mostly be concerned with finite dimensional Hilbert spaces. We recall that the time reversal transformation $\mathcal{T}$ reverses the momentum of particles $\mathcal{T}|p\rangle = |-p\rangle$ and leaves unchanged the position eigenstates $\mathcal{T}|x\rangle = |x\rangle$ and is described by an anti-linear transformation in order to preserve the commutation relations[2]. Since $\mathcal{T}e^{i\phi}|x\rangle = e^{-i\phi}|x\rangle$, the previous definitions are valid only for particular choices of the position and momentum eigenvectors. Even though what we have outlined would suggest that $\mathcal{T}^2 = \mathbb{1}$, a second alternative is however possible when further degrees of freedom are present, for example we might have a spin-half particle and define $\mathcal{T}$ such that

$$\mathcal{T}|x\rangle|\uparrow\rangle = i|x\rangle|\downarrow\rangle \qquad \mathcal{T}|x\rangle|\downarrow\rangle = -i|x\rangle|\uparrow\rangle,$$

in this case $\mathcal{T}^2 = -\mathbb{1}$. It has been shown that $\mathcal{T}^2 = \pm\mathbb{1}$ are the only two possible alternatives with the minus sign characterising Fermionic systems [161].

$\mathcal{T}$ commutes with the parity reflection operator $\mathcal{P}$ whose action mirrors the spatial coordinate of the system $\mathcal{P}|p\rangle = |-p\rangle$ and $\mathcal{P}|x\rangle = |-x\rangle$ with $\mathcal{P}^2 = \mathbb{1}$.

A $\mathcal{PT}$-symmetric system is described by a Hamiltonian satisfying the relation

$$\mathcal{PT}\, H\, (\mathcal{PT})^{-1} = H.$$

Examples of $\mathcal{PT}$ systems can be $H = \hat{T} + V(x) + iW(x)$ constructed by adding a spatially symmetric real potential $V(x)$ and an antisymmetric imaginary potential $iW(x)$ to the kinetic contribution $\hat{T}$. Being the composition of a linear and an anti-linear transformation, $\mathcal{PT}$ is anti-linear and therefore it is not certain that there is a particular choice of the eigenvectors of H that are also eigenvectors of $\mathcal{PT}$ even when $[H, \mathcal{PT}] = 0$. However, when an eigenstate of the Hamiltonian is also eigenstate of $\mathcal{PT}$, we can infer that the eigenvalue of the energy associated with it is real, indeed

$$\begin{aligned} H\ \mathcal{PT}|\varepsilon\rangle &= H\lambda|\varepsilon\rangle = \lambda H|\varepsilon\rangle = \lambda\varepsilon|\varepsilon\rangle \\ \mathcal{PT}\, H|\varepsilon\rangle &= \mathcal{PT}\ \varepsilon|\varepsilon\rangle = \varepsilon^*\mathcal{PT}\ |\varepsilon\rangle = \varepsilon^*\lambda|\varepsilon\rangle \\ H\ \mathcal{PT}|\varepsilon\rangle &= \mathcal{PT}\, H|\varepsilon\rangle \Rightarrow \varepsilon = \varepsilon^* \end{aligned}$$

where we have assumed that $|\varepsilon\rangle$ is an eigenvector of H with eigenvalue ε and an eigenvector of $\mathcal{PT}$ with eigenvalue λ and, since $\mathcal{PT}$ is invertible, $\lambda \neq 0$. For parametrised $\mathcal{PT}$ systems, the region of the parameter space where the eigenvectors of the Hamiltonian are also $\mathcal{PT}$ symmetric is called the unbroken symmetry region and has attracted great interest because of its real spectrum of energy. Additionally, in the symmetry broken regions, where for some eigenstate of the energy $\mathcal{PT}|\varepsilon\rangle \neq \lambda|\varepsilon\rangle$, $\mathcal{PT}$ links "conjugate" pairs of eigenvectors:

$$H(\mathcal{PT}|\varepsilon\rangle) = \mathcal{PT}\, H|\varepsilon\rangle = \mathcal{PT}\ \varepsilon|\varepsilon\rangle = \varepsilon^*(\mathcal{PT}|\varepsilon\rangle) \implies \left|\varepsilon^*\right\rangle = (\mathcal{PT}|\varepsilon\rangle)$$

[2] A summary of the properties of $\mathcal{T}$ can be found in the "Symmetry in quantum mechanics" chapter of [161].

6.2.1 Pseudo-Hermiticity and state normalisation

An operator H possesses a complete biorthogonal eigenbasis system [162], if there is a set of states $\{|n,A\rangle_+\}$ and $\{|n,A\rangle_-\}$ such that:

$$\begin{aligned} H\,|n,a\rangle_+ &= \varepsilon_n\,|n,a\rangle_+ \\ H^\dagger\,|n,a\rangle_- &= \varepsilon_n^*\,|n,a\rangle_- \\ {}_-\langle m,b|n,a\rangle_+ &= \delta_{nm}\delta_{ab} \\ \sum_n\sum_a |n,a\rangle_+\,\langle n,a|_- &= \mathbb{1}. \end{aligned} \tag{6.1}$$

$|n,a\rangle_+$ are often known as right eigenvectors of H while $|n,a\rangle_-$ are called left eigenvectors of H. Possessing the spectral property typical of a $\mathcal{PT}$ system, either completely real spectrum or "paired conjugated" eigenvectors, together with two discrete and complete orthonormal bases of eigenvectors characterises what is called pseudo-hermiticity [162, 163]. This property, that is generally independent from the $\mathcal{PT}$ symmetry, defines an operator $\hat{O}$ as η-pseudo-Hermitian if there exists an automorphism[3] η such that $\hat{O}^\dagger = \eta\,\hat{O}\,\eta^{-1}$. Furthermore, if $\eta = AA^\dagger$, and is therefore Hermitian, the spectrum of $\hat{O}$ is completely real and A defines a second automorphism that transforms $\hat{O}$ into an Hermitian operator $\hat{o} = A^\dagger\hat{O}\left(A^\dagger\right)^{-1}$ preserving its spectrum. While in the presence of a pseudo-Hermitian Hamiltonian H, the indefinite[4] inner product $n(a,b) = \langle a|\left(\eta\,|b\rangle\right)$ is preserved through the evolution, when $\eta = AA^\dagger$ such an inner product is also positive definite and can be used to formulate a new probabilistic interpretation of the quantum model.

Due to their spectral properties, a large intersection exists between pseudo-Hermitian systems and $\mathcal{PT}$ symmetric systems. However, the two properties are not equivalent; for example, a $\mathcal{PT}$ system at the exceptional point lacks a complete eigenbasis and it is not pseudo-Hermitian [164]. The intersection between the two sets of Hamiltonians is interesting because one can construct a positive definite norm $n(a,b) = \langle a|\left(\mathcal{C}\mathcal{PT}\,|b\rangle\right)$ for $\mathcal{PT}$ systems in the unbroken regime. Note that the positive definite norm construction would map the $\mathcal{PT}$ Hamiltonian to a new Hermitian one without changing its spectrum so it is not possible whenever the spectrum of the Hamiltonian is not completely real. The operator $\mathcal{C}$, that commutes with $\mathcal{PT}$ and H, is introduced to ensure the positivity of the scalar product [165]. However, when this new metric is adopted, the physical results will be identical to what can be obtained with a Hermitian Hamiltonian system [166]. Accepting the new metric, a $\mathcal{PT}$ system in the unbroken symmetry regime is merely a way of looking at a normal system through a distortion glass, whose role is played by $A^\dagger$, that makes common observables such as x and p (in the Hermitian Hilbert space) appear as non Hermitian operators in the space where the Hamiltonian is $\mathcal{PT}$-symmetric. Because of this, we will focus on the alternative

[3] With automorphism we are referring to an invertible linear transformation from the Hilbert space in itself.

[4] An indefinite inner product $n(\cdot,\cdot)$ of a vector a with itself (n(a,a)) is not necessarily positive nor negative.

approach where the usual Dirac scalar product is used and the probability is defined in each cass by normalising the scalar product over the current Dirac norm of the state. However, we acknowledge that a significant part of the literature about $\mathcal{PT}$ Hamiltonians prefer to adopt the pseudo-Hermiticity based norm definition. Additionally, it has been pointed out that normalising the states over their Dirac norm can lead to conflicting results when multipartite systems are considered, for example the entanglement between two qubits could be increased by the action of a local $\mathcal{PT}$ Hamiltonian or superluminal communication could be achieved [167, 168]. These paradoxes arise because the state normalisation approach acts as a non local transformation of the state[167], and the dynamics of the $\mathcal{PT}$ Hamiltonian is effectively non-local even though all terms in the Schrödinger equation are local. Additionally, we like to point out that complications also arise when a single particle is involved in the normalisation process. Let's assume that a system is in the state $|a\rangle$ with probability p_a or in a state $|b\rangle$ with probability $p_b = 1 - p_a$. Evolving the two states independently using a non-Hermitian Hamiltonian into the Schrödinger equation will bring us to two possible states $|a(t)\rangle$ and $|b(t)\rangle$. Two different results are obtained whether the two states are normalised before constructing the density matrix (ρ_1) or if the mixed state is normalised over its trace (ρ_2):

$$\begin{aligned} \rho_1 &= p_a \frac{|a(t)\rangle\langle a(t)|}{\langle a(t)|a(t)\rangle} + p_b \frac{|b(t)\rangle\langle b(t)|}{\langle b(t)|b(t)\rangle}, \\ \rho_2 &= \frac{p_a |a(t)\rangle\langle a(t)| + p_b |b(t)\rangle\langle b(t)|}{p_a \langle a(t)|a(t)\rangle + p_b \langle b(t)|b(t)\rangle}. \end{aligned} \tag{6.2}$$

Both density matrices have a unit trace but they are not equivalent. In agreement with literature, in the following we will use the second definition, that is equivalent to evolving the density matrices with the Von Neumann equation assuming the non Hermitian Hamiltonian, and then normalising the state by dividing it by its trace. However, we note that, similarly to what is presented in [156], it is possible to write a non-linear Von Neumann equation that would describe the evolution of the two alternative density matrix evolution rules:

$$\begin{aligned} \frac{\mathrm{d}\rho_1}{\mathrm{d}t} &= -i\left(H\rho_1 - \rho_1 H^\dagger\right) + i\sqrt{\rho_1}\left(H - H^\dagger\right)\sqrt{\rho_1}, \\ \frac{\mathrm{d}\rho_2}{\mathrm{d}t} &= -i\left(H\rho_2 - \rho_2 H^\dagger\right) + i\,\mathrm{tr}\left[H\rho_2 - \rho_2 H^\dagger\right]\rho_2. \end{aligned} \tag{6.3}$$

6.2.2 Applications of PT-symmetric systems

The theory of classical $\mathcal{PT}$ systems, generally featuring spatially symmetric gain and loss regions, has been successfully tested in multiple fields and has already found several applications. Photonic ones include unidirectionality of integrated optical components, advanced mode selection in laser cavities, possibility for energy efficient all-optical modulation based on coherent perfect absorbers, and chiral lasers [169]. The interplay between $\mathcal{PT}$ photonics and phononics has also led to designs for improved phonon lasers [170]. Recently, an example

of an application of anti-parity-time symmetry[5] has also been explored in a heat conduction experiment leading to a phase transition between diffusive and stationary conditions [171].

The attempt to discover the peculiar properties of quantum mechanical $\mathcal{PT}$ systems is more recent but the investigation of $\mathcal{PT}$ symmetric systems in the realm of correlated many-body systems has already predicted new universality classes [172]. Also, foundational theorists suggest that $\mathcal{PT}$ theories could be compatible with other alternative, although exotic, formulations of quantum mechanics [160, 173]. It has been shown that $\mathcal{PT}$ symmetric systems may result in a lower sensitivity to external sources of decoherence [174], suggesting their possible use in quantum technology. Also, $\mathcal{PT}$ Hamiltonians are supposed to make transformations between two orthogonal states more time-energy efficient [175]. Interest towards the application of $\mathcal{PT}$ systems in quantum information processing is further motivated by a natural tendency of their Hamiltonian to direct the state towards a particular non trivial final state [176]. A protocol that uses such a feature for preparing multiple relevant quantum states (W[6], GHZ[7], Bell pair) in a XY transverse Ising spin chain has been proposed [177]. At the same time, the non-unitary evolution of the state, in the unbroken $\mathcal{PT}$ symmetric phase, generates a periodic revival of the quantum information stored in a state [178].

A further side application is described in [179], where the exceptional point of a superconducting system is used to optimise heat transfer from a quantum device.

6.3 Simulation of PT-symmetric systems

In the last few years, researchers have been able to reproduce physical systems whose effective evolution maps onto a $\mathcal{PT}$ Hamiltonian. While photonics led the progress of classical technology harnessing $\mathcal{PT}$ dynamics [169], its potential role in the quantum $\mathcal{PT}$-technology scenario contrasts with the predictions that emphasised the effects of induced noise obtained in a linear optical system with gain and loss[180]. Nonetheless, the simulation of $\mathcal{PT}$ systems has been performed in optics as well as in other platforms such as spin system, superconducting qubit, nuclear magnetic resonance, cold atoms. The methodologies used can be sorted into two main categories: the first consists in realising an Hamiltonian that, upon post-selection, returns the same evolution of the observable quantities as for the $\mathcal{PT}$ Hamiltonian; the other one is to compute the desired non-unitary transformation and dilate this transformation in a larger Hilbert space.

The Hamiltonian approach itself can be separated into two methods: passive $\mathcal{PT}$ systems and Hamiltonian dilation, often correlated to the intention of expressing the norm of the

[5] For anti-parity-time symmetric Hamiltonians $\mathcal{PT}H\mathcal{PT} = -H$.

[6] An example of W state is $|W\rangle = 0.5(|1,0,0,0\rangle + |0,1,0,0\rangle + |0,0,1,0\rangle + |0,0,0,1\rangle)$.

[7] An example of GHZ (Greenberger–Horne–Zeilinger) state is $|GHZ\rangle = \frac{1}{\sqrt{2}}(|0,0,0\rangle + |1,1,1\rangle)$.

state respectively with the Dirac norm or the $\mathcal{CPT}$ norm. A passive $\mathcal{PT}$ approach is based on the equivalence, after normalisation, of the evolution produced by a $\mathcal{PT}$ Hamiltonian and by a non-$\mathcal{PT}$ one that features only mode selective losses (elements with negative imaginary parts on the diagonal of the Hamiltonian) [181–184]. In formula

$$H_{\mathcal{PT}} = i\gamma\mathbb{1} + H_0 - iD \implies e^{-iHt} = e^{\gamma t}e^{-i(H_0-iD)t},$$

where $H_{\mathcal{PT}}$ is the $\mathcal{PT}$ Hamiltonian, H_0 is Hermitian, and D represents a real non-negative valued diagonal matrix. The factor $e^{\gamma t}$ can be treated as a scaling factor of the state norm while $e^{-i(H_0-iD)t}$ is implemented by adding losses, or decaying into external channels, through the evolution of a Hermitian system. Hamiltonian dilation, instead, is usually based on the Naimark dilation [185]. This is, however, feasible only when the eigenvalues of $H_{\mathcal{PT}}$ are real. The dilation returns a Hamiltonian defined on the product of the original system Hilbert space and an additional qubit. Upon a specific initialisation and post-selection of the state of the qubit, the desired effective dynamic is reproduced and preserves the $\mathcal{CPT}$ norm. A more general version, that has been introduced to be able to demonstrate the phase-transition of a $\mathcal{PT}$ system, covering both unbroken and broken symmetry regimes, has been tested on a spin system [186]. This extension, however, requires the introduction of a time dependent dilated Hamiltonian.

Unitary dilation methods can naturally be applied to both unbroken and broken symmetry regimes, and to more general non-unitary evolutions, too. Particular cases of unitary dilation are reported in [187] where additional optical modes, treated as an environment qubit, are used to experimentally address the effect of local $\mathcal{PT}$ evolution on entangled qubits encoded in two photons. Unitary dilation and Hamiltonian dilation are both used in [188] while a digital version of unitary dilation, based on ancillary qubits, is reported in [189].

6.3.1 The simulation model we adopted

The simulation model we adopt to reproduce $\mathcal{PT}$ symmetric quantum dynamics is based on the Halmos dilation (see Sec. 2.1.6). Although the simulation procedure we are going to describe can be applied to a generic non-Hermitian Hamiltonian, we will only consider the family of Hamiltonians $H_N(\gamma)$ defined on N modes of the form:

$$H_N(\gamma) = -J\sum_{k=1}^{N-1}\left(|k\rangle\langle k+1| + |k+1\rangle\langle k|\right) + i\gamma\left(|1\rangle\langle 1| - |N\rangle\langle N|\right) \tag{6.4}$$

and we further set the energy scale of the system fixing $J = 1$. Doing so, apart from the system size N, the only free parameter left is the degree of Hermiticity violation γ. $H_N(\gamma)$ describes a linear chain of localised modes with nearest neighbour coupling and symmetric gain ($k = 1$) and loss ($k = N$) sites at the two ends. Moreover, we consider $\mathcal{P} = \sum_{k=1}^{N}|k\rangle\langle N+1-k|$ and $\mathcal{T}$ is

such that $\mathcal{T}\,\alpha\,|k\rangle = \alpha^*\,|k\rangle$ and $\mathcal{T}^2 = \mathbb{1}$. Based on these definitions, it is easy to see that $H_N(\gamma)$ is $\mathcal{PT}$-symmetric:

$$\mathcal{T}\,H_N(\gamma)\,\mathcal{T}^{-1} = \mathcal{P}\,H_N(\gamma)\,\mathcal{P} = H_N(-\gamma) = H_N(\gamma)^\dagger \tag{6.5}$$

$$\mathcal{PT}\,H_N(\gamma)\,(\mathcal{PT})^{-1} = H_N(\gamma). \tag{6.6}$$

Also, $H_N(\gamma)$ becomes Hermitian when $\gamma = 0$. When N is even, the system presents an exceptional point $\gamma_c = \pm 1$, conversely these critical values shift to $\gamma_c = \pm\sqrt{\frac{N+1}{N-1}}$ when N is odd and $N \geq 3$. The unbroken symmetry region corresponds to $|\gamma| < \gamma_c$ while the $\mathcal{PT}$ symmetry is broken for $|\gamma| > \gamma_c$. A detailed analysis of this Hamiltonian is available in [190].

We will indicate as $G_N(\gamma,t) = \exp\left[-iH_N(\gamma)t\right]$ the non-unitary time evolution operator obtained from $H_N(\gamma)$. To be able to reproduce the non-unitary time evolution on our optical circuit and apply the Halmos dilation, we rescale $G_N(\gamma,t)$. For each evolution time t, we divide $G_N(\gamma,t)$ by its operator norm $\|G_N(\gamma,t)\|$ as a function of time, that is, by its largest singular value. In doing so we obtain the contraction

$$\tilde{G}_N(\gamma,t) = \frac{G_N(\gamma,t)}{\|G_N(\gamma,t)\|}. \tag{6.7}$$

Then, using $\tilde{G}_N(\gamma,t)$ we construct the following dilation $U_{2N}(\gamma,t)$ in a $2N$-dimensional Hilbert space:

$$U_{2N}(\gamma,t) = \begin{bmatrix} \tilde{G}_N(\gamma,t) & iD_N(\gamma,t) \\ iD_N^*(\gamma,t) & \tilde{G}_N^\dagger(\gamma,t) \end{bmatrix} \tag{6.8}$$

where the off-diagonal matrix is given by

$$D_N(\gamma,t) = \sqrt{\mathbb{1} - \tilde{G}_N(\gamma,t)\tilde{G}_N^\dagger(\gamma,t)}. \tag{6.9}$$

The simulation than proceeds by configuring the integrated interferometer to implement $U_{2N}(\gamma,t)$ for a sequence of time steps while injecting single photons into the device. In such a model, using $U_{2N}(\gamma,t)$ as transfer matrix for the linear optical system, a single photon injected in the first N input modes of the system is transformed by $\tilde{G}_N(\gamma,t)$ every time this leaves the system from the first N output modes. In particular, every probability estimation normalised over the state norm, is unaffected by the scaling factor $\|G_N(\gamma,t)\|$:

$$\frac{\left|\langle m|G_N(\gamma,t)|\psi\rangle\right|^2}{\langle\psi|G_N^\dagger(\gamma,t)G_N(\gamma,t)|\psi\rangle} = \frac{\|G_N(\gamma,t)\|^2\left|\langle m|\tilde{G}_N(\gamma,t)|\psi\rangle\right|^2}{\|G_N(\gamma,t)\|^2\langle\psi|\tilde{G}_N^\dagger(\gamma,t)\tilde{G}_N(\gamma,t)|\psi\rangle} \tag{6.10}$$

for any state $|m\rangle$ onto which we are projecting as result of a measurement. It is important to note that among the alternative unitary dilations of $\tilde{G}_N(\gamma,t)$, $U_{2N}(\gamma,t)$ has the advantage of including the time reverse evolution of $\tilde{G}_N(\gamma,t)$ since

$$\mathcal{T}\,\tilde{G}_N(\gamma,t)\,\mathcal{T}^{-1} = \mathcal{T}\sum_k \frac{\left(-iH(\gamma)t\right)^k}{k!}\,\mathcal{T}^{-1} = \sum_k \frac{\left(iH^\dagger(\gamma)t\right)^k}{k!} = \tilde{G}_N^\dagger(\gamma,t). \tag{6.11}$$

Thus, the extended Hilbert space where the dilation is defined can be understood as composed by a forward and a backward in time (reversed) evolving subspaces that will be mapped, respectively, on the first and last N modes of our interferometer. However, $D_N(\gamma,t)$ couples the modes of the two subspaces. The non-Hermitian behaviour of the $\mathcal{PT}$ symmetric system is the result of observations restricted to the forward subspace while no information about the system is retrieved when it transforms into the reverse modes. However, our model also imposes that if the system is observed only in the reverse subspace, it would follow the same evolution laws upon time reversal transformation.

In the following section we will go into the details of the individual experiments characterised by multiple initial states with distinctive properties and performed in the different regions of the parameter space. In addition to the model described, we will also consider a mapping from the state of our simulator to the tensor product of two bosonic Hilbert spaces associated to the modes of the integrated interferometer that map into the forward and reverse subspaces. In this case, the role of $D_N(\gamma,t)$ is to transfer excitations between the two systems whose occupancy number can therefore change. In the text, when it is necessary to distinguish between the states $|k\rangle$ of our simulated model and the photonic Fock state of our optical simulator, we will use the subscript p for the latter. For example, for $N=3$, Fock states $\{|1_p0_p0_p\rangle, |0_p1_p0_p\rangle, |0_p0_p1_p\rangle\}$, respectively, encode the states $\{|1\rangle, |2\rangle, |3\rangle\}$ and we call $|\text{vac}\rangle$ the states like $|0_p0_p0_p\rangle$ with no photons in any of the modes of the subsystem. Furthermore, subscripts F or R will differentiate between the forward and reverse subsystems, or equivalently, between the first or last N modes of our interferometer used to encode the corresponding subspace.

6.4 Simulation results

Given the number of optical modes that we can control with our chip (see Chapter 3), we performed simulations with 4- and 6- dimensional unitaries ($N=2$ or $N=3$). In particular, the smaller dimension was necessary when we wanted to perform projective measurements on the evolved states using physically separate elements of the chip from those used to simulate the state evolution. In all the experiments, the counts coming from the detectors have been corrected to take into account the detector efficiency and a single photon pair source has been used. Single photon data refer to coincidental detection of the heralding photon and a photon detected at one of the 4 or 6 output modes of the chip involved in the simulation. In the appendix (App. B), we report the closed form of $G_N(\gamma,t)$ for these 2 low dimensional cases.

6.4.1 Unbroken and broken symmetry regimes

The advantage of a unitary dilation method is the ability to simulate the evolution in the unbroken symmetry regime as well as in the broken symmetry regime, including the particular evolution at the exceptional point. In the first set of measurements, we fix $N = 2$ and inject a single photon in our simulator to encode the state $|1\rangle_F$. Looking at the evolution of the probability of detecting the excitation in the modes of the forward system, see Fig. 6.1, it is possible to observe the oscillation of the probability of detecting $|\text{vac}\rangle_F$ meaning that the photon leaked in the reverse subsystem; data are shown for two values in the unbroken symmetry regime ($\gamma = 1/4$, $\gamma = 1/\sqrt{2}$). Following the solid lines, representing the theory curves, a discontinuity of the derivative of the probability is visible. It is also possible to observe how the evolution is periodic and the period $T = 2\pi/\sqrt{1-\gamma^2}$ increases as γ approaches the exceptional point.

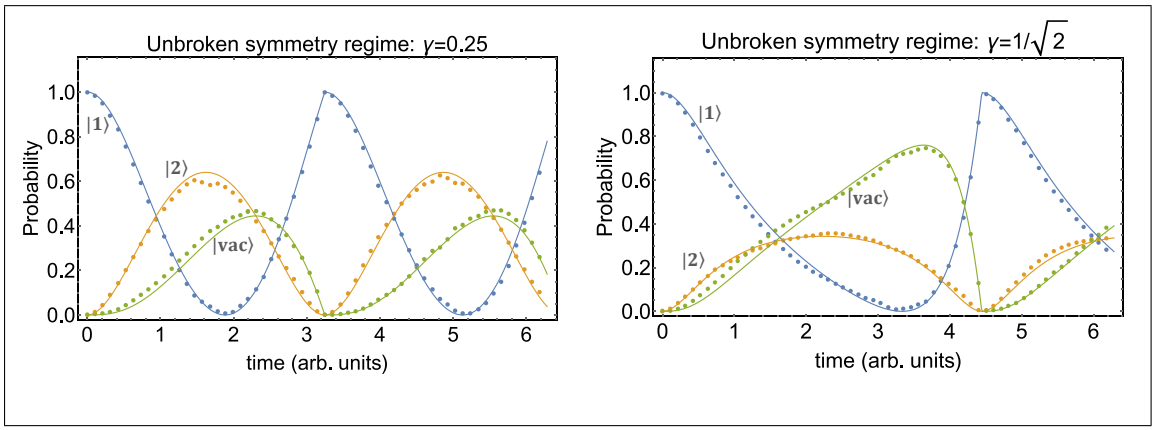

Figure 6.1: Probability evolution of an excitation in the forward subsystem Probability of detecting an excitation initialised in the mode $|1\rangle$ and evolving according to $U_4(\gamma, t)$. Experimental points refer to the probability of detecting different states of the forward subsystem ($|1\rangle$: blue, $|2\rangle$ yellow, $|\text{vac}\rangle$ green) for $\gamma = 0.25$ and $\gamma = 1/\sqrt{2}$. Solid lines represent theory curves.

From the time evolution of $U_4(\gamma, t)$, it is formally possible to derive a time dependent Hamiltonian

$$H_{\text{eff}}(t) = i\left(\frac{\partial U_4(\gamma,t)}{\partial t}\right)U_4^{-1}(\gamma,t),$$

that would generate such evolution. However, the singularity in the derivative of $U_4(\gamma, t)$ implies a singularity in $H_{\text{eff}}(t)$. The evolution becomes differentiable once we restrict to those events when the excitation is detected in the forward system reproducing the exact dynamics due to $H_2(\gamma)$. In Fig. 6.2 we report the results of such evolution in the Hermitian regime ($\gamma = 0$), characterised by a sinusoidal oscillation between the two modes of the system; in the non-Hermitian $\mathcal{PT}$-symmetric phase ($\gamma = 1/\sqrt{2}$) characterised by non-sinusoidal periodic behaviour; at the exceptional point ($\gamma = \gamma_c = 1$) at which the system loses its periodicity and

in the symmetry broken regime ($\gamma = 1.1$) where the evolution of the state is dominated by the exponential behaviour.

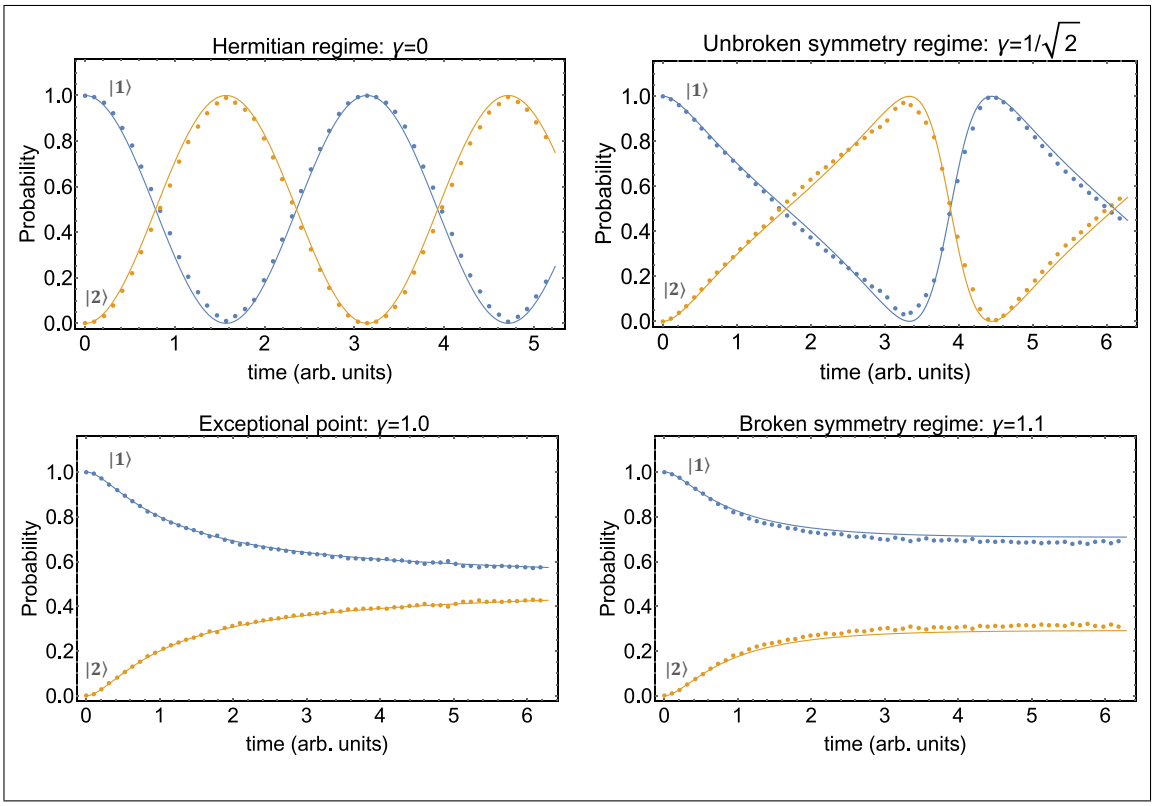

Figure 6.2: Evolution of a $\mathcal{PT}$ system in multiple regions of the parameter space Probability of detecting a 2-level $\mathcal{PT}$ system initialised as $|1\rangle$ and evolving according to $H_2(\gamma)$. Experimental points refer to the probability of detecting the particle in the mode associated to the forward subspace ($|1\rangle$: blue, $|2\rangle$ yellow) for different values of γ. Probabilities are normalised to a unit probability of detecting the photon in the forward subspace. Solid lines represent theory curves.

We further explore 3-dimensional systems using all the six modes of the chip. We prepared the system in three input states across two input modes of the forward ($\left|\psi_1(t=0)\right\rangle_{\mathrm{F}}$ and $\left|\psi_2(t=0)\right\rangle_{\mathrm{F}}$) or reverse ($\left|\psi_3(t=0)\right\rangle_{\mathrm{R}}$) subspace. The states we chose are related by symmetry transformations.

$$\left|\psi_1(t=0)\right\rangle_{\mathrm{F}} = \frac{|1\rangle_{\mathrm{F}} - i\,|2\rangle_{\mathrm{F}}}{\sqrt{2}} = \frac{\left|1_p 0_p 0_p\right\rangle_{\mathrm{F}} - i\left|0_p 1_p 0_p\right\rangle_{\mathrm{F}}}{\sqrt{2}} \otimes \left|0_p 0_p 0_p\right\rangle_{\mathrm{R}} \tag{6.12}$$

represents a state coherently superposed across gain ($k = 1$) and neutral ($k = 2$) site of the forward system;

$$\begin{aligned}\left|\psi_2(t=0)\right\rangle_{\mathrm{F}} &= \frac{i\,|2\rangle_{\mathrm{F}} + |3\rangle_{\mathrm{F}}}{\sqrt{2}} = \frac{i\left|0_p 1_p 0_p\right\rangle_{\mathrm{F}} + \left|0_p 0_p 1_p\right\rangle_{\mathrm{F}}}{\sqrt{2}} \otimes \left|0_p 0_p 0_p\right\rangle_{\mathrm{R}} \\ &= \mathcal{PT}\left|\psi_1(t=0)\right\rangle_{\mathrm{F}}\end{aligned} \tag{6.13}$$

is the result of a $\mathcal{PT}$ transformation of $\left|\psi_1(t=0)\right\rangle_{\mathrm{F}}$ and therefore extends over the loss site ($k=3$);

$$\begin{aligned}\left|\psi_3(t=0)\right\rangle_{\mathrm{R}} &= \frac{|1\rangle_{\mathrm{R}} + i\,|2\rangle_{\mathrm{R}}}{\sqrt{2}} = \left|0_p 0_p 0_p\right\rangle_{\mathrm{F}} \otimes \frac{\left|1_p 0_p 0_p\right\rangle_{\mathrm{R}} + i\left|0_p 1_p 0_p\right\rangle_{\mathrm{R}}}{\sqrt{2}} \\ &= \mathcal{T}\left|\psi_1(t=0)\right\rangle_{\mathrm{R}}\end{aligned} \tag{6.14}$$

is prepared in the reverse subspace and is analogous to the state $\mathcal{T}\left|\psi_1(t=0)\right\rangle_{\mathrm{F}}$ except for the subspace it is prepared in.

In figure Fig. 6.3 we report the evolution of the above-mentioned states in a time interval encompassing both negative and positive time. The symmetry relations in the initial states translate to a symmetric state evolution because the Hamiltonian preserves such symmetries. We can observe that

$$\begin{aligned}\left\langle k\middle|\psi_2(t)\right\rangle &= \langle k|G_3(\gamma,t)\left|\psi_2(0)\right\rangle = \langle k|\mathcal{PT}G_3(\gamma,-t)\mathcal{PT}\left|\psi_2(0)\right\rangle = \langle 4-k|\mathcal{T}G_3(\gamma,-t)\left|\psi_1(0)\right\rangle \\ &= \langle 4-k|\mathcal{T}\left|\psi_1(-t)\right\rangle = \left\langle 4-k\middle|\psi_1(-t)\right\rangle^*\end{aligned} \tag{6.15}$$

and since $H_{\mathrm{N}}(\gamma) = H_{\mathrm{N}}^{\mathrm{T}}(\gamma)$ we also have

$$\begin{aligned}\left\langle k\middle|\psi_3(t)\right\rangle_{\mathrm{R}} &= \langle k|G_3(\gamma,t)^\dagger\left|\psi_3(0)\right\rangle = \langle k|\mathcal{T}G_3(\gamma,t)\mathcal{T}\left|\psi_3(0)\right\rangle = \langle k|\mathcal{T}G_3(\gamma,t)\left|\psi_1(0)\right\rangle \\ &= \langle k|\mathcal{T}\left|\psi_1(t)\right\rangle = \left\langle k\middle|\psi_1(t)\right\rangle^*.\end{aligned} \tag{6.16}$$

The symmetry in the evolution manifests in the unbroken symmetry regime ($\gamma = 0.5\gamma_{\mathrm{c}} = \sqrt{2}/2$) as well as in the broken symmetry regime ($\gamma = 1.1\gamma_{\mathrm{c}} = 1.1\sqrt{2}$). By mirroring the evolution of $\left|\psi_2\right\rangle$ represented by filled dots with respect to the time=0 axes, it is possible to see how the green curves of ψ_2 behave as the blue ones of ψ_1 and ψ_3 that is exchanging $k=1$ with $k=3$. The same happens swapping blue with green.

We specify that the state preparation, that converts input Fock states in the desired states, is necessarily compiled together with $U_6(\gamma,t)$ before being dialled on the chip because a generic 6 modes unitary requires all the physical degrees of freedom of our device. The data refer to the detection events when the excitation is found in the same subspace it was initialised in.

To conclude the description of the symmetry properties of our model, we show the effect of the evolution for two-photon states. Again, we initialised the system in two symmetric states:

$$\begin{aligned}|\Omega_1\rangle &= \left|1_p 1_p 0_p\right\rangle_{\mathrm{F}} \otimes \left|0_p 0_p 0_p\right\rangle_{\mathrm{R}} \\ |\Omega_2\rangle &= \mathcal{PT}|\Omega_1\rangle = \left|0_p 1_p 1_p\right\rangle_{\mathrm{F}} \otimes \left|0_p 0_p 0_p\right\rangle_{\mathrm{R}}\end{aligned} \tag{6.17}$$

and simulate the system for negative and positive evolution time scanning γ across the different regimes. This time we report the probability of detecting unbunched two-photon states normalised over the 15 possible two-fold detection patterns over 6 modes.

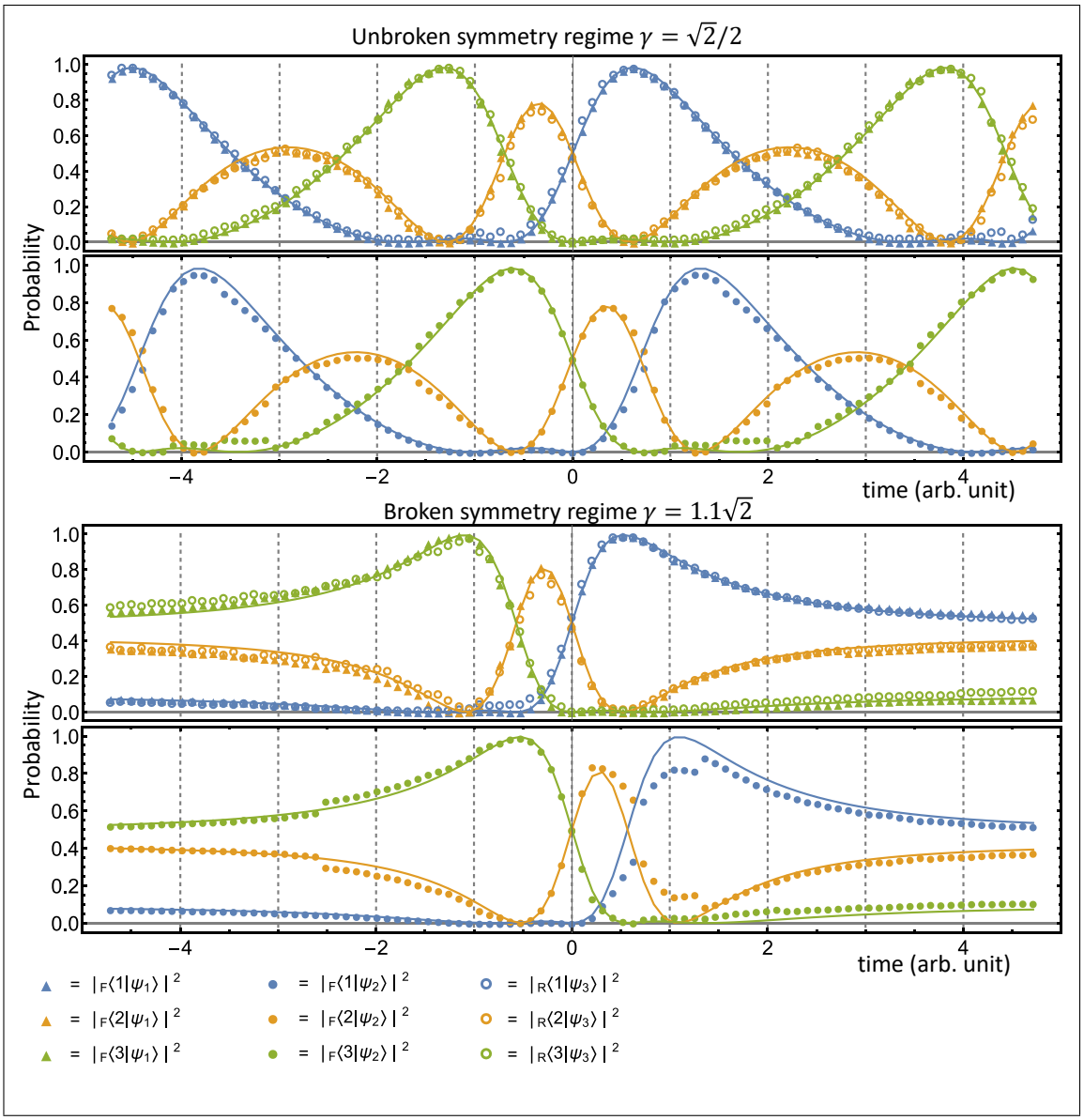

Figure 6.3: Evolution of a 3-dimensional $\mathcal{PT}$ system initialised in three symmetric input states Data points, marked according to the legend in the bottom of the picture, refer to the evolution of the 3 input states $|\psi_1(t=0)\rangle_F = (|1\rangle_F - i|2\rangle_F)/\sqrt{2}$; $|\psi_2(t=0)\rangle_F = (i|2\rangle_F + |3\rangle_F)/\sqrt{2}$; $|\psi_3(t=0)\rangle_R = (|1\rangle_R + i|2\rangle_R)/\sqrt{2}$ The probability of observing the states in the same subspace (F/R) they are prepared in is normalised to unity. Data, superposed to solid theory lines, show how $|\langle k|\psi_1(t)\rangle|^2 = |\langle 4-k|\psi_2(-t)\rangle|^2 = |\langle k|\psi_3(t)\rangle|^2$ in agreement with the evolution described by $H_3(\gamma)$.

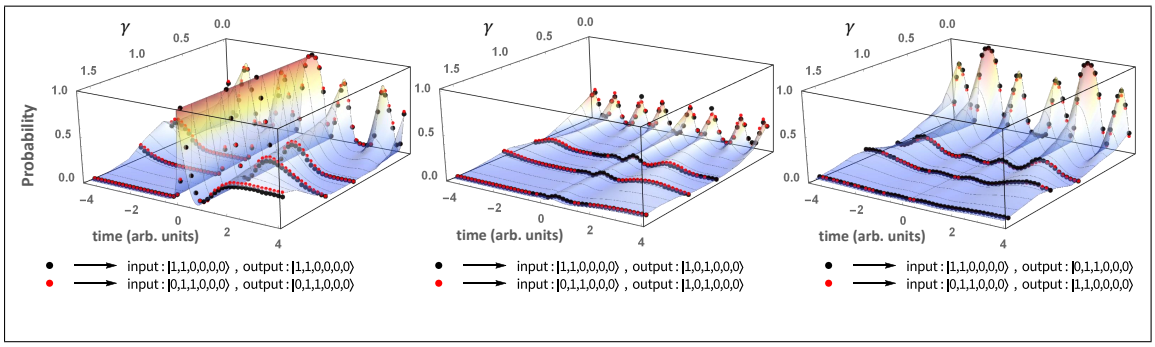

Figure 6.4: Transition probability between two-photon states Data representing the evolution of the input states $|\Omega_1\rangle = \left|1_p 1_p 0_p\right\rangle_{\mathrm{F}} \otimes \left|0_p 0_p 0_p\right\rangle_{\mathrm{R}}$ and $|\Omega_2\rangle = \left|0_p 1_p 1_p\right\rangle_{\mathrm{F}} \otimes \left|0_p 0_p 0_p\right\rangle_{\mathrm{R}}$. The plots show the probability of detecting the output patterns $\left|1_p 1_p 0_p\right\rangle_{\mathrm{F}} \otimes \left|0_p 0_p 0_p\right\rangle_{\mathrm{R}}$, $\left|1_p 0_p 1_p\right\rangle_{\mathrm{F}} \otimes \left|0_p 0_p 0_p\right\rangle_{\mathrm{R}}$, and $\left|0_p 1_p 1_p\right\rangle_{\mathrm{F}} \otimes \left|0_p 0_p 0_p\right\rangle_{\mathrm{R}}$, with dots corresponding to experimental data. Data collected for the state $|\Omega_2\rangle$ (in red) have been plotted in the reverse temporal direction. Data related to $|\Omega_2\rangle$ follow the same evolution as for $|\Omega_1\rangle$, provided that the output patterns $\left|1_p 1_p 0_p\right\rangle_{\mathrm{F}}$ and $\left|0_p 1_p 1_p\right\rangle_{\mathrm{F}}$ are exchanged. The probability of the 15 un-bunched two-photon output patters over 6 modes are normalised to unit.

Fig. 6.4 shows the data for the probability of finding the patterns $\left|1_p 1_p 0_p\right\rangle_{\mathrm{F}}$, $\left|1_p 0_p 1_p\right\rangle_{\mathrm{F}}$ and $\left|0_p 1_p 1_p\right\rangle_{\mathrm{F}}$ for the two input states and for values of γ in the Hermitian, unbroken and broken symmetry regimes ($\gamma \in \{0,\ \sqrt{2}/5,\ 3\sqrt{2}/4,\ 1.1\sqrt{2}\}$). We note that, due to the $\mathcal{PT}$ symmetry between these input states, we expect their evolution to proceed in opposite directions in time and to present an exchange of probabilities between the observation of the patterns $\left|1_p 1_p 0_p 0_p 0_p 0_p\right\rangle$ and $\left|0_p 1_p 1_p 0_p 0_p 0_p\right\rangle$. To ease the comparison with the input state $|\Omega_1\rangle$, data collected for the input state $|\Omega_2\rangle$ have been plotted in the reverse temporal direction. By increasing the value of γ, the system undergoes the transition from the unbroken to the broken symmetry phase, as for the single excitation case. Thus the unitary dilation method also allows for observation of $\mathcal{PT}$ symmetric evolution in the context of multi-particle dynamics.

6.4.2 Time dependent Hamiltonian evolution

In this section, we wanted to experimentally recreate the evolution of a state due to a time dependent $\mathcal{PT}$ Hamiltonian. We effected this experiment with an iterative approach that required us to reconstruct the state of the system at time t_i and then use it as input for the simulation that reproduces the state at time $t_{i+1} = t_i + \delta t$. The focus is on a single qubit constrained in the forward subspace so that the simulation maps to the dynamics described by $H_2(\gamma(t))$. However, to estimate the change in norm of the pure states composing the mixed input state, according to the second line of equation Eq. 6.2, the coincidences with the heralding photon are recorded at each output mode of the simulator.

Additionally, we chose to dynamically define our time varying Hamiltonian based on

the evaluation of a cost function implementing, de facto, an optimisation procedure on the evolution of the system. Since $\mathcal{PT}$ Hamiltonians could be used as resource generation in quantum information protocols, we looked for a potential resource metric for a single qubit and we set the cost function to be a coherence witness [191]. We were interested in the coherence of the state in the orthonormal basis $B = \{|+\rangle, |-\rangle\} = \{\frac{|1\rangle+|2\rangle}{\sqrt{2}}, \frac{|1\rangle-|2\rangle}{\sqrt{2}}\}$ comprised of the eigenvectors of $H_2(\gamma = 0) = -\sigma_x$, that is the Hermitian Hamiltonian in the absence of a $\mathcal{PT}$-symmetric potential. With respect to this basis, a *maximally coherent state* is a balanced superposition of the two states in B therefore we set the state

$$|+i\rangle \equiv \frac{e^{i\frac{\pi}{2}}|+\rangle + e^{-i\frac{\pi}{2}}|-\rangle}{\sqrt{2}} = \frac{|1\rangle + i|2\rangle}{\sqrt{2}}$$

to be our target state[8]. Thus we aimed to evolve the state using a time dependent $\mathcal{PT}$ potential to increase the cost function

$$C[\rho] = \frac{\langle +i|\rho|+i\rangle}{\mathrm{tr}[\rho]}. \tag{6.18}$$

To prove the capability of the $\mathcal{PT}$ system, we simulated the evolution as occurring in a noisy channel affected by dephasing. This translates to the following evolution equation

$$\frac{\partial\rho}{\partial t} = -i\left(H(\gamma(t))\rho - \rho H^{\dagger}(\gamma(t))\right) + 0.5p(\sigma_x\rho\sigma_x - \rho) \tag{6.19}$$

where p is the dephasing rate of the system, and $\gamma(t)$ is the time varying $\mathcal{PT}$ potential.

In the experiment, $\gamma(t)$ was calculated before each interval in which the evolution was segmented. The protocol started with $\gamma(t_0) = 0$ and a qubit $\rho(t_0)$ encoded in the forward system. To choose γ, at the beginning of each interval, we compared several potential values $\gamma_p(t_i)$. For each of these, we set our chip to implement $U_4(\gamma_p(t_i), \delta t)$ and we used it to transform ρ_{i-1}. This state was then projected on $|i\rangle$ to estimate $C[\rho]$. In order not to allow rapid changes of the time dependent $\mathcal{PT}$ potential, we chose $\gamma_p(t_i)$ such that $\left|\gamma_p(t_i) - \gamma(t_{i-1})\right| \leq 0.25$ and we further restricted $\gamma_p(t_i)$ to be an element of the discrete set $\{0.025\ k\}_{k=0}^{k=40}$ therefore avoiding the broken symmetry regime beyond the exceptional point. The value for $\gamma(t_i)$ was chosen as the $\gamma_p(t_i)$ among those allowed that maximised $C[\rho]$. Knowing $\gamma(t_i)$, we evolved ρ_{i-1} with $U_4(\gamma(t_i), \delta t)$ and performed a state tomography on ρ_i measuring the expectation values of the three Pauli operators.

Dealing with mixed states, the state preparation consisted in numerically decomposing ρ_{i-1} as the mixture of its two eigenstates ($\rho_{i-1} = w_1\rho_1 + w_2\rho_2$) that were then prepared as input states. The results from the evolution of ρ_1 and ρ_2 were weighted by their original weights in the mixture (w_1 and w_2) multiplied by the norm of the pure states once evolved. The norm estimation was based on the ratio between the counts detected in the forward

[8] Note that $|+i\rangle$ is also the only right eigenvector at the exceptional point.

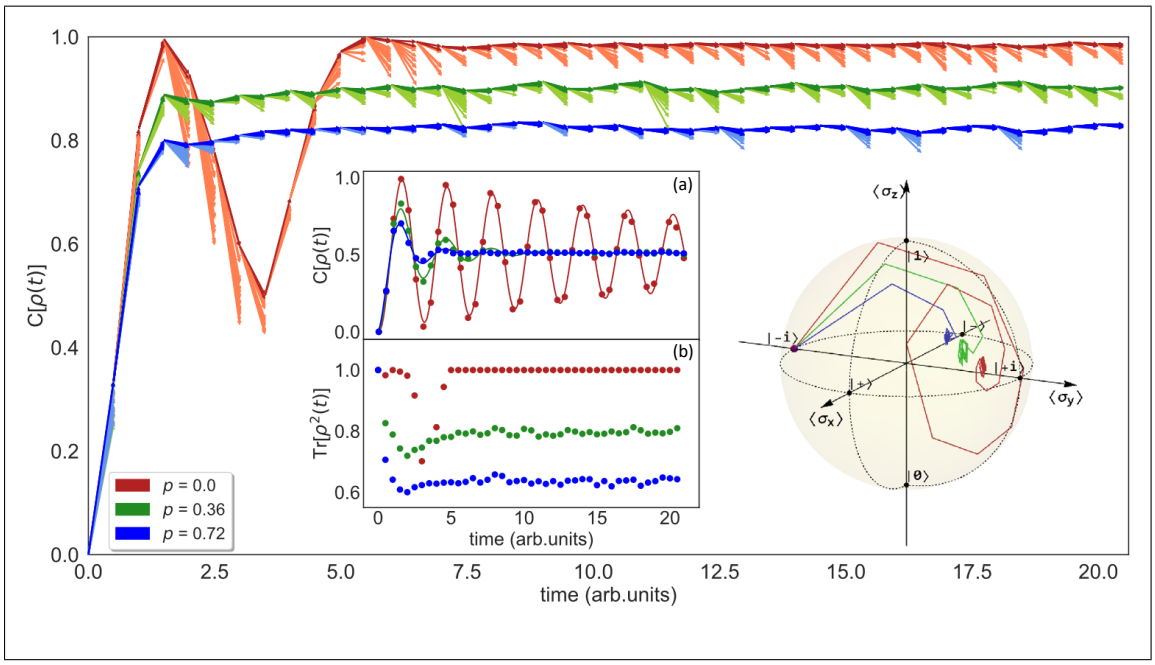

Figure 6.5: Time dependent $\mathcal{PT}$ Hamiltonian evolution in a dephasing channel. Evolution of the cost function defined in Eq. 6.18 obtained with a time dependent $\mathcal{PT}$ Hamiltonian resulting from a feedback optimisation algorithm. The data refer to the input state $|-i\rangle$ and different values of dephasing rate, p. Arrows indicate the cost function for each of the γ_p values tested at each time step, with the colour of the arrows corresponding to the magnitude of γ_p. Inset (a) shows the evolution without the optimisation protocol, subject to the same nominal dephasing. Experimental data are represented by dots, the solid line is a numerical fit to the data to extract the effective dephase rate. Inset (b) shows the purity of the states. On the right, the evolution of the states on the Bloch sphere is also shown.

and in the reverse subspaces. The reconstructed density matrix obtained from the weighted combination of $\rho_1(t_i)$ and $\rho_2(t_i)$ was then classically modified by applying the transformation

$$\rho \rightarrow \rho + 0.5p(\sigma_x \rho \sigma_x - \rho)\delta t. \tag{6.20}$$

to account for the effect of the dephasing channel. The result of this transformation became the input for the next iteration step.

Fig. 6.5 shows the results of the evolution of the input state $|-i\rangle = (|1\rangle - i\,|2\rangle)/\sqrt{2}$ for three nominal values of $p \in \{0, 0.36, 0.72\}$ and $\delta t = 0.5$. For comparison, the evolution obtained in the absence of the $\mathcal{PT}$ potential ($\gamma = 0\,\forall\, t$) is shown in the inset (a).

The solution of Eq. 6.19 with $\gamma = 0$, for an initial state ρ_0, is:

$$\begin{aligned} \rho_0 &= \begin{pmatrix} 0.5+a & b+ic \\ b-ic & 0.5-a \end{pmatrix} \\ \rho(t) &= \begin{pmatrix} 0.5 & b \\ b & 0.5 \end{pmatrix} + e^{-p\,t}\left(\cos(2t)\begin{pmatrix} a & ic \\ -ic & -a \end{pmatrix} + \sin(2t)\begin{pmatrix} c & -ia \\ ia & -c \end{pmatrix}\right), \end{aligned} \tag{6.21}$$

so the cost function in the inset is expected to oscillate as

$$C[\rho(t)] = 0.5 + (a\sin(2t) - c\cos(2t))e^{-p\ t}. \tag{6.22}$$

This relation was used to estimate the effective dephasing rate of the system fitting the track of the cost function of the evolving states with:

$$C[\rho(t_i)] = c_1 + c_2\sin(c_3 t_i + c_4)e^{-p_x t_i}.$$

The fitted function is reported as solid line in the inset graph. The experimentally retrieved values, obtained from three alternative input states, are $\{0.04, 0.40, 0.70\} \pm 0.02$. It is visible how the simulation itself, as well as the imperfection in the tomography procedure, adds an extra unknown contribution to the noise channel.

The main diagram in Fig. 6.5 shows that the optimisation loop over the time dependent Hamiltonian allows us to reach a steady state of the evolution by using the effect of the complex potential $i\gamma$ to counteract the detrimental effect of dephasing. Without this correcting effect, the final overlap of the qubit with the target state would be fixed at 0.5. The equilibrium value of the cost function decreases with increasing dephasing rate but is kept above the threshold value of 0.5, thanks to the effect of the time dependent $\mathcal{PT}$-Hamiltonian. The purity of the state can be read from the inset and the evolution of the state is also represented on the Bloch sphere.

6.4.3 Evolution of coupled PT symmetric systems

Up to now, we have focused on the properties of a single $\mathcal{PT}$ system. However, our dilation method is designed to couple two subspaces. The same unitary $U_{2N}(\gamma, t)$ of Eq. 6.8, that correctly describes the open system nature of the forward subspace, can be used to produce a larger set of non unitary evolutions beyond the single $\mathcal{PT}$ Hamiltonian. In the following, we are going to initialise our simulator with single photons superposed over the forward and reverse modes of the device and analyse which repercussions this has on the entropy and on observables such as $\mathcal{P}$. We also considered mixed states, in the extended $2N$-dimensional Hilbert space, whose statistics were reproduced by preparing a collection of pure input states and averaging the results of their simulated evolution. To be able to perform an independent state reconstruction of the states produced by our simulator, we restrict to $N = 2$ and use the last diagonal of components of the chip to perform projective measurements.

In the first set of measurements, we focused on the unbroken symmetry phase, $\gamma = 0.5$, and we performed a complete state tomography of the states of the 4-dimensional Hilbert space after the evolution with $U_4(\gamma, t)$. For this, we used 3 cascaded interferometers to project on the 20 elements of 5 mutually unbiased basis. The top left 2×2 submatrix of the 4-dimensional density matrix gave, upon normalisation, the density matrix for the

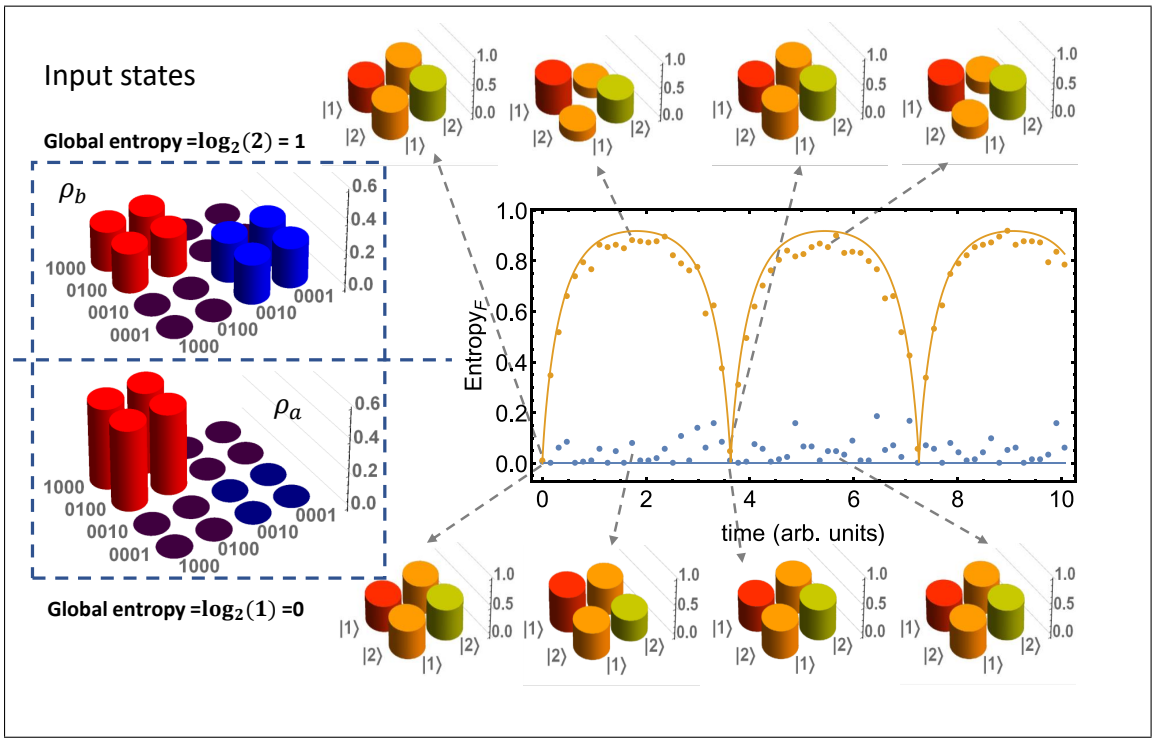

Figure 6.6: Entropy evolution of an initially pure state. Evolution of two global states (ρ_a and ρ_b) resulting in the same density matrix in the forward subspace corresponding to a pure state:

$$\rho_a = \begin{pmatrix} 0.5 & 0.5 & 0 & 0 \\ 0.5 & 0.5 & 0 & 0 \\ 0 & 0 & 0 & 0 \\ 0 & 0 & 0 & 0 \end{pmatrix} \quad \text{and} \quad \rho_b = \begin{pmatrix} 0.25 & 0.25 & 0 & 0 \\ 0.25 & 0.25 & 0 & 0 \\ 0 & 0 & 0.25 & 0.25 \\ 0 & 0 & 0.25 & 0.25 \end{pmatrix}.$$

Bar charts report the absolute value of the density matrix elements reconstructed from state tomography.

forward subspace. When required, the input state preparation is combined with $U_4(0.5, t)$ in a single transfer matrix implemented on the chip. In Fig. 6.6, we show the evolution of the entropy of the system projected in the forward subspace for two alternative input states that correspond to identical density matrices once normalised. The first state is a globally pure state:

$$\rho_a = 0.5(|1\rangle_F + |2\rangle_F)(\langle 1|_F + \langle 2|_F)$$

and the second state is a globally mixed state

$$\rho_b = 0.25(|1\rangle_F + |2\rangle_F)(\langle 1|_F + \langle 2|_F) + 0.25(|1\rangle_R + |2\rangle_R)(\langle 1|_R + \langle 2|_R).$$

Due to the loss of unitarity, the entropy of a $\mathcal{PT}$ system may change with time but upon normalisation, if the initial state is pure, it would remain pure. However, according to our open system model, the part of the system stored in the reverse subspace can manifest with

an entropy variation of the forward system if the global system starts in a mixed state. The projection of a pure state onto a smaller subspace, instead, returns a pure state (see for example Fig. 6.9). Similarly, in Fig. 6.7, we observe the evolution of a completely mixed state whose entropy variation with time is conditioned by the original coherence shared with the modes of the reverse subspace.

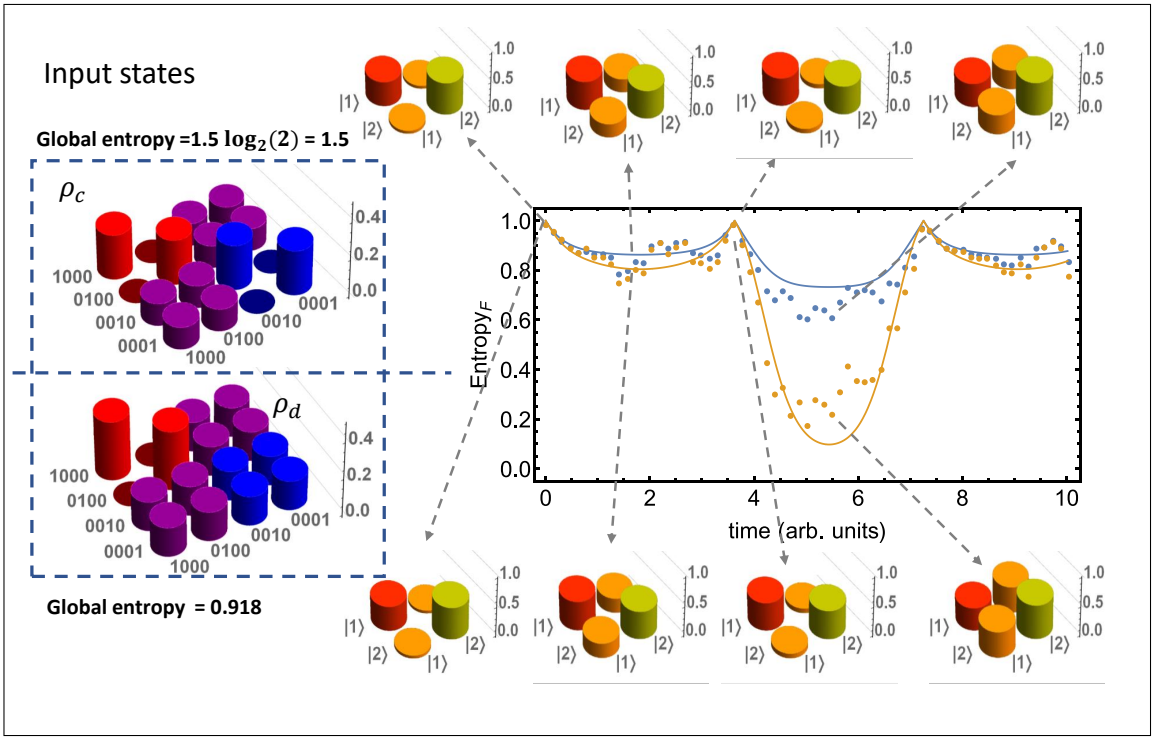

Figure 6.7: Entropy evolution of an initially completely mixed state. Evolution of two global states (ρ_c and ρ_d) resulting in the same density matrix in the forward subspace corresponding to a a completely mixed state:

$$\rho_c = \begin{pmatrix} 0.25 & 0 & -0.125 & 0.125 \\ 0 & 0.25 & 0.125 & -0.125 \\ -0.125 & 0.125 & 0.25 & 0 \\ 0.125 & -0.125 & 0 & 0.25 \end{pmatrix} \quad \text{and} \quad \rho_d = \begin{pmatrix} 1/3 & 0 & -1/6 & 1/6 \\ 0 & 1/3 & 1/6 & -1/6 \\ -1/6 & 1/6 & 1/6 & -1/6 \\ 1/6 & -1/6 & -1/6 & 1/6 \end{pmatrix}.$$

Bar charts report the absolute value of the density matrix elements reconstructed from state tomography.

We also observed the interplay between the forward and reverse subspaces by probing the parity of the forward system. It is worth noting that since $\mathcal{P}.H_N(\gamma).\mathcal{P} = H_N(\gamma)^\dagger$, the system is $\mathcal{P}$-pseudo-Hermitian and $\mathcal{P}$ is a constant of motion in the sense that $G_N^\dagger(\gamma,t).\mathcal{P}.G_N(\gamma,t) = \mathcal{P}$, indeed:

$$\mathcal{P}.A = A^\dagger.\mathcal{P} \implies \exp\left(iA^\dagger\right).\mathcal{P}.\exp(-iA) = \exp\left(iA^\dagger\right).\exp\left(-iA^\dagger\right).\mathcal{P} = \mathcal{P}$$

However, adopting the normalisation procedure based on the usual Dirac norm, the expectation value of $\mathcal{P}$ is inversely proportional to the norm of the state as function of time.

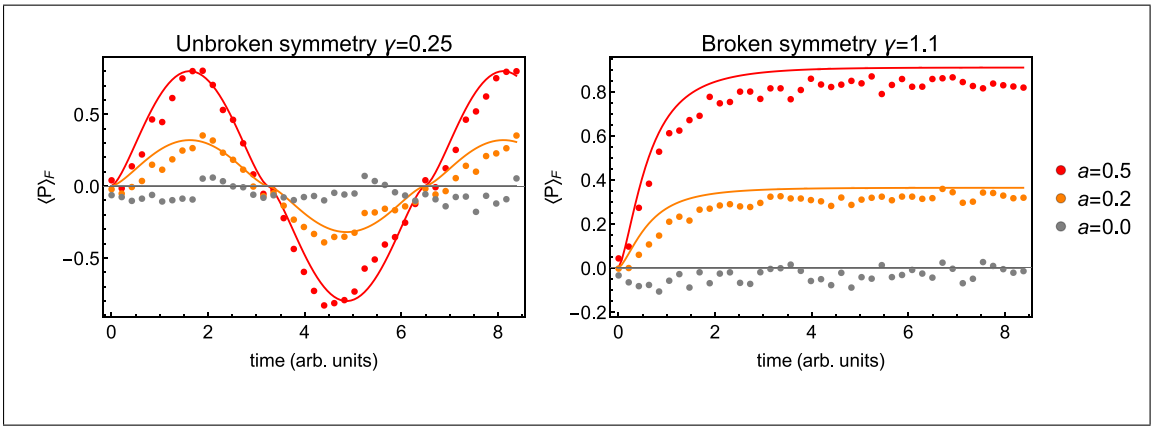

Figure 6.8: Expectation value of $\mathcal{P}$ as function of the coherence between forward and reverse subspaces. Simulation of a system coherently superposed across the forward and reverse subspaces initialised in the state $\rho_0(a) = 0.5(|1\rangle_F \langle 1|_F + |1\rangle_R \langle 1|_R) + a(|1\rangle_F \langle 1|_R + |1\rangle_R \langle 1|_F)$, the parameter a characterising the degree of coherence between the two systems. In the unbroken symmetry regime ($\gamma = 0.25$), the amplitude of the oscillations of $\langle\mathcal{P}\rangle_F$ are determined by the level of coherence of the input state. In the broken symmetry regime ($\gamma = 1.1$), the level of coherence of the input state dictates the saturation level of $\langle\mathcal{P}\rangle_F$.

Nonetheless, if $\langle\psi(0)|\,\mathcal{P}\,|\psi(0)\rangle = 0$, this will be zero at all times. On the contrary, in Fig. 6.8 it is possible to observe how the coherence between the same mode of the forward and reverse subspaces can be used to control the oscillations of the expectation value of $\mathcal{P}$ in the forward system. The data shown refer to a parametric input state

$$\rho = \begin{pmatrix} 0.5 & 0 & a & 0 \\ 0 & 0 & 0 & 0 \\ a & 0 & 0.5 & 0 \\ 0 & 0 & 0 & 0 \end{pmatrix}.$$

The amplitude of the characteristic oscillations in the unbroken symmetry regime reduces if the coherence between the states $|1\rangle_F$ and $|1\rangle_R$ decreases and it vanishes if the input is only a statistical mixture of $|1\rangle_F$ and $|1\rangle_R$. In the broken symmetry phase, $\langle\mathcal{P}\rangle$ no longer exhibits oscillatory behaviour because the system loses its periodicity but the asymptotic configuration of the system changes monotonically as function of the initial coherence between the two subsystems.

In Fig. 6.9 we plot the entropy and parity data for a globally pure state ρ_e with coherence across all the modes of our model:

$$\rho_e = 0.25\ (|1\rangle_F - |2\rangle_F + |1\rangle_R - |2\rangle_R)\ (\langle 1|_F - \langle 2|_F + \langle 1|_R - \langle 2|_R).$$

The expectation value of $\mathcal{P}$ varies over a large range while the state , except for experimental imperfections, remains pure during the evolution.

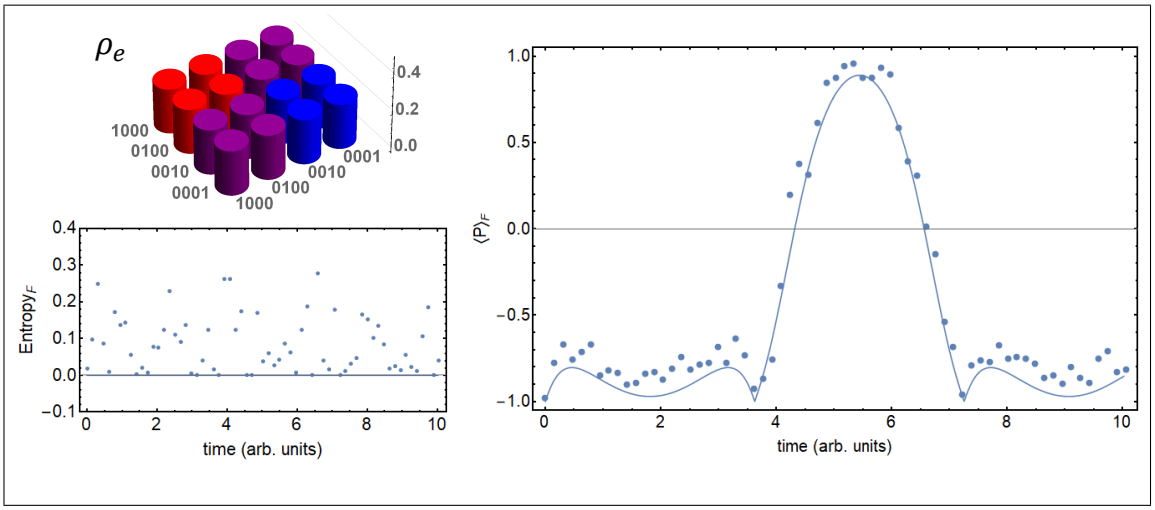

Figure 6.9: Evolution of a pure global state. Simulation of the state $\rho_e = 0.25\ (|1\rangle_F - |2\rangle_F + |1\rangle_R - |2\rangle_R)\ (\langle 1|_F - \langle 2|_F + \langle 1|_R - \langle 2|_R)$ evolving in the unbroken symmetry regime ($\gamma = 0.5$). The coherence between the two subspaces affects the parity of the system in the forward subspace but no effect on the entropy is predicted.

6.5 Discussion

To compare alternative physical models, it is important to perform accurate experiment as well as detailed theoretical calculations. In the realm of quantum mechanics and quantum field theory the computational power of our traditional computers and classical algorithms is already struggling to give reliable predictions about models for many body condensed matter physics but also for fundamental interactions such as those described by quantum chromodynamics. For these problems, a quantum computer could be used to make more sophisticated predictions [192].

Further developments of these theories, potentially beyond the current prescription of quantum mechanics, are likely to require a similar computational effort to be tested against the current models. In such a scenario, we envisage that quantum processors, including quantum simulators, whose component dynamics is reliably described by conventional quantum mechanics, could still be employed to perform part of the computation required by the future theories, by means of adequate mappings.

Here, we started by analysing $\mathcal{PT}$-symmetric Hamiltonians showing how these can be simulated in a linear interferometer by means of the unitary dilation technique that is also applicable to other forms of non-Hermitian Hamiltonian. Such deviation from standard quantum mechanical prescription is currently investigates in multiple context of quantum field theory [158–160, 173]. Moreover, we noted that the evolution generated by these unconventional Hamiltonians, with a suitable measurement probability definition (Eq. 6.2), maps onto instances of non-linear von Neumann equation linking these models to other

potential tests of quantum mechanics [193].

Our simulation is able to reproduce the exact symmetry regime, where the periodic evolution of the system is due to the realness of the Hamiltonian eigenvalues, the evolution at the exceptional point, and the broken symmetry regime where the system tends to asymptotic states. In particular, we showed how the specific symmetries of our model manifest in a three level $\mathcal{PT}$ system and how those are preserved when the same linear optical device is used to transform two-photon states.

With the aid of the quantum simulator, we also explored the effect of a dephasing channel on an evolving $\mathcal{PT}$ qubit and showed how a well designed time varying Hamiltonian can be engineered to steer a quantum states towards a target resource state. Finally, making use of the open system nature of our mapping, we simulate the evolution of systems whose dynamics is affected by the presence of additional scattering modes in the Hilbert space that can cause entropy fluctuation in the system restricted to a smaller subspace.

By accessing larger quantum device, it will be possible to simulate theories with more complex deviations from the standard quantum prescriptions although the effective advantage of the quantum hardware will depend on the particular model and on the available mappings.

CHAPTER 7

PERTURBATIVE OPEN SYSTEM QUANTUM SIMULATION WITH PHOTONICS

Outline

Some of the open questions in quantum mechanics, such as the emergence of classical and thermodynamic behaviours, are strongly related to our ability to describe the evolution of a quantum system interacting with the surrounding environment. While a deep understanding of these topics can help improving the quality of the future quantum computers, there is also hope that the greater computational power that these machines will achieve will help to accurately simulate open system models that would otherwise be intractable on classical computers. Although at a preliminary stage, here I will present few theoretical results that might be useful for near term quantum devices to decrease the circuit depth required to perform open quantum systems simulation.

In particular, in this chapter I will describe a new simulation procedure for treating the dynamics arising from the interactions between a system and an environment. In analogy with the Dyson's series[1], I express the solution to the master equation as a perturbative series that has relevant connections to the theory of collision models [194], developed in recent years to reproduce the evolution of open systems. Additionally, even though this simulation method is applicable to a generic platform, I will show why it is particularly appealing for a photonic implementation since it can exploit the probabilistic generation of heralded single photons to represent the stochastic properties of the environment.

[1]Even though the Dyson's series was developed for quantum field theory, its non-relativistic derivation can be found in the approximation methods chapter of [161].

In the first section, I will discuss the main features of the *collision model* in the context of open system simulation. This will help understanding the proposed simulation model presented in the second section together with few numerical simulations. The third section is dedicated to the particularity of the suggested photonic implementation of the model that takes advantage of the *scattershot* photon generation (see Sec. 2.5.2). In the same section, I will also present the optical circuits designed for a small scale implementation of this model. Finally, in the last section, I will discuss possible developments of the technique.

Contributions

The simulation method discussed in this chapter was conceived by myself. I performed the numerical simulation presented in the text and carried out its mapping on a photonic circuit. In designing the silicon photonic chip submitted to the foundry, I benefited from a large library of photonic components developed in the past years by the QETLabs group.

7.1 Collision model

In recent years, a new method has been developed to reproduce the dynamics of open systems called *collision model*. In their seminal paper [194], Ziman et al. investigated the potentiality of constructing a one-parameter discrete semigroup map $\mathcal{E}_k$ such that

- $\mathcal{E}_0 \equiv \mathbb{1}$
- $\mathcal{E}_1(\rho_s) \equiv \mathrm{tr}_e \left[U \rho_s \otimes \eta_e U^\dagger \right]$
- $\mathcal{E}_{k+1}(\rho_s) \equiv \mathcal{E}_1(\mathcal{E}_k(\rho_s))$
- $\mathcal{E}_k \equiv (\mathcal{E}_1)^k$
- $\mathcal{E}_A \circ \mathcal{E}_B = \mathcal{E}_{A+B}$

where ρ_s is the state of the system of interest S, and η_e represents the state of an ancillary system playing the role of a uncorrelated environment. Moreover, U describes an instantaneous interaction (collision) between the system and the ancillary state. In later works [195], the system is also let explicitly evolve as an isolated systems for a time τ between one collision and the following one while the original paper absorbed this into the action of $\mathcal{E}_k$. Since multiple identical copies of η_e are used throughout the evolution, each collision depends neither on the evolution time nor on the previous interactions. To indicate at what time during the evolution an environment ancillary state interacts with S, we will make use of the notation η_k with $k \in \mathbb{N}$. Generally speaking, the system becomes entangled with the state of the ancillary qubits it interacted with. However, for the purpose of simulating

the system evolution, the information stored in η_k can be traced out right after the ancillary state collided with the system. Thanks to this, the memory overhead required for the simulation of a collision model is limited.

It was shown that given a collision model, it is often possible to determine a continuous evolution map $\tilde{\mathcal{E}}_t$ describing a Markovian process such that $\tilde{\mathcal{E}}_{k\tau} = \mathcal{E}_k$ by defining

$$\tilde{\mathcal{E}}_t = \lim_{k \to t/\tau} (\mathcal{E}_1)^k .$$

In their examples, they realised a decaying map, leading to an homogenisation process [2] between the environment and the system, and two dephasing maps in mutually unbiased bases. Their choice of U consisted in a partial swap[3] or in a partial control-not[4], both acting between a single qubit system and an ancillary qubit. Follow-up work [196] clarified that a particular collision model determines a valid continuous semigroup associated to a Markovian evolution only if it is possible to find a Lindbladian operator G [43] such that $\mathcal{E}_1 = e^G$.

It is appreciable how it is possible to give, in some contexts, a strong physical motivation to the collision model. Let's think for example to the evolution of a molecule (the system) in a surrounding gas (the environment). With a certain frequency, a random element of the gas will happen to be close enough to the molecule that they can interact until they will be separate again. Considering a large number of particles in the gas, the probability of a particle to collide multiple times with our molecule is likely to be negligible and assuming an environment at finite temperature, we can neglect classical and quantum correlations between the particles that compose it. Under these assumptions we can assume that the quantum state of the incoming particle can be described statistically and represented by a single mixed state. Finally, in order to keep the model simple, the time interval between two consecutive random collisions can be assumed equal to its mean value. Knowing the physics of the interaction between the molecule and the gas, a pertinent choice of U can be made.

Few years after the seminal paper, it was pointed out how collision models could also be used to describe several non-Markovian systems by simply relaxing some of the assumptions of the original proposal, unveiling the great potentiality of this technique [195, 197–199]. Non-Markovian interactions are generally more complex to be dealt with than Markovian evolution since a fraction of the correlation between system and environment, often quantum in nature, needs to be recorded for later use. A Markovian evolution appears as a further level of simplification of an otherwise non-Markovian system.

The first method proposed to obtain an effective non divisible quantum channel have been achieved preparing the environment qubits in an entangled state even though the system

[2] The homogenisation process determines that $\lim_{k\to\infty} \mathcal{E}_k(\rho_s) = \eta_e$.

[3] Said S the unitary that exchanges the state of the two spins, the partial swap can be written as $U = \cos(\theta)\mathbb{1} + i\sin(\theta)S$.

[4] The partial control-not can be written as $U = \cos(\theta)\mathbb{1} + i\sin(\theta)$ C-Not

and the environment are separable until the first interaction occurs [197]. A non divisible quantum channel $\mathcal{E}_A$ cannot be written as the concatenation of other non trivial quantum channels meaning that if $\mathcal{E}_A = \mathcal{E}_B \circ \mathcal{E}_C$ then either $\mathcal{E}_B$ or $\mathcal{E}_C$ are unitary. Similarly, non-Markovian evolution has been observed in a collision model where the ancillary environment system η_k after interacting with the system in the k-th collision, also interacts with η_{k+1}. The degrees of freedom of the state η_k can then be traced out before ρ_s performs its $k+1$-th collision [198]. A third way of obtaining a non-Markovian evolution by means of a collision model is to describe the environment as composed by an intermediate systems S_{bridge} and a collection of separable ancillary systems η_k [195]. While S_{bridge} directly interacts with the ancillary systems by means of discrete collisions, the system of interest S is only directly coupled to S_{bridge} by means of a coupling Hamiltonian. The tracing out of the information of the environment is only performed on the ancillary states leaving the possibility for information to flow back from S_{bridge} to S. For example, with this approach, the authors showed that it is possible to reproduce the dynamics of an excited atom in a lossy cavity. A further application of the collision model appeared in [199], where the authors investigated the appearance of spontaneous synchronisation between two quantum system that share the same environment.

In addition to this growing theoretical framework, also practical implementation in quantum simulators have been investigated. Many of these are focused on quantum optics, where proof-of-principle experiments have now been reported [200–202].

7.2 Perturbative solutions of the open system dynamics

We now describe the new simulation method we propose. While this first derivation only accounts for time dependent Markovian dynamics, we are confident that the model we propose could be expanded to cover a larger family of quantum evolutions following approaches similar to those adopted by the collision model community. Indeed, even if our method is based on different premises, the end point of our derivation does not differ strongly from the collision model itself.

We start by considering the following master equation:

$$\frac{\partial}{\partial t}\rho = -i\left[H,\rho\right] + L(t)\left[\rho\right] \tag{7.1}$$

where H represents the Hermitian Hamiltonian of the system of interest S if isolated, L is a time dependent super operator that represents the additional effect of an environment, and ρ is the state of S. To preserve the properties of ρ (see Sec. 2.1.1), we require $L(t)$ to satisfy

(i) $\forall t$ and physical ρ, $\quad \text{tr}\left[L(t)[\rho]\right] = 0$ (to preserve the trace of ρ)

(ii) $\forall t$ and physical ρ, $\quad \left(L(t)[\rho]\right)^\dagger = L(t)[\rho]$ (to preserve the hermiticity of ρ)

(iii) $\exists \tau > 0$ such that $\forall t$ and physical ρ, $\quad \rho + \tau L(t)[\rho]$ is positive definite (to ensure that ρ remains positive definite).

We finally require the linearity of L and assume that $\|L(t)[A]\|/\|A\| < \beta$ for all Hermitian operators A where $\|.\|$ indicates the Frobenius norm. We will indicate with U the unitary that describes the dynamics due to H, therefore:

$$\frac{\partial}{\partial t} U_{t,t_0} = -iHU_{t,t_0} \qquad U_{t_0,t_0} = \mathbb{1}.$$

With these premises, the solution to the differential equation can be written as a series. The sequence of the partial sums $\rho^{(n)}$ of this series is

$$\rho^{(n)}(t) = \sum_{k=0}^{k=n} \mathrm{I}^{(k)}(t) \tag{7.2}$$

where $\mathrm{I}^{(0)} = U_{t,0}\rho(0)U_{t,0}^{\dagger}$ and for $k > 0$ the integrals $\mathrm{I}^{(k)}$ are given by

$$\mathrm{I}^{(k)}(t) = \int_0^t \int_0^{t_1} \cdots \int_0^{t_{k-1}} U_{t,t_1} L_{t_1} \left[\ldots U_{t_{k-1},t_k} L_{t_k} \left[U_{t_k,0}\rho(0)U_{t_k,0}^{\dagger} \right] U_{t_{k-1},t_n}^{\dagger} \ldots \right] U_{t,t_1}^{\dagger} \mathrm{d}t_k \ldots \mathrm{d}t_1 \tag{7.3}$$

that can be written as a recursive relation

$$\mathrm{I}^{(n+1)}(t) = \int_0^t U_{t,t_1} L_{t_1} \left[\mathrm{I}^{(n)}(t_1) \right] U_{t,t_1}^{\dagger} \mathrm{d}t_1. \tag{7.4}$$

Here the temporal argument of $L(t)$ have been changed to subscript for compactness.

This solution can be interpreted as a free evolution between time intervals (t_i, t_{i+1}) stochastically interleaved by instantaneous changes operated by L for an increasing number of times. The more applications of L are considered, the higher the accuracy of the approximation. The form of this series is in close resemblance to the Dyson series developed for time dependent Hamiltonian perturbations [161]. In the worst case scenario, in a finite dimension Hilbert space, the norm of each subsequent $\rho^{(n)}$ increases by $\frac{t^n \beta^n}{n!}$. The proof of the mathematical properties of the above solution can be found in App. C; the same approach to the solution of the Eq. 7.1 is discussed in [203] in the context of quantum trajectories.

The properties shown above are, however, not sufficient yet to implement this perturbative simulation on a quantum device. A first tentative approach to use this perturbative expansion would be to truncate the above series and numerically approximate the integrals $\mathrm{I}^{(k)}$. Assuming for example a Monte Carlo method, for each random ordered sequence $t_1 > \ldots > t_k$ the experiment would need to generate the state described by

$$U_{t,t_1} L_{t_1} \left[\ldots U_{t_{k-1},t_k} L_{t_k} \left[U_{t_k,0}\rho_0^{(0)}U_{t_k,0}^{\dagger} \right] U_{t_{k-1},t_k}^{\dagger} \ldots \right] U_{t,t_1}^{\dagger}$$

and perform the desired measurement upon it. The effective expectation value would then be given by the sum of the results from the experiments with increasing perturbation order.

Unfortunately, this cannot be directly performed in an experiment because $L(t)[\rho]$, as well as $\mathrm{I}^{(k)}$, is not a valid density matrix (being traceless) and cannot represent the state of a system obtained from a single experiment.

A solution to this problem can be found by replacing L with an associated transformation:

$$G(t)[\rho] = \rho + \tau L(t)[\rho]$$

where τ satisfies the condition in (iii). After introducing the alternative integral

(7.5)
$$\mathrm{J}^{(n)}(t) = \int_0^t \int_0^{t_1} \cdots \int_0^{t_{n-1}} U_{t,t_1} G_{t_1} \left[\ldots U_{t_{n-1},t_n} G_{t_n} \left[U_{t_n,0} \rho_0^{(0)} U_{t_n,0}^\dagger \right] U_{t_{n-1},t_n}^\dagger \ldots \right] U_{t,t_1}^\dagger \mathrm{d}t_n \ldots \mathrm{d}t_1,$$

the contribution from the different integrals can be weighted appropriately to retrieve the expression in Eq. 7.2. Indeed, defining $\mathrm{J}^{(0)} = \mathrm{I}^{(0)}$, the state at time t can be written as

(7.6)
$$\rho^{(n)}(t) = \sum_{k=0}^{n} c_n \mathrm{J}^{(k)}(t).$$

As an example, we will walk through the first perturbative order ($n = 1$) before providing with the general expression derived in App. C.

(7.7)
$$\begin{aligned}
\rho^{(1)} &= U_{t,0}\rho(0)U_{t,0}^\dagger + \int_0^t U_{t,t_1} L(t_1)[U_{t_1,0}\rho(0)U_{t_1,0}^\dagger] U_{t,t_1}^\dagger \mathrm{d}t_1 \\
&= \left(1 - \frac{t}{\tau}\right) U_{t,0}\rho(0)U_{t,0}^\dagger + \frac{1}{\tau}\int_0^t U_{t,t_1}(\mathbb{1} + \tau L(t_1))[U_{t_1,0}\rho(0)U_{t_1,0}^\dagger] U_{t,t_1}^\dagger \mathrm{d}t_1 \\
&= c_0 U_{t,0}\rho(0)U_{t,0}^\dagger + c_1 \int_0^t U_{t,t_1} G(t_1)[U_{t_1,0}\rho(0)U_{t_1,0}^\dagger] U_{t,t_1}^\dagger \mathrm{d}t_1 \\
&= c_0 \mathrm{J}^{(0)}(t) + c_1 \mathrm{J}^{(1)}(t)
\end{aligned}$$

In this example, $c_0 = (1 - \frac{t}{\tau})$ and $c_1 = 1/\tau$. When an increasing order of perturbation is considered, the value of each coefficient must be recalculated. If the N-th perturbative order is considered, the expression of the coefficients $c_{N-k}^{(N)}$ with $k \in [0, N]$ is given by the equations:

(7.8)
$$c_{N-k}^{(N)} = \tau^{N-k} \sum_{p=0}^{k} \frac{1}{p!} \left(-\frac{t}{\tau}\right)^p$$

that happens to be the expansion series of $\tau^{N-k} e^{-\frac{t}{\tau}}$. We note that τ is mainly an expedient to make $J^{(n)}$ accessible to an actual simulator. However, a larger τ corresponds to a transformation G closer to the ideal transformation L and it will also reduce the coefficients of the higher order integrals that are more challenging to estimate with good accuracy.

The realisation of the transformation G can be performed similarly to the collision model applying a unitary transformation between S and an ancillary system of comparable size (see also Sec. 2.1.4). In particular, in quantum optics, some transformation G can be obtained as result of heralded multi-photon gates.

Ultimately, this shows how the simulation of a system interacting with an environment can be modelled as a (weighted) sum of probabilistic processes where the system interacts a variable number of times with the environment by means of discrete unitary transformations between the two systems. However, few features differentiate this result from the collision model.

- Our simulation model is introduced to approximate the solution of a given master equation as opposed to finding a master equation that reproduces the simulated evolution in discrete times.

- The number of interactions between system and environment is assumed fixed even though the accuracy of the simulation decreases for longer evolution time. As displayed in the numerical modeling included in the next section, to keep a constant error in the simulation, the order of the approximation should scale almost linearly with the evolution time.

- The interaction between system and environment happens in random times and as we will see, this can determine an advantage for those platforms that rely on a non probabilistic resource generation as photonics.

- Multiple experiments are required to infer the information about the simulated system because multiple different integrals $\mathrm{J}^{(m)}$ needs to be evaluated. Setting the maximum number of interactions between system and environment, the algorithm prescribes different coefficients to be used for each of the $\mathrm{J}^{(m)}$ contributions. When $t > \tau$ some of those coefficients will be negative.

7.2.1 Numerical simulation

Here we provide few examples of the numerical performance of the algorithm, without focusing on the particular experimental realisation. We briefly address the accuracy of the solution for an increasing order of approximation in comparison with a Trotterisation-like approach (see Sec. 2.5) based on an higher number of non-unitary evolution steps in the simulation process. For these simulations, the chosen exemplary system is a small chain of three spin-1/2 particles interacting with a nearest neighbour potential and a magnetic mean field in a randomly chosen direction $\hat{\mathbf{n}} = (0.610,\ 0.790,\ 0.057)$ introduced to break the symmetry of the system.

We will indicate with $S_z^{(j)}$ the Pauli-z operator of the j-th particle and with $\vec{S}^{(j)} = \left(S_x^{(j)}, S_y^{(j)}, S_z^{(j)}\right)$ the vector of the spin operators for the same particle assuming a tensor product with the identity transformation acting on the other two particles. The dimension-

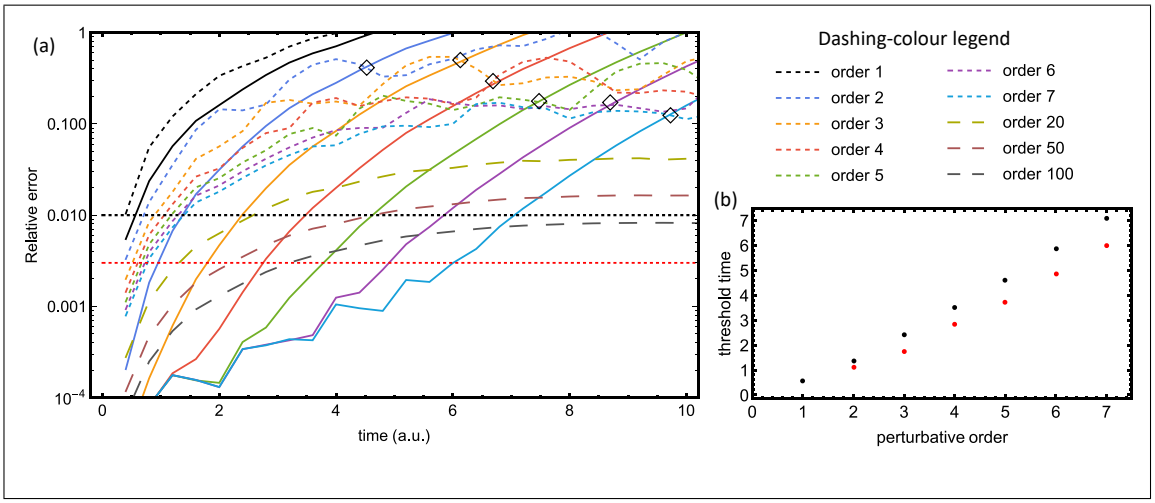

Figure 7.1: Relative error for different perturbation orders of the approximated solution. (a): Solid lines of the different colours refer to the evolution performed adopting our perturbative expansion of the solution up to order n while dashed lines of the same colour refer to the approximate solution based on Eq. 7.11 where s is the order of approximation. Open diamonds indicate the crossover points of the two methods for $n = s$. (b): Maximum evolution time for achieving relative error less than 0.01 (black dots) or 0.003 (red dots) at different perturbation order.

less time-independent Hamiltonian therefore reads:

$$\hat{H} = S_z^{(2)} \left(S_z^{(1)} + S_z^{(3)}\right) + \hat{\mathbf{n}} \cdot (\vec{S}^{(1)} + \vec{S}^{(2)} + \vec{S}^{(3)}). \tag{7.9}$$

The initial state is set as the entangled GHZ state $\frac{|\uparrow\uparrow\uparrow\rangle + |\downarrow\downarrow\downarrow\rangle}{\sqrt{2}}$ while we chose L to generate a uniform dephasing channel in the spin up/down eigenbasis basis

$$B = \{\,|\uparrow\uparrow\uparrow\rangle, |\uparrow\uparrow\downarrow\rangle, |\uparrow\downarrow\uparrow\rangle, |\uparrow\downarrow\downarrow\rangle, |\downarrow\uparrow\uparrow\rangle, |\downarrow\uparrow\downarrow\rangle, |\downarrow\downarrow\uparrow\rangle, |\downarrow\downarrow\downarrow\rangle\,\}$$

$$L[\rho] = -0.3\left(\rho - \sum_{|x\rangle \in B} |x\rangle\langle x|\,\rho\,|x\rangle\langle x|\right). \tag{7.10}$$

In Fig. 7.1 (a) we show, in solid lines, the time evolution of the relative error derived by the n-order perturbative approximation for $n \in \{1,2,3,4,5,6,7\}$ expressed as

$$\frac{\left\|\rho^{(n)}(t) - \rho_{\text{exact}}(t)\right\|}{\left\|\rho_{\text{exact}}(t)\right\|}$$

using the Frobenius norm. The relevant integrals are calculated using the Monte Carlo method with 300,000 samples and the "exact" evolved state is estimated discretising the evolution law in Eq. 7.1 for tiny $\delta t = 10^{-5}$ and linearising the evolution as

$$\rho(t+\delta t) \approx \rho(t) + \left(-i\left[H, \rho(t)\right] + L(t)\left[\rho(t)\right]\right)\delta t.$$

The dashed lines in the same plot report, instead, the evolution of the error derived by a coarse grain simplification of Eq. 7.1. For $s \in \{1,2,3,4,5,6,7,20,50,100\}$, the initial state is transformed applying s times the following map:

$$K\left(\frac{t}{s}\right)[\rho] = U\left(\frac{t}{2s}\right).\left\{U\left(\frac{t}{2s}\right).\rho.U^{\dagger}\left(\frac{t}{2s}\right) + \frac{t}{s}L\left[U\left(\frac{t}{2s}\right).\rho.U^{\dagger}\left(\frac{t}{2s}\right)\right]\right\}.U^{\dagger}\left(\frac{t}{2s}\right). \tag{7.11}$$

That is, the evolution is divided in s intervals, and the system evolves in these intervals sequentially applying the two non commuting transformations $U\left(\frac{t}{s}\right)$ and $\left(\mathbb{I} + \frac{t}{s}L[\circ]\right)$, the latter being the linearisation of the non Hermitian dynamics. Dotted lines are placed at error levels of 0.003 and 0.01 as visual aid.

The perturbative method we propose results in a much smaller error at short evolution time compared to an equivalent number of non-unitary steps used in the alternative simulation (dashed lines of the same colour). For example, it is possible to appreciate that at the 7-th order of approximation, the result is better than those obtained with $s = 100$ in the approximation methods in Eq. 7.11 up to $t = 6.5$. Noticeably, the scaling of the relative error due to the two methods as function of time is different even when $n = s$ and leads to a cross over of the performance of the two approaches for a fixed number of non-unitary transformation allowed. However, the crossover, indicated with open diamonds in the plot, happens at a significant level of noise above 0.1 and the order of the approximation is just not sufficient for both methods.

In Fig. 7.1 b, we show that when fixing a threshold error value, the scaling of the required perturbative order of approximation is linear. On the vertical axis, the plot shows the evolution time at which the specific order of approximation determines an error greater than 0.01 (black dots) or 0.003 (red dots). The estimated threshold time is the result of a polynomial fit of the numerically simulated values showed in Fig. 7.1 a. The graph suggests that a linear scaling of the perturbative order with desired evolution time suffices to maintain the error below a given threshold.

7.3 Photonic quantum simulations based on probabilistic heralded sources

One of the great limitations of simulating and computating with quantum optical systems with discrete variables is the probabilistic nature of the generation of resource states (single photons, pairs of entangled photons, GHZ state ...) as well as the non-deterministic controlled operations between their quantum states due to the non interacting nature of the photons. Here we show how these limitations can be mitigated in the perturbative simulation model we propose. In particular, we will focus on the probabilistic nature of the environment states η_k required to generate the transformation G assuming that the production of the initial

state ρ_0 of the system S can be done deterministically or, at least, that its production can be correctly assessed without compromising the simulation procedure.

Concerning the generation of single photons, we first note that the mixed state composed of vacuum and a single photon could already be used as environment state to generate some transformation G that do not preserve the number of photons in the system. An example of this practice is reported in [202]. The information transferred to the environment qubit can be traced out simply ignoring the state of the η_k after it interfered with S. We further note that, in this configuration, post-selecting those events where the number of photons is preserved is not directly compatible with our simulation model, that would otherwise prescribe that the number of photons is preserved at each system-environment interaction. This non-photon preserving approach, however, complicates the assessment of the initial state generation of the system and is generally inconvenient in a scenario where the linear loss of the photons is not negligible.

As an alternative procedure, we propose to implement our simulation algorithm with optical system constantly restricting the number of photon in the system after each interaction. We are considering that S is composed of qudits, each of them encoded on a single photon superposed over d spatial modes and potentially sharing initial entanglement [89]. In order to infer the number of photons in S after its interaction, it is important to know the number of photons entering the interferometer from the environment modes before the interaction as well as monitoring the environment after the interaction. For simplicity, we will consider environment states composed of single photons. After the evolution, the state of the environment is checked to verify that a single photon is detected in the environment system so that an effective transformation G is applied on S. At the end of the simulation, the system is measured post-selecting those events when a single photon is present in each of the qudits, signifying that no photon has been lost in the process (neglecting multiphoton contamination). Some post-selected optical qubit gates are discussed in 2.2.6. We point out that some of them, for example the post-selected C-Not and C-Z gates, may act as identity transformations when no photon is provided in the control or ancillary register.

Although good quality single photon sources with high generation and extraction efficiency could be used to generate a photon than transformed into η_k or generally used as resource photon for non-unitary gate G, in the following we will focus on the possibility of using heralded single photons obtained from photon pair sources and how to get the best out of it. We will indicate with ν the probability of generating the photon pair from a single source. Additionally, we would indicate with δ the probability of post-selecting an identity transformation on S when a particular gate is attempted without providing the necessary ancillary photon (for example $\delta = 1/3$ for the mentioned C-Not). The idea we promote is to distribute N gate operations between S and the environment photons interleaved with unitary transformations implementing the free evolution of S. Each control operation has

its control register connected to a single probabilistic, but heralded, single photon source. The probability $\mathrm{Post}(N,m)$ of post-selecting the correct gate operation when m environment single photon states are successfully injected is given by

$$\mathrm{Post}(N,m) = \delta^{N-m}\ p_0^m, \tag{7.12}$$

where p_0 is the probability of post-selecting the gate operation when the ancillary photons are provided (for example $p_0 = 1/9$ for the mentioned C-NOT). Due to the probabilistic nature of the N photon sources, the generation of the m photons is function of the number of sources that attempt the generation. Taking this into account, the probability $P(N,m,\nu)$ of observing an m-th order interaction event is

$$\mathrm{P}(N,m,\nu) = (p_0\nu)^m \binom{N}{m} (1-\nu)^{N-m}\,\delta^{N-m}. \tag{7.13}$$

It is then possible to optimise N to increase the probability of these scattershot events. We note that each firing source pattern would correspond to a different final evolution but, in our simulation protocol, each of them is useful for the final estimation of the expectation value of the evolved system. Indicating with $g(m,\nu)$ all the coefficients that do not depend on N, the partial derivative of the probability is:

$$\frac{\partial P}{\partial N} = g(m,\nu)\times\left[\sum_{k=0}^{m-1}\frac{1}{N-k} + \ln\Big(\delta(1-\nu)\Big)\right]\times\Big(\delta(1-\nu)\Big)^N \times \prod_{k=0}^{m-1}(N-k) \tag{7.14}$$

and using the approximation

$$\sum_{k=0}^{m-1}\frac{1}{N-k} \approx \int_0^m \frac{1}{N-k+0.5}\mathrm{d}k = \ln\left(\frac{N+0.5}{N-m+0.5}\right)$$

we obtain the condition

$$\frac{\partial P}{\partial N} = 0 \Rightarrow \ln\Big(\frac{\delta(1-\nu)(N+0.5)}{N-m+0.5}\Big) = 0 \iff N = \frac{m}{1-\delta(1-\nu)} - 0.5 \tag{7.15}$$

that for the C-Not gate corresponds to

$$N = \frac{3m-1-0.5\nu}{2+\nu}. \tag{7.16}$$

Substituting N from Eq. 7.16 into Eq. 7.13 we obtain the following expression for the rate enhancement due to a number of sources $N > m$,

$$\frac{\mathrm{P}\left(\frac{m}{1-\delta(1-\nu)}-0.5,m,\nu\right)}{\nu^m\mathrm{Post}(m,m)} = \binom{\frac{m}{1-\delta(1-\nu)}-0.5}{m}\Big(\delta(1-\nu)\Big)^{\frac{m\delta(1-\nu)}{(1-\delta(1-\nu))}-0.5}. \tag{7.17}$$

To grasp the scaling of this function, let's consider the limit for small ν, large m and finite $\delta > 0.5/m$:

$$\lim_{\nu\to 0}\frac{\mathrm{P}\left(\frac{m}{1-\delta},m,\nu\right)}{\nu^m\mathrm{Post}(m,m)} = \binom{\frac{m}{1-\delta}}{m}\Big(\delta\Big)^{\frac{m\delta}{(1-\delta)}} \approx \frac{1}{\sqrt{2\pi\delta m}}\left(\frac{1}{1-\delta}\right)^m. \tag{7.18}$$

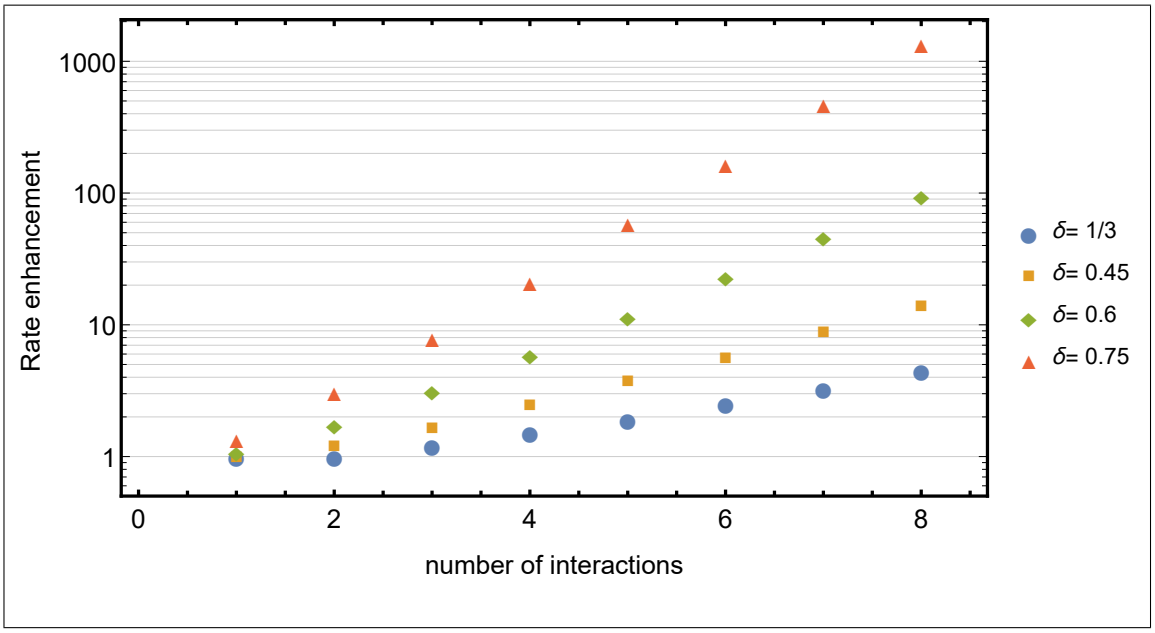

Figure 7.2: Event rate increase due to scattershot approach in the perturbative simulation. Relative event rate increase achievable for different values of the idle gate probability δ (see main text) versus and increasing number of successfully heralded interaction gates G. Data refer to an heralded single photon generation rate $\nu = 0.1$

The advantage obtained is exponential in the number of targeted interactions with the environment but the coefficient of the exponent, $-\ln(1-\delta)$, depends on δ. In the Fig. 7.2 we report the actual advantage obtained considering $\nu = 0.1$ and assuming $\delta \in \{0.75,\ 0.6,\ 0.45,\ 1/3\}$ for $1 < m < 8$. While the advantage obtained is negligible for $\delta = 1/3$, higher probability gates would largely benefit from the scattershot like approach. It is worth to mention that the probability of generating m heralded photons from m sources and successfully post-select as many gates decreases exponentially with m therefore, without further techniques, experiments are anyway limited to $m \lesssim 10$.

7.3.1 Chip design

In Fig. 7.3 is presented the schematic of an integrated silicon photonic circuit designed to implement proof of principle experiments of the perturbative simulation method. The injected pump light is split among six sFWM spiral sources generating squeezed states of light. Assuming external filters symmetrically centred around the pump wavelength to collect signal and idler generated photons, each spiral acts as an effective photon pair source. A pair generated in superposition between the two system sources can be used as entangled system state. Each of the environment sources has one of the photons from the pair routed straight to the output ports to herald the generation of a single photon in the desired channel. Reconfigurable interferometers that couple the system photons with the

modes of the environment source can be used to implement a family of non-unitary gates on the system upon heralding of the desired state of the environment after the interaction. The unitary evolution of the system, defined by U, is compiled in the mentioned interferometer up to a final transformation implemented in the final measurement stage, which allows us to probe the system state after the evolution. Correct detection patterns are those involving two photons in the system modes and heralding photons from the interaction interferometer matching the heralding signal from the source.

The circuit is based on MMI structures to implement balanced coupling between two spatial modes and on thermal phase-shifters to implement phase rotations that are also used as tunable parameter in MZI interferometer to implement variable beam-splitters. The chip features grating coupler to inject and extract light from the guided modes of the waveguides. Asymmetric MZIs are chosen to remove the pump light right after the sources to prevent further generation in the interferometric part of the chip. Electrical pads can be connected via wirebonding to external power supplies and distribute the current to each active heater of the circuit.

7.4 Discussion

The simulation method suggested in this chapter is meant to offer the possibility to separate the coherent evolution of a state from the statistical effect of its interaction with the environment. As simulations show, this procedure can become advantageous in the number of gates required to recreate the effects of interactions between system and environment. The shorter circuit depth is however at the expense of an increased number of experimental repetitions required to accurately approximate the integrals on which the simulation is based. We recognise that such compromise is mostly desirable in the NISQ[5] era since longer circuit depth would significantly increase the error rate of the device in absence of error correcting codes. Alternative approaches that trade the complexity of the single simulation instance with the necessity of multiple experimental run have also been proposed in previous works under the name of Monte Carlo wave-function or quantum jump method [204, 205].

The suggested procedure does not address the problem of the Hamiltonian evolution between two consecutive discrete interactions with the environment. Assuming an application in a NISQ device, this evolution can be performed both analogically and digitally depending on the capability of the platform. Similarly, the non-unitary transformation G can either be applied as a result of a unitary transformation implemented between the system and the environment qubits in a digital quantum computer, or be the result of a finite time evolution that couples the system to external degrees of freedom.

[5]Noise Intermediate Scale Quantum (device)

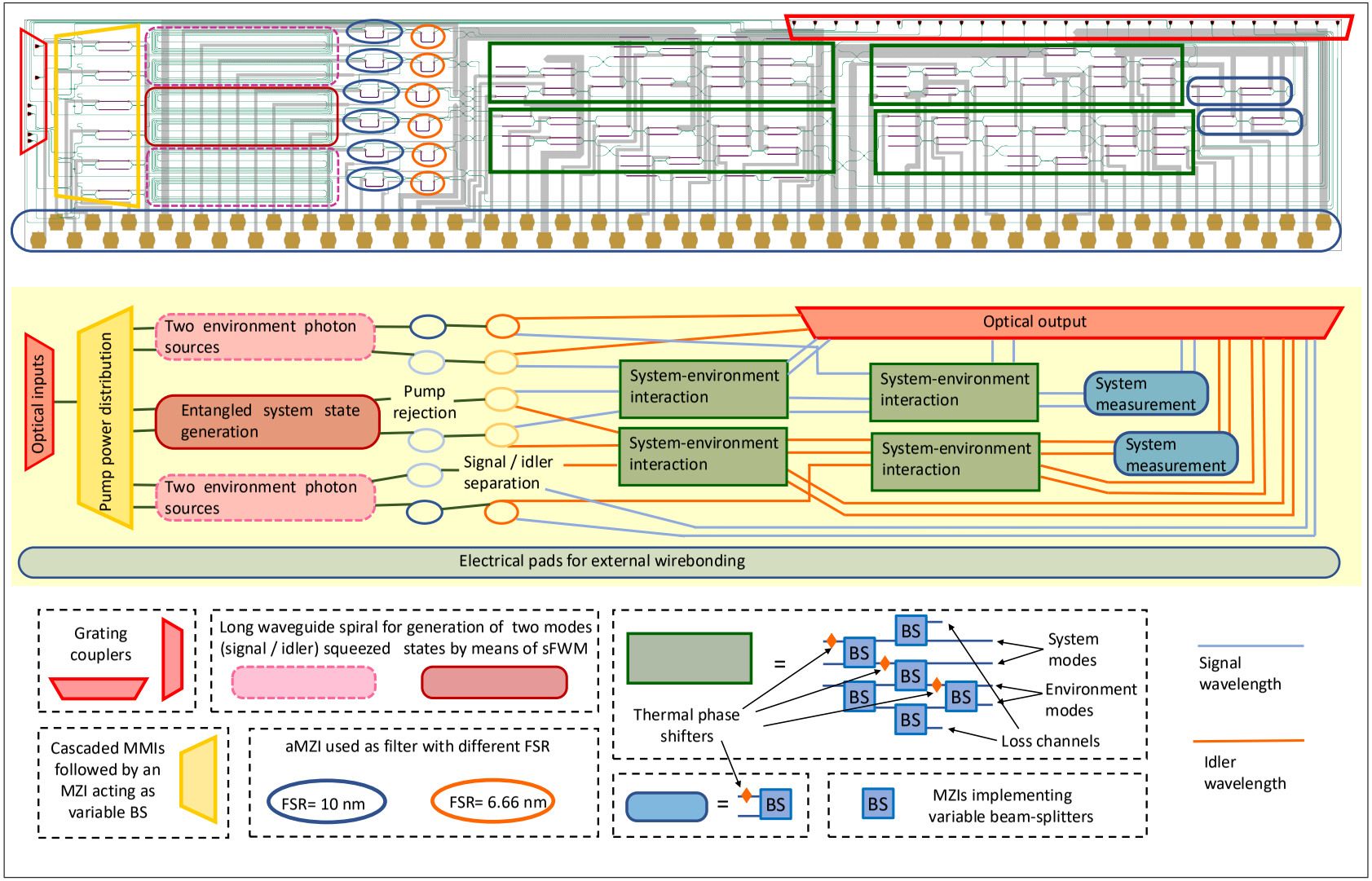

Figure 7.3: Circuit layout and functional diagram for perturbative simulations. Top diagram represents the actual 2-dimensional layout (GDSII file) of the fabricated silicon based integrated optical chip for proof of principle demonstration of the perturbative simulation scheme. Coloured boxed enclose different functional components. In the middle diagram, the role of the different components is explained adopting the same colour scheme and spatial distribution of the circuit above. In the bottom legend, the effective photonic components adopted are indicated. The list of acronyms and details about the individual components are introduced in Sec. 2.3.

One unfortunate feature is the introduction of coefficients $c_k^{(n)}$ that are not positive definite. In this prospective, the solution can probably arrive from a redefinition of the approximation order as the most likely number of interaction occurring between system and environment so that the state of the system would be rewritten as

$$\tilde{\rho}^{(n)} = \sum_{k=\ell_n}^{k=\mathrm{up}_n} w_k^{(n)} \rho^{(k)}$$

where ℓ_n and up_n are a lower and upper bounds, yet to be determined, and the positive weights $w_k^{(n)}$ are such that $\sum_{k=\ell_n}^{k=\mathrm{up}_n} w_k^{(n)} = 1$ and present a maximum at $k = n$. Even though this solution would require to increase the maximum number of non-unitary transformations to apply to the system, the scattershot-like simulation would easily incorporate it because of the finite probability of generating event with $n < m \leq N$. A further investigation should also address the possibility of replacing the operator G with a different function of the operator L such as

$$\tilde{G}(t)[\rho] = \rho + \tau L(t)[\rho] + \frac{\tau^2}{2} L(t)[L(t)[\rho]] \approx e^{\tau L(t)}[\rho].$$

Since this framework has been developed for dealing with Markovian processes, further progress needs to be made to adapt this protocol to the simulation of non-Markovian evolution. In particular, similarly to what has been tested in the collision model, a potential avenue is the introduction of correlations between the environment states used to implement G at different instants.

About the photonic implementation of the simulation method, we do not expect the scattershot approach to be sufficient for simulating classically intractable problems; however, it is important that our simulation procedure is at an advantage when dealing with probabilistic resource generation. The introduction of feed-forward between the sources and the interferometers implementing G would make it possible to reach higher ν and $\delta \approx 1$. Adoption of teleportation methods could instead be used for boosting the probability p_0 of the individual gates [63, 206].

CHAPTER 8

CONCLUSION

This thesis was motivated by the possibility of using integrated photonics for early quantum application. Many are the challenges to be faced to reach the complexity necessary to achieve practical advantages compared to classical devices. This work dedicated to few of them: the certification of the hardware performance, the formulation of mapping to interesting problems and improvement over the resource required for certain simulation tasks.

In Chapter 4, we tested a recently proposed algorithm, named phaselift, for the characterisation of linear optical circuits particularly favourable for integrated programmable devices. The algorithm relies on a trusted input state preparation superpose across the modes of the system but can be performed with a classical source of light and photodotectors facilitating its application to large scale systems. The comparable results derived from alternative sets of input states (drawn from the uniform and the RECR distributions) confirm that a low complexity state preparation stage can be adopted. Furthermore we suggest that the same technique could in principle offer an insight on unpredicted behaviour of the system, due to hidden degrees of freedoms, that are possible cause of detrimented results in quantum interference experiment. Based on a mathematical proof we provide about optical circuits interfaced to multimode detectors, the information retrieved from the phaselift algorithm would suffice to predict the multiphoton statistic of these optical systems. We showed how the same mathematical relation might be used to lower the computational cost of validating large size boson sampling with binned output statistics.

On the characterisation side, we also implemented a procedure to quantify the effect of linear and quadratic crosstalk, relatable to electrical and thermal effects. Keeping pace with the improvements in photonic designs will require increasingly accurate strategies to bound

the error levels. The procedure is able to detect small changes of the phase encoded in the MZI, caused by voltage applied to other heaters, and translate that in an effective correction for the MZI setting.

In Chapter 5, we presented an example of simulation of physical system relevant for industry and society constituting a promising example of pre-universal application of integrated optics quantum technology. We proposed and tested a mapping between molecular vibrations in harmonic approximation and multi-photon interference in linear optical device. We then enriched the complexity of the simulated model by introducing techniques to take into account the anharmonicity of the interatomic potential and the interaction between the molecule and the environment. The sampling from the statistics generated by our quantum simulator can be used in an hybrid algorithm as we showed in a molecule dissociation simulation.

In Chapter 6, we investigated quantum solutions for the simulation of models beyond the standard prescription of quantum mechanics. We adapted our photonic circuit to simulate models of non-unitary evolution of parity-time symmetric systems with two and three levels governed by non-Hermitian Hamiltonians. We then implemented the simulation of a non-Hermitian qubit with an optimised time varying Hamiltonian in order to contrast a noisy environment and preserve the coherence of the system. We also showed that the dilation procedure and the post-selection adopted for the simulation of the parity-time symmetric system can be used to give rise to a larger family of density matrix evolution laws.

Finally, in Chapter 7, we addressed some of the limitation of linear optics that is the probabilistic generation of resource states. We proposed an open system simulation scheme that compromise multiple simulation instances in favour of shorter depth circuit. We designed a circuit that implements such scheme using probabilistic single photon sources and a family of post-selected gates that operate as idle when ancillary photons are not provided. We numerically showed that it is in principle possible to use these methods to achieve an exponential improvement of the successful event rate from the simulation.Although, the actual performance will depend on the details of the simulation.

The results presented in this document can guide the implementation of open system analogue simulations on larger programmable integrated photonic circuits, and provides tools to gauge the quality of the future devices. We conclude noting that the last ten years have witnessed a rapid increase in the complexity of linear optical experiments [108, 207, 208]. However, game-changing results such as the incorporation of feedforward schemes or deterministic photon-photon interaction in a monolithic architecture are crucial to close the performance gap with alternative quantum technology platforms such as trapped ions and superconducting qubits.

APPENDIX A

SIMULATION OF MOLECULAR VIBRATION: COMPLEMENTARY INFORMATION

In Sec. 5.3.1 we simulated the evolution of a molecule in a dephasing environment. We used a simplified equation described in Eq. 5.9. We see that the operators

$$\hat{Z}_k = \exp\left(\frac{2\pi i k}{6}\sum_{g=0}^{5} a_g^\dagger a_g\, g\right) = \exp\left(\frac{2\pi i k}{6}\sum_{g=0}^{5} n_g\, g\right) \tag{A.1}$$

commute with the Hamiltonian of the normal modes of the molecule. In particular $\hat{Z}_0$ is the identity operator. The solution to the differential equation is given by

$$\rho(t) = \frac{1-e^{-\Gamma t}}{6}\sum_{k=0}^{5} \hat{Z}_k e^{-i\hat{H}t}\rho(0)e^{i\hat{H}t}\hat{Z}_k^\dagger + e^{-\Gamma t}e^{-i\hat{H}t}\rho(0)e^{i\hat{H}t}. \tag{A.2}$$

To show this, we note that for a generic state ρ,

$$\begin{aligned}\sum_{k=0}^{5}\left[\hat{Z}_k\left(\sum_{n=0}^{5}\hat{Z}_n\rho\hat{Z}_n^\dagger\right)\hat{Z}_k^\dagger - \sum_{n=0}^{5}\hat{Z}_n\rho\hat{Z}_n^\dagger\right] &= \sum_{k=0}^{5}\left[\left(\sum_{n=0}^{5}\hat{Z}_{n\oplus k}\rho\hat{Z}_{n\oplus k}^\dagger\right) - \sum_{n=0}^{5}\hat{Z}_n\rho\hat{Z}_n^\dagger\right] \\ &= \sum_{k=0}^{5}\left[\sum_{m=0}^{5}\hat{Z}_m\rho\hat{Z}_m^\dagger - \sum_{n=0}^{5}\hat{Z}_n\rho\hat{Z}_n^\dagger\right] = 0,\end{aligned} \tag{A.3}$$

where $\oplus$ is used to represent the sum modulo 6 and we used the property that $\hat{Z}_{n+6} = \hat{Z}_n$. Substituting Eq. A.2 in the left hand side term Eq. 5.9, using the relation Eq. A.3, we get to relation

$$\dot{\rho} = -i\left[\hat{H},\rho\right] + \frac{\Gamma}{6}e^{-\Gamma t}\sum_{k=0}^{5}\left(\hat{Z}_k e^{-i\hat{H}t}\rho(0)e^{i\hat{H}t}\hat{Z}_k^\dagger - e^{-i\hat{H}t}\rho(0)e^{i\hat{H}t}\right) \tag{A.4}$$

Also, the time derivative of $\rho(t)$ from equation Eq. A.2 reads:

$$\begin{aligned}\dot{\rho}(t) &= -i\left[H,\rho(t)\right] + \frac{\Gamma e^{-\Gamma t}}{6}\sum_{k=0}^{5}\hat{Z}_k e^{-i\hat{H}t}\rho(0)e^{i\hat{H}t}\hat{Z}_k^{\dagger} - \Gamma e^{-\Gamma t}e^{-i\hat{H}t}\rho(0)e^{i\hat{H}t} \\ &= -i\left[H,\rho(t)\right] + \frac{\Gamma e^{-\Gamma t}}{6}\sum_{k=0}^{5}\left(\hat{Z}_k e^{-i\hat{H}t}\rho(0)e^{i\hat{H}t}\hat{Z}_k^{\dagger} - e^{-i\hat{H}t}\rho(0)e^{i\hat{H}t}\right).\end{aligned} \tag{A.5}$$

proving that Eq. A.2 is the solution of Eq. 5.9 with initial state $\rho(0)$

APPENDIX B

QUANTUM SIMULATION OF PARITY-TIME SYMMETRIC SYSTEMS: COMPLEMENTARY INFORMATION

We briefly report the expression of $G_N(\gamma,t)$ for these low dimensional cases for which $G_N(\gamma,t)$ has a simple closed form. For $N=2$, since $H_2^2(\gamma)=(1-\gamma^2)I_2$, the time evolution operator in the unbroken symmetry phase is given by

$$G_2\left(\gamma<\gamma_c,t\right)=\cos(\epsilon t)I_2-\frac{i}{\epsilon}\sin(\epsilon t)H_2(\gamma)$$

where $\epsilon=\sqrt{1-\gamma^2}$ and I_N represents the N-dimensional identity matrix. In the broken symmetry phase $\gamma>1$, this can be rewritten using $\Gamma=\sqrt{\gamma^2-1}$ as

$$G_2\left(\gamma>\gamma_c,t\right)=\cosh(\Gamma t)I_2-\frac{i}{\Gamma}\sinh(\Gamma t)H_2(\gamma)$$

At the boundary of these two phases, the exceptional point, the evolution involves neither oscillatory nor exponential terms but increases linearly with time:

$$\lim_{\gamma\to\gamma_{C^-}}G_2\left(\gamma<\gamma_c,t\right)=\lim_{\gamma\to\gamma_{C^+}}G_2\left(\gamma>\gamma_c,t\right)=G_2\left(\gamma_c,t\right)=I_2-i\ t\ H_2(1)$$

For $N=3$, due to the relation $H_3^3(\gamma)=(2-\gamma^2)H_3(\gamma)$, the time evolution operator in the unbroken symmetry phase is given by

$$G_3\left(\gamma<\gamma_c,t\right)=I-i\frac{1}{\epsilon}H_3\left(\gamma\right)\sin(\epsilon t)-\frac{1}{\epsilon^2}H_3^2\left(\gamma\right)(1-\cos(\epsilon t)).$$

where $\epsilon=\sqrt{2-\gamma^2}$. Instead, in the broken symmetry phase $\left(\gamma>\gamma_c=\sqrt{2}\right)$, calling $\Gamma=\sqrt{\gamma^2-2}$, the evolution operator can be written as

$$G_3\left(\gamma>\gamma_c,t\right)=I-i\frac{1}{\Gamma}H_3\left(\gamma\right)\sinh(\Gamma t)+\frac{1}{\Gamma^2}H_3\left(\gamma\right)^2(1-\cosh(\Gamma t)).$$

APPENDIX C

PERTURBATIVE OPEN SYSTEM QUANTUM SIMULATION WITH PHOTONICS: COMPLEMENTARY INFORMATION

Let's consider a finite dimensional Hilbert space $\mathscr{H}$ and the space $\mathscr{B}(\mathscr{H})$ of all linear operators from $\mathscr{H}$ to $\mathscr{H}$. Given a physically valid density matrix ρ (see Sec. 2.1.1), let's assume that L is a linear superoperator from $\mathscr{B}(\mathscr{H})$ to $\mathscr{B}(\mathscr{H})$ that respects the following conditions:

(i) $\forall t$ and physical ρ, $\quad \mathrm{tr}\left[L(t)[\rho]\right] = 0$

(ii) $\forall t$ and physical ρ, $\quad \left(L(t)[\rho]\right)^\dagger = L(t)[\rho]$

(iii) $\exists\ \beta$ such that $\forall t$ and $\forall$ Hermitian operator $A \in \mathscr{B}$, $\quad \frac{\|L(t)[A]\|}{\|A\|} < \beta$

We are now showing that the solution to the differential equation

$$\frac{\partial}{\partial t}\rho = -i\left[H,\rho\right] + L(t)\left[\rho\right] \tag{C.1}$$

with initial condition $\rho(0) = \rho_0$, is given by the limit of the sequence $\rho^{(n)}$ recursively defined as

$$\begin{aligned}
\rho^{(0)} &= U(t)\rho_0 U^\dagger(t) \\
\rho^{(1)} &= \rho^{(0)} + \int_0^t U(t,t_1)L(t_1)[\rho^{(0)}(t_1)]U^\dagger(t,t_1)\mathrm{d}t_1 \\
&\vdots \\
\rho^{(n+1)} &= \rho^{(n)} + \int_0^t U(t,t_n)L(t_n)[\rho^{(n)}(t_n) - \rho^{(n-1)}(t_n)]U^\dagger(t,t_n)\mathrm{d}t_n
\end{aligned} \tag{C.2}$$

where U describes the evolution of the system in the purely Hamiltonian problem ($\frac{\partial}{\partial t}U = -iHU$).

Convergence proof

We first note that in a finite dimensional system, complex Hermitian matrices form a vector space over the real number field and a generic Hermitian operator A can be written as $A = \sum_k \alpha_k \rho_k$ where ρ_k are valid density matrices and α_k are real coefficients. Because of the linearity of L and of the adjunction operation, we can extend the property (ii) to generic Hermitian operators A, indeed:

$$(L(t)[A])^\dagger = \sum_k \alpha_k \left(L(t)[\rho_k]\right)^\dagger = \sum_k \alpha_k L(t)[\rho_k] = L(t)[A]$$

To show that $\rho^{(n)}$ converges for each t, we define an auxiliary sequence $a_n = \left\|\rho^{(n)} - \rho^{(n-1)}\right\|$. Using the invariance of the Frobenius norm under unitary transformations, we see that the following inequality holds:

$$\begin{aligned} a_1(t) &= \left\| \int_0^t U(t,t_1) L(t_1)[\rho^{(0)}(t_1)] U^\dagger(t,t_1) \mathrm{d}t_1 \right\| \\ &\leq \int_0^t \left\| L(t_1)[\rho^{(0)}(t_1)] \right\| \mathrm{d}t_1 \leq \beta \int_0^t \left\|\rho_0\right\| \mathrm{d}t_1 = \beta \left\|\rho_0\right\| t. \end{aligned}$$

We then rely on the inductive hypotheses that

$$a_n(t) \leq \frac{\left\|\rho_0\right\|}{n!} (\beta t)^n$$

to prove that

(C.3)

$$\begin{aligned} a_{n+1} \equiv \left\|\rho^{(n+1)} - \rho^{(n)}\right\| &\leq \int_0^t \left\| L(t) \left[\rho^{(n)}(t_n) - \rho^{(n-1)}(t_n)\right] \right\| \mathrm{d}t_n \leq \beta \int_0^t \left\| \rho^{(n)}(t_n) - \rho^{(n-1)}(t_n) \right\| \mathrm{d}t_n \\ &= \beta \int_0^t a_n(t_n) \mathrm{d}t_n \leq \beta \frac{\left\|\rho_0\right\|}{n!} \int_0^t (\beta t_n)^n \, \mathrm{d}t_n = \frac{\left\|\rho_0\right\|}{(n+1)!} (\beta t)^{n+1} \end{aligned}$$

Hence, we have proven by induction that $a_n(t) \leq \frac{\left\|\rho_0\right\|}{n!} (\beta t)^n \quad \forall t$ and n. Thanks to this, Eq. C.2 can be rewritten obtaining the following inequality:

(C.4)

$$\begin{aligned} \left\|\rho^{(N+n)} - \rho^{(N)}\right\| &= \left\| \sum_{k=N}^{N+n} \int_0^t U(t,t_k) L(t_k) [\rho^{(k)}(t_k) - \rho^{(k-1)}(t_k)] U^\dagger(t,t_k) \mathrm{d}t_k \right\| \\ &\leq \beta \sum_{k=N}^{N+n} \int_0^t a_k(t_k) \mathrm{d}t_k \leq \beta \|\rho_0\| \sum_{k=N}^{N+n} \int_0^t \frac{(\beta t)^k}{k!} \mathrm{d}t_k = \left\|\rho_0\right\| \sum_{k=N}^{N+n} \frac{1}{(k+1)!} (\beta t)^{k+1} \\ &\leq \left\|\rho_0\right\| \frac{(\beta t)^{N+1}}{(N+1)!} \sum_{k=0}^{n} \frac{1}{k!} (\beta t)^k \leq \left\|\rho_0\right\| \frac{(\beta t)^{N+1}}{(N+1)!} e^{\beta t}. \end{aligned}$$

Since $\left\|\rho_0\right\|$ is bounded by the system dimension, for every t, the last term of the inequality can be made arbitrary small by choosing a sufficiently large N and independently from n. This finally proves the convergence of the sequence $\rho^{(n)} \quad \forall t$.

Proving the solution to Eq. C.1

We now verify that the limit of $\rho^{(n)}$ is actually the solution of Eq. C.1. Using the expanded expression

$$\rho^{(n+1)} = \rho^{(0)} + \sum_{k=1}^{k=n} \int_0^t U(t,t_k)L(t_k)[\rho^{(k)}(t_k) - \rho^{(k-1)}(t_k)]U^\dagger(t,t_k)\mathrm{d}t_k$$

we note that because of the linearity of L and of the integral, it reduces to

$$\rho^{(n+1)} = \rho^{(0)} + \int_0^t U(t,t_n)L(t_n)[\rho^{(n)}(t_n)]U^\dagger(t,t_n)\mathrm{d}t_n \tag{C.5}$$

Its derivative is then given by

$$\begin{aligned} \frac{\partial}{\partial t}\rho^{(n+1)}(t) &= -i\left[H,\rho^{(0)}\right] + L(t)[\rho^{(n)}(t)] - i\left[H, \int_0^t U(t,t_n)L(t_n)[\rho^{(n)}(t_n)]U^\dagger(t,t_n)\mathrm{d}t_n\right] \\ &= -i\left[H,\rho^{(n+1)}\right] + L(t)[\rho^{(n)}(t)] \end{aligned} \tag{C.6}$$

where we have used the definition of $\rho^{(0)}$, the relation $\frac{\partial}{\partial t}U = -iHU$ and the Leibniz integral rule. Eq. C.6 proves that, in the limit $n \to \infty$, the sequence $\rho^{(n)}$ tends to the solution of the differential equation Eq. C.1.

Expressing the $\rho^{(n)}$ as a partial sum (parturbative expansion)

The sequence $\rho^{(n)}$ also corresponds to the partial sum of a series defined using the following integrals:

$$\mathrm{I}^{(n)}(t) = \int_0^t \int_0^{t_1} \cdots \int_0^{t_{n-1}} U_{t,t_1}L_{t_1}\left[\ldots U_{t_{n-1},t_n}L_{t_n}\left[\rho^{(0)}(t_n)\right]U^\dagger_{t_{n-1},t_n}\ldots\right]U^\dagger_{t,t_1}\mathrm{d}t_n\ldots\mathrm{d}t_1 \tag{C.7}$$

where the time dependence of the operators has been moved to the subscript for compactness. In particular, we will define $\mathrm{I}^{(0)} = \rho^{(0)}$. By definition, we can see that

$$\mathrm{I}^{(n+1)}(t) = \int_0^t U_{t,t_1}L_{t_1}\left[\mathrm{I}^{(n)}(t_1)\right]U^\dagger_{t,t_1}\mathrm{d}t_1 \tag{C.8}$$

and using this property, we get

$$\begin{aligned} \rho^{(0)} &= U(t,0)\rho_0U^\dagger(t,0) = \mathrm{I}^{(0)} \\ \rho^{(1)} &= \mathrm{I}^{(0)} + \mathrm{I}^{(1)} \\ &\vdots \\ \rho^{(n+1)} &= \left(\sum_{k=0}^{k=n}\mathrm{I}^{(k)}\right) + \int_0^t U(t,t_1)L(t_1)\left[\mathrm{I}^{(n)}(t_1)\right]U^\dagger(t,t_1)\mathrm{d}t_1 = \sum_{k=0}^{k=n+1}\mathrm{I}^{(k)} \end{aligned} \tag{C.9}$$

To be able to physically transform the states according to L we need to introduce a close transformation G such that

$$G(t)[\rho] = \rho + \tau L(t)[\rho],$$

This transformation can then substitute L and lead to the definition of a new integral family:

$$\mathrm{J}^{(n)}(t) = \int_0^t \int_0^{t_1} \cdots \int_0^{t_{n-1}} U_{t,t_1} G_{t_1} \left[\ldots U_{t_{n-1},t_n} G_{t_n} \left[\rho^{(0)}(t_n) \right] U^\dagger_{t_{n-1},t_n} \ldots \right] U^\dagger_{t,t_1} \mathrm{d}t_n \ldots \mathrm{d}t_1. \tag{C.10}$$

Using these it is possible to provide a further alternative expression for $\rho^{(n)}$:

$$\begin{aligned} \rho^{(0)} &= \mathrm{J}^{(0)} \\ \rho^{(1)} &= c_0^{(1)} \mathrm{J}^{(0)} + c_1^{(1)} \mathrm{J}^{(1)} \\ &\vdots \\ \rho^{(n)} &= \sum_{k=0}^{k=n} c_k^{(n)} \mathrm{J}^{(k)}. \end{aligned} \tag{C.11}$$

We note that, similarly to Eq. C.8, the following relation holds:

$$\begin{aligned} \mathrm{J}^{(n+1)}(t) &= \int_0^t U_{t,t_1} G_{t_1} \left[\mathrm{J}^{(n)}(t_1) \right] U^\dagger_{t,t_1} \mathrm{d}t_1 \\ &= \int_0^t U_{t,t_1} \mathrm{J}^{(n)}(t_1) U^\dagger_{t,t_1} \mathrm{d}t_1 + \tau \int_0^t U_{t,t_1} L_{t_1} \left[\mathrm{J}^{(n)}(t_1) \right] U^\dagger_{t,t_1} \mathrm{d}t_1 \end{aligned} \tag{C.12}$$

Determining the expansion coefficients

To find the expression of the $c_k^{(n)}$ coefficients, we need to rewrite the $\mathrm{J}^{(n)}$ integrals as sum of $\mathrm{I}^{(k)}$ integrals. For this scope, we are going to prove that:

$$\mathrm{J}^{(n)}(t) = \sum_{k=0}^{k=n} \left(\frac{t^{n-k} \tau^k}{(n-k)!} \mathrm{I}^{(k)} \right). \tag{C.13}$$

To demonstrate this identity we will make use of the following chain of equations:

(C.14)

$$\begin{aligned} &\int_0^t \frac{t_1^m}{m!} U_{t,t_1} \mathrm{I}^{(n+1)}(t_1) U^\dagger_{t,t_1} \mathrm{d}t_1 + \int_0^t \frac{t_1^{m+1}}{(m+1)!} U_{t,t_1} L(t_1) \left[\mathrm{I}^{(n)}(t_1) \right] U^\dagger_{t,t_1} \mathrm{d}t_1 \\ &= \int_0^t \frac{t_1^m}{m!} \left(\int_0^{t_1} U_{t,t_2} L(t_2) \left[\mathrm{I}^{(n)}(t_2) \right] U^\dagger_{t,t_2} \mathrm{d}t_2 \right) \mathrm{d}t_1 + \int_0^t \frac{t_1^{m+1}}{(m+1)!} U_{t,t_1} L(t_1) \left[\mathrm{I}^{(n)}(t_1) \right] U^\dagger_{t,t_1} \mathrm{d}t_1 \\ &= \int_0^t \frac{\mathrm{d}}{\mathrm{d}t_1} \left[\frac{t_1^{m+1}}{(m+1)!} \left(\int_0^{t_1} U_{t,t_2} L(t_2) \left[\mathrm{I}^{(n)}(t_2) \right] U^\dagger_{t,t_2} \mathrm{d}t_2 \right) \right] \mathrm{d}t_1 \\ &= \frac{t^{m+1}}{(m+1)!} \left(\int_0^t U_{t,t_2} L(t_2) \left[\mathrm{I}^{(n)}(t_2) \right] U^\dagger_{t,t_2} \mathrm{d}t_2 \right) = \frac{t^{m+1}}{(m+1)!} \mathrm{I}^{(n+1)} \end{aligned}$$

We note that for $n = 0$ the relation in Eq. C.13 is true by definition. Also, once $\mathrm{J}^{(0)}(t_1) = \rho^{(0)}(t_1)$ is replaced in Eq. C.12, it is visible that Eq. C.13 is valid also for $n = 1$. Finally, using

Eq. C.13 as inductive hypotheses and sequentially using Eq. C.12 and Eq. C.14, we have

(C.15)

$$\begin{aligned}
\mathrm{J}^{(n+1)}(t) &= \sum_{k=0}^{k=n} \frac{\tau^k}{(n-k)!} \left(\int_0^t t_1^{n-k} U_{t,t_1} \mathrm{I}^{(k)}(t_1) U_{t,t_1}^\dagger \mathrm{d}t_1 + \tau \int_0^t t_1^{n-k} U_{t,t_1} L_{t_1} \left[\mathrm{I}^{(k)}(t_1) \right] U_{t,t_1}^\dagger \mathrm{d}t_1 \right) \\
&= \int_0^t \frac{t_1^n}{n!} \mathrm{I}^{(0)}(t) \mathrm{d}t_1 + \sum_{k=0}^{k=n-1} \tau^{k+1} \left(\int_0^t \frac{t_1^{n-k-1}}{(n-k-1)!} U_{t,t_1} \mathrm{I}^{(k+1)}(t_1) U_{t,t_1}^\dagger \mathrm{d}t_1 \right) \\
&+ \sum_{k=0}^{k=n-1} \tau^{k+1} \left(\int_0^t \frac{t_1^{n-k}}{(n-k)!} U_{t,t_1} L_{t_1} \left[\mathrm{I}^{(k)}(t_1) \right] U_{t,t_1}^\dagger \mathrm{d}t_1 \right) + \tau^{n+1} \int_0^t U_{t,t_1} L_{t_1} \left[\mathrm{I}^{(n)}(t_1) \right] U_{t,t_1}^\dagger \mathrm{d}t_1 \\
&= \frac{t^{n+1}}{(n+1)!} \mathrm{I}^{(0)} + \sum_{k=0}^{k=n-1} \tau^{k+1} \frac{t_1^{n-k}}{(n-k)!} \mathrm{I}^{(k+1)} + \tau^{n+1} \mathrm{I}^{(n+1)} \\
&= \sum_{k=0}^{k=n+1} \left(\frac{t^{n+1-k} \tau^k}{(n+1-k)!} \mathrm{I}^{(k)} \right)
\end{aligned}$$

proving the validity of Eq. C.13 $faralln$.

The expression for the coefficients $c_x^{(n)}$ can be found solving the following equation:

$$\rho^{(n)} = \sum_{x=0}^{x=n} c_x^{(n)} \sum_{k=0}^{k=x} \left(\frac{t^{x-k} \tau^k}{(x-k)!} \mathrm{I}^{(k)} \right) = \sum_{x=0}^{n} \mathrm{I}^{(x)}. \tag{C.16}$$

The same problem, where a solution independent from the values of $\mathrm{I}^{(n)}$ is required, can be formulated as a list $n+1$ non-homogeneous linear equation indexed by $0 \leq k \leq n$:

$$\sum_{x=k}^{x=n} c_x^{(n)} \left(\frac{t^{x-k} \tau^k}{(x-k)!} \right) = 1 \tag{C.17}$$

The system is described by a triangular matrix, therefore we can write a recursive relation for the elements of the solution:

$$\begin{aligned}
&k = n \implies \quad c_n^{(n)} = \tau^{-n} \\
&k = m-1 \implies \quad c_{m-1}^{(n)} = \tau^{1-m} \left(1 - \sum_{x=m}^{x=n} c_x^{(n)} \frac{t^{x-m+1} \tau^{m-1}}{(x-m+1)!} \right).
\end{aligned} \tag{C.18}$$

For convenience, we will make a change of notation $d_k^{(n)} = c_{n-k}^{(n)}$ so that the recursive relation reads:

$$d_{k+1}^{(n)} = \frac{1}{\tau^{n-k-1}} \left(1 - \sum_{x=n-k}^{x=n} d_{n-x}^{(n)} \frac{t^{x-n+k+1} \tau^{n-k-1}}{(x-n+k+1)!} \right) = \frac{1}{\tau^{n-k-1}} \left(1 - \sum_{q=0}^{q=k} d_q^{(n)} \frac{t^{k+1-q} \tau^{n-k-1}}{(1+k-q)!} \right). \tag{C.19}$$

We have already showed that $d_0^{(n)} = \tau^{-n}$. Our intention it is now to show that the explicit form of $d_k^{(n)}$ is given by:

$$d_k^{(n)} = \frac{1}{\tau^{n-k}} \sum_{p=0}^{p=k} \frac{1}{p!} \left(-\frac{t}{\tau} \right)^p \tag{C.20}$$

We will operate by induction assuming that the above relation is true from $k = 0$ up to $k = m < n$ and we will show that this implies that Eq. C.20 is also satisfied for $k = m + 1$. By replacing our inductive hypotheses in Eq. C.19 we obtain:

$$d_{m+1}^{(n)} = \frac{1}{\tau^{n-m-1}}\left(1 - \sum_{q=0}^{q=m}\left(\frac{t^{m+1-q}\tau^{n-m-1}}{\tau^{n-q}\,(m+1-q)!} \times \sum_{p=0}^{p=q}\frac{1}{p!}\left(-\frac{t}{\tau}\right)^{p}\right)\right) \tag{C.21}$$

By redefining the extremes of the two nested sums, and using the expansion formula of a binomial power, the following equations are deduced:

(C.22)

$$\begin{aligned}
d_{m+1}^{(n)} &= \frac{1}{\tau^{n-m-1}}\left(1 - \sum_{q=0}^{q=m}\left(\left(\frac{t}{\tau}\right)^{m+1-q}\frac{1}{(m+1-q)!} \times \sum_{x=0}^{x=q}\frac{1}{(q-x)!}\left(-\frac{t}{\tau}\right)^{q-x}\right)\right) && < \text{defining } x = q - p \\
&= \frac{1}{\tau^{n-m-1}}\left(1 - \sum_{x=0}^{x=m}\left(\left(\frac{t}{\tau}\right)^{m+1-x} \times \sum_{q=x}^{q=m}\frac{1}{(m+1-q)!}\frac{1}{(q-x)!}(-1)^{q-x}\right)\right) && < \text{swap the summation order} \\
&= \frac{1}{\tau^{n-m-1}}\left(1 - \sum_{x=0}^{x=m}\left(\left(\frac{t}{\tau}\right)^{m+1-x} \times \sum_{g=0}^{q=m-x}\frac{1}{(m+1-g-x)!}\frac{(-1)^{g}}{g!}\right)\right) && < \text{defining } g = q - x \\
&= \frac{1}{\tau^{n-m-1}}\left(1 - \sum_{x=0}^{x=m}\left(\left(\frac{t}{\tau}\right)^{m+1-x}\frac{1}{(m+1-x)!}\left((1-1)^{m+1-x} - (-1)^{m+1-x}\right)\right)\right) \\
&= \frac{1}{\tau^{n-m-1}}\left(1 + \sum_{x=0}^{x=m}\left(\left(-\frac{t}{\tau}\right)^{m+1-x}\frac{1}{(m+1-x)!}\right)\right) \\
&= \frac{1}{\tau^{n-m-1}}\left(1 + \sum_{k=1}^{k=m+1}\left(-\frac{t}{\tau}\right)^{k}\frac{1}{(k)!}\right) = \frac{1}{\tau^{n-m-1}}\left(\sum_{k=0}^{k=m+1}\left(-\frac{t}{\tau}\right)^{k}\frac{1}{(k)!}\right)
\end{aligned}$$

proving that Eq. C.20 is valid $\forall k \leq n$

BIBLIOGRAPHY

[1] J. P. Lowe and K. A. Peterson, *Quantum chemistry*.
Elsevier Academic Press, 3rd edn. ed., 2006.

[2] J. M. Hollas, *Modern spectroscopy*.
Chichester: J. Wiley, 4th edn. ed., 2004.

[3] L. Wang, "Quenching methods for chemical reaction dynamics within mixed quantum/classical approximation," *Phys. Chem. Chem. Phys.*, vol. 2, pp. 2883–2892, 2000.

[4] R. G. Arns, "The other transistor: early history of the metal-oxide semiconductor field-effect transistor," *Engineering Science and Education Journal*, vol. 7, pp. 233–240, Oct 1998.

[5] T. H. Maiman, "Stimulated optical radiation in ruby," *Nature*, vol. 187, pp. 493–494, 1960.

[6] A. V. Eletskiĭ, "Excimer lasers," *Soviet Physics Uspekhi*, vol. 21, pp. 502–521, jun 1978.

[7] J. S. Lilley, *Nuclear physics : principles and applications.*
Wiley (Manchester Physics Series), 2013.

[8] P. K. Nayak, S. Mahesh, H. J. Snaith, and D. Cahen, "Photovoltaic solar cell technologies: analysing the state of the art," *Nature Reviews Materials*, vol. 4, no. 4, pp. 269–285, 2019.

[9] A. Shukla and U. Kumar, "Positron emission tomography: An overview," *Journal of Medical Physics*, vol. 31, no. 1, pp. 13–21, 2006.

[10] P. A. Bottomley, "Nmr imaging techniques and applications: A review," *Review of Scientific Instruments*, vol. 53, no. 9, pp. 1319–1337, 1982.

[11] N. Brunner, D. Cavalcanti, S. Pironio, V. Scarani, and S. Wehner, "Bell nonlocality," *Rev. Mod. Phys.*, vol. 86, pp. 419–478, Apr 2014.

[12] B. Hensen, H. Bernien, A. E. Dreaú, A. Reiserer, N. Kalb, M. S. Blok, J. Ruitenberg, R. F. Vermeulen, R. N. Schouten, C. Abellán, W. Amaya, V. Pruneri, M. W. Mitchell, M. Markham, D. J. Twitchen, D. Elkouss, S. Wehner, T. H. Taminiau, and R. Hanson, "Loophole-free Bell inequality violation using electron spins separated by 1.3 kilometres," *Nature*, vol. 526, no. 7575, pp. 682–686, 2015.

[13] T. Heine, "Grand challenges in computational materials science: From description to prediction at all scales," *Frontiers in Materials*, vol. 1, p. 7, 2014.

[14] M. Arndt, A. Ekers, W. von Klitzing, and H. Ulbricht, "Focus on modern frontiers of matter wave optics and interferometry," *New Journal of Physics*, vol. 14, p. 125006, dec 2012.

[15] O. Morsch and M. Oberthaler, "Dynamics of bose-einstein condensates in optical lattices," *Rev. Mod. Phys.*, vol. 78, pp. 179–215, Feb 2006.

[16] H. Bernien, B. Hensen, W. Pfaff, G. Koolstra, M. S. Blok, L. Robledo, T. H. Taminiau, M. Markham, D. J. Twitchen, L. Childress, and R. Hanson, "Heralded entanglement between solid-state qubits separated by three metres," *Nature*, vol. 497, no. 7447, pp. 86–90, 2013.

[17] D. DiVincenzo and IBM, "The physical implementation of quantum computation," *Fortschritte der Physik*, vol. 48, 03 2000.

[18] T. D. Ladd, F. Jelezko, R. Laflamme, Y. Nakamura, C. Monroe, and J. L. O'Brien, "Quantum computers," *Nature*, vol. 464, no. 7285, pp. 45–53, 2010.

[19] A. Montanaro, "Quantum algorithms: An overview," *npj Quantum Information*, vol. 2, no. 1, pp. 1–8, 2016.

[20] A. Finnila, M. Gomez, C. Sebenik, C. Stenson, and J. Doll, "Quantum annealing: A new method for minimizing multidimensional functions," *Chemical Physics Letters*, vol. 219, no. 5, pp. 343 – 348, 1994.

[21] J. I. Cirac and P. Zoller, "Goals and opportunities in quantum simulation," *Nature Physics*, vol. 8, 2012.

[22] J. Preskill, "Quantum computing in the nisq era and beyond," 2018.

[23] R. P. Feynman, "Simulating physics with computers," *International Journal of Theoretical Physics*, vol. 21, pp. 467–488, Jun 1982.

[24] A. Politi, M. J. Cryan, J. G. Rarity, S. Yu, and J. L. O'Brien, "Silica-on-silicon waveguide quantum circuits," *Science*, vol. 320, no. 5876, pp. 646–649, 2008.

[25] N. C. Harris, G. R. Steinbrecher, M. Prabhu, Y. Lahini, J. Mower, D. Bunandar, C. Chen, F. N. Wong, T. Baehr-Jones, M. Hochberg, S. Lloyd, and D. Englund, "Quantum transport simulations in a programmable nanophotonic processor," *Nature Photonics*, vol. 11, no. 7, pp. 447–452, 2017.

[26] C. Shen, Z. Zhang, and L.-M. Duan, "Scalable implementation of boson sampling with trapped ions," *Phys. Rev. Lett.*, vol. 112, p. 050504, Feb 2014.

[27] Y. Shen, Y. Lu, K. Zhang, J. Zhang, S. Zhang, J. Huh, and K. Kim, "Quantum optical emulation of molecular vibronic spectroscopy using a trapped-ion device," *Chem. Sci.*, vol. 9, pp. 836–840, 2018.

[28] S. Ding, G. Maslennikov, R. Hablützel, H. Loh, and D. Matsukevich, "Quantum parametric oscillator with trapped ions," *Phys. Rev. Lett.*, vol. 119, p. 150404, Oct 2017.

[29] M. Hofheinz, E. M. Weig, M. Ansmann, R. C. Bialczak, E. Lucero, M. Neeley, A. D. O'Connell, H. Wang, J. M. Martinis, and A. N. Cleland, "Generation of Fock states in a superconducting quantum circuit," *Nature*, vol. 454, no. 7202, pp. 310–314, 2008.

[30] X. Gu, A. F. Kockum, A. Miranowicz, Y. xi Liu, and F. Nori, "Microwave photonics with superconducting quantum circuits," *Physics Reports*, vol. 718-719, pp. 1 – 102, 2017.

[31] S. Goldstein, S. Korenblit, Y. Bendor, H. You, M. R. Geller, and N. Katz, "Decoherence and interferometric sensitivity of boson sampling in superconducting resonator networks," *Phys. Rev. B*, vol. 95, p. 020502, Jan 2017.

[32] C. M. Bender and S. Boettcher, "Real spectra in non-hermitian hamiltonians having PT symmetry," *Physical Review Letters*, vol. 80, no. 24, pp. 5243–5246, 1998.

[33] I. Rotter and J. P. Bird, "A review of progress in the physics of open quantum systems: Theory and experiment," *Reports on Progress in Physics*, vol. 78, no. 11, 2015.

[34] M. A. Nielsen and I. L. Chuang, *Quantum Computation and Quantum Information*. Cambridge, UK: Cambridge University Press, 10th anniversary. ed., 2010.

[35] M. Schlosshauer, *Decoherence and the Quantum-To-Classical Transition*. Berlin, Germany: Springer, the frontiers collection. ed., 2007.

[36] D. F. Walls and G. J. Milburn, *Quantum optics*. Berlin, Germany: Springer, 2nd ed., 2008.

[37] B. E. A. Saleh and M. C. Teich, *Fundamentals of photonics*. Chicester: Wiley (Wiley Series in Pure and Applied Optics), 2nd ed., 2013.

[38] R. Horodecki, P. Horodecki, M. Horodecki, and K. Horodecki, "Quantum entanglement," *Rev. Mod. Phys.*, vol. 81, pp. 865–942, Jun 2009.

[39] M. Brune, S. Haroche, J. M. Raimond, L. Davidovich, and N. Zagury, "Manipulation of photons in a cavity by dispersive atom-field coupling: Quantum-nondemolition measurements and generation of "schrödinger cat" states," *Phys. Rev. A*, vol. 45, pp. 5193–5214, Apr 1992.

[40] G. Nogues, A. Rauschenbeutel, S. Osnaghi, M. Brune, J. M. Raimond, and S. Haroche, "Seeing a single photon without destroying it," *Nature*, vol. 400, no. 6741, pp. 239–242, 1999.

[41] C. Guerlin, J. Bernu, S. Deléglise, C. Sayrin, S. Gleyzes, S. Kuhr, M. Brune, J. M. Raimond, and S. Haroche, "Progressive field-state collapse and quantum non-demolition photon counting," *Nature*, vol. 448, no. 7156, pp. 889–893, 2007.

[42] J.-P. Poizat, J.-F. Roch, and P. Grangier, "Quantum non-demolition measurements in optics and quantum optical repeaters," *Fundamentals of Quantum Optics III*, pp. 289–305, 2007.

[43] G. Lindblad, "On the generators of quantum dynamical semigroups," *Comm. Math. Phys.*, vol. 48, no. 2, pp. 119–130, 1976.

[44] B. L. Hu, J. P. Paz, and Y. Zhang, "Quantum brownian motion in a general environment: Exact master equation with nonlocal dissipation and colored noise," *Phys. Rev. D*, vol. 45, pp. 2843–2861, Apr 1992.

[45] L. Diósi, N. Gisin, and W. T. Strunz, "Non-markovian quantum state diffusion," *Phys. Rev. A*, vol. 58, pp. 1699–1712, Sep 1998.

[46] J. J. Schäffer, "On unitary dilations of contractions," *Proceedings of the American Mathematical Society*, vol. 6, no. 2, pp. 322–322, 1955.

[47] A. Einstein, "Über einen die erzeugung und verwandlung des lichtes betreffenden heuristischen gesichtspunkt," *Annalen der Physik*, vol. 322, no. 6, pp. 132–148, 1905.

[48] O. Richardson and K. T. Compton, "Liii. the photoelectric effect," *The London, Edinburgh, and Dublin Philosophical Magazine and Journal of Science*, vol. 24, no. 142, pp. 575–594, 1912.

[49] R. A. Millikan, "A direct determination of "h."," *Phys. Rev.*, vol. 4, pp. 73–75, Jul 1914.

[50] P. A. M. Dirac, *The Principles of Quantum Mechanics*.
Clarendon Press, 1930.

[51] F. Schwabl, *Advanced Quantum Mechanics*.
Berlin, Heidelberg: Springer Berlin Heidelberg, second ed. advanced texts in physics ed., 2004.

[52] A. Einstein, B. Podolsky, and N. Rosen, "Can quantum-mechanical description of physical reality be considered complete?," *Phys. Rev.*, vol. 47, pp. 777–780, May 1935.

[53] Z. Y. Ou, S. F. Pereira, H. J. Kimble, and K. C. Peng, "Realization of the einstein-podolsky-rosen paradox for continuous variables," *Phys. Rev. Lett.*, vol. 68, pp. 3663–3666, Jun 1992.

[54] M. S. Kim, W. Son, V. Bužek, and P. L. Knight, "Entanglement by a beam splitter: Nonclassicality as a prerequisite for entanglement," *Phys. Rev. A*, vol. 65, p. 032323, Feb 2002.

[55] G. Masada, K. Miyata, A. Politi, T. Hashimoto, J. L. O'Brien, and A. Furusawa, "Continuous-variable entanglement on a chip," *Nature Photonics*, vol. 9, no. 5, pp. 316–319, 2015.

[56] S. Stanisic, N. Linden, A. Montanaro, and P. S. Turner, "Generating entanglement with linear optics," *Phys. Rev. A*, vol. 96, p. 043861, Oct 2017.

[57] S. Scheel, "Permanents in linear optical networks," *arXiv*, 2004.

[58] C. K. Hong, Z. Y. Ou, and L. Mandel, "Measurement of subpicosecond time intervals between two photons by interference," *Phys. Rev. Lett.*, vol. 59, pp. 2044–2046, Nov 1987.

[59] E. R. Caianiello, "On quantum field theory — i: explicit solution of dyson's equation in electrodynamics without use of feynman graphs," *Il Nuovo Cimento (1943-1954)*, vol. 10, pp. 1634–1652, Dec 1953.

[60] S. Aaronson and A. Arkhipov, "The computational complexity of linear optics," 2010.

[61] S.-H. Tan and P. P. Rohde, "The resurgence of the linear optics quantum interferometer — recent advances & applications," *Reviews in Physics*, vol. 4, p. 100030, 2019.

[62] S. Scheel, K. Nemoto, W. J. Munro, and P. L. Knight, "Measurement-induced nonlinearity in linear optics," *Physical Review A - Atomic, Molecular, and Optical Physics*, vol. 68, no. 3, p. 13, 2003.

[63] E. Knill, R. Laflamme, L. R. Knill E, and M. G. J, "A scheme for effcient quantum computation with linear optics," *Nature*, vol. 409, no. January, 2001.

[64] T. C. Ralph, N. K. Langford, T. B. Bell, and A. G. White, "Linear optical controlled-not gate in the coincidence basis," *Phys. Rev. A*, vol. 65, p. 062324, Jun 2002.

[65] H. F. Hofmann and S. Takeuchi, "Quantum phase gate for photonic qubits using only beam splitters and postselection," *Phys. Rev. A*, vol. 66, p. 024308, Aug 2002.

[66] J. Wang and Y. Long, "On-chip silicon photonic signaling and processing: a review," *Science Bulletin*, vol. 63, no. 19, pp. 1267 – 1310, 2018.

[67] M. Billah, T. Hoose, T. Onanuga, N. Lindenmann, P. Dietrich, T. Wingert, M. Goedecke, A. Hofmann, U. Troppenz, M. Moehrle, A. Sigmund, W. Freude, and C. Koos, "Multi-chip integration of lasers and silicon photonics by photonic wire bonding," *CLEO: Science and Innovations, CLEO-SI 2015*, vol. 5, no. 7, p. 2267, 2015.

[68] C. A. Finardi, R. R. Panepucci, S. Tenenbaum, and L. T. Zanvettor, "Characterization of ring modulators and broadband photodetectors in silicon photonics for 25 gb/s interconnection," in *2015 SBMO/IEEE MTT-S International Microwave and Optoelectronics Conference (IMOC)*, pp. 1–4, Nov 2015.

[69] J. P. Sprengers, A. Gaggero, D. Sahin, S. Jahanmirinejad, G. Frucci, F. Mattioli, R. Leoni, J. Beetz, M. Lermer, M. Kamp, S. Höfling, R. Sanjines, and A. Fiore, "Waveguide superconducting single-photon detectors for integrated quantum photonic circuits," *Applied Physics Letters*, vol. 99, no. 18, p. 181110, 2011.

[70] C. Schuck, X. Guo, L. Fan, X. Ma, M. Poot, and H. X. Tang, "Quantum interference in heterogeneous superconducting-photonic circuits on a silicon chip," *Nature Communications*, vol. 7, pp. 1–7, 2016.

[71] F. Raffaelli, G. Ferranti, D. H. Mahler, P. Sibson, J. E. Kennard, A. Santamato, G. Sinclair, D. Bonneau, M. G. Thompson, and J. C. F. Matthews, "A homodyne detector integrated onto a photonic chip for measuring quantum states and generating random numbers," *Quantum Science and Technology*, vol. 3, p. 025003, feb 2018.

[72] E. Kuramochi, "Manipulating and trapping light with photonic crystals from fundamental studies to practical applications," *J. Mater. Chem. C*, vol. 4, pp. 11032–11049, 2016.

[73] L. B. Soldano and E. C. M. Pennings, "Optical multi-mode interference devices based on self-imaging: principles and applications," *Journal of Lightwave Technology*, vol. 13, pp. 615–627, April 1995.

[74] R. K. Gupta, S. Chandran, and B. K. Das, "Wavelength-independent directional couplers for integrated silicon photonics," *Journal of Lightwave Technology*, vol. 35, pp. 4916–4923, Nov 2017.

[75] M. Nedeljkovic, C. G. Littlejohns, A. Z. Khokhar, M. Banakar, W. Cao, J. S. Penades, D. T. Tran, F. Y. Gardes, D. J. Thomson, G. T. Reed, H. Wang, and G. Z. Mashanovich, "Silicon-on-insulator free-carrier injection modulators for the mid-infrared," *Opt. Lett.*, vol. 44, pp. 915–918, Feb 2019.

[76] C. Wang, M. Zhang, X. Chen, M. Bertrand, A. Shams-Ansari, S. Chandrasekhar, P. Winzer, and M. Lončar, "Integrated lithium niobate electro-optic modulators operating at CMOS-compatible voltages," *Nature*, vol. 562, no. 7725, pp. 101–104, 2018.

[77] M. Inamoto, T. Maruyama, and K. Iiyama, "Mach-zehnder interferometric optical switch with mems phase shifter," *Optical and Quantum Electronics*, vol. 41, pp. 599–604, Jun 2009.

[78] J. Komma, C. Schwarz, G. Hofmann, D. Heinert, and R. Nawrodt, "Thermo-optic coefficient of silicon at 1550 nm and cryogenic temperatures," *Applied Physics Letters*, vol. 101, no. 4, p. 041905, 2012.

[79] H. Gao, Y. Jiang, Y. Cui, L. Zhang, J. Jia, and L. Jiang, "Investigation on the thermo-optic coefficient of silica fiber within a wide temperature range," *Journal of Lightwave Technology*, vol. 36, pp. 5881–5886, Dec 2018.

[80] G. Gilardi, W. Yao, H. Rabbani Haghighi, X. J. Leijtens, M. K. Smit, and M. J. Wale, "Deep trenches for thermal crosstalk reduction in InP-based photonic integrated circuits," *Journal of Lightwave Technology*, vol. 32, no. 24, pp. 4262–4268, 2014.

[81] F. Chao, "Trench structure improvement of thermo-optic waveguides," *International Journal of Applied Science and Engineering*, vol. 5, no. 1, pp. 1–5, 2007.

[82] R. Marchetti, C. Lacava, L. Carroll, K. Gradkowski, and P. Minzioni, "Coupling strategies for silicon photonics integrated chips [invited]," *Photon. Res.*, vol. 7, pp. 201–239, Feb 2019.

[83] R. N. Patel, T. Schröder, N. Wan, L. Li, S. L. Mouradian, E. H. Chen, and D. R. Englund, "Efficient photon coupling from a diamond nitrogen vacancy center by integration with silica fiber," *Light: Science and Applications*, vol. 5, no. May 2015, pp. 1–6, 2016.

[84] X. Guo, C. L. Zou, C. Schuck, H. Jung, R. Cheng, and H. X. Tang, "Parametric down-conversion photon-pair source on a nanophotonic chip," *Light: Science and Applications*, vol. 6, no. 5, pp. 1–8, 2017.

[85] D. Bonneau, *Integrated quantum photonics at telecommunication wavelength in silicon-on-insulator and lithium niobate platforms.*
PhD thesis, University of Bristol, 2014.

[86] G. P. Agrawal, *Nonlinear fiber optics.*
San Diego:Academic Press (Optics and photonics), 3rd ed., 2001.

[87] M. Borghi, C. Castellan, S. Signorini, A. Trenti, and L. Pavesi, "Nonlinear silicon photonics," *Journal of Optics*, vol. 19, p. 093002, aug 2017.

[88] J. W. Silverstone, D. Bonneau, K. Ohira, N. Suzuki, H. Yoshida, N. Iizuka, M. Ezaki, C. M. Natarajan, M. G. Tanner, R. H. Hadfield, V. Zwiller, G. D. Marshall, J. G. Rarity, J. L. O'brien, and M. G. Thompson, "On-chip quantum interference between silicon photon-pair sources," *Nature Photonics*, vol. 8, no. 2, pp. 104–108, 2014.

[89] J. Wang, S. Paesani, Y. Ding, R. Santagati, P. Skrzypczyk, A. Salavrakos, J. Tura, R. Augusiak, L. Mančinska, D. Bacco, D. Bonneau, J. W. Silverstone, Q. Gong, A. Acín, K. Rottwitt, L. K. Oxenløwe, J. L. O'Brien, A. Laing, and M. G. Thompson, "Multidimensional quantum entanglement with large-scale integrated optics," *Science*, vol. 360, no. 6386, pp. 285–291, 2018.

[90] N. Charles, J. Lawrence, N. Jovanovic, P. G. Tuthill, B. Norris, P. Stewart, S. Gross, and M. Withford, "Techniques for designing physically path-length matched optical circuitry," in *Proceedings of the International Quantum Electronics Conference and Conference on Lasers and Electro-Optics Pacific Rim 2011*, p. C1123, Optical Society of America, 2011.

[91] M. Reck, A. Zeilinger, H. J. Bernstein, and P. Bertani, "Experimental realization of any discrete unitary operator," *Phys. Rev. Lett.*, vol. 73, pp. 58–61, Jul 1994.

[92] W. R. Clements, P. C. Humphreys, B. J. Metcalf, W. S. Kolthammer, and I. A. Walsmley, "Optimal design for universal multiport interferometers," *Optica*, vol. 3, p. 1460, dec 2016.

[93] J. Carolan, C. Harrold, C. Sparrow, E. Martín-López, N. J. Russell, J. W. Silverstone, P. J. Shadbolt, N. Matsuda, M. Oguma, M. Itoh, G. D. Marshall, M. G. Thompson,

J. C. F. Matthews, T. Hashimoto, J. L. O'Brien, and A. Laing, "Universal linear optics," *Science*, vol. 349, no. 6249, pp. 711–716, 2015.

[94] D. Karki, V. Stenger, A. Pollick, and M. Levy, "Thin-film magnetless faraday rotators for compact heterogeneous integrated optical isolators," *Journal of Applied Physics*, vol. 121, no. 23, p. 233101, 2017.

[95] E. Diamanti, H. K. Lo, B. Qi, and Z. Yuan, "Practical challenges in quantum key distribution," *npj Quantum Information*, vol. 2, no. 1, pp. 1–12, 2016.

[96] V. Giovannetti, S. Lloyd, and L. Maccone, "Quantum-enhanced measurements: Beating the standard quantum limit," *Science*, vol. 306, no. 5700, pp. 1330–1336, 2004.

[97] P. W. Shor, "Algorithms for quantum computation: discrete logarithms and factoring," in *Proceedings 35th Annual Symposium on Foundations of Computer Science*, pp. 124–134, Nov 1994.

[98] S. Lloyd, "Universal quantum simulators," *Science*, vol. 273, no. 5278, pp. 1073–1078, 1996.

[99] M. Schuld, I. Sinayskiy, and F. Petruccione, "An introduction to quantum machine learning," *Contemporary Physics*, vol. 56, no. 2, pp. 172–185, 2015.

[100] C. Zoufal, A. Lucchi, and S. Woerner, "Quantum Generative Adversarial Networks for Learning and Loading Random Distributions," *npj Quantum Information*, 2019.

[101] J. R. McClean, J. Romero, R. Babbush, and A. Aspuru-Guzik, "The theory of variational hybrid quantum-classical algorithms," *New Journal of Physics*, vol. 18, p. 023023, feb 2016.

[102] X. S. Ma, B. Dakic, W. Naylor, A. Zeilinger, and P. Walther, "Quantum simulation of the wavefunction to probe frustrated Heisenberg spin systems," *Nature Physics*, vol. 7, no. 5, pp. 399–405, 2011.

[103] A. Peruzzo, J. McClean, P. Shadbolt, M. H. Yung, X. Q. Zhou, P. J. Love, A. Aspuru-Guzik, and J. L. O'Brien, "A variational eigenvalue solver on a photonic quantum processor," *Nature Communications*, vol. 5, no. May, 2014.

[104] F. Cardano, F. Massa, H. Qassim, E. Karimi, S. Slussarenko, D. Paparo, C. de Lisio, F. Sciarrino, E. Santamato, R. W. Boyd, and L. Marrucci, "Quantum walks and wavepacket dynamics on a lattice with twisted photons," *Science Advances*, vol. 1, no. 2, 2015.

[105] J. C. Matthews, K. Poulios, J. D. Meinecke, A. Politi, A. Peruzzo, N. Ismail, K. Wörhoff, M. G. Thompson, and J. L. O'Brien, "Observing fermionic statistics with photons in arbitrary processes," *Scientific Reports*, vol. 3, 2013.

[106] J. Wang, S. Paesani, R. Santagati, S. Knauer, A. A. Gentile, N. Wiebe, M. Petruzzella, J. L. O'brien, J. G. Rarity, A. Laing, and M. G. Thompson, "Experimental quantum Hamiltonian learning," *Nature Physics*, vol. 13, no. 6, pp. 551–555, 2017.

[107] H. Wang, J. Qin, X. Ding, M.-C. Chen, S. Chen, X. You, Y.-M. He, X. Jiang, Z. Wang, L. You, J. J. Renema, S. Hoefling, C.-Y. Lu, and J.-W. Pan, "Boson sampling with 20 input photons in 60-mode interferometers at 10^{14} state spaces," 2019.

[108] L.-K. Chen, Z.-D. Li, X.-C. Yao, M. Huang, W. Li, H. Lu, X. Yuan, Y.-B. Zhang, X. Jiang, C.-Z. Peng, L. Li, N.-L. Liu, X. Ma, C.-Y. Lu, Y.-A. Chen, and J.-W. Pan, "Observation of ten-photon entanglement using thin bib3o6 crystals," *Optica*, vol. 4, pp. 77–83, Jan 2017.

[109] A. Neville, C. Sparrow, R. Clifford, E. Johnston, P. M. Birchall, A. Montanaro, and A. Laing, "Classical boson sampling algorithms with superior performance to near-term experiments," *Nature Physics*, vol. 13, no. 12, pp. 1153–1157, 2017.

[110] P. Clifford and R. Clifford, "The classical complexity of boson sampling," 2017.

[111] H.-S. Zhong, Y. Li, W. Li, L.-C. Peng, Z.-E. Su, Y. Hu, Y.-M. He, X. Ding, W. Zhang, H. Li, L. Zhang, Z. Wang, L. You, X.-L. Wang, X. Jiang, L. Li, Y.-A. Chen, N.-L. Liu, C.-Y. Lu, and J.-W. Pan, "12-photon entanglement and scalable scattershot boson sampling with optimal entangled-photon pairs from parametric down-conversion," *Phys. Rev. Lett.*, vol. 121, p. 250505, Dec 2018.

[112] A. P. Lund, A. Laing, S. Rahimi-Keshari, T. Rudolph, J. L. O'Brien, and T. C. Ralph, "Boson sampling from a gaussian state," *Phys. Rev. Lett.*, vol. 113, p. 100502, Sep 2014.

[113] S. Barkhofen, T. J. Bartley, L. Sansoni, R. Kruse, C. S. Hamilton, I. Jex, and C. Silberhorn, "Driven boson sampling," *Phys. Rev. Lett.*, vol. 118, p. 020502, Jan 2017.

[114] J. Carolan, *Universal linear optics : characterisation, verification and computation*.
PhD thesis, University of Bristol, 2016.

[115] C. Sparrow, *Quantum interference in universal linear optical devices for quantum computation and simulation*.
PhD thesis, Imperial College London, 2017.

[116] P. J. Shadbolt, *Complexity and Control in Quantum Photonics*.
PhD thesis, University of Bristol, 2015.

[117] M. H. Elsheikh, D. A. Shnawah, M. F. M. Sabri, S. B. M. Said, M. H. Hassan, M. B. A. Bashir, and M. Mohamad, "A review on thermoelectric renewable energy: Principle parameters that affect their performance," *Renewable and Sustainable Energy Reviews*, vol. 30, pp. 337 – 355, 2014.

[118] O. optics Shop, "Description of the v-grooved fibre array products." `https://www.ozoptics.com/ALLNEW_PDF/DTS0083.pdf`.

[119] A. Fedrizzi, T. Herbst, M. Aspelmeyer, M. Barbieri, T. Jennewein, and A. Zeilinger, "Anti-symmetrization reveals hidden entanglement," *New Journal of Physics*, vol. 11, 2009.

[120] M. Barbieri, E. Roccia, L. Mancino, M. Sbroscia, I. Gianani, and F. Sciarrino, "What Hong-Ou-Mandel interference says on two-photon frequency entanglement," *Scientific Reports*, vol. 7, no. 1, pp. 1–6, 2017.

[121] M. Tanida, R. Okamoto, and S. Takeuchi, "Highly indistinguishable heralded single-photon sources using parametric down conversion," *Opt. Express*, vol. 20, pp. 15275–15285, Jul 2012.

[122] E. J. Candes, T. Strohmer, and V. Voroninski, "Phaselift: Exact and stable signal recovery from magnitude measurements via convex programming," *Communications on Pure and Applied Mathematics*, vol. 66, 08 2013.

[123] D. Suess, *Due to, or in spite of? The effect of constraints on efficiency in quantum estimation problems*.
PhD thesis, University of Cologne, 2018.

[124] A. Laing and J. L. O'Brien, "Super-stable tomography of any linear optical device," *arXiv*, 2012.

[125] S. Rahimi-Keshari, M. A. Broome, R. Fickler, A. Fedrizzi, T. C. Ralph, and A. G. White, "Direct characterization of linear-optical networks," *Optics Express*, vol. 21, p. 13450, jun 2013.

[126] I. Dhand, A. Khalid, H. Lu, and B. C. Sanders, "Accurate and precise characterization of linear optical interferometers," *Journal of Optics*, vol. 18, no. 3, 2016.

[127] M. Tillmann, C. Schmidt, and P. Walther, "On unitary reconstruction of linear optical networks," *Journal of Optics*, vol. 18, no. 11, 2016.

[128] N. Spagnolo, E. Maiorino, C. Vitelli, M. Bentivegna, A. Crespi, R. Ramponi, P. Mataloni, R. Osellame, and F. Sciarrino, "Learning an unknown transformation via a genetic approach," *Scientific Reports*, vol. 7, no. 1, pp. 1–7, 2017.

[129] D. Gross, F. Krahmer, and R. Kueng, "A Partial Derandomization of PhaseLift Using Spherical Designs," *Journal of Fourier Analysis and Applications*, vol. 21, no. 2, pp. 229–266, 2015.

[130] L. Mandel, "Photon interference and correlation effects produced by independent quantum sources," *Physical Review A*, vol. 28, no. 2, pp. 929–943, 1983.

[131] C. Sparrow, E. Martín-López, N. Maraviglia, A. Neville, C. Harrold, J. Carolan, Y. N. Joglekar, T. Hashimoto, N. Matsuda, J. L. O'Brien, D. P. Tew, and A. Laing, "Simulating the vibrational quantum dynamics of molecules using photonics," *Nature*, vol. 557, pp. 660–667, may 2018.

[132] B. H. Bransden and J. C. J., *Physics of Atoms and Molecules*.
London, UK: Longman, 1983.

[133] B. Cooper and P. J. Knowles, "Benchmark studies of variational, unitary and extended coupled cluster methods," *Journal of Chemical Physics*, vol. 133, no. 23, 2010.

[134] M. Kobus, P. H. Nguyen, and G. Stock, "Coherent vibrational energy transfer along a peptide helix," *The Journal of Chemical Physics*, vol. 134, no. 12, p. 124518, 2011.

[135] A. S. Alnaser, M. Kübel, R. Siemering, B. Bergues, N. G. Kling, K. J. Betsch, Y. Deng, J. Schmidt, Z. A. Alahmed, A. M. Azzeer, J. Ullrich, I. Ben-Itzhak, R. Moshammer, U. Kleineberg, F. Krausz, R. De Vivie-Riedle, and M. F. Kling, "Subfemtosecond steering of hydrocarbon deprotonation through superposition of vibrational modes," *Nature Communications*, vol. 5, no. May, pp. 3–8, 2014.

[136] C. R. Jacob and M. Reiher, "Localizing normal modes in large molecules," *The Journal of Chemical Physics*, vol. 130, no. 8, p. 084106, 2009.

[137] B. Efron, "Second thoughts on the bootstrap," *Statist. Sci.*, vol. 18, pp. 135–140, 05 2003.

[138] J. Lindner, P. Vöhringer, M. S. Pshenichnikov, D. Cringus, D. A. Wiersma, and M. Mostovoy, "Vibrational relaxation of pure liquid water," *Chemical Physics Letters*, vol. 421, no. 4-6, pp. 329–333, 2006.

[139] W. Mizukami and D. P. Tew, "A second-order multi-reference perturbation method for molecular vibrations," *The Journal of Chemical Physics*, vol. 139, no. 19, p. 194108, 2013.

[140] A. Javadi, I. Söllner, M. Arcari, S. L. Hansen, L. Midolo, S. Mahmoodian, G. Kiršansk, T. Pregnolato, E. H. Lee, J. D. Song, S. Stobbe, and P. Lodahl, "Single-photon non-linear optics with a quantum dot in a waveguide," *Nature Communications*, vol. 6, pp. 6–10, 2015.

[141] M. Gullans, D. Chang, F. Koppens, J. Garcia de Abajo, and M. Lukin, "Single-photon nonlinear optics with graphene plasmons," *Physical review letters*, vol. 111, p. 247401, 12 2013.

[142] R. J. Levis, G. M. Menkir, and H. Rabitz, "Selective bond dissociation and rearrangement with optimally tailored, strong-field laser pulses," *Science*, vol. 292, no. 5517, pp. 709–713, 2001.

[143] C. Brif, R. Chakrabarti, and H. Rabitz, "Control of quantum phenomena: past, present and future," *New Journal of Physics*, vol. 12, p. 075008, jul 2010.

[144] M. L. Hause, Y. H. Yoon, and F. F. Crim, "Vibrationally mediated photodissociation of ammonia: The influence of N-H stretching vibrations on passage through conical intersections," *Journal of Chemical Physics*, vol. 125, no. 17, 2006.

[145] J. Huh, G. G. Guerreschi, B. Peropadre, J. R. Mcclean, and A. Aspuru-Guzik, "Boson sampling for molecular vibronic spectra," *Nature Photonics*, vol. 9, no. 9, pp. 615–620, 2015.

[146] J. A. Nelder and R. Mead, "A Simplex Method for Function Minimization," *The Computer Journal*, vol. 7, no. 4, pp. 308–313, 1965.

[147] I. A. Walmsley, A. Eckstein, J. J. Renema, A. A. Valido, J. Huh, W. R. Clements, A. Lita, S. W. Nam, W. S. Kolthammer, and T. Gerrits, "Approximating vibronic spectroscopy with imperfect quantum optics," *Journal of Physics B: Atomic, Molecular and Optical Physics*, vol. 51, no. 24, p. 245503, 2018.

[148] J. Nokkala, F. Arzani, F. Galve, R. Zambrini, S. Maniscalco, J. Piilo, N. Treps, and V. Parigi, "Reconfigurable optical implementation of quantum complex networks," *New Journal of Physics*, vol. 20, no. 5, 2018.

[149] J. A. Stride, P. H. Dallin, and U. A. Jayasooriya, "Intermolecular fermi resonance," *The Journal of Chemical Physics*, vol. 119, no. 5, pp. 2747–2752, 2003.

[150] J. M. Arrazola, T. R. Bromley, and P. Rebentrost, "Quantum approximate optimization with Gaussian boson sampling," *Physical Review A*, vol. 98, no. 1, pp. 1–10, 2018.

[151] P. Bocchieri and A. Loinger, "Quantum recurrence theorem," *Physical Review*, vol. 107, no. 2, pp. 337–338, 1957.

[152] B. Cooper and P. J. Knowles, "Benchmark studies of variational, unitary and extended coupled cluster methods," *Journal of Chemical Physics*, vol. 133, no. 23, 2010.

[153] Y. Ben-Aryeh, A. Mann, and I. Yaakov, "Rabi oscillations in a two-level atomic system with a pseudo-Hermitian Hamiltonian," *Journal of Physics A: Mathematical and General*, vol. 37, no. 50, pp. 12059–12066, 2004.

[154] M. M. Sternheim and J. F. Walker, "Non-Hermitian Hamiltonians, decaying states, and perturbation theory," *Physical Review C*, vol. 6, no. 1, pp. 114–121, 1972.

[155] M. Castagnino and S. Fortin, "Non-Hermitian Hamiltonians in decoherence and equilibrium theory," *Journal of Physics A: Mathematical and Theoretical*, vol. 45, no. 44, 2012.

[156] E. M. Graefe, H. J. Korsch, and A. E. Niederle, "Mean-field dynamics of a non-hermitian bose-hubbard dimer," *Phys. Rev. Lett.*, vol. 101, p. 150408, Oct 2008.

[157] T. Gao, E. Estrecho, K. Y. Bliokh, T. C. Liew, M. D. Fraser, S. Brodbeck, M. Kamp, C. Schneider, S. Höfling, Y. Yamamoto, F. Nori, Y. S. Kivshar, A. G. Truscott, R. G. Dall, and E. A. Ostrovskaya, "Observation of non-Hermitian degeneracies in a chaotic exciton-polariton billiard," *Nature*, vol. 526, no. 7574, pp. 554–558, 2015.

[158] U. D. Jentschura and B. J. Wundt, "Pseudo-hermitian quantum dynamics of tachyonic spin-1/2 particles," *Journal of Physics A: Mathematical and Theoretical*, vol. 45, p. 444017, oct 2012.

[159] K. Jones-Smith and H. Mathur, "Relativistic non-hermitian quantum mechanics," *Phys. Rev. D*, vol. 89, p. 125014, Jun 2014.

[160] C. M. Bender and P. D. Mannheim, "No-ghost theorem for the fourth-order derivative pais-uhlenbeck oscillator model," *Physical Review Letters*, vol. 100, no. 11, pp. 1–4, 2008.

[161] J. Sakurai and J. J. Napolitano, *Modern Quantum Mechanics: Pearson new international edition.*
Harlow, UK: Pearson Education Limited, 2nd edition. ed., 2014.

[162] A. Mostafazadeh, "Pseudo-Hermiticity versus PT symmetry: The necessary condition for the reality of the spectrum of a non-Hermitian Hamiltonian," *Journal of Mathematical Physics*, vol. 43, no. 1, pp. 205–214, 2002.

[163] W. Pauli, "On Dirac's new method of field quantization," *Reviews of Modern Physics*, vol. 15, no. 3, pp. 175–207, 1943.

[164] C. M. Bender and P. D. Mannheim, "Exactly solvable PT-symmetric Hamiltonian having no Hermitian counterpart," *Physical Review D - Particles, Fields, Gravitation and Cosmology*, vol. 78, no. 2, pp. 1–20, 2008.

[165] C. M. Bender, "Making sense of non-Hermitian Hamiltonians," *Reports on Progress in Physics*, vol. 70, no. 6, pp. 947–1018, 2007.

[166] A. Mostafazadeh, "Exact PT-symmetry is equivalent to Hermiticity," *Journal of Physics A: Mathematical and General*, vol. 36, no. 25, pp. 7081–7091, 2003.

[167] S. L. Chen, G. Y. Chen, and Y. N. Chen, "Increase of entanglement by local PT - symmetric operations," *Physical Review A - Atomic, Molecular, and Optical Physics*, vol. 90, no. 5, pp. 1–5, 2014.

[168] Y.-C. Lee, M.-H. Hsieh, S. T. Flammia, and R.-K. Lee, "Local PT Symmetry Violates the No-Signaling Principle," *Physical Review Letters*, vol. 112, no. 13, p. 130404, 2014.

[169] L. Feng, R. El-Ganainy, and L. Ge, "Non-Hermitian photonics based on parity-time symmetry," *Nature Photonics*, vol. 11, no. 12, pp. 752–762, 2017.

[170] H. Jing, S. K. Özdemir, X. Y. Lü, J. Zhang, L. Yang, and F. Nori, "PT -symmetric phonon laser," *Physical Review Letters*, vol. 113, no. 5, pp. 1–5, 2014.

[171] Y. Li, Y. G. Peng, L. Han, M. A. Miri, W. Li, M. Xiao, X. F. Zhu, J. Zhao, A. Alù, S. Fan, and C. W. Qiu, "Anti-parity-time symmetry in diffusive systems," *Science*, vol. 364, no. 6436, pp. 170–173, 2019.

[172] Y. Ashida, S. Furukawa, and M. Ueda, "Parity-time-symmetric quantum critical phenomena," *Nature Communications*, vol. 8, pp. 1–6, 2017.

[173] D. C. Brody and E. M. Graefe, "On complexified mechanics and coquaternions," *Journal of Physics A: Mathematical and Theoretical*, vol. 44, no. 7, 2011.

[174] B. Gardas, S. Deffner, and A. Saxena, "PT -symmetric slowing down of decoherence," *Physical Review A*, vol. 94, no. 4, pp. 1–5, 2016.

[175] C. M. Bender, D. C. Brody, H. F. Jones, and B. K. Meister, "Faster than Hermitian quantum mechanics," *Physical Review Letters*, vol. 98, no. 4, pp. 2–5, 2007.

[176] Y. N. Joglekar, F. A. Onanga, and A. K. Harter, "Time-invariant $\mathscr{PT}$ product and phase locking in $\mathscr{PT}$-symmetric lattice models," *Phys. Rev. A*, vol. 97, p. 012128, Jan 2018.

[177] C. Li and Z. Song, "Generation of Bell, W, and Greenberger-Horne-Zeilinger states via exceptional points in non-Hermitian quantum spin systems," *Physical Review A - Atomic, Molecular, and Optical Physics*, vol. 91, no. 6, pp. 1–7, 2015.

[178] K. Kawabata, Y. Ashida, and M. Ueda, "Information Retrieval and Criticality in Parity-Time-Symmetric Systems," *Physical Review Letters*, vol. 119, no. 19, pp. 1–6, 2017.

[179] M. Partanen, J. Goetz, K. Y. Tan, K. Kohvakka, V. Sevriuk, R. E. Lake, R. Kokkoniemi, J. Ikonen, D. Hazra, A. Mäkinen, E. Hyyppä, L. Grönberg, V. Vesterinen, M. Silveri, and M. Möttönen, "Exceptional points in tunable superconducting resonators," *Physical Review B*, vol. 100, no. 13, pp. 1–17, 2019.

[180] S. Scheel and A. Szameit, "PT-symmetric photonic quantum systems with gain and loss do not exist," *EPL (Europhysics Letters)*, vol. 122, p. 34001, 06 2018.

[181] L. Xiao, X. Zhan, Z. H. Bian, K. K. Wang, X. Zhang, X. P. Wang, J. Li, K. Mochizuki, D. Kim, N. Kawakami, W. Yi, H. Obuse, B. C. Sanders, and P. Xue, "Observation of topological edge states in parity-time-symmetric quantum walks," *Nature Physics*, vol. 13, no. 11, pp. 1117–1123, 2017.

[182] M. Naghiloo, M. Abbasi, Y. N. Joglekar, and K. W. Murch, "Quantum state tomography across the exceptional point in a single dissipative qubit," *Nature Physics*, 2019.

[183] J. Li, A. K. Harter, J. Liu, L. de Melo, Y. N. Joglekar, and L. Luo, "Observation of parity-time symmetry breaking transitions in a dissipative Floquet system of ultracold atoms," *Nature Communications*, vol. 10, no. 1, pp. 1–7, 2019.

[184] F. Klauck, L. Teuber, M. Ornigotti, M. Heinrich, S. Scheel, and A. Szameit, "Observation of PT-symmetric quantum interference," *Nature Photonics*, 2019.

[185] U. Günther and B. F. Samsonov, "Naimark-Dilated PT-Symmetric Brachistochrone," *Physical Review Letters*, vol. 101, no. 23, pp. 1–4, 2008.

[186] Y. Wu, W. Liu, J. Geng, X. Song, X. Ye, C. K. Duan, X. Rong, and J. Du, "Observation of parity-time symmetry breaking in a single-spin system," *Science*, vol. 364, no. 6443, pp. 878–880, 2019.

[187] S. Yu, K. Sun, B.-H. Liu, Y.-J. Han, J.-S. Tang, G. Chen, G.-C. Guo, Y.-N. Sun, D.-Y. He, C.-F. Li, Y.-T. Wang, and J.-S. Xu, "Experimental investigation of the no-signalling principle in parity–time symmetric theory using an open quantum system," *Nature Photonics*, vol. 10, no. 10, pp. 642–646, 2016.

[188] L. Xiao, K. Wang, X. Zhan, Z. Bian, K. Kawabata, M. Ueda, W. Yi, and P. Xue, "Observation of critical phenomena in parity-time-symmetric quantum dynamics," 2018.

[189] J. Wen, C. Zheng, X. Kong, S. Wei, T. Xin, and G. Long, "Experimental demonstration of a digital quantum simulation of a general PT -symmetric system," *Physical Review A*, vol. 99, no. 6, pp. 1–8, 2019.

[190] L. Jin and Z. Song, "Solutions of PT -symmetric tight-binding chain and its equivalent Hermitian counterpart," *Physical Review A - Atomic, Molecular, and Optical Physics*, vol. 80, no. 5, pp. 1–7, 2009.

[191] A. Streltsov, G. Adesso, and M. B. Plenio, "Colloquium: Quantum coherence as a resource," *Rev. Mod. Phys.*, vol. 89, p. 041003, Oct 2017.

[192] U.-J. Wiese, "Towards quantum simulating qcd," *Nuclear Physics A*, vol. 931, pp. 246 – 256, 2014.
QUARK MATTER 2014.

[193] T. Jordan, "Reconstructing a nonlinear dynamical framework for testing quantum mechanics," *Annals of Physics*, vol. 225, no. 1, pp. 83 – 113, 1993.

[194] M. Ziman, P. Štelmachovič, and V. Bužek, "Description of Quantum Dynamics of Open Systems Based on Collision-Like Models," *Open Systems & Information Dynamics*, vol. 12, pp. 81–91, Mar 2005.

[195] S. Lorenzo, F. Ciccarello, and G. M. Palma, "Composite quantum collision models," *Physical Review A*, vol. 96, no. 3, pp. 1–11, 2017.

[196] M. Ziman and V. Bužek, "Open system dynamics of simple collision models," *Quantum Dynamics and Information*, Oct 2010.

[197] T. Rybár, S. N. Filippov, M. Ziman, and V. Bužek, "Simulation of indivisible qubit channels in collision models," *Journal of Physics B: Atomic, Molecular and Optical Physics*, vol. 45, no. 15, 2012.

[198] R. McCloskey and M. Paternostro, "Non-Markovianity and system-environment correlations in a microscopic collision model," *Physical Review A - Atomic, Molecular, and Optical Physics*, vol. 89, no. 5, pp. 1–6, 2014.

[199] G. Karpat, I. Yalçınkaya, and B. Çakmak, "Quantum synchronization in a collision model," *Physical Review A*, vol. 100, no. 1, p. 12133, 2019.

[200] J. Jin and C.-S. Yu, "Non-markovianity in a collision model with environmental block," *New Journal of Physics*, vol. 20, 10 2017.

[201] J. Jin, V. Giovannetti, R. Fazio, F. Sciarrino, P. Mataloni, A. Crespi, and R. Osellame, "All-optical non-markovian stroboscopic quantum simulator," *Phys. Rev. A*, vol. 91, p. 012122, Jan 2015.

[202] Á. Cuevas, A. Geraldi, C. Liorni, L. D. Bonavena, A. De Pasquale, F. Sciarrino, V. Giovannetti, and P. Mataloni, "All-optical implementation of collision-based evolutions of open quantum systems," *Scientific Reports*, vol. 9, no. 1, pp. 1–8, 2019.

[203] K. Hornberger, *Introduction to Decoherence Theory*.
Berlin, Heidelberg: Springer Berlin Heidelberg, 2009.

[204] J. Dalibard, Y. Castin, and K. Mølmer, "Wave-function approach to dissipative processes in quantum optics," *Phys. Rev. Lett.*, vol. 68, pp. 580–583, Feb 1992.

[205] M. B. Plenio and P. L. Knight, "The quantum-jump approach to dissipative dynamics in quantum optics," *Reviews of Modern Physics*, vol. 70, no. 1, pp. 101–144, 1998.

[206] D. Gottesman and I. L. Chuang, "Demonstrating the viability of universal quantum computation using teleportation and single-qubit operations," *Nature*, vol. 402, no. 6760, pp. 390–393, 1999.

[207] J. Carolan, J. D. Meinecke, P. J. Shadbolt, N. J. Russell, N. Ismail, K. Wörhoff, T. Rudolph, M. G. Thompson, J. L. O'Brien, J. C. Matthews, and A. Laing, "On the experimental verification of quantum complexity in linear optics," *Nature Photonics*, vol. 8, no. 8, pp. 621–626, 2014.

[208] C. Reimer, S. Sciara, P. Roztocki, M. Islam, L. Romero Cortés, Y. Zhang, B. Fischer, S. Loranger, R. Kashyap, A. Cino, S. T. Chu, B. E. Little, D. J. Moss, L. Caspani, W. J. Munro, J. Azaña, M. Kues, and R. Morandotti, "High-dimensional one-way quantum processing implemented on d-level cluster states," *Nature Physics*, vol. 15, no. 2, pp. 148–153, 2019.